Signal Theory and Processing

for

Burst-mode and ScanSAR Interferometry

Jürgen Holzner

Ph.D.

The University of Edinburgh

2002

ABSTRACT

ScanSAR data provides wide swath coverage and fast revisit times at the expense of resolution. Moreover, the ENVISAT/ ASAR alternating polarisation mode uses the burst-mode acquisition to map the scene quasi-simultaneous in two polarisations. Both modes are also attractive for interferometric applications, e.g. efficient topographic mapping of large areas and monitoring of large scale motions. A single-pass ScanSAR interferometer was flown during the 11-day Shuttle Radar Topographic Mission (SRTM). Repeat-pass ScanSAR data are routinely available from RADARSAT-1 and ENVISAT/ ASAR and the coming RADARSAT-2 and ALOS/ PALSAR mission will also provide ScanSAR imaging modes.

This thesis provides a complete description of interferometric burst-mode and ScanSAR signal characteristics, algorithms for interferometric processing, and options for the efficient utilisation of the wide-swath data. In the course of the examinations the following problems are addressed: derivation of burst-mode interferogram expectation values, coherence, and power spectral densities; relationship of interferogram spectrum and coherence; revision of standard assumptions in SAR interferometry; Doppler centroid estimation, azimuth scanning pattern synchronisation; common band filtering and resampling in the presence of high squint; beam alignment, timing and baseline optimisation, interferogram formation, and selection of a suitable processing concept for ScanSAR data. A new fast time-variant interpolator for burst-mode data is introduced and tested. Several processing options are described that exploit the flexibility of burst-mode and ScanSAR data. From the two basic processing options available (single burst and multiple coherent burst), a third, hybrid processing options was synthesised that makes efficient use of the burst-mode and ScanSAR data properties. A prototype of this processor was implemented and tested using a RADARSAT-1 ScanSAR Narrow data set. In this way, RADARSAT-1 repeat-pass ScanSAR interferometry is demonstrated. The generated digital elevation model (DEM) has quality better than DTED-1. Moreover, after interferometric processing the ScanSAR interferogram resembles a coarse resolution strip-map interferogram and, hence, possibly all applications of SAR interferometry may benefit from ScanSAR data. In particular, the data is favourable for those applications gaining from the wide swath extend and the fast revisit times or from the increase in information as for the alternating polarisation mode.

Keywords: SAR, ScanSAR, Burst-mode, Interferometry, Signal Theory, Processing, Algorithms, Autocorrelation Function, Power Spectral Density, DEM, RADARSAT-1

DECLARATION

I declare that this thesis has been composed by myself and the work presented and described is my own, unless otherwise stated.

Jürgen Holzner, September 2002

Contents

Preface

My personal experience – My motivation to go on to do a PhD was to find out more about mathematics, physics, and signal processing and to apply my knowledge scientifically, to develop something new. What I found was highly interesting and I immediately got acquainted with SAR as a non-trivial imaging technique, complex signal processing, multi-dimensional signals and properties, estimation methods, and SAR interferometry. It was an adventure to explore ScanSAR interferometry, its theory and processing.

An important experience was conducting this PhD as a joint project with the Remote Sensing Technology Institute at DLR and the Department of Geography at the University of Edinburgh. I got to know many people who became colleagues and friends. I experienced the diversity of research and the different perspectives on remote sensing in both organisations. While as a group member at the Remote Sensing Technology Institute, the aim is to process and provide remote sensing data of the highest quality, in the remote sensing group at the Department of Geography the emphasis is on a specific application, that is, on extracting information from the remote sensing data provided and verifying it in situ measurements.

Every research student at the Department of Geography completes a so-called 'Frontiers Course' which introduced me into the philosophy of Karl Raimund Popper. I enjoyed several excurses into his findings and quote parts of his article on 'Truth, Rationality, and the Growth of Scientific Knowledge' in this thesis which was published in the book 'Conjectures and Refutations'.

Acknowledgements - There are many people who contributed to my PhD years at the Remote Sensing Technology Institute (IMF) DLR at Oberpfaffenhofen and at the Geography Department at the University of Edinburgh in Scotland.

First of all I express my thanks to Tim Malthus (Department of Geography, University of Edinburgh) and Richard Bamler (IMF) for making this joint PhD project possible. I thank both for their research advice and training in scientific writing. In particular, I appreciated Tim Malthus' help in organising all the little things that are necessary to complete a part time PhD over a large distance. I thank him for being a friend, introducing Scotland to me and providing accomodation during my time in Scotland. I am very grateful to Richard Bamler for his enthusiasm and criticism as well as the many insights into burst-mode, SAR, InSAR theory and processing.

I also very much appreciated the help of my colleagues at IMF: Birgit Schättler for many hours of decoding piles of RADARSAT raw data bits and introducing me to the operation of DLRs BSAR processor; Michael Eineder for many technical discussions and for making his fast interferometric phase simulator available; Ulrich Steinbrecher for building a prototype time domain ScanSAR processor; Helko Breit for providing the software libraries for the range compression and a ScanSAR point target simulator and Nico Adam for the support with all the fundamental modules of DLR's GENESIS processor. Thanks also to Walter Knöpfle (DFD/DLR) for mosaicking 550 USGS DTED-2 DEM tiles and his aid with his geo-coding tools. Thank you Conny for being the best secretary Richard Bamler could have found.

I thank Ian Cumming (University of British Columbia, Vancouver/ Canada) for sharing his advice and experience in ScanSAR and SAR during his time as a guest scientist at DLR.

Many thanks to Iain Woodhouse also for his ability to introduce me directly to the roots of radar physics by exploring the Doppler effect in SAR.

I very much appreciated the help of Mihai Datcu in giving me deeper insight into Bayesian statistics and various methods of estimation.

There are several people at the University of Applied Sciences in Nürnberg (FHN) I want to mention. I greatly appreciated the support of Michael Braun for opening up the ScanSAR interferometry project at DLR, Heinz Brünig for his great help with the search for a suitable PhD project, Jürgen Zech for his stimulus and experience when I was beginning my joint German – Scottish PhD undertaking, and, finally, Rolf Brigola and F. Vogler for their advice in applied mathematics and physics during my time at FHN.

Above all, thanks to my family and friends for their encouragement and tolerance during the four years of my doctorate.

And most importantly I want to thank my partner Karin for her strength, steady encouragement, and love.

Structure of the thesis – The first Chapter provides an introduction to the subject of the thesis. Section two outlines the necessary background to SAR interferometry, SAR interferometric processing, as well as to burst-mode and ScanSAR imaging. Chapter three discusses the properties and theoretical aspects of interferometric burst-mode signals and their processing. The equivalence of the two basic processing options for burst-mode data is proven. Section four gives a complete overview of algorithms for interferometric processing of the burst-mode data and their integration into several burst-mode and ScanSAR processing concepts. These concepts are evaluated with respect to their efficiency and prototyping capability. In the following section the processing of an example RADARSAT-1 ScanSAR Narrow data set to a ScanSAR DEM and its evaluation is described. Chapter 6 comprises an overview of previous missions which collected ScanSAR data and supplies recommendations for the processing of ScanSAR and burst-mode data. Chapter 7 discusses and summarises the contributions of the thesis.

List of Symbols

u^*		complex conjugate of the complex number u
$\otimes$		cross-correlation operator : $g(t) \otimes h(t) = \int g^*(t)\, h(t+\tau)\, dt$
$*$		convolution operator : $g(t) * h(t) = \int g^*(t')\, h(t'-t)\, dt$
$\propto$		proportionality : $g(t) = k\, h(t)$
$\approx$		approximation : $\int \lvert g(t) - h(t) \rvert^2\, dt$ ='small'
$(r,x,z)^T = \begin{pmatrix} r \\ x \\ z \end{pmatrix}$		transpose of a vector
$\frac{\partial}{\partial x}$		partial derivative
α	[rad]	terrain angle
β	[rad]	squint angle
$\chi(.)$		complex reflectivity function
$\delta(.)$		Dirac or delta distribution also called impulse function
ε	[rad]	angle between two interferometric orbits
ϕ	[rad]	(interferometric) phase
γ	[1]	coherence
γ'	[1]	phase stability
$\hat{\gamma}'$	[1]	phase stability estimate
λ	[m]	wavelength
$\varphi(.)$	[rad]	azimuth history phase

κ	[s]	mis-registration
		(also used with unit [samples])
θ	[rad]	incidence angle
ρ	[s]	resolution
σ		standard deviation
τ	[s]	azimuth time lag between two samples
		(also used with unit [samples])
ϑ	[s]	slant range time
ξ	[rad]	baseline angle
$\Delta\xi$	[rad]	baseline angle error
$\Delta\hat{\xi}$	[rad]	baseline angle error estimate
υ	[s]	range time lag of two samples
		(also used with unit [samples])
ζ	[rad]	angle measured by an interferometer
$A(.)$		antenna weighting possibly including processor weighting
		for sidelobe surpression
ACF		acronym for autocorrelation function
$\arg(.)$		operator for retrieving the argument or phase of a complex number
$\arg\max_{\kappa}(.)$		operator for retrieving the position κ where the argument is maximum
δaz	[samples]	remaining tiny mutual mis-registrations of the interferometric partners in azimuth direction
$\vec{B}$	[m]	baseline vector
$B(n)$		function representing the burst pattern
B	[m]	baseline length

$B_{\parallel}$	[m]	parallel baseline component
$B_{\perp}$	[m]	perpendicular baseline component
$B_{\perp,crit}$	[m]	critical baseline of an interferometer
ΔB	[m]	baseline lenght error
$\Delta\hat{B}$	[m]	baseline lenght error estimate
c	[m/s]	speed of light
CNR		clutter-to-noise ratio
$d(t)$, $D(f)$		SAR raw data
DFT{.}		discrete Fourier transform
E{.}		expectation value operator
f	[Hz]	frequency variable
f_0	[Hz]	radar frequency
f_ϕ	[Hz]	fringe frequency
f_{DC}	[Hz]	Doppler centroid frequency
$f_{c,rg}$	[Hz]	range spectrum centre frequency
$\Delta f_{c,rg}$	[Hz]	$\Delta f_{c,rg} = f_{c,rg} - f_0$, frequency shift of range spectrum off the radars frequency
F{.}		Fourier transform operator
FM	[Hz/s]	frequency modulation rate
f_z	[Hz]	frequency in z direction (height)
grad(.)		gradient operator
h	[m]	terrain height
$h_{2\pi}$	[m/cycle]	height of ambiguity
$h_A(.)$, $H_A(.)$		impulse response and transfer function of the strip-map SAR end-to-end system ($H_A(.)$ is the Fourier transform of $h_A(.)$)

$h_C(.),\ H_C(.)$	impulse response and transfer function of the burst-mode SAR end-to-end system for multiple coherent burst images ($H_C(.)$ is the Fourier transform of $h_C(.)$)
$h_n(.),\ H_n(.)$	impulse response and transfer function of the burst-mode SAR end-to-end system for a single burst image of index n ($H_n(.)$ is the Fourier transform of $h_n(.)$)
$h_r(.)$	reconstruction kernel for SAR processing
$h_{raw,A}(.), H_{raw,A}(.)$	impulse response and transfer function of the strip-map SAR acquisition system or raw data ($H_{raw,A}(.)$ is the Fourier transform of $h_{raw,A}(.)$)
$h_{raw,C}(.), H_{raw,C}(.)$	impulse response and transfer function of the burst-mode SAR acquisition system or raw data for a burst train ($H_{raw,C}(.)$ is the Fourier transform of $h_{raw,C}(.)$)
$h_{raw,n}(.),\ H_{raw,n}(.)$	impulse response and transfer function of the burst-mode SAR acquisition system or raw data for a single burst image of index n ($H_n(.)$ is the Fourier transform of $h_n(.)$)
$i = u_1\ u_2^*$	interferogram pixel obtained as complex conjugate multiplication of the image pixels of a pair of interferometric SAR images
i_A	interferogram pixel of the strip-map interferogram
i_B	interferogram pixel after multilooking of N_L single burst interferogram pixels i_n
i	interferogram pixel of the multiple coherent burst interferogram
i_n	interferogram pixel of the single burst interferogram

IRF		acronym for impulse response function
$k = \frac{2\pi}{\lambda}$	[rad/m]	wavenumber
K_R	[Hz/s]	range chirp rate
n_{PRF}		index of the PRF band
N_B		number of burst range echo lines
N_L		number of burst looks
N_n		number of range lines of a burst image represented at a sampling frequency of PRF_n
N_P		number of range lines in-between burst acquisitions
N_S		number of swathes
E		energy
PRF	[Hz]	pulse repetition frequency, azimuth sampling frequency
PRF_n	[Hz]	azimuth sampling frequency for the efficient representation of burst mode data; Nyquist frequency
PRF_D	[Hz]	sampling frequency required for detected multiple coherent burst data
PSD		acronym for power spectral density
$q(.)$, $Q(.)$		range weighting window
r , R	[m]	range distance satellite-target, space domain range co-ordinate
$\vec{R}$	[m]	range vector
R_0	[m]	zero Doppler range distance satellite-target, range distance of the satellite with respect to the target at the point of closest approach

$\mathrm{R}_{uu}(.)$		autocorrelation function of the signal u
$R_{uu,C}(.)$		autocorrelation function of multiple coherent burst data $u_C(.)$
$\mathrm{R}_{uu,n}(.)$		autocorrelation function of a single burst
$\hat{\mathrm{R}}_{uu,}[.]$		estimator for the autocorrelation function of a single burst
$\breve{\mathrm{R}}_{uu,n}(.)$		continous time variable equivalent of $\hat{\mathrm{R}}_{uu,}[.]$
$\mathrm{rect}\left(\frac{t}{T}\right)$		rect function $\mathrm{rect}\left(\frac{t}{T}\right)=\begin{cases}1 & for \quad -T/2 \le t \le T/2 \\ 0 & elsewhere\end{cases}$
δrg	[samples]	remaining tiny mutual mis-registrations of the interferometric partners in azimuth direction
$\vec{S}$	[m]	satellite position vector measured from the Earth's centre
$\mathrm{S}_{uu}(.)$		power spectral density (PSD) of the signal u
$\overline{\mathrm{S}}_{uu}(.)$		normalized power spectral density of the signal u
$\widetilde{\mathrm{S}}_{uu}(.)$		approximate power spectral density power spectral density of the signal u
$\mathrm{sinc}(x)=\frac{\sin(\pi x)}{\pi x}$		sinc function
SNR		signal-to-noise ratio
t	[s]	azimuth time variable
$\vec{T}$	[m]	target position vector measured from the Earth's centre
t_c	[s]	SAR acquisition offset time corresponding to the Doppler centroid
T_A	[s]	SAR aperture time
T_B	[s]	burst duration
T_P	[s]	burst cycle time

T_{PRF}	[s]	time duration corresponding to the PRF $T_{PRF} = PRF/\lvert FM\rvert$
$\mathrm{tri}\left(\frac{t}{T}\right)$		tri function $\mathrm{tri}\left(\frac{t}{T}\right) = \begin{cases} 1-\lvert t\rvert & for \quad -T \le t \le T \\ 0 & elsewhere \end{cases}$
x	[m]	space domain azimuth co-ordinate in [m]
u_1 , u_2		SAR image signals of a pair of interferometric partners
v_S	[m/s]	spacecraft or platform velocity
W_A	[Hz]	(processed) azimuth bandwidth of the strip-map SAR system $W_A = \lvert FM\rvert T_A$
W_B	[Hz]	burst bandwidth $W_B = \lvert FM\rvert T_B$
W_D	[Hz]	bandwidth of the detected multiple coherent burst signal
W	[Hz]	frequency period of bursts $W_P = \lvert FM\rvert T_P$
W	[Hz]	range bandwidth

List of Figures

List of Tables

... it is only through a problem that
we become conscious of holding a theory.
It is the problem which challenges us to learn;
to advance our knowledge;
to experiment; and to observe.
- *Truth, Rationality, and the Growth of Scientific Knowledge (Popper 1963).*

Chapter 1

Introduction

1.1 Background

Remote sensing plays an important role in the collection of information about the Earth and other planets of the solar system. Various instruments are installed on probes, satellites, and airborne carriers. These include optical, infra red, and radar instruments which use a wide range of the electromagnetic spectrum for the exploration of the planetary surfaces. Remote sensing instruments usually operate in the range from a hundredth to a thousandth of a μm to several millimetre wavelengths. Sensors for measuring concentrations of trace gases operate in the very short wavelength sector of the spectrum. Instruments working in the area of the visible light (0.4 to 0.7 μm) map vegetation cover, weather situation, land-use, geological characteristics, and water constituents of the ocean. Infrared and thermal infrared systems enable the measurement of surface temperatures of land bodies and the oceans. Finally, microwave and radar antennas explore the environment with wavelength in the order of centimetres or tens of centimetres.

There are three fundamental types of spaceborne radar sensors: imagers, altimeters, and scatterometers. Imaging radars are commonly used when high resolution large scale images are desired. Applications are in mapping, geology, forestry, ice cover monitoring, hydrology,

land use mapping, and oceanography. Stereo configurations are utilised for the reconstruction of surface topography and sensing of surface deformations. Radar altimeters are applied to surface height measurement of the land and ocean surface. A typical application is ocean circulation studies. Finally, scatterometers map the surface reflectivity so that measurements of surface roughness, vegetation cover, and soil-moisture may be achieved.

Since radars are active sensors, i.e. they take care of the illumination of the scene themselves, they are characterised by their capability to be used under all weather conditions at any time of day. On the other hand this implies high power consumption.

Radar imagers or Synthetic Aperture Radars (SARs) were and are employed on several exploratory missions, e.g. the surfaces of the Earth and Venus. SEASAT, SIR-A/B/C, SRTM, ERS-1/2, ENVISAT, and RADARSAT are some of the main sources for high resolution, wide swath images for the remote sensing of the Earth. The missions Magellan and Cassini provided and will provide a view beneath the opaque atmosphere of Venus and Titan (a Moon of Saturn). Common swath width of the radars are from several tens of kilometres to about 100 km and resolutions are available in the metre to km range. SAR is an acquisition technique that allows the imaging at the previously described resolution with antennas of modest size. SAR is a non-trivial imaging technique, this means SAR images are obtained in two steps: first the so-called raw data is acquired and, second, the raw data is processed (focussed) to obtain a high resolution SAR image.

The focussed SAR images provide intensity and phase information. Image intensity is a measure for the characteristics of the scattering surface layer. The more energy is backscattered from a position the brighter is the related image resolution cell value. Phase information is gained along with intensity. It is a value affected mainly by two phenomena: propagation and the backscattering component. The backscattering component is a random effect that depends on the physical properties of the imaged surface patch (dielectric constant, conductivity). For the propagation component the distance between instrument and surface patch as well as the refractivity of the propagation medium are determining factors. Along its path through the atmosphere the propagation of the illuminating and backscattered pulse is affected, e.g. by water vapour in the troposphere and electron content in the ionosphere.

There are essentially three options or modes of acquiring SAR data: strip-map, ScanSAR, and Spotlight. In strip-map acquisition, the scene is continuously illuminated in a pulsed fashion and the returning signal, backscattered from the ground, is recorded. In this way, infinitely

long images of the earth surface can be acquired. However, there are two design issues that have to be considered which limit the swath width of a SAR to about 100 km: blind ranges and range ambiguities. Blind ranges are the range positions where no backscattered pulse can be recorded, since the antenna is transmitting. Range ambiguities are backscattered pulses from a previous pulse that interferes with the current pulse echo. In order to overcome these problems ScanSAR or scanned SARs were invented. With ScanSAR modes a sequence of pulses – a so-called burst – is sent out, then the antenna is steered to a swath parallel to the first one, and another burst of backscattered pulses is achieved. This continues possibly to a third imaging swath until the antenna illumination or beam is steered back to the first swath. In this way wide imaging swaths from 300 km to 700 km become feasible allowing more frequent revisits of the same area. The price to be paid for this wide swath coverage is the loss in resolution. A coarser resolution is obtained, since less backscattered pulses per image position are recorded. ScanSAR is operated by the RADARSAT-1 instrument and by ENVISAT/ASAR. With Spotlight mode the aim is the opposite: the further improvement of image resolution. By continuously steering the antenna to a certain area on ground the illumination time for any position in the scene is increased. Thus, image resolutions in the submetre regime may be obtained from spaceborne sensors.

ScanSAR is in fact a special type of a burst-mode SAR. Other implementations of a burst-mode do not steer the antenna beam to another swath but remain in the same illumination configuration, however, the antenna changes polarisation when transmitting or receiving the electromagnetic wave signal. Thus, the bursted operation allows the quasi-simultanious acquisition of an area in two polarisations. This concept has been implemented by the so-called alternating polarisation mode and is operated by the instrument ENVISAT/ASAR. Another burst-mode was operated during the Magellan mission to Venus. During acquisition of data from Venus' surface the time-slots between the SAR bursts were used to operate a separate altimeter antenna and to switch the radar antenna to a passive radiometer mode. All in all, burst-modes are utilised to collect additional information (wide area, polarisation, instrument data) or to save data rate at the expense of along track resolution.

A stereo-like technique called SAR interferometry (InSAR) evaluates the phase information of the SAR images. In interferometric SAR two or more SAR images are combined to so-called interferograms. The SAR images are either obtained at repeated passes (repeat-pass interferometry) over the area of consideration or acquired in a single flyby (single-pass interferometry). Interferometry finds its main application in reconstruction of surface

topography, surface deformation sensing (differential InSAR or DInSAR), and vegetation change monitoring. For the former applications atmospheric effects are a source of error but it was shown that on the other hand SAR interferometry may be applied to mapping of atmospheric situations. SAR interferograms provide height or deformation information on a high resolution wide area basis and, hence, SAR interferometry is an efficient mapping tool for remote sensing information. Digital elevation models generated from SAR interferometry support, for example georectification of remote sensing data provided by radar or optical imaging sensors. Surface deformation maps allow statements on glacier flows and may be utilised to study surface deformations induced by earthquakes. SAR interferometry has become an established source of Earth surface information for geophysicists, geologists, biologists, and governmental institutions like mapping agencies.

Since burst-mode images like any other SAR image also carry phase information, they can also be applied in interferometry. In this way all the advantages of the bursted mode data are utilised interferometrically and new fields of interferometric application arise. In the case of the ScanSAR mode the wide swath mapping capability and the resulting fast revisit times are favourable for efficient topographic mapping and monitoring of the Earth's surface: reduced need for post processing (mosaicking) of large area high resolution digital elevation models (DEMs) as well as frequent coverage for differential InSAR and vegetation change observation. There are several current and future missions that are a steady source of burst-mode and ScanSAR data. Among them are RADARSAT-1 and ENVISAT as well as the coming missions RADARSAT-2 and ALOS/PALSAR. An impressive example for the possibilities of ScanSAR interferometry is the Shuttle Radar Topography Mission (SRTM). Within 11 days in February 2000, a single-pass interferometer mapped the Earth's land mass between ±60° longitude with resolutions in the order of 30 m. Thus, a global height data set of quality unknown to this date could be established.

However, the complicated signal structure and properties of burst-mode data as well as the lack of products suitable for interferometric processing are the main reason why burst-mode or ScanSAR interferometry (InScanSAR) has not been widely utilised in the remote sensing community so far.

1.2 Literature Review

ScanSAR Mode and Its Application

ScanSAR ('vertically scanned-beam SAR', 'wide swath synthetic aperture radar' or 'scanned SAR') was proposed in (Moore et al. 1981) to overcome the narrow swath limitations of conventional SAR modes (~100 km; SEASAT, ERS-1, ERS-2). However, the gain in swath width is traded-off with reduced resolution (Moore et al. 1981; Tomiyasu 1981). Typical resolutions are 50 m to 1 km per pixel, and swath widths of 300 km to 500 km are available (Raney et al. 1991; Karnevi et al. 1994). Applications of ScanSAR imagery include sea ice monitoring (Karvonen and Simila 1998; Sandven et al. 1998; Li et al. 2001), retrieval of ocean wind fields (Horstmann et al. 2001), and regional mapping (Nazarenko et al. 1997).

Missions Operating ScanSAR

ScanSAR has become a routine acquisition mode with today's SAR missions. Data is available from the Canadian RADARSAT-1 satellite, which is the first system to supply ScanSAR data operationally (Luscombe 1988; Raney et al. 1991). Soon, ENVISAT/ASAR will also provide ScanSAR and burst-mode data at a routine basis (Karnevi et al. 1994). RADARSAT-2 (Thompson et al. 2001), the ALOS/PALSAR (Shimada et al. 2002), and possibly RADARSAT-3 (Lee and James 2001) will also be sources for ScanSAR data in near the future. Dedicated missions operating burst-mode and ScanSAR data were the Magellan mission to Venus (Williams 2001), the SIR-C mission (Jordan et al. 1995; Chang et al. 1996), and the Shuttle Radar Topographic Mapping Mission (SRTM). During the 11-day SRTM in February 2000 the wide swath imaging property of the C-band antenna allowed the mapping of 80% of the Earth's surface (Jordan et al. 1996; Werner 2000).

Burst-mode and ScanSAR Signal Characteristics

A description of ScanSAR and burst-mode signal characteristics may be found in various articles: (Jin 1992), (Monti Guarnieri et al. 1994), (Monti Guarnieri et al. 1995), (Monti Guarnieri and Prati 1996), and (Bamler and Eineder 1996). (Monti Guarnieri and Prati 1996) and (Bamler and Eineder 1996) offer more detailed discussions on the topic. The main properties of ScanSAR and burst-mode data are low bandwidth and their band-pass characteristic with azimuth-varying centre frequency (section 3.1.1). In addition, if not corrected, a unique effect of burst-mode and ScanSAR data called "scalloping" shows up as

an azimuth dependent variation or modulation of the ScanSAR image intensity, e.g. (Bamler 1995; Mittermayer et al. 1996). Another issue in ScanSAR imaging is the need for calibration of the individual swaths that contribute to the final ScanSAR product. The aim is to avoid different radiometric characteristics for the individual beams (Luscombe 1993; Hawkins et al. 2001).

ScanSAR Interferometry

Since ScanSAR is inherently coherent (i.e. phase information may be provided along with intensity information in the image matrices) and, when properly processed, it can also be applied to wide swath interferometric mapping. ScanSAR interferometry (InScanSAR) was first proposed in (Monti Guarnieri et al. 1994) and was further elucidated in (Monti Guarnieri et al. 1995) and (Monti Guarnieri and Prati 1996). Along with proposing the technique, the need for alignment of the burst azimuth scanning patterns (section 4.1.4) and the relevance of azimuth fringe frequencies to burst-mode data were also described.

Burst pattern mis-alignment reduces coherence (section 2.1.2) and must be corrected prior to interferogram formation. The previously listed papers propose a solution applying an azimuth-varying filtering scheme. An alternative approach to the burst scanning pattern problem was proposed in (Bamler and Eineder 1996). With this procedure only the common raw data lines are input into the ScanSAR processor. The impact of scanning pattern mis-alignment and receiver noise on interferogram phase were illustrated using simulated data in (Cumming 1998).

Azimuth spectral shift as a result of local slopes reduces coherence and suitable filtering has to account for the mutual displacement of the spectral components. This effect is analogous to the well-known (range) wave-number shift (Gatelli et al. 1994). However, the azimuth spectral shift is only significant for very low resolution ScanSARs and rough terrain.

Of particular interest are co-registration properties of the signals, resampling, and beam alignment. Little has been published addressing these issues. In (Scheiber and Moreira 2000) an algorithm was proposed that evaluates interferometric phase instead of the cross-correlation coefficient for the co-registration of burst-mode data. Additionally, some co-registration properties were discussed. However, there is no publication showing a thorough the co-registration properties of burst-mode data and how these can be adopted for efficient interferometric processing of burst-mode data. When the burst-mode signals are represented at their Nyquist sampling frequency, a resampling algorithm matched to the special signal

properties of burst-mode data is a key step to the operational processing of the burst-mode data. (Bamler and Holzner 2001) proposed a fast and efficient burst-mode resampler but it was not evaluated using real data. Furthermore, no publications are available that address the problem of interferometric beam alignment and the properties of the interferometric phase in the overlap area of the swaths.

(Bamler et al. 1998) proposed two processing methods for burst-mode interferogram formation: single burst image and multiple (coherent) burst image interferogram formation (section 3.2). The first method was utilised for SRTM/SIR-C ScanSAR data processing (Hensley et al. 2000). These two techniques are commonly considered equivalent with respect to the phase behaviour of the resulting interferogram. However, there is no theoretical proof for this assumption. In fact, there are no standard and assessed tools or procedures in previous publications that allow the exploration of the properties of strip-map and burst-mode interferograms and, finally, also to proving of the equivalence of the two processing options. Furthermore, each burst-mode processing option offers specific advantages that may be integrated into a hybrid processing scheme. For the single burst processing option, the low data space requirements are a precondition for an operational operation of an interferometric ScanSAR processor. On the other hand, the multiple coherent burst data offers superior co-registration properties (section 4.2.1).

A complex ScanSAR data set may be combined with a second ScanSAR (ScanSAR-ScanSAR interferometry) or strip-map SAR (ScanSAR-SAR interferometry) data set to obtain an interferogram. In this respect, ScanSAR-SAR interferometry is a solution to the problem of resolution reduction in the case of burst scanning mis-alignment. The feasibility of both options was first demonstrated in (Monti Guarnieri et al. 1995) using simulated data based on raw products from ERS-1. In (Bamler et al. 1998) the feasibility for real ScanSAR data acquired by RADARSAT-1 was subsequently demonstrated for ScanSAR-ScanSAR and ScanSAR-SAR interferometry.

Digital Elevation Models from ScanSAR Data

Several DEMs from ScanSAR data exist. Firstly, during the SRTM the Earth's surface was mapped using single-pass interferometer operated in a scanned SAR mode. Moreover, a ScanSAR DEM produced from RADARSAT-1 data using traditional stereo techniques was presented in (Marra et al. 1998). However, a ScanSAR DEM from RADARSAT-1 repeat-pass data using interferometric techniques has not previously been generated and evaluated.

Phase Preserving Processing of ScanSAR Data

The product lists of current and near-future satellite missions do not include interferometric (complex-valued) ScanSAR products. Therefore, ScanSAR interferometry still requires phase preserving processing of the raw data product. Efficient algorithms for phase preserving ScanSAR focussing are available in literature: (Monti Guarnieri and Prati 1996; Moreira et al. 1996; Cumming et al. 1997; Wong et al. 1997; Lanari et al. 1998; Monti Guarnieri et al. 1999). ScanSAR processing also involves Doppler centroid estimation (Jin 1996; Mittermayer et al. 1996), and Doppler ambiguity resolution (Jin 1994).

For very low resolution ScanSAR data, for example for ENVISAT/ASAR's Global Monitoring mode, an optimal focussing method has been described in (Monti Guarnieri et al. 1999) and (Monti Guarnieri and Guccione 2001).

RADARSAT-1 Interferometry

Since the data used in this thesis originates from RADARSAT-1, issues of RADARSAT-1 interferometry are of importance. Interferometry with RADARSAT-1 data was first demonstrated by (Vachon and Geudtner 1996) and a detailed analysis of strip-map mode interferometry utilising standard and fine beam mode was demonstrated in (Geudtner 2001). RADARSAT-1 is not yaw steered. Hence, high Doppler centroid values occur and require adaptation of the spectral filtering process during interferometric processing (Geudtner 2001). In contrast to ERS-1/-2 and ENVISAT, the orbit maintenance of RADARSAT-1 and the supplied orbit parameter quality is not particularly favourable for interferometric applications (Armour et al. 1997; Rufenacht et al. 1997). Therefore, suitable strategies for data order and baseline estimation are necessary (Geudtner 2001).

1.3 Aims and Objectives

This thesis aims to

- provide a thorough insight into the signal properties, data structures, and process options of interferometric burst-mode and ScanSAR data
- show how to make efficient interferometric use of burst-mode and ScanSAR data
- show that after suitable interferometric processing of the burst-mode and ScanSAR data the interferograms resemble coarse resolution strip-map interferograms and, hence, a wide range of the SAR interferometric applications may benefit from burst-mode data

by achieving the following objectives:

- provision of an overview of burst-mode and ScanSAR interferometric signal properties.
- proof of the equivalence of the two burst-mode processing options available.
- overview of the algorithms available for processing burst-mode and ScanSAR data.
- filling in existing gaps in knowledge about burst-mode and ScanSAR signals and their processing including co-registration, resampling, and beam-alignment.
- outline of various burst-mode data structures and processing concepts, their comparison, and the proposal of an optimal burst-mode and ScanSAR processor.
- implementation and test of a prototype of the proposed optimal processor.
- generation and evaluation of a digital elevation model from a sample RADARSAT-1 ScanSAR Narrow data set.

1.4 Publications

Some of the processing aspects (azimuth scanning pattern synchronisation, Doppler estimation, high squint ScanSAR interferometry, beam alignment) of ScanSAR data and for the particular ScanSAR Narrow data set were published in (Bamler and Holzner 2000). A review paper giving a rough overview of the interferometric signal characteristics, a recipe-like description of the processing of the ScanSAR Narrow data set, and presenting a digital elevation model of repeat-pass ScanSAR interferometry is in print (Holzner and Bamler 2001). Both papers are attached as an appendix.

People involved in a fruitful critical discussion of a problem often rely, if only unconsciously, upon two things: the acceptance by all parties of the common aim of getting at the truth, or at least nearer to the truth, and a considerable amount of common background knowledge. This does not mean that either of these two things is an indispensable basis of every discussion, or that these two things are themselves 'a priori', and cannot be critically discussed in their turn. It only means that criticism never starts from nothing, even though every one of its starting points may be challenged, one at a time, in the course of the critical debate.

- *Truth, Rationality, and the Growth of Scientific Knowledge (Popper 1963).*

Chapter 2

Background

This section reviews the basics of SAR interferometry and of the ScanSAR imaging mode. For SAR interferometry an overview is given followed by a discussion on topographic mapping from interferometric signals, signal characteristics, and processing techniques. Then the concepts of ScanSAR data acquisition, scalloping, and burst multi-looking are described.

2.1 SAR Interferometry

In SAR interferometry (InSAR) an interferogram is the combination of two or more complex-valued SAR images. SAR image acquisition, processing, and properties are well understood and several reviews and tutorials are available, e.g. (Tomiyasu 1978; Elachi 1988; Bamler 1992; Bamler and Schättler 1993; Schreier 1993; Woodhouse 2000). InSAR is a sensitive measurement technique that compares two SAR acquisitions which differ in at least one imaging parameter, e.g. flight path, acquisition time, wavelength (Bamler and Hartl 1998). Applications of SAR interferometry include estimation of the Earth's surface movement (Zebker and Rosen 1994), determination of atmospheric parameters (Hanssen 1999), biomass estimation (Askne et al. 1997), and the retrieval of bio- and geophysical parameters (Borgeaud and Wegmüller 1996; Wegmüller and Werner 1997). For the purpose of this thesis only across

track interferometry for topographic reconstruction is considered (figure 2.1), i.e. flight path and acquisition time may differ.

Across-track SAR interferometers come in two models: single-pass interferometers record the two SAR images required simultaneously by using a transmit/receive antenna and a secondary receive antenna mounted some distance away. These interferometers are technically limited in baseline extent (that is, the physical distance between the two antennas when imaging the same position on ground) but are superior when temporal decorrelation is considered. They are usually flown on aircrafts. The Shuttle Radar Topographic Mission (SRTM) is the only single-pass interferometer that has been used so far in orbit (Jordan et al. 1996). Repeat–pass interferometers, on the other hand, use images taken at different times, e.g. separated by days or months. Examples are the ERS-1/2 satellites as well as RADARSAT-1 and ENVISAT/ASAR. Since this thesis is based on data from RADARSAT-1, i.e. a repeat-pass spaceborne InSAR system, the equations given refer to repeat-pass interferometer configuration (Bamler and Hartl 1998).

Extensive discussions on SAR interferometry for topographic mapping are given in (Zebker and Goldstein 1986; Gabriel and Goldstein 1988; Schwäbisch 1995; Bamler and Hartl 1998; Rosen et al. 2000). Therefore, only very basic principles are outlined in the following sections.

2.1.1 Topographic reconstruction using SAR interferometry

The imaging geometry of an interferometer is shown in figure 2.1. For the following description phase noise is neglected, a homogenous propagation medium is assumed: the Earth's surface is not moving, and the positions SAR_1, SAR_2, and P are within the same plane. (It is assumed that the scatterers in the SAR images are focussed to their zero-Doppler positions, i.e. at the position where sensor and scatterer have the smallest distance (Bamler and Hartl 1998)). Interferometry for topographic mapping evaluates the wave's propagation path difference $\Delta R = R_2 - R_1$ [m] for a certain position P seen by both radars.

The measured interferometric phase

$$\phi = \phi_2 - \phi_1 = \frac{4\pi}{\lambda} \Delta R \qquad \text{[rad]} \tag{2.1}$$

is the difference between the individual SAR phases:

(2.2) $$\phi_1 = 2\,k\,R_1 + \phi_{scatt,1} \text{ [rad]}$$

and

(2.3) $$\phi_2 = 2\,k\,R_2 + \phi_{scatt,2} \quad \text{[rad]}$$

where $k = 2\pi/\lambda$ [rad/m], with λ [m] the radar's wavelength. This means each SAR phase has a propagation component $2\,k\,R_1$ ($2\,k\,R_2$) and a scatterer-dependent component $\phi_{scatt,1}$ ($\phi_{scatt,2}$). For the moment that the scatterer components are assumed to cancel out. The interferometric phase in equation (2.1) is then a direct and very sensitive measure for the propagation difference of the electromagnetic pulses. As a result of the factor $2\,k$ in equation (2.1), the round trip signal path differences can be measured as a fraction of the wavelength which in the case of a C-Band radar is in the order of 5.6 cm.

By measuring the path distance $\Delta R = R_2 - R_1$ the across-track SAR interferometer is an instrument resolving the look angle $\theta(h)$. This property can be made explicit by means of the parallel baseline:

(2.4) $$\Delta R \approx B_{\parallel} = B\sin(\xi - \theta(h)) \qquad (B << R)$$

with baseline length B and baseline angle ξ. From here only a simple rearrangement is required to relate interferometric phase (equation (2.1)) to the look angle $\theta(h)$:

(2.5) $$\theta(h) = \xi - \arcsin\left(\frac{\phi}{2kB}\right).$$

Hence, given the satellite positions, the iso-range circle (R_1 is known), and the look angle the position of the point P in 3-D space may be retrieved.

The phase as used in equations (2.1) and (2.5) cannot be estimated directly, however. Only a wrapped version may be retrieved from the SAR data which is ambiguous by integer multiples of 2π. It is the task of phase unwrapping to retrieve good estimates for the absolute interferometric phase from the wrapped phases.

There are three main parameters related to the sensivity of the SAR interferometer: phase-to-height conversion factor, height of ambiguity, and (local) fringe frequency.

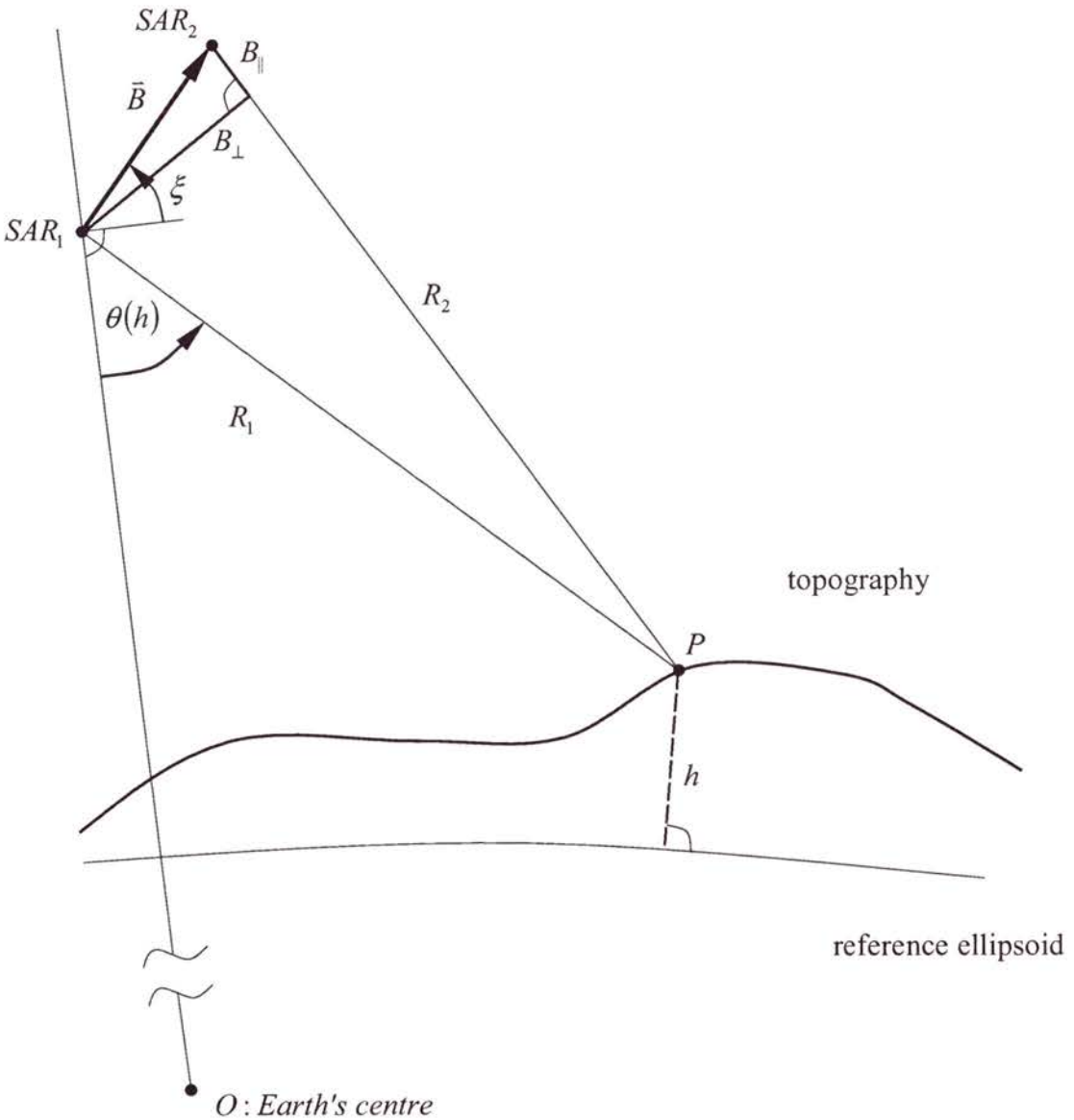

Figure 2.1: Imaging geometry of a SAR interferometer. Flight paths are perpendicular into the plane.

Interferometer sensivity with respect to height can be derived using figure 2.2. Without lack of generality a situation is sketched where $B_{\parallel} = 0$ for the point P. Only the perpendicular baseline

(2.6) $$B_{\perp} = B\cos(\xi - \theta(h))$$

determines how a change in look angle $d\theta$ converts into a change $d\Delta R$ in propagation path difference (equation (2.4)):

(2.7) $$d\theta = -\frac{d\Delta R}{B_{\perp}}$$

with sign as indicated in figure 2.2. (Figure 2.2 shows positions of constant ΔR by hyperbolas to the right of the reference line where $\Delta R = 0$).

Moving along the iso-range arc from position P to P' changes look angle

(2.8) $$d\theta = \frac{d\zeta}{R}$$

and height

(2.9) $$dh = d\zeta \sin(\theta)$$

with $d\zeta$ the distance of P and P' measured along the arc $R = const.$

From equations (2.7) and (2.8) the relationship between $d\zeta$ and $d\Delta R$ is found (Bamler and Hartl 1998):

(2.10) $$d\Delta R = -\frac{B_{\perp}}{R} d\zeta \,.$$

Hence, the look angle is replaced by a 'local' variable $d\zeta$ that measures distances perpendicular to the look direction in the vicinity of P. By virtue of this Taylor expansion, the co-ordinate system has moved and rotated from SAR_1 to the point P on ground.

Finally, the sensivity of the interferometer phase with respect to height is obtained by inserting equations (2.9) and (2.10) in (2.1) (Bamler and Hartl 1998):

(2.11) $$\frac{d\phi}{dh} = -2\,k\frac{B_{\perp}}{R\sin\theta} \qquad [\text{rad / m}].$$

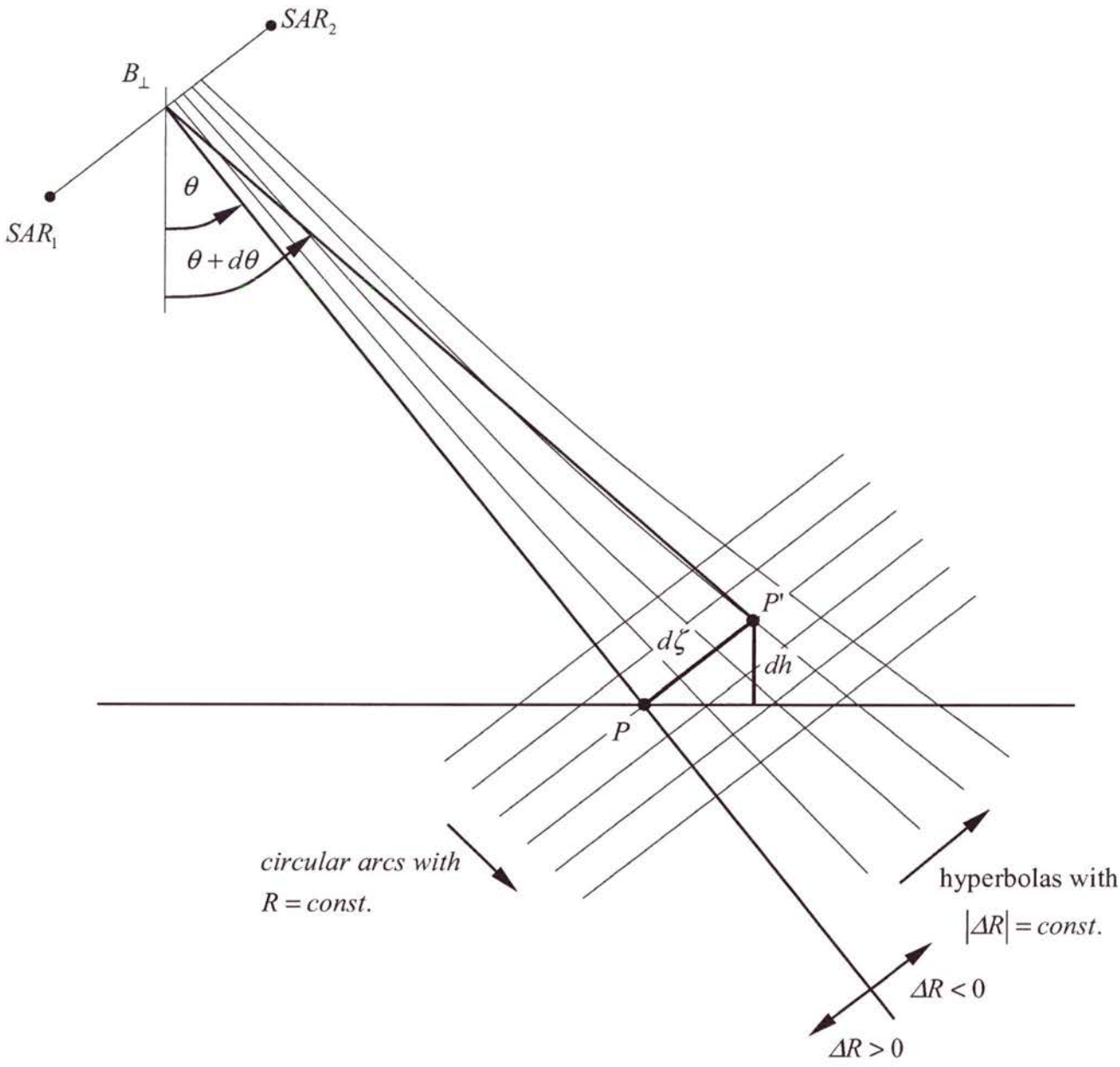

Figure 2.2: Model for interferometric mapping of terrain height. The interferometric phase resolves the angle θ by measuring ΔR and, hence, is able to retrieve height dh.

In practice, this means that after reduction of a reference surface (e.g. an ellipsoid representing the reference positions P) from the interferogram (see section 0), the remaining phase is a direct measure of the height with sensivity (2.11). In this way, a 'flattened' interferogram (figure 2.3) appears as a topographic map projected into the azimuth slant range geometry with height contour lines according to the height of ambiguity (that is, the height interval corresponding to an interferogram phase change of 2π) (Bamler and Hartl 1998):

(2.12) $$h_{2\pi} = \frac{\lambda}{2}\frac{R\sin\theta}{B_\perp} \quad [\mathrm{m}]$$

The local fringe frequency in range direction can be obtained from an extension of the above consideration as (Gatelli et al. 1994; Bamler and Hartl 1998):

(2.13) $$f_\phi = \frac{1}{2\pi}\frac{\partial\phi}{\partial R} = -\frac{2B_\perp}{\lambda\, R\tan(\theta-\alpha)} \text{ in } [\mathrm{m}^{-1}] \text{ or } f_\phi = -f_0\frac{B_\perp}{R\tan(\theta-\alpha)} \text{ in [Hz]}$$

with f_0 the radar carrier frequency and α the local terrain angle which is positive when sloping towards the radar. Local fringe frequency refers to the number of phase wraps given the incidence angle and local slope for an interferometer with perpendicular baseline $B_\perp$.

Note, that these interferometer parameters are only valid in the vicinity of the point P (Taylor expansion) and vary with height, range and azimuth position.

a) amplitude

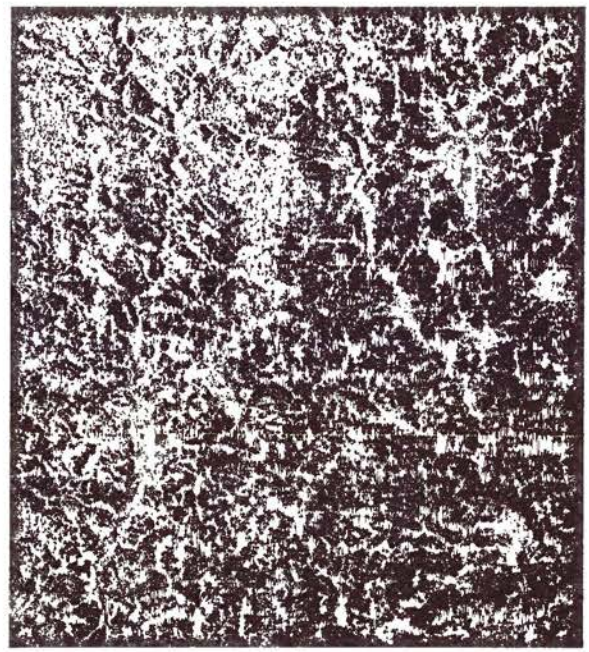

b) interferogram phase

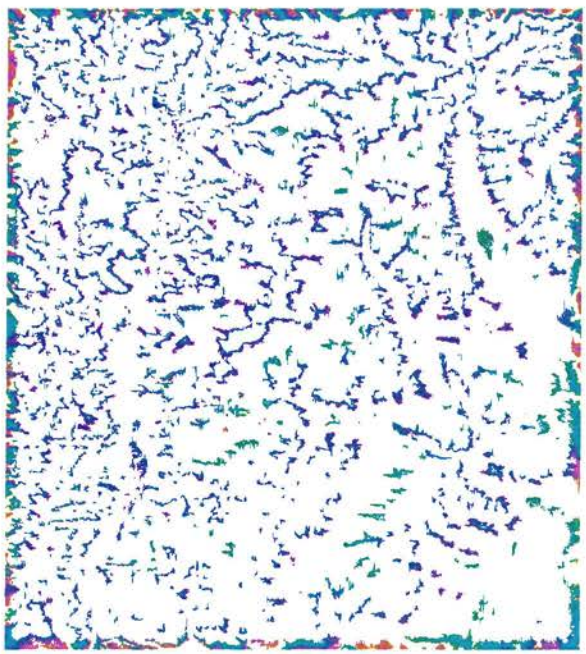

c) coherence map

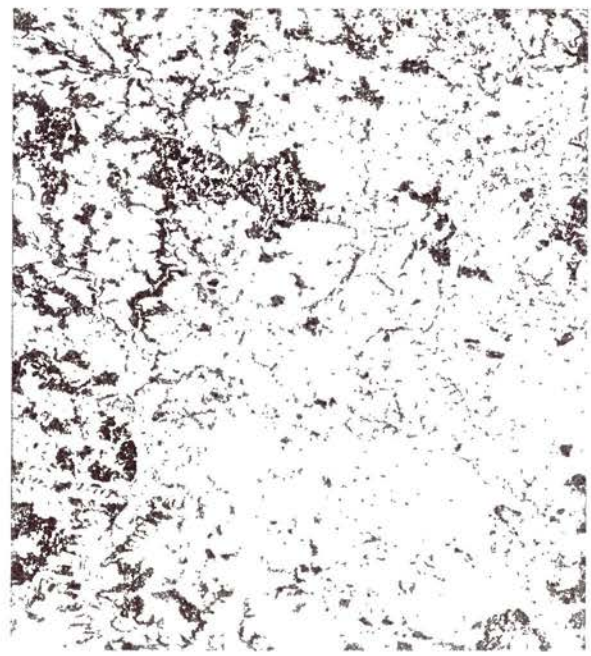

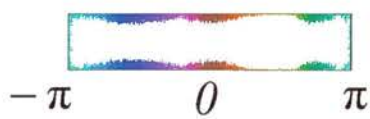

Figure 2.3: Amplitude $|u_1|$, interferogram phase ϕ, and coherence of a ERS-1/-2 tandem pair acquired over a test site near Ronneburg, Germany (baseline: $B_\perp$=137 m ; $h_{2\pi}$=72 m).

2.1.2 Coherence

Coherence is defined as the complex correlation coefficient:

$$\gamma = \frac{\mathrm{E}\left\{ u_1 u_2^* \right\}}{\sqrt{\mathrm{E}\left\{ |u_1|^2 \right\} \mathrm{E}\left\{ |u_2|^2 \right\}}} \qquad (2.14)$$

giving a measure for the similarity of the SAR signals by its magnitude $|\gamma|$. It is the normalised expectation value of the interferogram pixel $i = u_1 u_2^*$, u_1 and u_2 are samples of the SAR images used to form the interferogram. The phase of γ is the interferometric phase. The coherence magnitude may take values between 0 and 1, and phase stability increases or interferometric phase variance decreases with increasing $|\gamma|$. Assuming ergodicity, i.e. that the ensemble average can be substituted by the spatial average, the coherence magnitude is estimated within an N-sample window:

$$|\hat{\gamma}| = \frac{\sum_N u_1 u_2^*}{\sqrt{\sum_N |u_1|^2 \sum_N |u_2|^2}} \qquad (2.15)$$

Using this equation, coherence may be interpreted as a phase stability measure (Figure 2.4 a and b). For high coherence the complex vectors $u_1 u_2^*$ within the estimation window have approximately the same orientation, i.e. phase. The vectors superpose in a way so that the resulting vector has approximately a magnitude that is the sum of the magnitudes of the individual vectors and its phase is the same as the phase of the individual vectors. In the case of low coherence the directions of the individual vectors strongly deviate and the resulting complex number has low magnitude and random phase.

In steep or rough terrain the complex vectors within the estimation window change rapidly, hence, an effect occurs as illustrated in figure 2.4 b). Hence, the coherence estimate is underestimated and depends on the local terrain rather than on the similarity of the SAR signals. Hence, the terrain phase should be reduced from the interferogram samples in the estimation window to obtain reasonable values:

$$\hat{\gamma} = \frac{\sum_N u_1 u_2^* \exp(-j\phi_{terrain})}{\sqrt{\sum_N |u_1|^2 \sum_N |u_2|^2}} \qquad (2.16)$$

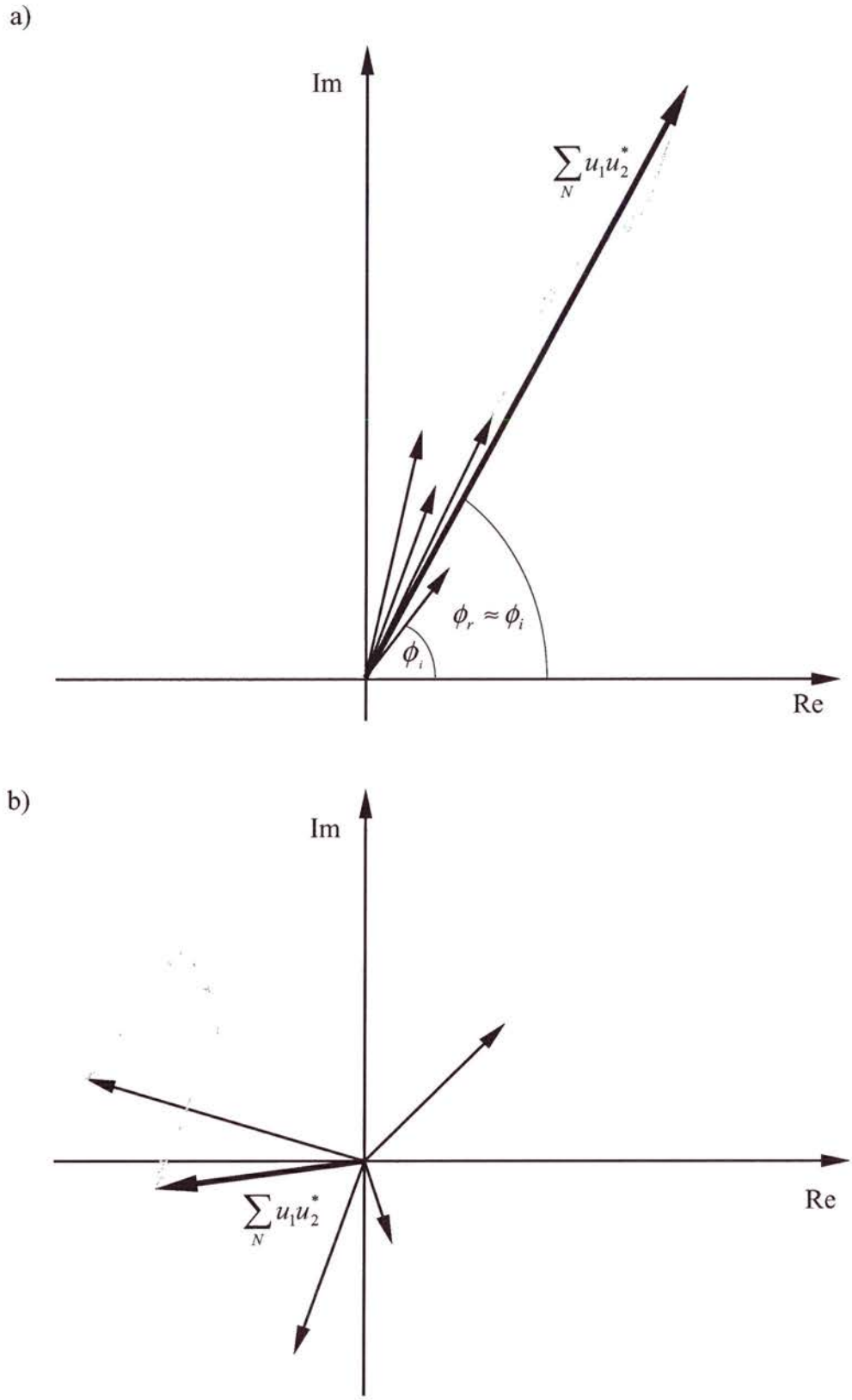

Figure 2.4: Coherence as phase stability measure: high coherence case a) and low coherence case b). For high coherence all vectors sum up to a strong response and the estimate is almost one.

The estimate in (2.15) (and (2.16)) deviates less and less from the actual coherence value for higher coherence of the signals and for a larger number of samples used for calculation (Bamler and Hartl 1998). In fact, the estimate as given in the above formula overestimates coherence. This means the obtained value of the estimate is larger than the actual coherence of the interferometric signals. In (Touzi and Lopes 1996) and (Touzi et al. 1999) the probability density function (PDF) of this estimate for the coherence magnitude $|\hat{\gamma}|$ is derived. The calculation is based on a jointly Gaussian process for the interferometric channels and the obtained PDF is:

$$p_{|\hat{\gamma}|}(d;N) = 2(N-1)\left(1-|\gamma|^2\right)^N d\left(1-d^2\right)^{N-2} {}_2F_1\left([N,N];[1];\gamma^2 d^2\right) \qquad (2.17)$$

where ${}_pF_q\left([a_1,...,a_p];[b_1,...,b_q];x\right)$ is the generalized or Barnes extended hypergeometric function (Wolfram 1999). With this distribution the expectation value of the estimate in (2.15) can be achieved:

$$E\{|\hat{\gamma}|,N\} = \frac{\Gamma(N)\,\Gamma(1+1/2)}{\Gamma(N+1/2)}\,{}_3F_2\left([3/2,N,N];[L+1/2,1];\gamma^2\right)\left(1-\gamma^2\right)^N \qquad (2.18)$$

where $\Gamma(.)$ is the Euler gamma function. This result explains the overestimation of in the case of low γ and with a decreasing number of samples N within the estimation window. It was confirmed with simulations in (Monti Guarnieri and Prati 1997).

Coherence or similarity of the interferometric SAR signals is influenced by several factors: SAR system noise (finite signal-to-noise ratio (SNR) and quantization noise, summarized in γ_{SNR}), differing imaging geometries (system transfer behaviour with respect to the scattering layer on ground also referred to as surface scattering: γ_H), volume scattering (or volume decorrelation: γ_V), and temporal change of the scattering layer on ground (temporal decorrelation: γ_χ) (Bamler and Hartl 1998). All influences contribute to the final coherence of the interferogram (Rodriguez and Martin 1992; Zebker and Villasenor 1992):

$$\gamma = \gamma_{SNR}\,\gamma_H\,\gamma_\chi\,\gamma_V \qquad (2.19)$$

Interferometric processing, as discussed in the next section, optimises the coherence of the interferogram. Influences of differing imaging geometries are accounted for in advance of interferogram formation and the factor γ_H can be increased to approximately 1 (for narrow

scattering layers). The impacts of temporal decorrelation and systems noise can be addressed by suitable filtering of the interferogram phase.

Figure 2.3 c) shows a coherence map of a ERS tandem data set (time in-between acquisitions is 1 day). Bright areas represent coherence close to unity and, hence, good phase quality. Dark coherence patches are probably forests where moving leaves or volume scattering may destroy correlation of the SAR signals.

2.1.3 Interferometric Signal Processing

This section describes the generation of an interferogram from two SAR images: a master or primary channel (SAR) image and a slave or secondary channel (SAR) image.

The basic interferogram system theoretical model and signal flow is illustrated in figure 2.5 (e.g. (Just and Bamler 1994; Bamler and Hartl 1998)). As for optical systems which extract specific spectral bands from the visible part of the full backscattered signal, a SAR image $u(t,\tau)$ (t: azimuth time variable, τ: range time variable) is also a bandpass extract of the 'complex reflectivity function' or 'complex backscattering function' (Hagberg et al. 1995; Bamler and Hartl 1998) with centre frequency f_0. In this thesis, the 'complex reflectivity function' is denoted $\chi(t,\tau)$ and referenced in a slant range-azimuth co-ordinate system. Note in this respect spatial frequencies (structure of the image amplitude) should not be confused with carrier or centre frequency (colour, scattering behaviour). Apart from the acquisition centre frequency, optical and radar systems differ in imaging geometry and illumination source. For the description of the behaviour of the SAR, the so-called end-to-end system impulse response $h_{SAR}(t,\tau)$ is defined (Rocca et al. 1989; Bamler 1992; Bamler and Schättler 1993; Bamler and Hartl 1998; Bara et al. 2000). An interferogram $i(t,\tau)$ is formed from the two SAR images $u_1(t,\tau)$ and $u_2(t,\tau)$ as their Hermitian product (conjugate complex multiplication).

Interferometric processing comprises several processing steps that are hidden in the simple model of figure 2.5. A refined flow chart of interferometric processing is depicted in figure 2.6 (Schwäbisch 1995; Eineder and Adam 1997; Roth 1999). The aim of interferometric processing before interferogram formation is to make the SAR images as similar as possible in order to optimise phase quality and coherence (Madsen et al. 1993; Geudtner 1995; Schwäbisch 1995; Geudtner 1998). Co-registration and common band filtering are required to account for the slight differences in imaging geometry.

After interferogram formation the interferogram phase is optimised for phase unwrapping. Steep terrain and noise (thermal and quantization noise, temporal decorrelation) introduce phase undersampling into the interferogram. In order to account for phase undersampling either the ellipsoid phase ('flat earth phase') or a coarse resolution terrain phase is subtracted from the measured phase ('interferogram flattening') (Schwäbisch 1995; Seymour 1999). Finally, suitable phase noise filtering smooths the phase prior to phase unwrapping. Using

suitable geo-coding algorithms the unwrapped phase is converted into a digital elevation model (DEM). The following section gives more insight into common band filtering.

Azimuth common band filtering

Common band filtering removes the non-common spectral components of the interferometric partners. In this way, the similarity of the signals and, hence, coherence and phase quality is optimised. Conducting common band filtering in advance of co-registration increases the accuracy of the co-registration estimate.

Figure 2.7 shows how along track (azimuth) ground frequencies are mapped into the SAR azimuth co-ordinate system (the range distance R is much larger than d). The mapped frequencies depend on the start and end aspect angles β_{Start} and β_{End} or equivalently to centre squint angle β_{DC} and the azimuth illumination time T_A used. A second SAR with an approximately parallel flight path will map the ground analogously. If this second SAR has a different Doppler centroid, i.e. different squint, a different part of the azimuth ground spectrum is imaged (figure 2.8). This means non-common spectral components occur. In contrast to range (see below), these components are mapped to frequencies outside the shared band.

Range common band filtering

The basic effect for range is illustrated in figure 2.9. It shows how a ground range frequency component is mapped into each individual SAR image slant-range co-ordinate. For SAR_1 and SAR_2, the look angles θ_1 and θ_2 are given. The ground range frequency $1/d$ is mapped to $1/d_1$ for SAR_1 and to $1/d_2$ for SAR_2 from the geometry. Hence, due to the bandpass character of the SAR, the images will carry non-common spectral components as illustrated in figure 2.10.

Figure 2.11 summarises and extends the above considerations. It depicts the bandwidth excerpts of the 3D ground reflectivity spectrum for a sufficiently small area around r_0 (Rocca et al. 1989; Bamler and Hartl 1998; Bara et al. 2000). The spectra are limited by the azimuth and range bandwidth of the SAR and centred around the radar's frequency f_0 along the axes specified by the angles β_1 – squint angle SAR 1 – and θ_1 – look angle SAR 1 – as well as β_2 – squint angle SAR 2 – and θ_2 – look angle SAR 2 (terrain angle: $\alpha = 0$; figure 2.11 a).

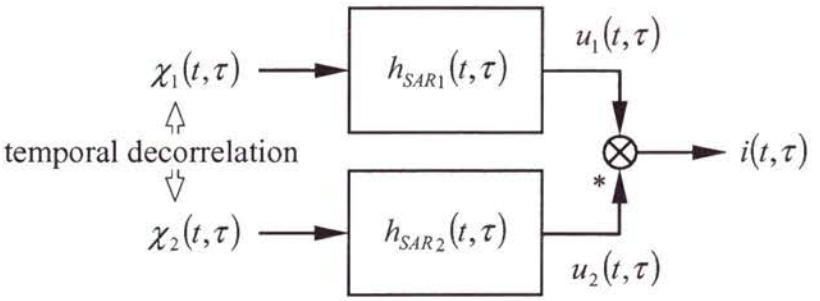

Figure 2.5: Simplified system theoretical model for SAR interferometry.

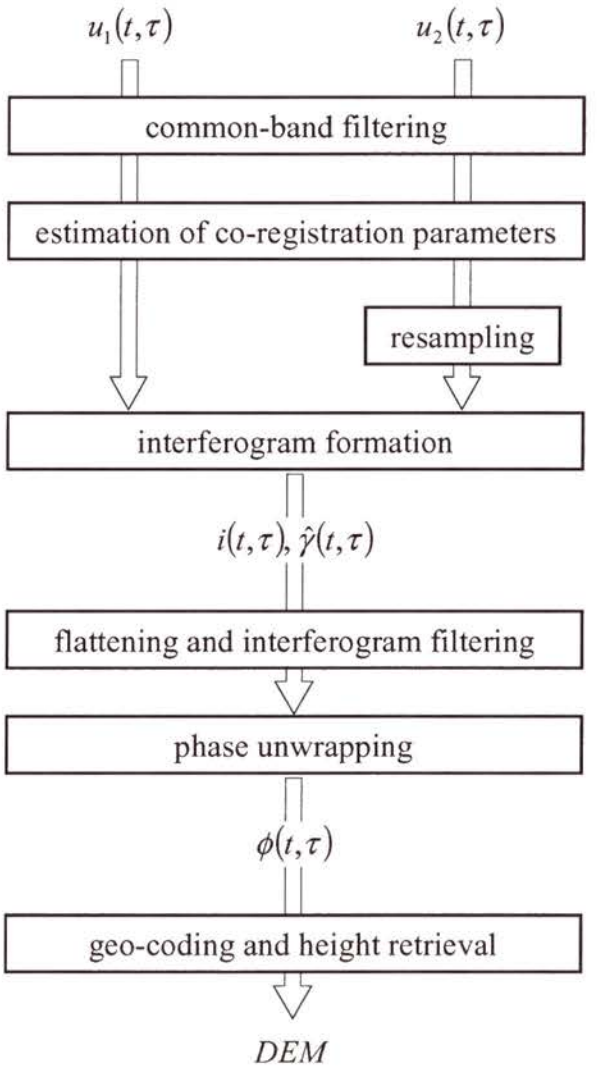

Figure 2.6: Generation of digital elevation models (DEMs) from interferometric data. From the filtered and co-registered SAR images u_1 and u_2 the interferogram i is formed. The DEM is obtained after geo-coding and height retrieval from the absolute (unwrapped) interferometric phase ϕ.

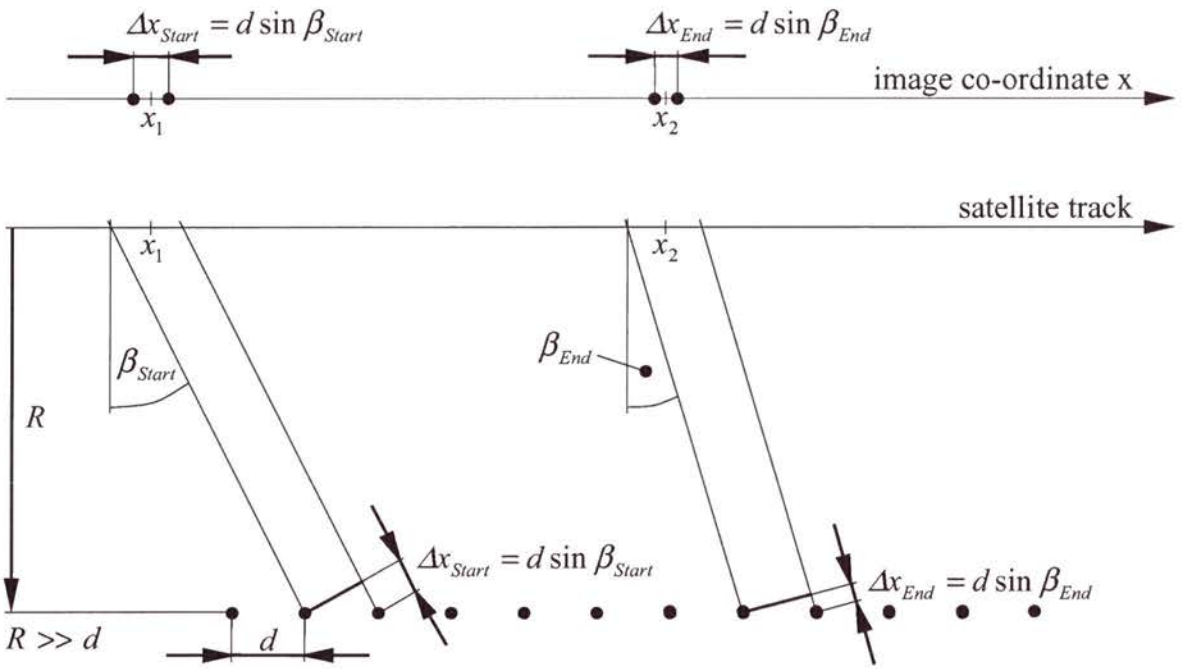

Figure 2.7: The recorded azimuth frequencies are determined by the start and end azimuth look angles (aspect angles) β_{Start} and β_{End}. A regular pattern with distance d is mapped into the SAR image azimuth co-ordinate by $d \cdot sin(\beta)$ since the SAR measures propagation delay in line of sight. The Doppler centroid is the azimuth frequency corresponding to the mean aspect angle referred to as squint angle: $\beta_{DC} = (\beta_{Start} + \beta_{End}) / 2$.

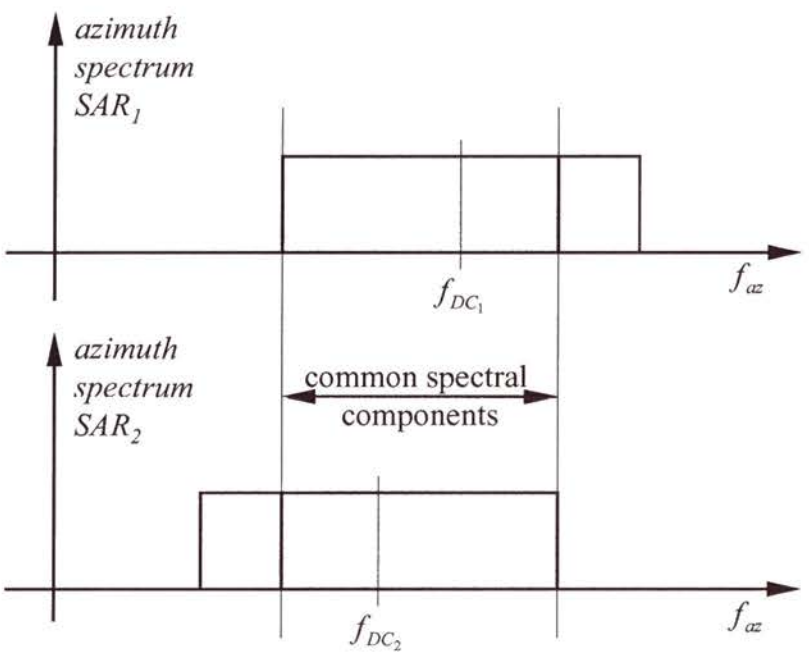

Figure 2.8: Common azimuth (Doppler) band of two SARs with different Doppler centroid frequencies (The antenna weighting is assumed to be corrected to a rectangular function).

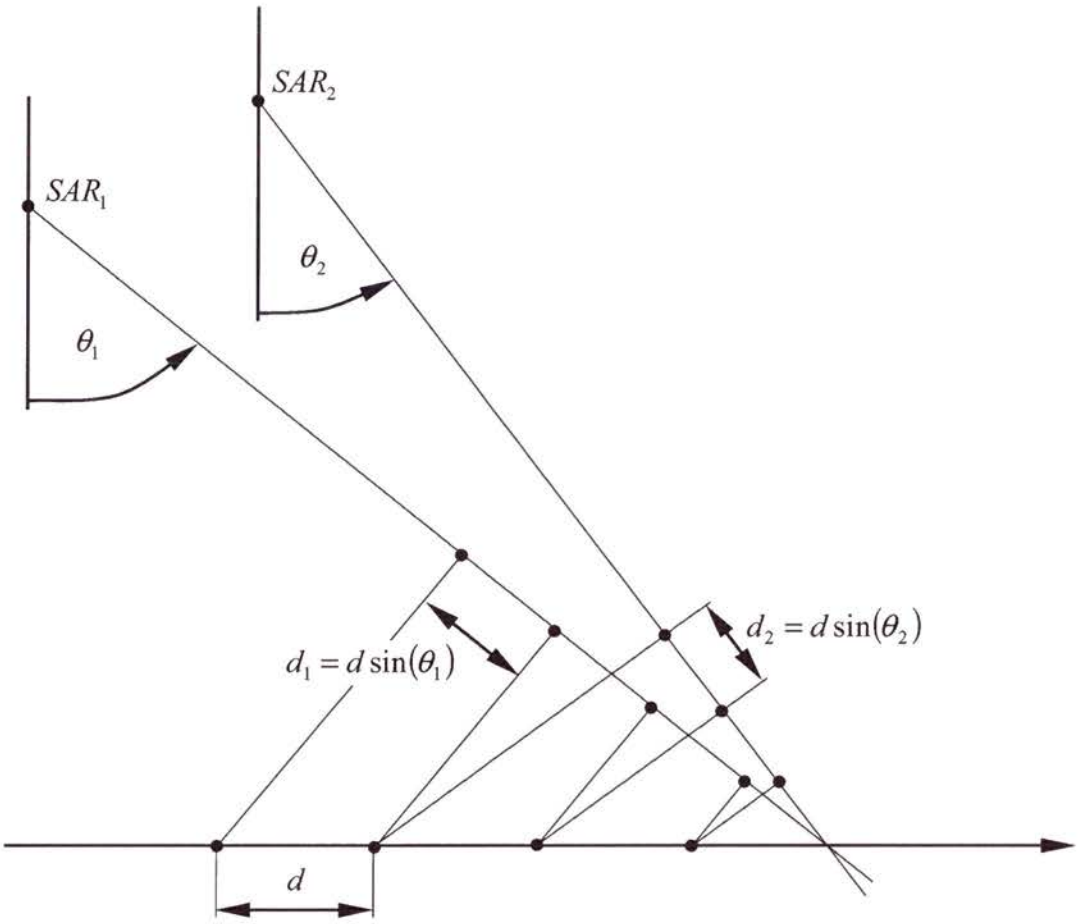

Figure 2.9: Mapping of a ground range frequency component to slightly different frequencies in the slant-range co-ordinates of the two SARs.

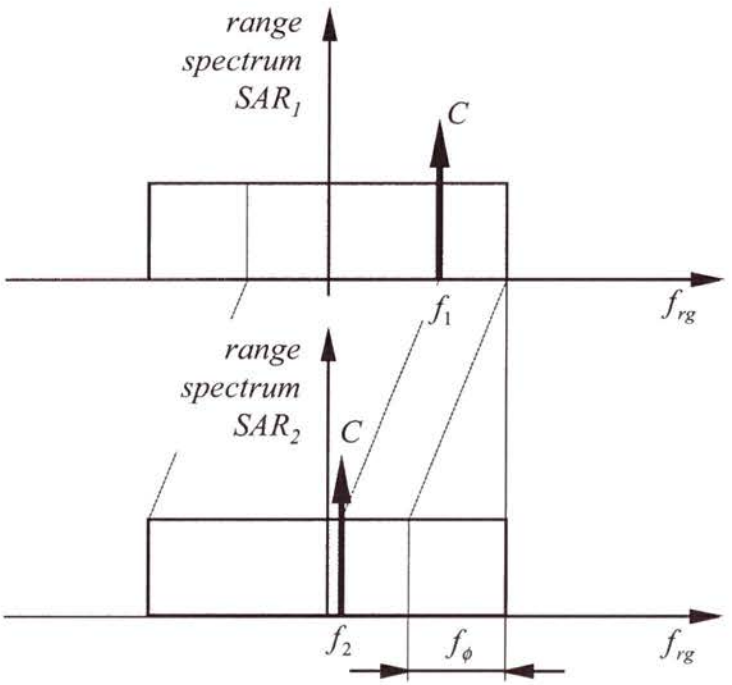

Figure 2.10: Common range spectrum bands of the SARs. A spectral component is found in both spectra at slightly different positions: $f_2=f_1+\Delta f$. The frequency shift is the fringe frequency: $\Delta f=f_\phi$.

a) azimuth frequency versus ground range frequency co-ordinate view

b) height co-ordinate frequency versus ground range frequency view

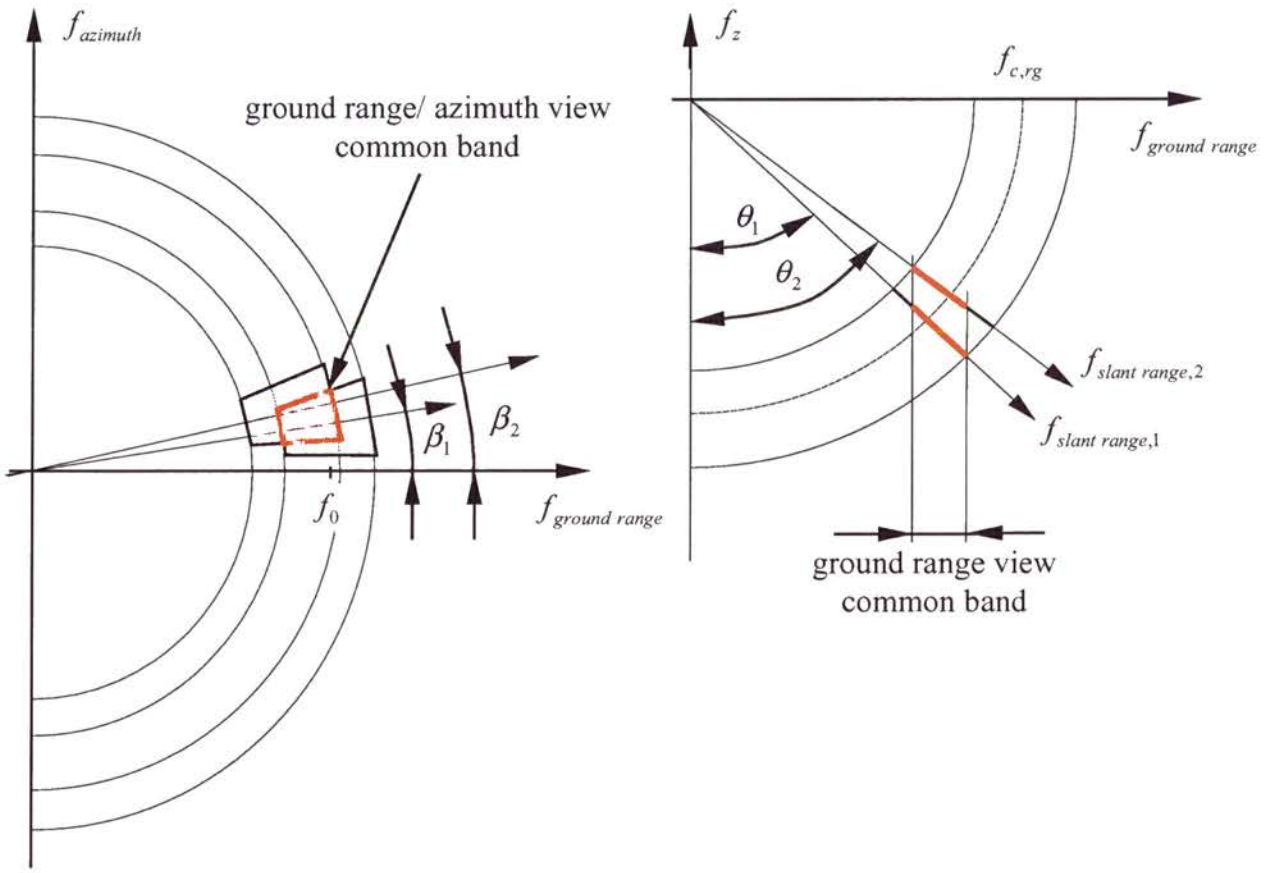

Figure 2.11: Bandwidth excerpts of the 3D ground reflectivity spectrum illustrated in azimuth/ground range frequency and height/ ground range frequency views.

The centre squint angles are related to the Doppler centroid f_{DC} by (Bamler and Schättler 1993; Bara et al. 2000):

$$\sin(\beta_i) = \frac{\lambda}{2}\frac{f_{DC,i}}{v_S},\ i = 1,2\,. \qquad (2.20)$$

with λ the radar's wavelength and v_S the satellite velocity. The usable spectral support for interferometry is exemplified by the red bold polygon in figure 2.11 a) and the red bold line in figure 2.11 b). It is the 'common band' of the SARs. When the interferogram is formed the spectra of the individual SAR signals are correlated. If the SAR signals are modelled as two band-limited partially correlated Gaussian signals, a cross-correlation peak will occur at the mutual shift (fringe frequency) of the frequency bands (section 4.1) (Zebker and Villasenor 1992; Bamler and Hartl 1998). From Fourier theory it is known that a peak in frequency domain will introduce a complex exponential term in time domain having linear phase, hence, the interferogram phase will show a phase ramp. This phase ramp can be also viewed as the difference of the two phase ramps of the individual SAR images determined by the centre frequencies of the common spectral components (figure 2.10: shaded area). According to the Gaussian model the common part of the partially correlated noise process will vanish when the interferogram is formed and only the terrain or geometric phase component will remain. The uncorrelated process components will add noise to the interferogram. Hence, in order to minimise the noise component in the interferogram the spectra are 'cut' or filtered to their shared bands (Bamler and Just 1993; Gatelli et al. 1994; Schwäbisch 1995; Bamler and Hartl 1998).

For the filtering of the SAR data the centre frequency and the amount of the mutual shift are important. The spectra are centred around (Rocca et al. 1989; Bamler and Holzner 2000; Bara et al. 2000; Geudtner 2001):

$$f_{c,rg} = f_0 \cos(\beta) = f_0\sqrt{1-\left(\frac{\lambda}{2}\frac{f_{DC}}{v_S}\right)^2} \qquad (2.21)$$

along the slant range axis in the view illustrated by figure 2.11 b).

This frequency offset is usually very small for yaw steered instruments like ERS and ENVISAT/ ASAR. However, for RADARSAT-1 the overall offset can be significant, in particular for low bandwidth modes (i.e. wide swath and ScanSAR modes). According to equation (2.20) a squint angle of 0.11° (1.08°) is obtained for a C-band instrument with

Doppler centroid of around 500 Hz (5 kHz), and satellite velocity of 7.5 km/s. In turn, the shift of the range spectrum toward lower frequencies is then 9.5 kHz (0.95 MHz). For ERS 9.5 kHz represents less than 1/1000 of the range spectrum width ($W_r = 15.5$ MHz) and is, hence, negligible. For the Wide swath mode of RADARSAT-1, with a bandwidth of 12 MHz a shift of 0.95 MHz at a Doppler of 5 kHz is likely and represents approximately 1/10 of the spectral width.

The mutual or spectral shift (Prati and Rocca 1992; Gatelli et al. 1994) between the usable spectra can be observed from figure 2.12. The fringe frequency relates to the range spectrum centre frequency by:

$$f_\phi = \frac{f_{c,rg}\, d\theta}{\tan\theta} \qquad (2.22)$$

where $d\theta$ is the difference of the look angles and $\theta = (\theta_1 + \theta_2)/2$ is the mean look angle. With

$$d\theta = \frac{B_\perp}{R} \qquad (2.23)$$

the fringe frequency is obtained as

$$f_\phi = f_{c,rg}\frac{B_\perp}{R\tan\theta}. \qquad (2.24)$$

When the terrain angle α is taken into consideration, this yields equation (2.13).

If the fringe frequency f_ϕ and the difference of the Doppler centroids Δf_{DC} are not accounted for by common band filtering, the overall coherence of the signals is reduced by the factor (Just and Bamler 1994):

$$\gamma_{cb} = \left(1 - \frac{f_\phi}{W_R}\right)\left(1 - \frac{\Delta f_{DC}}{W_A}\right) \qquad (2.25)$$

where W_R is the range bandwidth and W_A the azimuth bandwidth. This factor becomes significant for large baselines and in rough terrain (large α).

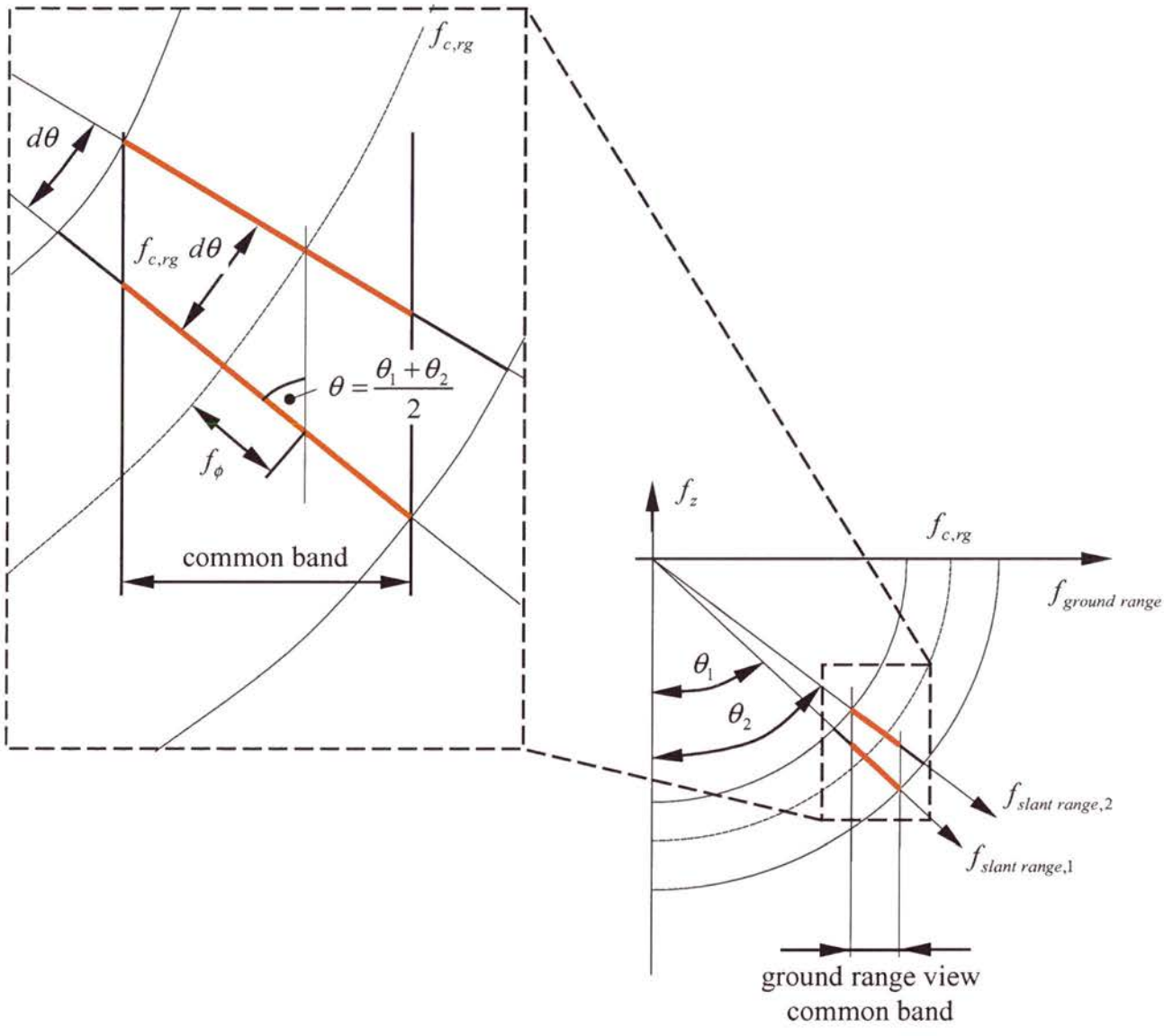

Figure 2.12: Derivation of the mutual spectral shift (fringe frequency) from the SAR spectrum configuration in the ground-range frequency versus height frequency diagram.

Figures 2.11 and 2.12 show, that for an increasing difference of the look angles θ_1 and θ_2 the amount of common spectral information of the SAR images reduces. The common band is determined by the difference of the range bandwidth W_R and the fringe frequency f_ϕ. This means, when the fringe frequency is equal or higher than the range bandwidth then no useful interferometric phase information can be extracted. From a geometrical point of view the difference of the look angles is determined by the perpendicular baseline $B_\perp$. The larger this baseline the larger the look angle difference and the smaller the band where the SAR signals have common frequency components. Consequently, there is a fringe frequency and perpedicular baseline where total decorrelation occurs. This baseline is referred to as critical baseline $B_{\perp,crit}$ (Gatelli et al. 1994; Bamler and Hartl 1998):

$$B_{\perp,crit} = \frac{W_R}{f_0} R \tan(\theta - \alpha). \qquad (2.26)$$

This equation is obtained from (2.13) by assuming the situation when the fringe frequency f_ϕ equals the range bandwidth W_R. Usually, much lower baselines are preferred in order to obtain a suitable spectrum overlap and, hence, interferometric range resolution. Lower baselines are also preferable for phase unwrapping, in particular in the presence of noise, since the fringe frequency or number of phase wraps per pixel is lower for a given slope α (Bamler and Hartl 1998). Note, that increasing the range bandwidth W_R allows larger critical baselines and, hence, interferometer sensivity (equation (2.11)).

All in all, common band filtering addresses the effect of the slightly different look angles of the SAR for flat terrain. This means that it tries to maximise γ_{cb}. Interferometric resolution at least for the range co-ordinate will never be as fine as the SAR range resolution since usable interferometric bandwidth depends on the difference in imaging geometries of the SARs. Common band filtering can be extended to more adaptive filtering approaches taking into account the impact of local terrain angle as expressed in equation (2.13) (Davidson and Bamler 1998; Monti Guarnieri and Rocca 1999; Fornaro and Monti Guarnieri 2002). These algorithms will further improve phase quality in rough terrain regions of the interferogram.

Co-registration

Due to the different flight paths of the satellites, the SAR images are acquired in slightly different geometries (figure 2.13 a). This means the signals are represented on different sampling grids which are possibly mutually rotated, scaled, and shifted. All these operations may be considered as shift in a small region of the two dimensional signal. (Just and Bamler 1994) showed that a mutual shift κ [fractions of a resolution cell] introduces a coherence drop according to:

$$\gamma(\kappa) = \mathrm{sinc}(\kappa) \qquad \text{with} \qquad \mathrm{sinc}(x) = \frac{\sin(\pi\, x)}{\pi\, x} \quad . \tag{2.27}$$

From this follows that for a mis-registration of one resolution cell (approximately one range sample) total decorrelation occurs then no phase information may be retrieved anymore. In order to optimise phase quality one of the images has to be rotated, re-scaled, and shifted (Just and Bamler 1994).

Co-registration includes the retrieval of the information to map the two SAR images onto each other and the subsequent resampling of the secondary channel image (figure 2.6) (Schwäbisch 1995). For conversion or transform of imaging co-ordinate systems (figure 2.13 b) a quadratic bi-variate polynomials ('resampling polynomial') of the form (Schwäbisch 1995):

$$\begin{pmatrix} x_2 \\ R_2 \end{pmatrix} = \begin{pmatrix} a_0 \\ b_0 \end{pmatrix} + \begin{pmatrix} a_1 \\ b_1 \end{pmatrix} R_1 + \begin{pmatrix} a_2 \\ b_2 \end{pmatrix} x_1 + \begin{pmatrix} a_3 \\ b_3 \end{pmatrix} R_1\, x_1 + \begin{pmatrix} a_4 \\ b_4 \end{pmatrix} {R_1}^2 + \begin{pmatrix} a_5 \\ b_5 \end{pmatrix} {x_1}^2 \tag{2.28}$$

where the a_i and b_i, $i = 0...5$, are the polynomial coefficients, $x_1\,(x_2)$ is the master (slave) azimuth co-ordinate, and $R_1\,(R_2)$ is the master (slave) range co-ordinate. These polynomials are determined by measuring shifts on small image patches which are well distributed over the image and calculating the polynomial that best fits the measured shifts in a least squares sense (Schwäbisch 1995).

Mutual shifts can be measured by conventional cross-correlation of the small detected image patches. This approach exploits the similarity of the amplitude structure of the images, i.e. if the scatterers have not changed very much over time, the scattering behaviour generates nearly the same contrast and speckle pattern and allows the registration of the image patches to within sub-pixel accuracy (Schwäbisch 1995).

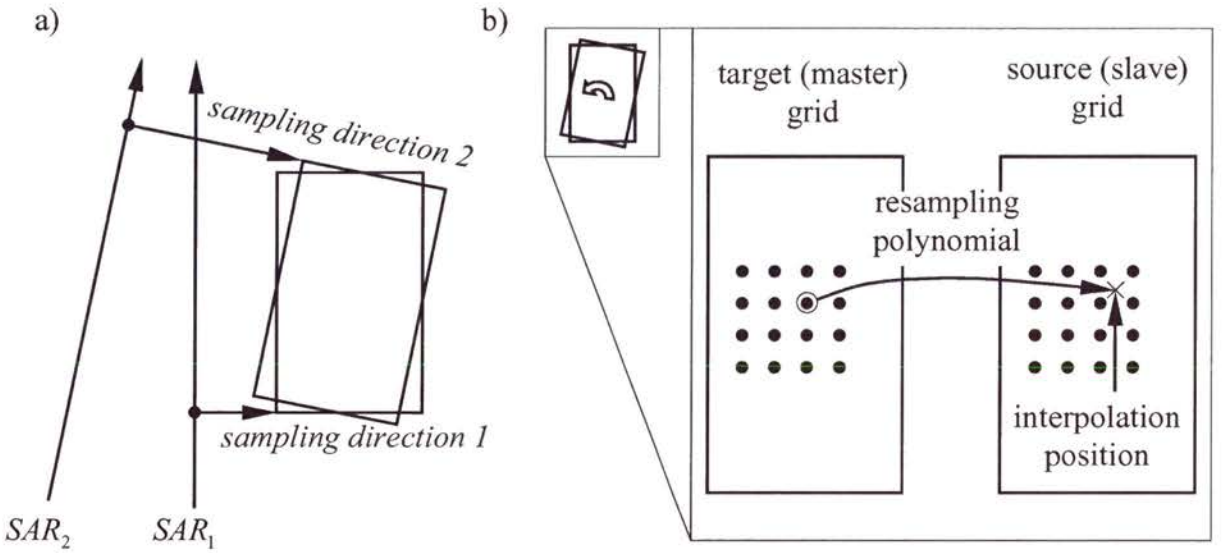

Figure 2.13: Image rotation due to different imaging geometries a) and resampling of the slave image using a resampling polynomial b). The resampling polynomial specifies the interpolation position in the slave image grid given the target (master) position. Thus, the resampling polynomials describes the transform of the slave positions into the master co-ordinate system.

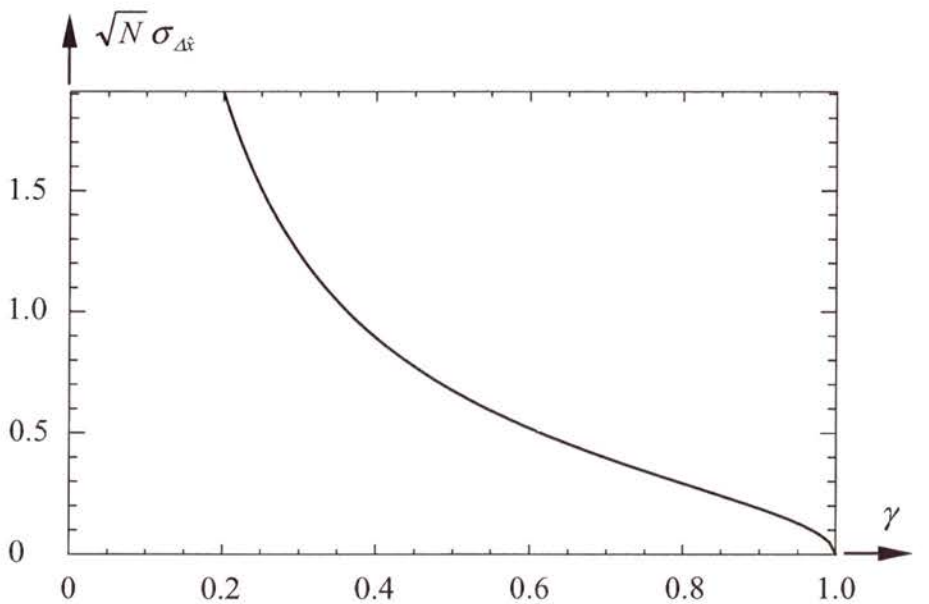

Figure 2.14: Accuracy or standard deviation of the shift estimate given N resolution cells in the image patch and a coherence of γ.

For a distributed target area in two partially correlated complex SAR images an estimate for the achievable co-registration accuracy using cross-correlation can be given (Bamler 2000). Cross-correlation of the complex SAR signals is then in fact the optimum (maximum likelihood) shift estimator. This process is also referred to as 'speckle tracking' (Gray et al. 1999; Bamler 2000). Accuracies of the shift estimates depend on the similarity of the signals, i.e. their coherence γ and to the number of independent samples N used for estimation (Bamler 2000):

$$\sigma_{\Delta x} = \sqrt{\frac{3}{2N}} \sqrt{\frac{1-\gamma^2}{\pi\gamma}} \quad . \qquad (2.29)$$

Figure 2.14 shows the $\sigma_{\Delta x}\sqrt{N}$ - γ - diagram, for the case image patches are used containing 200 resolution cells and a local coherence of 0.8 an accuracy for the shift estimates of 0.03 fractions of a resolution cell is obtained. Equation (2.29) indicates that the better the coherence or similarity of the signals, the better the result for the measured shift. Thus, optimisation of the coherence with common band filtering in advance of co-registration has a direct impact on the quality of the co-registration process.

In addition to the described approach of SAR image co-registration, several alternative techniques and implementations were published: (Gabriel and Goldstein 1988; Madsen et al. 1993; Madsen 1995; Rufino et al. 1998; Scheiber and Moreira 2000).

2.2 ScanSAR imaging mode

ScanSAR mode trades off swath width and resolution (Moore et al. 1981; Tomiyasu 1981). Today's sensors like RADARSAT-1 and ENVISAT/ASAR operate ScanSAR modes with swath widths of 300 km to 500 km at pixel resolutions ranging from 50 m to 1 km (Luscombe 1988; Raney et al. 1991; Brown 1993; Karnevi et al. 1994).

ScanSAR data acquisition starts with acquiring N_B [range lines] at a pulse repetition frequency PRF [Hz] with the antenna beam steered to a near range look angle θ_1 (figure 2.15). This sequence of raw data lines is referred to as '(raw data) burst' and its duration is denoted as $T_B = N_B / PRF$ [s]. The antenna beam is then directed to a second swath parallel to the first one (look angle θ_2) and a second burst is acquired. The individual swaths are also called 'subswaths', 'beams', or 'subbeams'. For the 2-swath system depicted in figure 2.15 the antenna beam is directed back to the near-nadir swath and another cycle of burst acquisition

starts. Within a single swath the bursts are acquired every T_P [s], referred to as burst cycle time. The burst cycle time is not necessarily a multiple of the azimuth sampling interval since in the individual swaths the SAR is operated at different *PRFs* due to timing issues (nadir returns and blind ranges). Nadir returns are strong echoes of pulses scattered back from the ground track of the satellite, in turn, corrupting the signal. Blind ranges are range positions were no echo may be detected since the antenna is transmitting energy (Currie and Brown 1992) at that time. Hence, the number of range lines $N_P = PRF \cdot T_P$ corresponding to the burst cycle period T_P is in general not integer.

Figure 2.16 illustrates the acquisition of one burst for two scatterers at t_0 and t_1. For the scatterers N samples of the azimuth phase history are collected. The individual scatterer histories are weighted by the antenna pattern $A(.)$ with extent limited to T , the antenna or synthetic aperture time of the SAR. Figure 2.16 also shows that the data collected for each scatterer (phase history and weighting) depends on the position of the scatterer with respect to the antenna's on-cycle. Moreover, from the figure it can also be observed that only scatterers within a time extent $[t_0 - (T_A - T_B)/2, t_0 + (T_A - T_B)/2]$ have an exposure time that corresponds to the full burst duration. If this is the criterion for validity, the valid ensemble of imaged scatterers covers an time extent of $T_A - T_B$.

The modulation of the image power of burst-mode and ScanSAR signals over azimuth is referred to as 'scalloping' (figure 2.17). In contrast to strip-map SAR which collects the same amount of energy for each scatterer (figure 2.18: left column), the energy collected for a scatterer depends on the antenna's on-cycle (figure 2.18: right column). Consequently, the intensity variation illustrated in Figure 2.17 will occur. If constant system (thermal) noise is assumed, the signal-to-noise ratio changes according to the signal power modulation of the image.

In order to obtain a continuous ScanSAR image at least every $T = T_A - T_B$ a new burst image has to be acquired. Then each scatterer would be represented by one azimuth look: $N_L = 1$. For radiometric reasons (scalloping), however, the ScanSAR is operated in a way so that $N_L > 1$ (burst) looks are obtained. The approximate (mean) number of (burst) looks per pixel is then obtained from $N_L = (T - T)/T$.

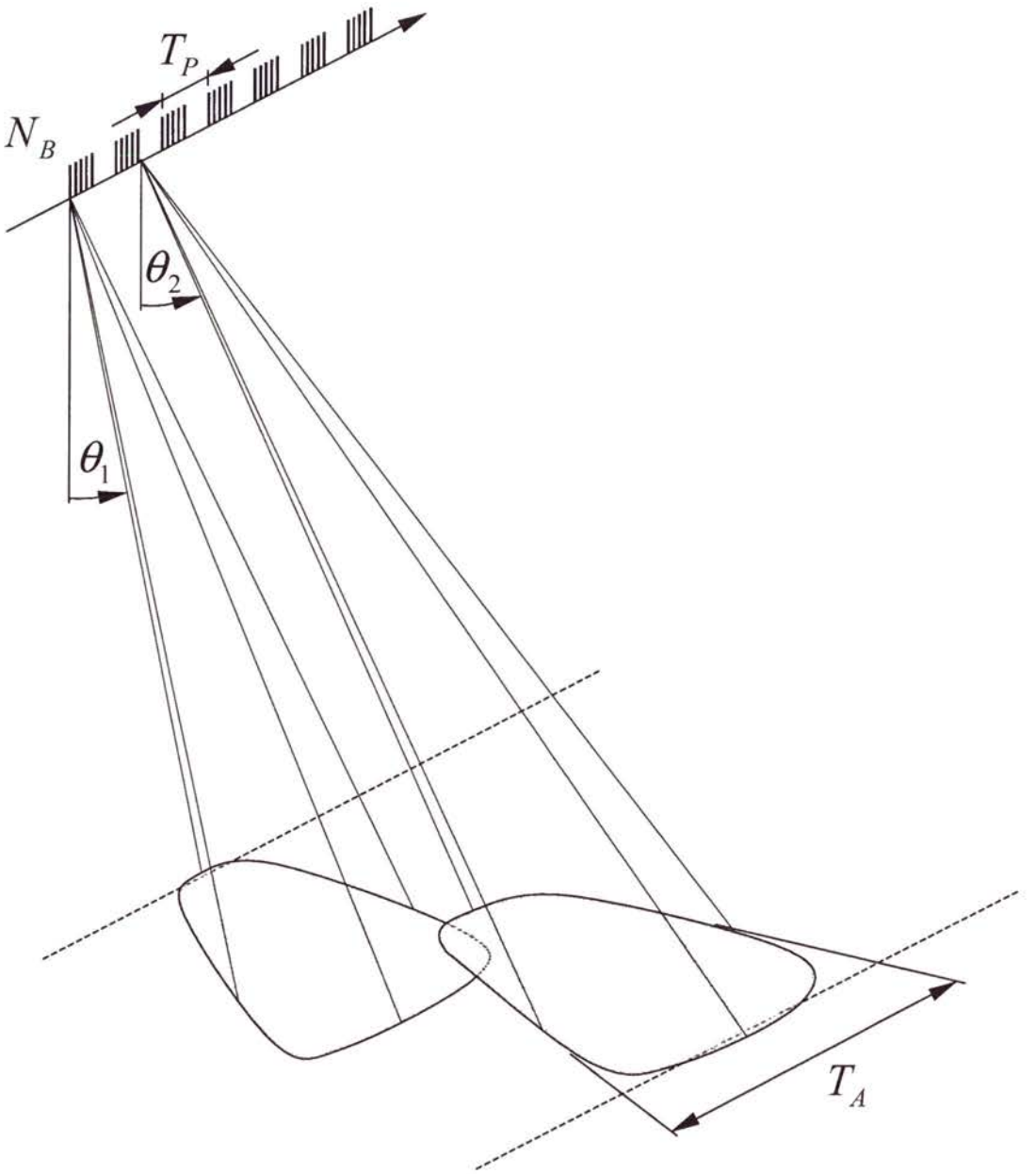

Figure 2.15: Two-beam ScanSAR data acquisition. The instrument acquires a sequence of echo lines ('burst') for the first swath. Then, the antenna is switched to the second swath, acquires a burst, and returns to first swath for another burst acquisition cycle.

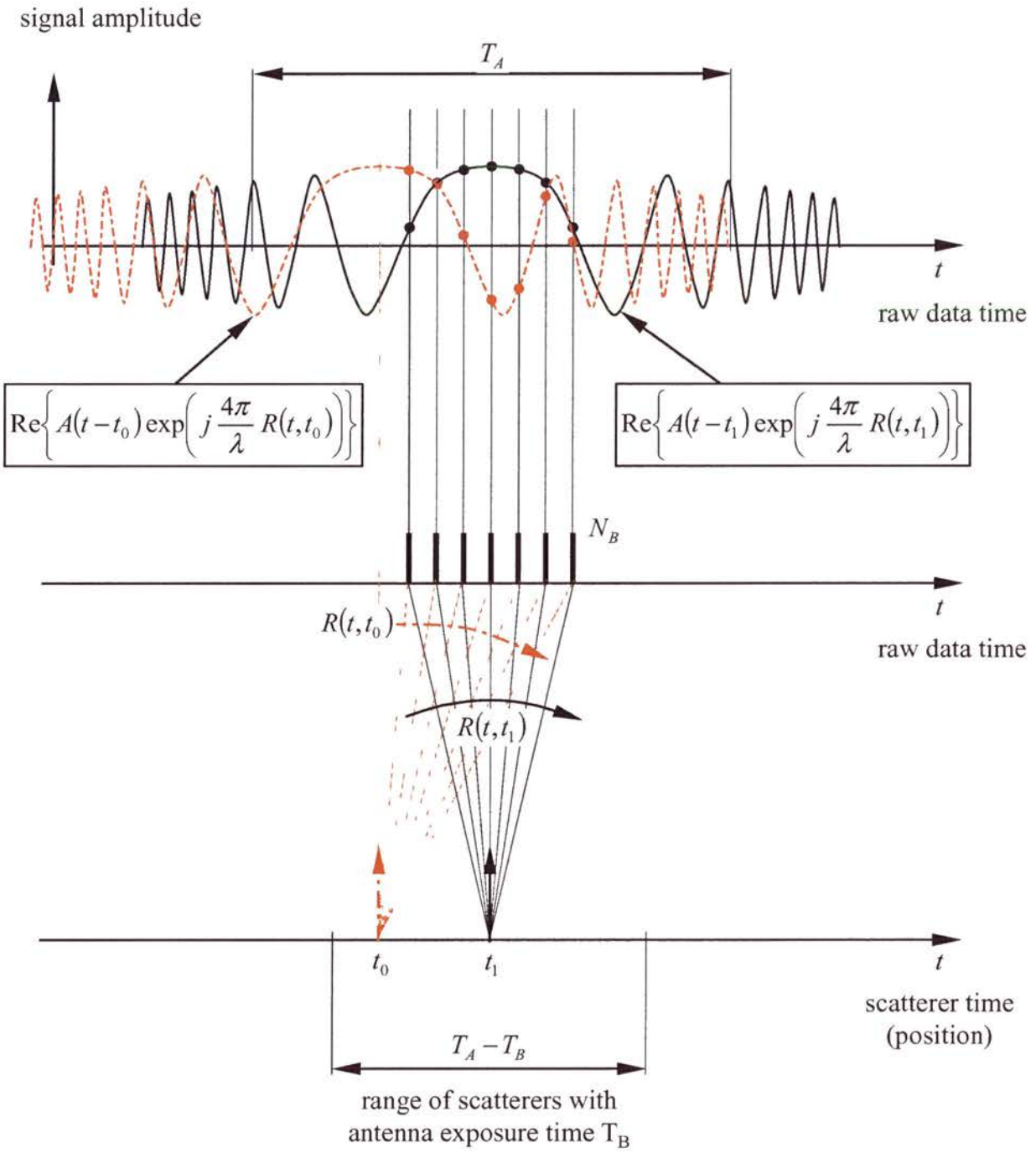

Figure 2.16: ScanSAR data acquisition for two scatterers at t_0 (red, dash-dot line) and t_1 (black, solid line). The centre diagram illustrates the acquired echo lines for one burst within one swath.

a) scalloping effect in a 1-look burst-mode image

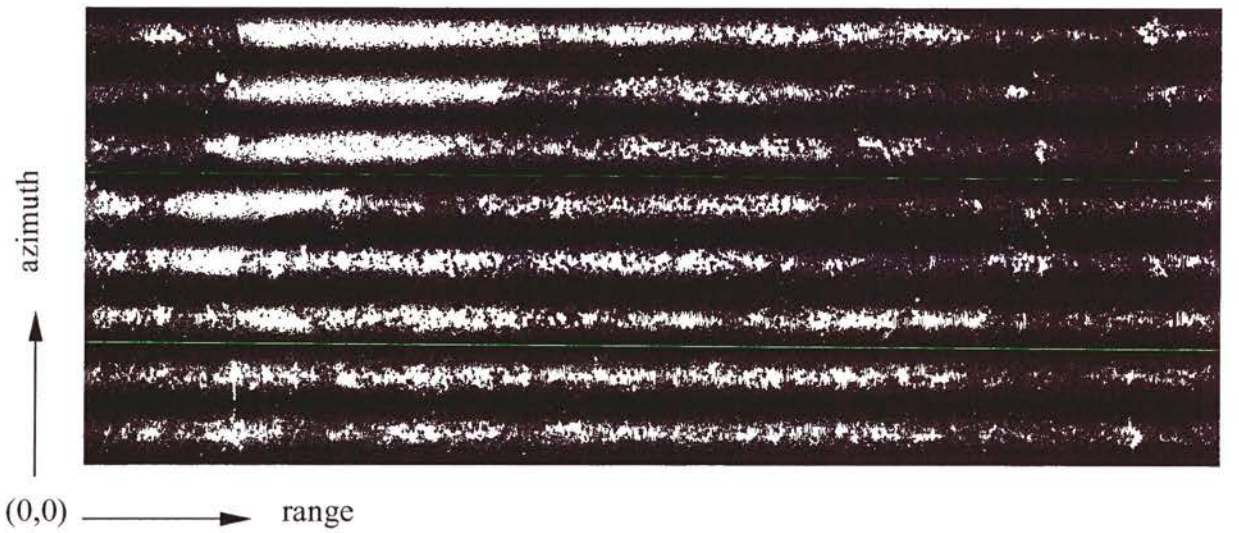

b) example normalised azimuth power profile of a)

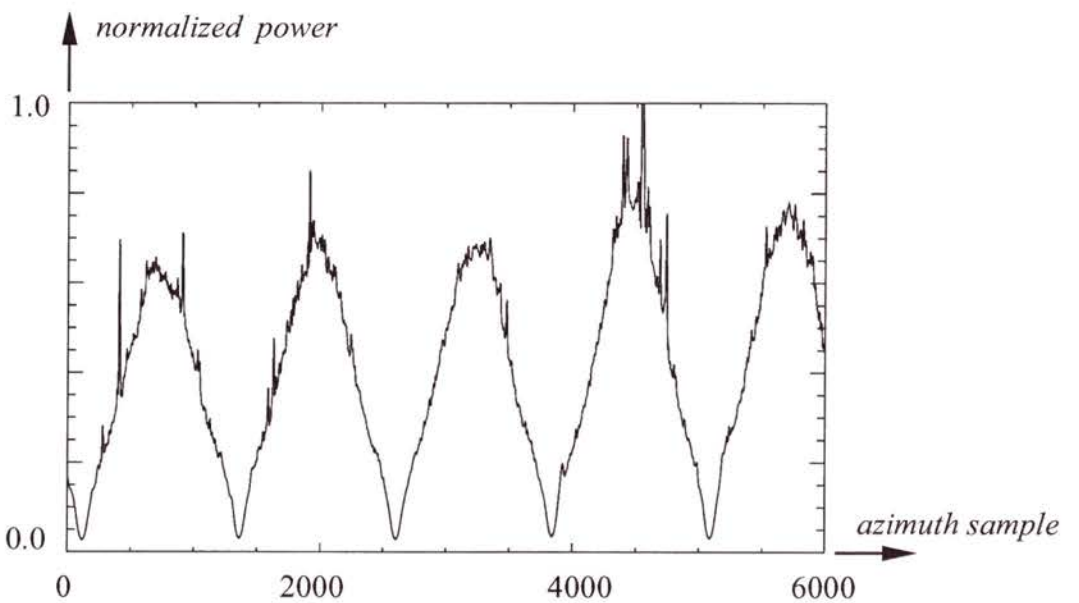

Figure 2.17: Effect of scalloping. Burst-mode image simulated from ERS data a) and normalised azimuth power profile b).

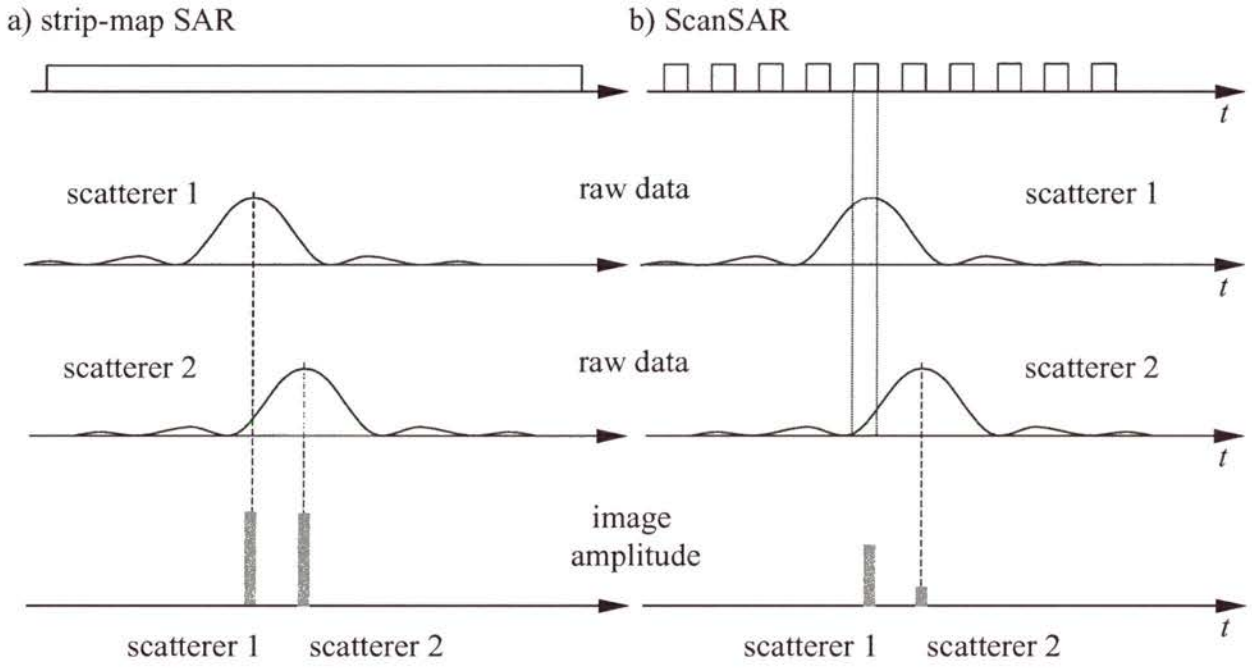

Figure 2.18: Scalloping effect in ScanSAR imaging. The upper, middle, and lower part of the figure represents the antenna on-off cycle, the energy collected for two scatterers by the SARs, and the compressed energy for the scatterer, respectively. For a strip-map SAR system a) the collected energy is the same for each individual scatterer. In contrast, the collected energy in the ScanSAR case b) depends on the relative position of the scatterer and the antenna on-cycle.

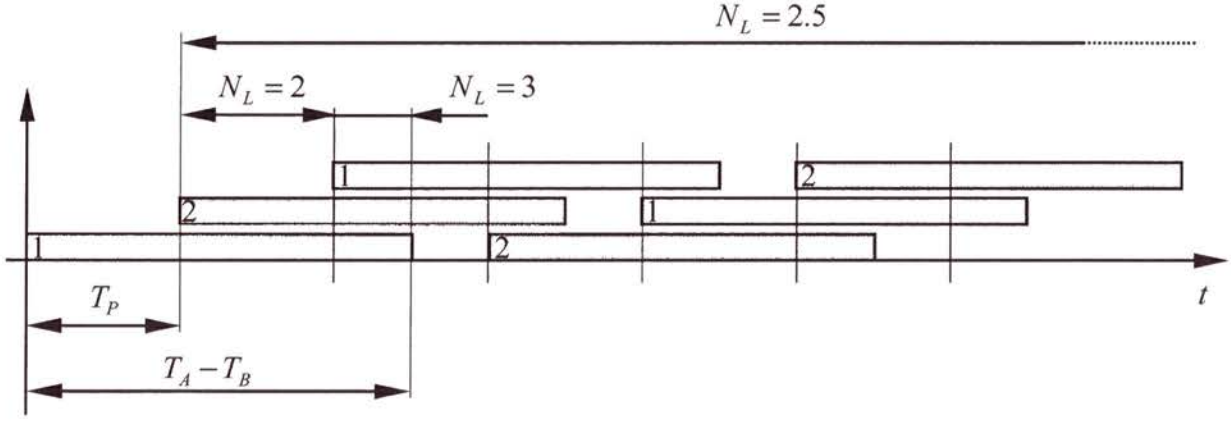

Figure 2.19: Burst timing configuration for the RADARSAT-1 ScanSAR Narrow data set (orbit: 10969, section 7.1).

An example timing configuration for the ScanSAR Narrow data set (orbit 10969, section 7.1) used in this thesis is illustrated in figure 2.19. The data set has a non-integer number of looks ($N_L = 2.5$). This means that for half of the image pixels two (three) burst looks are available. From figure 2.19 it can be observed that the burst looks indexed with 1 have some overlap with preceding and following bursts. Such areas are useful, for example for mode operation tests as well as processing and calibration verifications. Swaths are acquired within the burst period time data for N_S , assuming the burst duration for the individual swaths are approximately the same, the burst duration T is in the order of T_P / N_S .

2.3 Summary

This section reviewed basic concepts of SAR interferometry and ScanSAR imaging. An overview of SAR interferometry comprises a summary of imaging geometry of the interferometer, retrieval of height information from interferometry, and main parameters of the interferometer. It further provided an introduction into the concept of coherence and the interferometric processing of SAR signals. For a basic understanding of ScanSAR imaging, the special acquisition technique was discussed introducing all terms and notation required for the following deliberations.

... it is through our theories that we learn to observe, that is to say, to ask questions which lead to new observations and to new interpretations. This is the way our observational knowledge growths. And the questions asked are, as a rule, crucial questions which may lead to answers that decide between competing theories. It is my thesis that it is the growth of our knowledge, our way of choosing between theories, in a certain problem situation, which makes science rational.

- Truth, Rationality, and the Growth of Scientific Knowledge (Popper 1963).

Chapter 3

Burst-mode Signal Theory

This chapter discusses the main properties of burst-mode and ScanSAR signals in two sections. Section 1 refers to ScanSAR and burst-mode complex SAR images and discusses their properties. In section 2 the characteristics of ScanSAR and burst-mode interferograms are discussed. ScanSAR data are contrasted with strip-map data in order to highlight the particularities of ScanSAR data. This in turn gives a thorough overview of the properties of burst-mode data. This is necessary for the proper interferometric processing and issues discussed in section 6.

3.1 Burst-Mode Signal and Spectral Properties

3.1.1 Point Scatterer Response

The variables t [s] and f [Hz] denote the azimuth time and corresponding Doppler frequency variable, respectively. All following excursions are outlined in the azimuth dimension, since the range dimension properties of the burst-mode and ScanSAR signals are the same as for strip-map mode. The azimuth signals are sampled at the pulse repetition frequency PRF [Hz] and the azimuth chirp rate is referred to by FM [Hz/s]. With the processed Doppler bandwidth W_A [Hz] the full synthetic aperture time is calculated as

$T_A = W_A / |FM|$ [s] or equivalently it is expressed in number of range lines by $N_A = PRF \cdot T_A$ [range lines]. The resolution of the SAR system is calculated from $\rho_A = a / W_A$ [s] with $a \approx 1$. The factor a depends on the shape of the azimuth antenna pattern and on the weighting window used in the SAR processor for side lobe reduction. Within this thesis a will be set to 1 for clarity.

With burst-mode (section 1.2), bursts with duration T_B are acquired having bandwidth $W_B = |FM| T_B$ [Hz] and resolution $\rho_B = 1/W_B$. Throughout this thesis it is assumed that the number N_B of range lines per burst is large enough for a sufficiently high time-bandwidth-product to use the stationary phase assumption (the low time-bandwidth-product case has been investigated by (Monti Guarnieri and Guccione 2001)). The fact that the number of range lines N_P corresponding to T_P is in general not an integer (section 1.2) is not substantial for the following signal description and will not be considered further since it can be correctly handled by the SAR processor.

The point-scatterer response for the strip-map raw data signal at position $t = t_0$ is (appendix A1):

$$h_{raw,A}(t;t_0) = A(FM\,(t-t_0)) \exp\left(j\,\pi\,FM\,(t-t_0)^2\right) \qquad (3.1)$$

with spectrum

$$H_{raw,A}(f;t_0) = A(f) \exp\left(-j\,\pi\,f^2/FM\right) \exp(-j\,2\pi\,t_0\,f) \qquad (3.2)$$

where a radiometric factor is neglected and continuous time variables are used for clarity.

The instantaneous frequency (principle of stationary phase) of the response is given by:

$$f_{inst}(t) = \frac{1}{2\pi}\dot{\varphi}(t) = FM(t-t_0) \qquad (3.3)$$

where $\varphi(t)$ is the argument of the exponential in equation (3.1). With $FM < 0$ the energy of the response is concentrated along a downward sloping straight line in a scatterer-time versus signal-frequency diagram (a time-frequency diagram) as shown in figure 3.1.

The response of the n[th] burst in the case of an acquisition in burst-mode is:

$$h_{raw,n}(t;t_0) = A(FM\,(t-t_0))\,\mathrm{rect}\left(\frac{t-n\,T_P}{T_B}\right)\exp\left(j\,\pi\,FM\,(t-t_0)^2\right) \qquad (3.4)$$

and its spectrum is obtained as

$$H_{raw,n}(f;t_0) = A(f)\,\mathrm{rect}\left(\frac{f+n\,W_P+FM\,t_0}{W_B}\right)\exp\left(-j\,\pi\,f^2/FM\right)\exp\left(-j\,2\pi\,t_0\,f\right) \qquad (3.5)$$

For the equations zero-Doppler steering of the antenna beam and a quadratic azimuth phase history were assumed. All spectra were obtained using the principle of stationary phase. Within this section, the function $A(f)$ denotes the spectral envelope of the signals. It includes both the two-way Doppler antenna pattern and any weighting and bandlimiting function that was applied during processing. By representing the frequency f via the stationary phase principle by $f = FM\,(t-t_0)$ the time domain envelope of the azimuth chirp is represented by $A(FM\,(t-t_0))$ with support $|t-t_0| \le T_A/2$ (cf. figure 3.1).

Figure 3.1 also illustrates the relationship of the burst-mode signal and its spectrum. Each burst contributes an approximately rectangular shaped (short a rect-shaped) bandpass spectrum at centre frequency $f = -(n\,W_P + FM\,t_0)$, which depends on the location t_0 of the point scatterer and the burst number n. The bursts in figure 3.1 are indicated as bold sections of the time frequency support of the strip-map time-frequency representation of the scatterer response. Slight distortions of the rect-function due to $A(f)$ are neglected in the following development. Often weighting of the bursts is applied in the processor for side-lobe control. In this case the single burst spectrum reflects the shape of the weighting function rather than a rect-function.

SAR processing removes the quadratic phase from the spectrum of equation (3.2) (Bamler and Schättler 1993). Hence, the shape of the focussed point target response $h_A(t;t_0)$ is the inverse Fourier transform of $A(f)$:

$$h_A(t;t_0) = a(t-t_0) \qquad (3.6)$$

where corresponding small and capital letters denote the Fourier transform pairs (e.g. $a(t) \leftrightarrow A(f)$). Since $A(f)$ is band-limited to $|f| \le W_A/2$, $h_A(t)$ has resolution ρ_A. Illustration 3.3 a) shows the real part of the range compressed raw data, a patch of the focussed SAR image and a 3D illustration for strong point like target (transponder) recorded

using a strip-map system. The data are ERS-1 data acquired with a Doppler centroid of about -300 Hz, therefore, the main lobe of the chirp is not centred in the raw data image.

If each of the bursts is processed individually, the burst's spectrum and point response – neglecting the spectral weighting function $A(f)$ – will be

$$H_n(f;t_0) = \mathrm{rect}\left(\frac{f + n\,W_P + FM\,t_0}{W_B}\right)\exp(-j\,2\pi\,t_0\,f) \qquad (3.7)$$

$$h_n(t;t_0) = \mathrm{sinc}(W_B\,(t-t_0))\exp(j\,2\,\pi\,FM\,(n\,T_P - t_0)\,(t-t_0)) \qquad (3.8)$$

with the inherent single burst resolution ρ_B. Individually processed or focussed 'bursts' of raw data echo lines are referred to as single 'burst images' or 'burst looks'. Figure 3.2 shows a comparison of a strip-map and a burst-mode SAR response magnitude (equations (3.6) and (3.8)) for parameters as given in section 7.1 and $T_A = 0.5\,\mathrm{sec}$. Illustration 3.3 shows the real part of the range compressed raw data of strip-map data and the corresponding burst-train for the case of a bursted acquisition, a patch of the focussed SAR images is illustrated together with a 3D illustration for the sample strong point like target.

The spectrum of the N_L coherently added burst images for one point scatterer from equation (3.7) is given by (cf. figure 3.4):

$$H_C(f;t_0) = \sum_{N_L}\mathrm{rect}\left(\frac{f + nW_P + FM\,t_0}{W_B}\right)\exp(-j\,2\pi\,f\,t_0) \qquad (3.9)$$

and corresponds to

(3.10)

$$\begin{aligned} h_C(t;t_0) &= \mathrm{sinc}(W_B\,(t-t_0))\sum_n \exp(j\,2\,\pi\,FM\,(n\,T_P - t_0)\,(t-t_0)) \\ &= \mathrm{sinc}(W_B\,(t-t_0))\exp(-j\,2\,\pi\,FM\,t_0\,(t-t_0))\sum_{N_L}\exp(-j\,2\,\pi\,n\,W_P\,(t-t_0)) \end{aligned}$$

in time domain representation (figure 3.5). Burst-mode images constructed from the coherent addition of individual bursts are called 'multiple coherent burst' or 'multiple coherent look' images. Figure 3.6 illustrates this type of burst-mode signals and contrasts it to the result for a single burst mode image. The data was simulated from the same data as shown in figure 3.3.

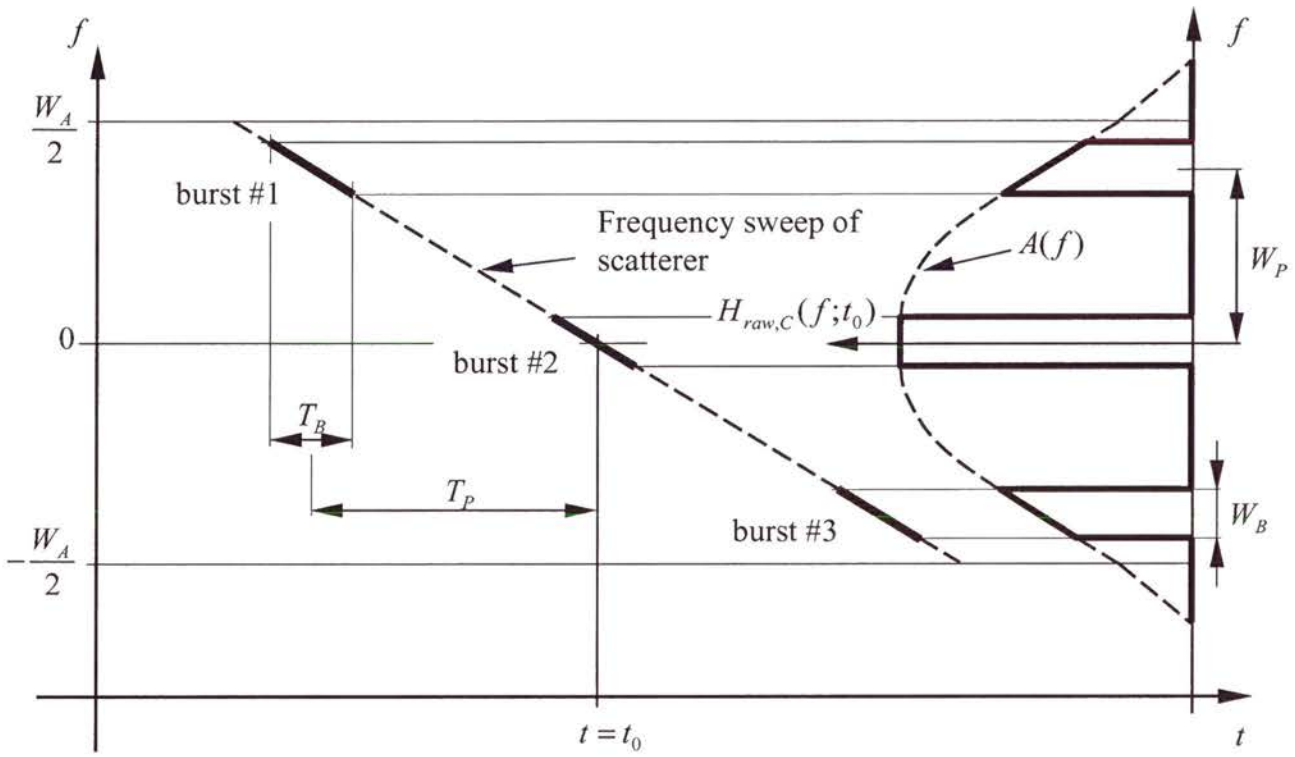

Figure 3.1: Time-frequency diagram of a single scatterer at $t=t_0$ (raw data time) , acquired with a 3 burst-look system. The frequency sweep of the scatterer, as acquired by a strip-map system, is indicated by the dashed line. From this chirp, only cuts or bursts are measured. On the right hand side the burst-mode transfer function for the scatterer is shown.

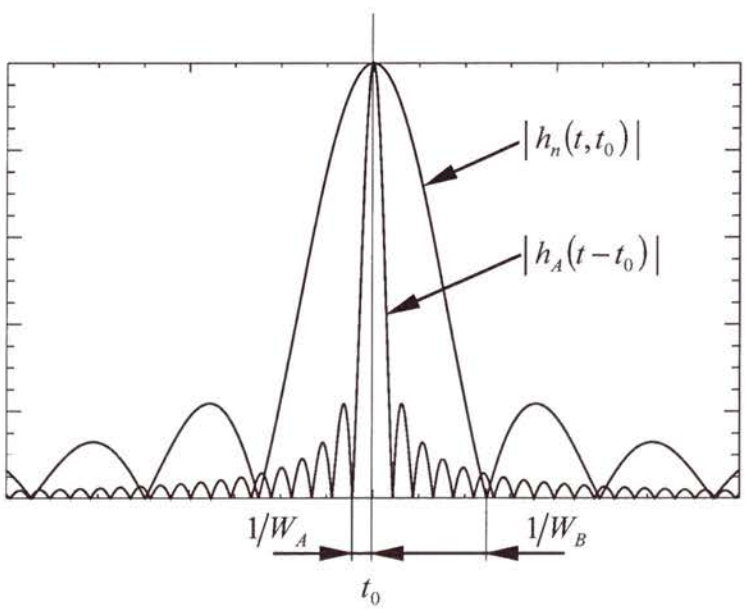

Figure 3.2: Comparison of the impulse response function of a single burst and of a full aperture SAR

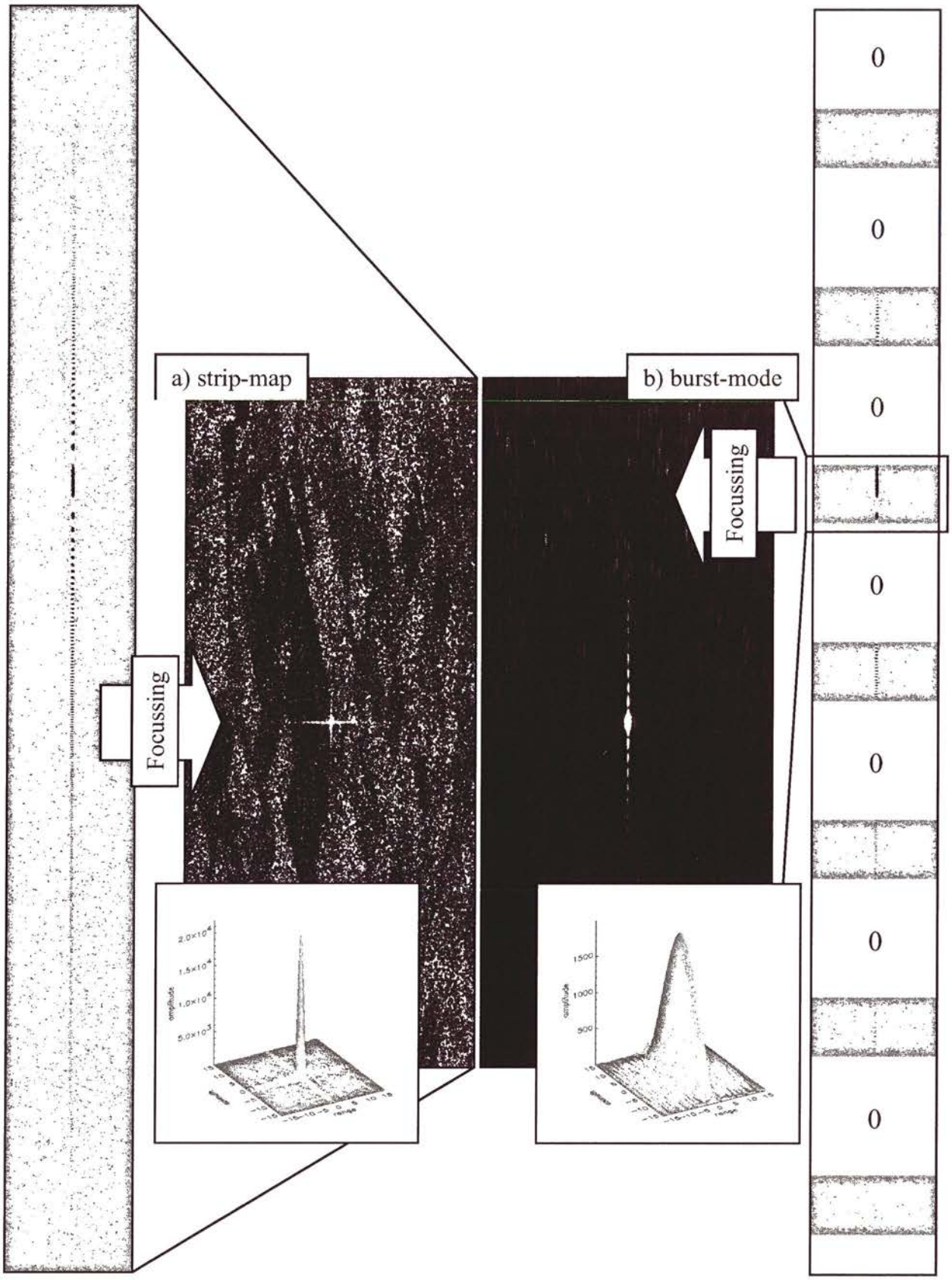

Figure 3.3: Comparison of the signals from a strip-map a) and from a single burst b) for a very strong point like target ($f_{DC} \approx$ -300 Hz). The real part of the range compressed raw data, the focussed image, and a 3D illustration of the point target (transponder) is illustrated (Simulated from ERS-1 data).

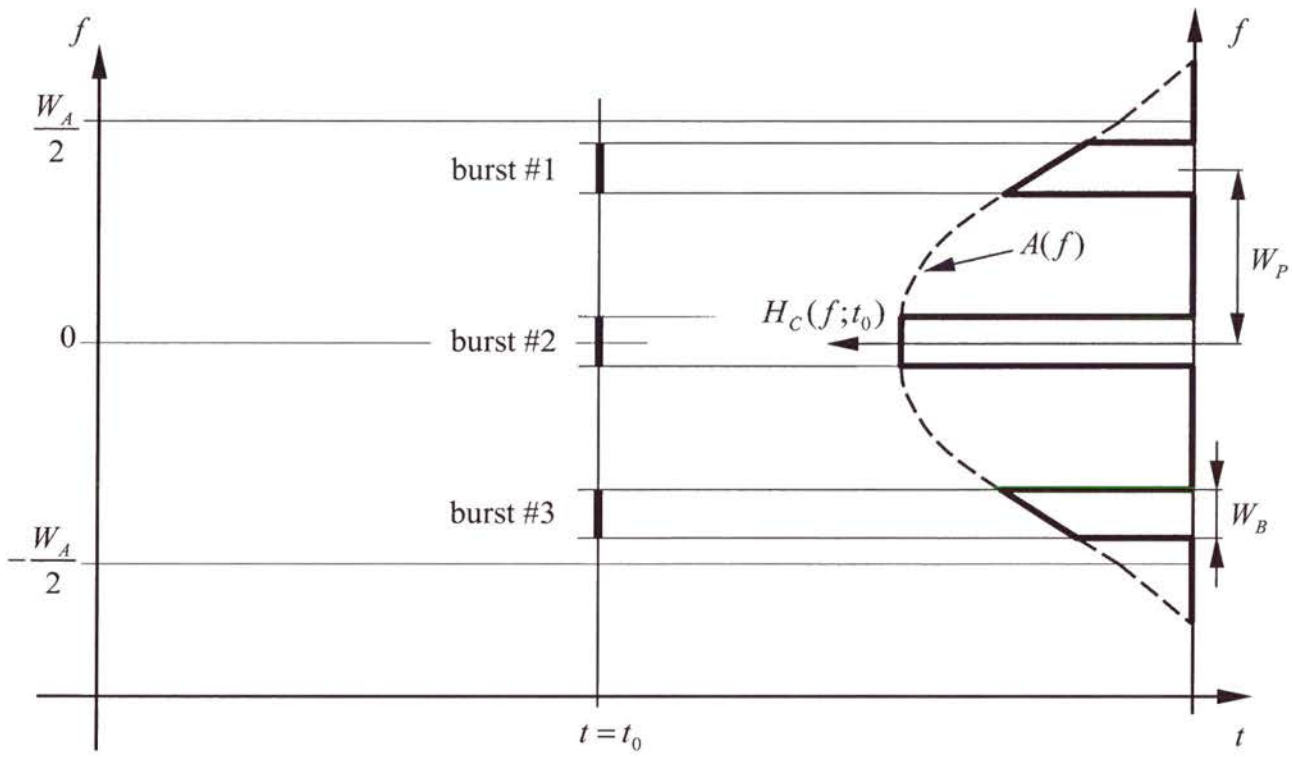

Figure 3.4: Time-frequency diagram of a single scatterer at $t=t_0$ (azimuth time in focussed image, scatterer time), acquired with a 3 burst-look system after azimuth focussing.

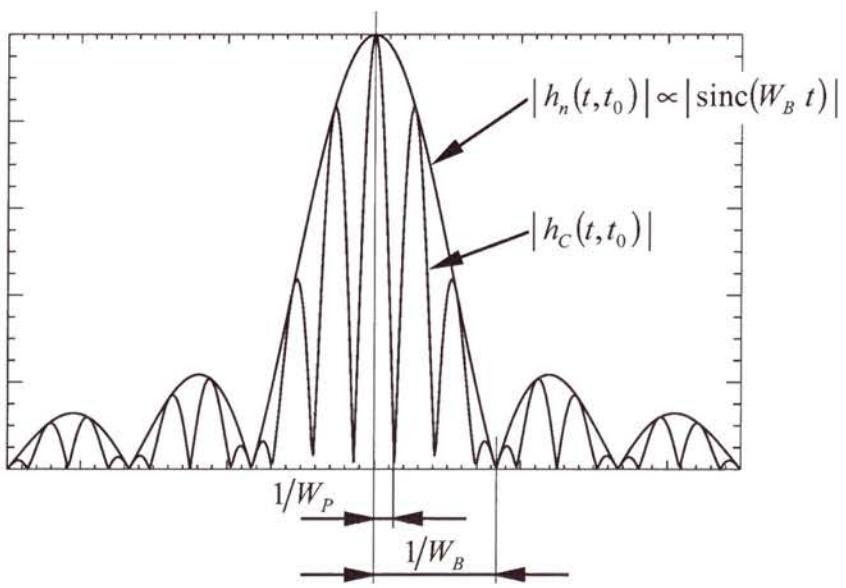

Figure 3.5: Multiple burst-mode signal impulse response. The highly modulating pattern of multiple coherent burst-mode data occurs due to the superposition of the centre frequencies of the individual bursts.

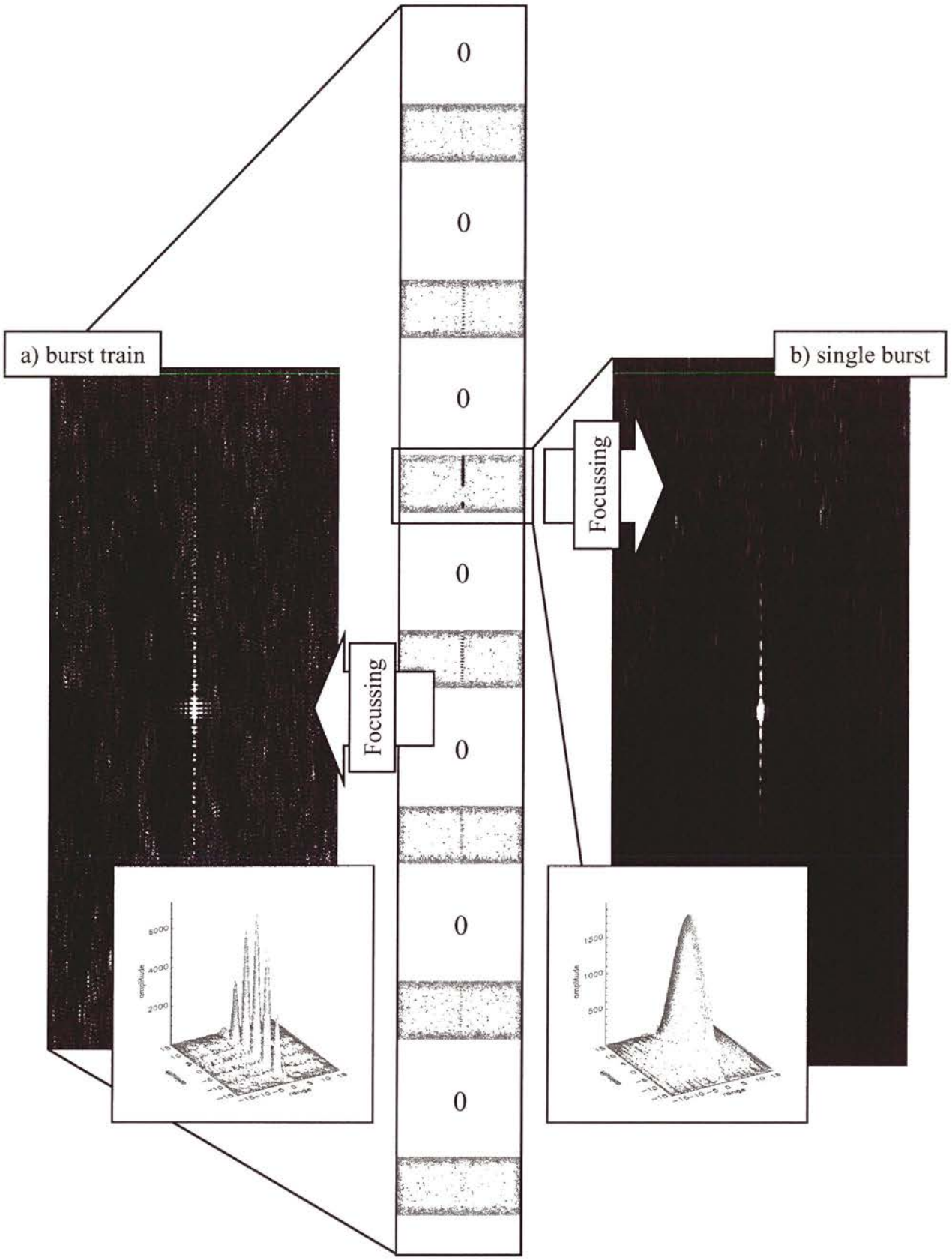

Figure 3.6: Comparison of the signal from a train of bursts a) and from a single burst b) for a very strong point like target ($f_{DC} \approx$ -300 Hz). The real part of the range compressed raw data, the focussed image, and a 3D illustration of the point target is illustrated (Simulated from ERS-1 data).

The impulse response of equation (3.10) as visualised in figure 3.5 has maxima if the complex phasors of the sum have the same orientation, i.e. for:

(3.11) $$\sum_{N_L} 2\pi\, n W_P \left(t - t_0\right) = k\, N_L\, 2\pi \qquad \text{with} \quad k \quad \text{integer}$$

at

(3.12) $$\left(t - t_0\right) = \frac{k}{W_P}$$

and minima for

(3.13) $$\sum_{N_L} 2\pi\, n W_P \left(t - t_0\right) = m\, 2\pi \quad \text{with} \quad m \quad \text{integer, } \textit{not a multiple of } N_L$$

at

(3.14) $$\left(t - t_0\right) = \frac{m}{N_L\, W_P}.$$

This characteristic of the multiple coherent burst point scatterer response is also evident from figure 3.6 a). It originates from the extinction and mutual amplification of the phasors in the sum of equation (3.10) equivalent to the diffraction patterns from a slit aperture grid known from optics.

3.1.2 Autocorrelation Function and Power Spectral Density of the Burst-Mode Signal

Natural scenes may be represented as a combination of deterministic (e.g. man made features like houses) or random targets (e.g. forest canopy layers). For the following derivations only distributed and homogenous targets are considered. A suitable model for these targets is a complex Gaussian process with zero mean since within a resolution cell many independent scatterers may be assumed to contribute to the return signal (Zebker and Goldstein 1986; Madsen 1987). Hence, the autocorrelation function (ACF) of the complex reflectivity function $\chi(t)$ is:

$$R_{\chi\chi}(\tau) = E\{\chi^*(t)\,\chi(s)\} = \delta(t-s) \qquad (3.15)$$

where unit variance was assumed, E{.} is the expectation value operator, and $\delta(t)$ is the Dirac distribution.

This assumption is used for the derivation of the auto-correlation function (ACF) of burst image *n*. The calculation (appendix A2) starts from

$$R_{uu,n}(t,\tau) = E\{u_n^*(t)\,u_n(t+\tau)\} \qquad (3.16)$$

with (see appendix A1):

$$u_n(t) = \int dt_0\; h_n(t,t_0)\,\chi(t_0)\,. \qquad (3.17)$$

Using equation (3.8) the ACF of the single burst image is finally found as (appendix A2):

$$R_{uu,n}(t,\tau) = W_B\,\mathrm{tri}\left(\frac{\tau}{T_B}\right)\mathrm{sinc}\left(\left(W_B - |FM\,\tau|\right)\tau\right)\exp\left(j\pi FM\left[2\left(nT_P - t\right)\tau - \tau^2\right]\right) \qquad (3.18)$$

This function is limited to $-T_B \le \tau \le T_B$ and has linear and quadratic phase components (figure 3.7). Moreover, the phase functions show a dependency on the position t which expresses the azimuth-variant behaviour of the burst signal; in other words, the signal is not stationary.

For a suitable approximation to (3.18), consider a small neighbourhood around the centre peak. In this vicinity, it is a sinc-like function $\mathrm{sinc}(W_B\tau)$ and the quadratic phase component may be neglected (appendix A2):

$$R_{uu,n}(t,\tau) \approx W_B\;\mathrm{sinc}(W_B\,\tau)\exp\left(j\,2\pi\,FM\,(nT_P - t)\,\tau\right)\mathrm{rect}\left(\frac{t}{2\,T_B}\right) \qquad (3.19)$$

Its Fourier transform is the (time variant) power spectral density (PSD) of the burst-mode data:

$$S_{uu,n}(f,t) \approx \mathrm{rect}\left(\frac{f + nW_P + FM\,t}{W_P}\right). \qquad (3.20)$$

This suggests that this approximate PSD may be also obtained as $|H_n(f;t)|^2$ (equation (3.7)) by considering the burst impulse response as a locally (scatterer-)time-invariant system. Note, however, that the Fourier transform of (3.18) may only be evaluated numerically or using the principle of stationary phase. Both methods do not provide information above the approximate PSD of equation (3.20). Hence, it is convenient and sufficient to use the approximate power spectral density of equation (3.20) for the following considerations (appendix A2).

Since the individual burst images are not correlated the following property of multiple burst image ACF can be found (appendix A2):

$$R_{uu,C}(t,\tau) = \sum_n R_{uu,n}(t,\tau) \qquad (3.21)$$

This equation is valid for use with the exact and with the approximated ACF (equations (3.18) and (3.19)). Inserting equation (3.19) yields

$$R_{uu,C}(t,\tau) \approx W_B\ \mathrm{sinc}(W_B\ \tau)\exp(j\,2\pi\,FM\,t\,\tau)\sum_n \exp(j\,2\pi\,nW_P\,\tau) \qquad (3.22)$$

The ACF of the multiple burst image has similar properties (equations (3.21) and (3.22)) as the point scatterer response from equation (3.10) and, for the multiple burst image PSD, is:

$$S_{uu,C}(f,t) \approx |H_C(f,t)|^2 \qquad (3.23)$$

This PSD was estimated from real data in a distributed target area (ScanSAR data set 10969, section 7.1) and is illustrated in figure 3.8 (cf. (Monti Guarnieri and Prati 1996)). It shows the azimuth dependent bandpass characteristic of the burst-mode data. Each target is represented by N_L spectral slices with bandwidth W_B and centre frequencies that, depending on the target's position, sweeping the available azimuth bandwidth ($-W_A/2$ to $W_A/2$).

a) amplitude of the burst-image ACF

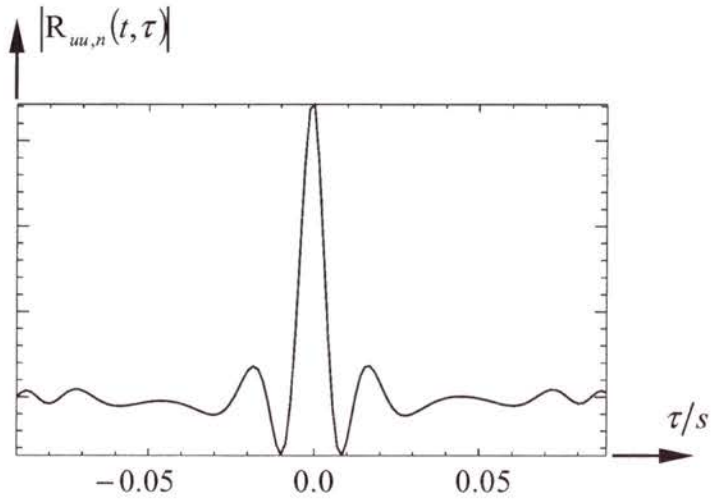

b) phase of the burst-image ACF

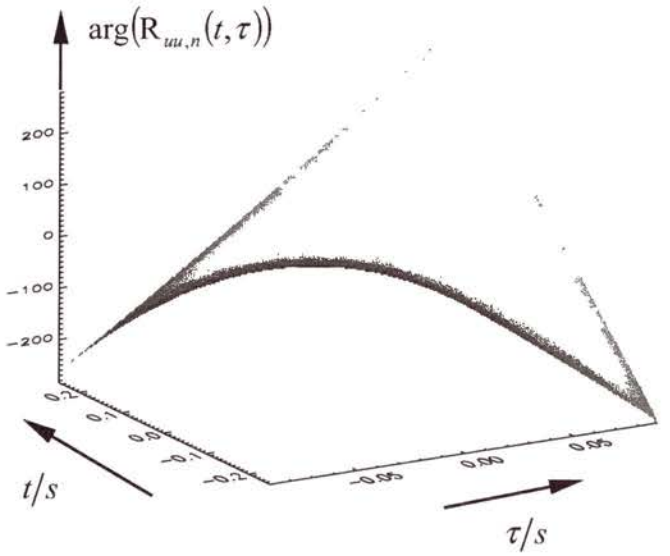

Figure 3.7: Autocorrelation function of burst-mode data. Amplitude $|R_{uu,n}(t,\tau)|$ a) and Phase $\arg(R_{uu,n}(t,\tau))$ b) of the burst-mode autocorrelation function (ScanSAR Narrow data set parameters from section 7.1: T_B= 0.09 sec, T_P= 0.1838 sec, n = 0, FM = -1950 Hz/sec.)

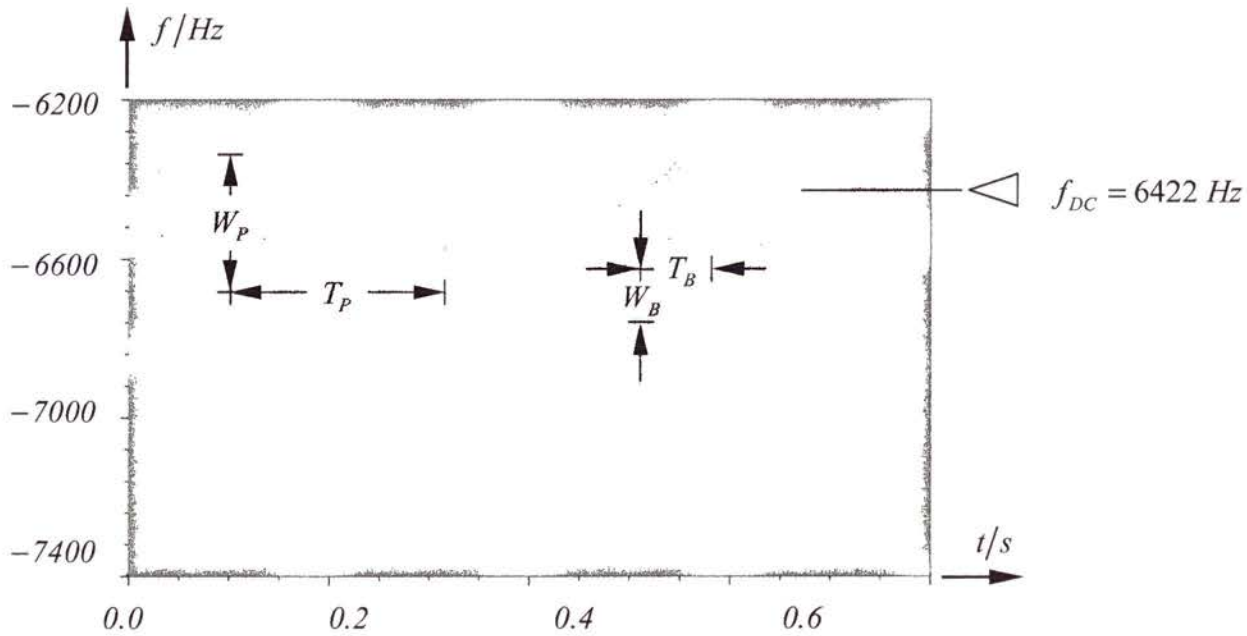

Figure 3.8: The power spectral density estimated from real data in a distributed target area (ScanSAR data set 10969, section 7.1). The energy of the bursted data is represented in the domain spanned by azimuth frequency versus azimuth time. In this multiple-coherent burst time-frequency diagram, the support of each individual burst has an upward slope, since from successive targets ‚earlier' sections of the phase history are extracted within one antenna on cycle (cf. figure 3.1).

3.1.3 Sampling of complex burst-mode signals

From equations (3.7) and (3.20) it is clear that the single burst-mode image signal can be represented at a sampling frequency lower than the acquisition PRF. The burst image signal has bandpass character with bandwidth W sweeping the frequency range $-W_A/2$ and $W_A/2$. Hence, if the burst is sampled at a lower sampling frequency $W_B < PRF_n < PRF$, the spectrum is wrapped back into the region $-PRF_n/2$ to $PRF_n/2$. However, the full spectrum can be reconstructed since the sampling frequency is larger than the scatterer's bandwidth. The interpolation operator must only know the mutual relationship of the scatterer spectra, i.e. the slope of frequency sweep FM. Operations like detection or interferogram formation generate a low pass signal of $2W$ (see below).

In contrast, multiple coherent burst image signals have a bandwidth comparable to the full strip-map SAR bandwidth with spectral components within the range $-W_A/2$ to $W_A/2$. This means subsampling would destroy the information of the individual scatterers. Multiple coherent burst-mode data must then be represented at a sampling frequency higher or equal to the processing bandwidth W_A.

3.2 Properties of the interferometric burst-mode signals

This section discusses the interferometric properties of burst-mode data. For illustration, properties, conventional strip-map data are compared to burst-mode data properties. Equations for coherence, auto-correlation function, and power spectral density are derived.

3.2.1 Interferometric Properties of Strip-map Signals

For the derivations, homogeneous targets are modelled as Gaussian stationary scatterers with the following complex reflectivity functions (Bamler 2000):

$$\begin{aligned} \chi_1(t) &= \sqrt{1-\gamma_T}\, a(t) + \sqrt{\gamma_T}\, c(t) \\ \chi_2(t) &= \left(\sqrt{1-\gamma_T}\, b(t) + \sqrt{\gamma_T}\, c(t)\right) \exp\left(-2\pi f_\phi t\right) \end{aligned} \qquad (3.24)$$

These two processes are mutually correlated, have coherence γ_T (temporal coherence), and a possible azimuth fringe frequency, referred to as f_ϕ. Sufficiently small analysis windows are assumed to consider f_ϕ constant (azimuth spectral shift is discussed in chapter 6.1.4). The model uses the functions $a(t)$, $b(t)$ and $c(t)$ that are mutually independent, zero-mean, white

circular complex Gaussian processes with unit variance. The two processes $\chi_1(t)$ and $\chi_2(t)$ have the cross-correlation function (CCF):

$$\mathrm{E}\{\chi_1(t)\,\chi_2^{*}(s)\} = \gamma_T\,\delta(t-s)\exp(+j\,2\pi\,f_\phi\,s) \qquad (3.25)$$

where $\delta(t)$ is the Dirac delta distribution and the asterisk "*" denotes complex conjugate.

The *i*-th focussed SAR channel signal, where $i = 1$ (master), 2 (slave), is the convolution of the end-to-end system impulse response function (3.6) with the individual channel complex reflectivity functions:

$$u_i(t) = \int dt_0\;\chi_i(t_0)\,h_{A,i}(t;t_0) \qquad (3.26)$$

The standard definition of coherence is:

$$\gamma = \frac{\mathrm{E}\{i(t)\}}{\sqrt{\mathrm{E}\{|u_1(t)|^2\}\,\mathrm{E}\{|u_2(t)|^2\}}}, \qquad (3.27)$$

where $i(t) = u_1(t)\,u_2^{*}(t)$ and γ are the interferogram value and the complex coherence, respectively.

For the coherence of a strip-map signal, the following expression can be found:

$$\gamma_A(f_\phi,t) = \gamma_T\exp(j\;2\pi\,f_\phi\,t)\,\frac{\int df\;H_{A,1}(f)\;H_{A,2}^{*}(f-f_\phi)}{\sqrt{\int df\;|H_{A,1}(f)|^2\int df\;|H_{A,2}(f)|^2}} \qquad (3.28)$$

where equation (3.26) and Parseval's theorem were used.

The power spectral density (PSD) of the strip-map interferogram is obtained by calculation of the auto-correlation function (ACF):

$$\begin{aligned} \mathrm{R}_{ii,A}(\tau,t) &= \mathrm{E}\{i^{*}(t)\,i(t+\tau)\} \\ &= \mathrm{E}\{u_1^{*}(t)\,u_2(t)\,u_1(t+\tau)\,u_2^{*}(t+\tau)\} \end{aligned} \qquad (3.29)$$

of the interferogram and transforming it into Fourier domain.

For the following step the well known Reed's theorem (Reed 1962) is used:

$$\begin{aligned} \mathrm{R}_{ii,A}(\tau) &= \mathrm{E}\{u_1^{*}(t)\,u_1(t+\tau)\}\;\mathrm{E}\{u_2(t)\,u_2^{*}(t+\tau)\} + \mathrm{E}\{u_1^{*}(t)\,u_2(t)\}\;\mathrm{E}\{u_1(t+\tau)\,u_2^{*}(t+\tau)\} \\ &= \mathrm{R}_{u_1u_1}(\tau)\;\mathrm{R}_{u_2u_2}^{*}(\tau) + \mathrm{E}\{i^{*}(t)\}\;\mathrm{E}\{i(t+\tau)\} \end{aligned} \qquad (3.30)$$

where $\mathrm{R}_{u_1u_1}(\tau)$ and $\mathrm{R}_{u_2u_2}(\tau)$ are the ACFs of $u_1(t)$ and $u_2(t)$, respectively.

A normalised version of the interferogram ACF is used which provides better comparability between different interferogram types – strip-map, single, and multiple coherent burst:

$$\overline{\mathrm{R}}_{ii,A}(\tau)=\frac{\mathrm{R}_{ii,A}(\tau)}{\mathrm{R}_{u_1u_1}(0)\mathrm{R}_{u_2u_2}(0)} \qquad (3.31)$$

Equations (3.30) and (3.27) are inserted into (3.31), hence:

$$\overline{\mathrm{R}}_{ii,A}(\tau)=\frac{\mathrm{R}_{u_1u_1}(\tau)\,\mathrm{R}^{*}_{u_2u_2}(\tau)}{\mathrm{R}_{u_1u_1}(0)\,\mathrm{R}_{u_2u_2}(0)}+\left|\gamma_A(f_\phi)\right|^2\exp\left(-j\,2\pi\,f_\phi\,\tau\right) \qquad (3.32)$$

The second term of the interferogram ACF consists of the squared coherence magnitude and the interferometric phase ramp through the azimuth spectral fringe frequency f_ϕ. The interferogram is wide-sense stationary, since the interferogram ACF only depends on the time lag τ between the considered interferogram pixels and since the coherence magnitude in (3.28) is constant. Finally, the normalised PSD of the interferogram is the Fourier transform of (3.32):

$$\overline{\mathrm{S}}_{ii,A}(f)=\frac{\mathrm{S}_{u_2u_2}(f)\otimes\mathrm{S}_{u_1u_1}(f)}{\int\mathrm{S}_{u_1u_1}(f)\,df\int\mathrm{S}_{u_2u_2}(f)\,df}+\left|\gamma_A(f_\phi)\right|^2\delta(f-f_\phi) \qquad (3.33)$$

where "$\otimes$" is the correlation operator.

In conclusion, the normalised interferogram PSD consists of the cross-correlation of the power spectra of the individual channels plus a Dirac delta distribution centred around the fringe frequency with a mass equal to the square of the coherence of the two SAR signals.

As an example signals of two identical strip-map SAR systems are considered. They have a rect-shaped transfer function centred around the same Doppler centroid and are perfectly co-registered. Hence, the coherence of the signals is (cf. equation (3.28)):

$$\gamma_A(f_\phi,t)=\gamma_T\,\mathrm{tri}\left(\frac{f_\phi}{W_A}\right)\exp\left(-j\,2\pi\,f_\phi\,t\right) \qquad (3.34)$$

For optimal coherence azimuth spectral shift filtering is applied yielding the maximum obtainable coherence value γ_T (temporal coherence component).

The PSD of the strip-map SAR signal is

$$\mathrm{S}_{u_1u_1}(f)=\mathrm{S}_{u_2u_2}(f)=\mathrm{rect}\left(\frac{f-f_{DC}}{W_A}\right), \qquad (3.35)$$

since the strip-map SAR impulse response is time-invariant. The interferogram PSD is then:

$$\overline{S}_{u,A}(f) = \frac{1}{W_A}\,\mathrm{tri}\left(\frac{f}{W_A}\right) + \left|\gamma_T\,\mathrm{tri}\left(\frac{f_\phi}{W_A}\right)\right|^2 \delta(f - f_\phi) \qquad (3.36)$$

This PSD consists of a tri-shaped pedestal with bandwidth $2W_A$, that is the correlation of the SAR power spectral density functions $S_{u_1u_1}(f)$ and $S_{u_2u_2}(f)$, and the spectral line centred at f_ϕ with mass $\gamma(f_\phi)$. Figure 3.9 illustrates the normalised power spectral density from equation (3.36). Obviously, $|\gamma|^2$ is the ratio of the impulse integral of the spectral line at the centre fringe frequency and the integral of the extended triangle spectrum. For comparison, figure 3.10 shows the measured interferogram power spectral density of an ERS data set. Deviations from spectra in figure 3.9 originate from the azimuth spectral weighting of the data.

3.2.2 Single Burst Interferograms

'Burst interferograms' or 'burst looks' are generated from individual interferometric complex burst image partners. The linear variation of the bandpass centre frequency with azimuth is the same for the corresponding master and slave image, hence, it cancels out in the burst interferogram. Burst interferograms may then be considered to be wide-sense stationary and to have low pass character with resolution $\rho_B/2$ (see below).

After interferogram formation the interferometric burst looks are mosaicked. This means they are properly shifted in azimuth with respect to each other and coherently added in the case of overlap. Since the individual burst interferograms were obtained from ScanSAR burst images which have non-overlapping support in the time-frequency diagram (cf. for example figure 3.3), the interferogram samples used for multi-looking are statistically independent (distributed scatterer model). Hence, when N_L burst looks are averaged, the final subswath interferogram exhibits a phase noise reduction equivalent to N_L-look formation in the strip-map mode SAR case.

a) strip-map

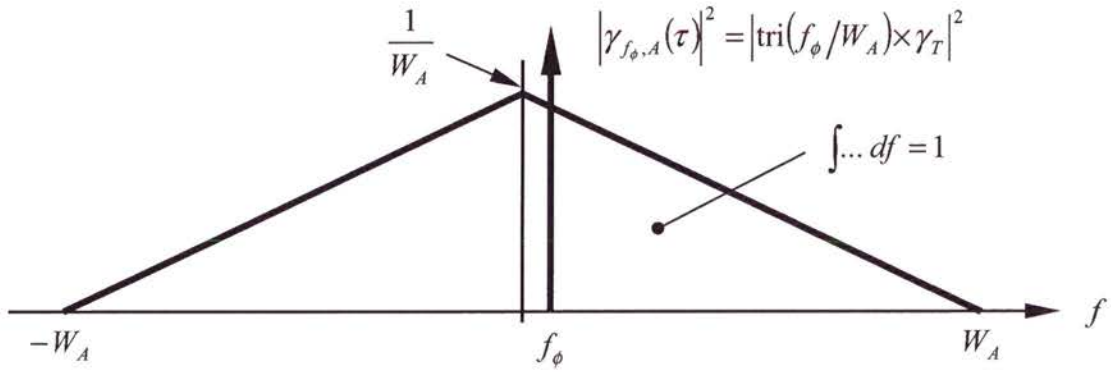

b) multi-looked single burst

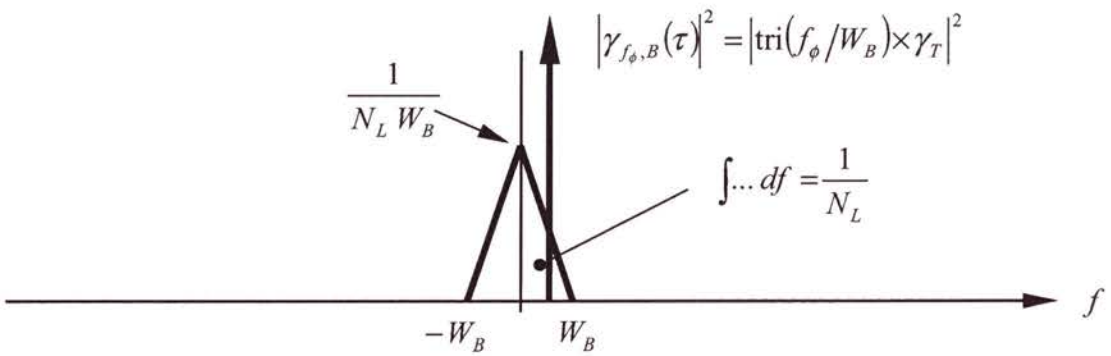

c) multiple coherent burst

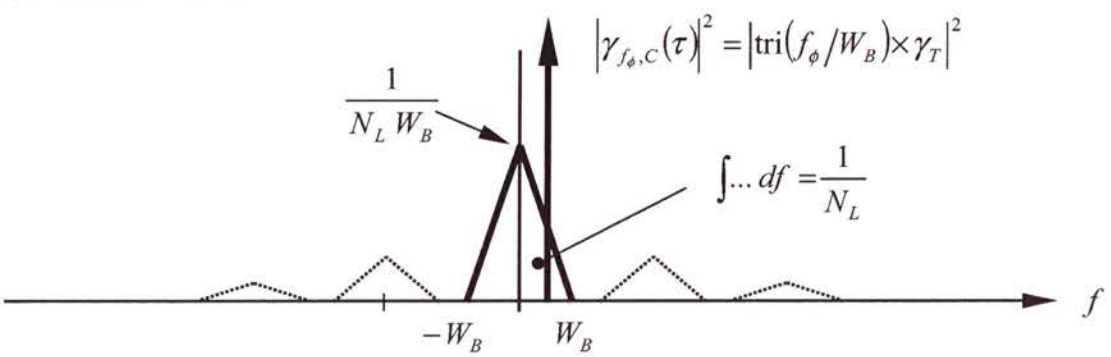

Figure 3.9: Azimuth power spectral densities (normalised) of strip-map, single burst, and multiple burst interferograms. Stationary Gaussian scattering and a linear phase ramp, i.e. a single fringe frequency , are assumed. The triangular shapes of the spectra apply for rect-shaped burst profiles. In case the bursts are weighted for side-lobe control the triangular spectra are replaced by the auto-correlation of the weighting function. Note, that the position of the Dirac function is restricted to the support $[-W_A/2, W_A/2]$ or $[-W_B/2, W_B/2]$ for the strip-map mode or burst-mode data, respectively.

a) strip-map interferogram PSD

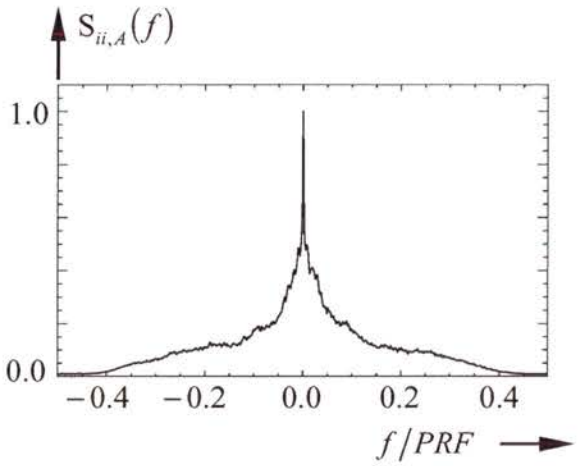

b) single burst PSD

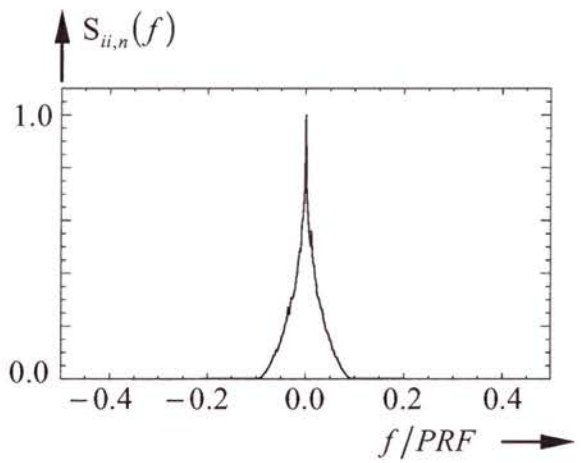

c) multilooked single burst PSD

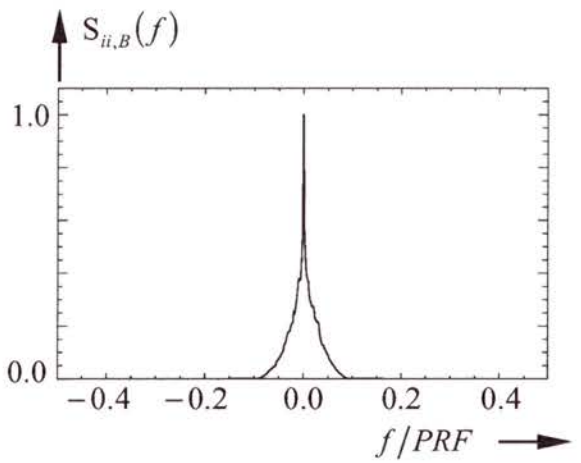

d) multiple coherent burst PSD ($N_L = 2$)

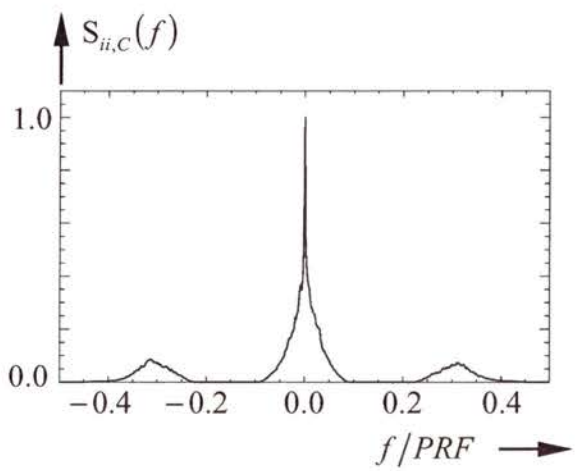

e) multiple coherent burst PSD after filtering

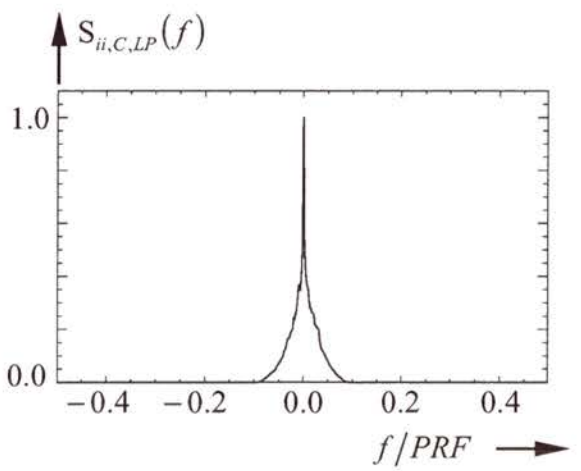

Figure 3.10: Interferogram azimuth power spectra estimated from real data in a distributed scatterer area: Strip-map a), single burst b) and c), multiple burst d) and e). The burst-mode data is based on ERS raw data: $N_L = 2$, $W_B/PRF = 0.092$, $W_P/PRF = 0.32$.

The derivation of the burst-mode interferogram power spectral density is very similar to the one of the strip-map interferograms. In the case of N_L looks it can be found that (appendix A3):

$$\overline{S}_{ii,B}(f) = \frac{1}{N_L}\frac{1}{W_B}\,\mathrm{tri}\left(\frac{f}{W_B}\right) + \left|\gamma_T\,\mathrm{tri}\left(\frac{f_\phi}{W_B}\right)\right|^2 \delta(f - f_\phi) \qquad (3.37)$$

Due to the multi-looking the integral of the triangle is reduced by $1/N_L$ and, hence, coherence or phase stability appears larger than in strip-map case. However, note that in the strip-map case the number of independent interferogram samples is higher by a factor of N_S (number of subswaths), i.e. at a particular resolution the strip-map interferogram will have lower phase variance. This variance reduction is a direct consequence of the trade-off between gain in swath width or polarisation information and resolution.

Burst-mode interferograms show a remarkable feature when the interferometric partners are mis-registered by a small shift κ (figure 3.11). The power spectral density of the interferogram is then ($f_\phi = 0$, appendix A3):

$$\overline{S}_{ii,B}(f) = \frac{1}{N_L}\frac{1}{W_B}\,\mathrm{tri}\left(\frac{f - FM\,\kappa}{W_B}\right) + \left|\gamma_T\,\frac{R_{uu,n}(t,\kappa)}{W_B}\right|^2 \delta(f - FM\,\kappa) \qquad (3.38)$$

with $R_{uu,n}(t,\tau)$ the autocorrelation function of equation (3.19). $\left|R_{uu,n}(t,\kappa)\right|^2$ is a function that does not depend on t anymore since only the phase of $R_{uu,n}(t,\tau)$ is time variant; hence, this interferogram PSD is wide-sense stationary as well.

Due to the shift of the spectral line by $f_\kappa = FM\,\kappa$, the interferogram will exhibit a linear phase:

$$\phi(\kappa) = 2\pi\,FM\,\kappa\,t + \phi_0 \qquad (3.39)$$

which is very sensitive to mis-registration with ϕ_0, a phase offset discussed below.

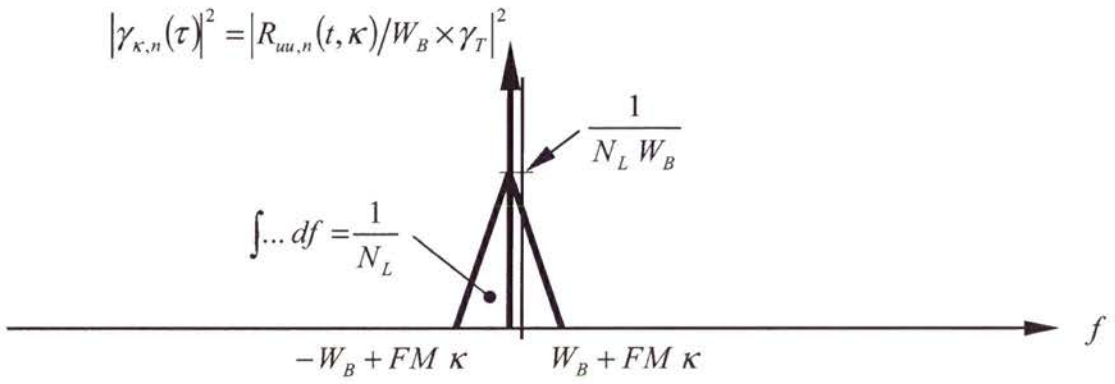

Figure 3.11: Burst interferogram power spectrum for non-zero mis-registration.

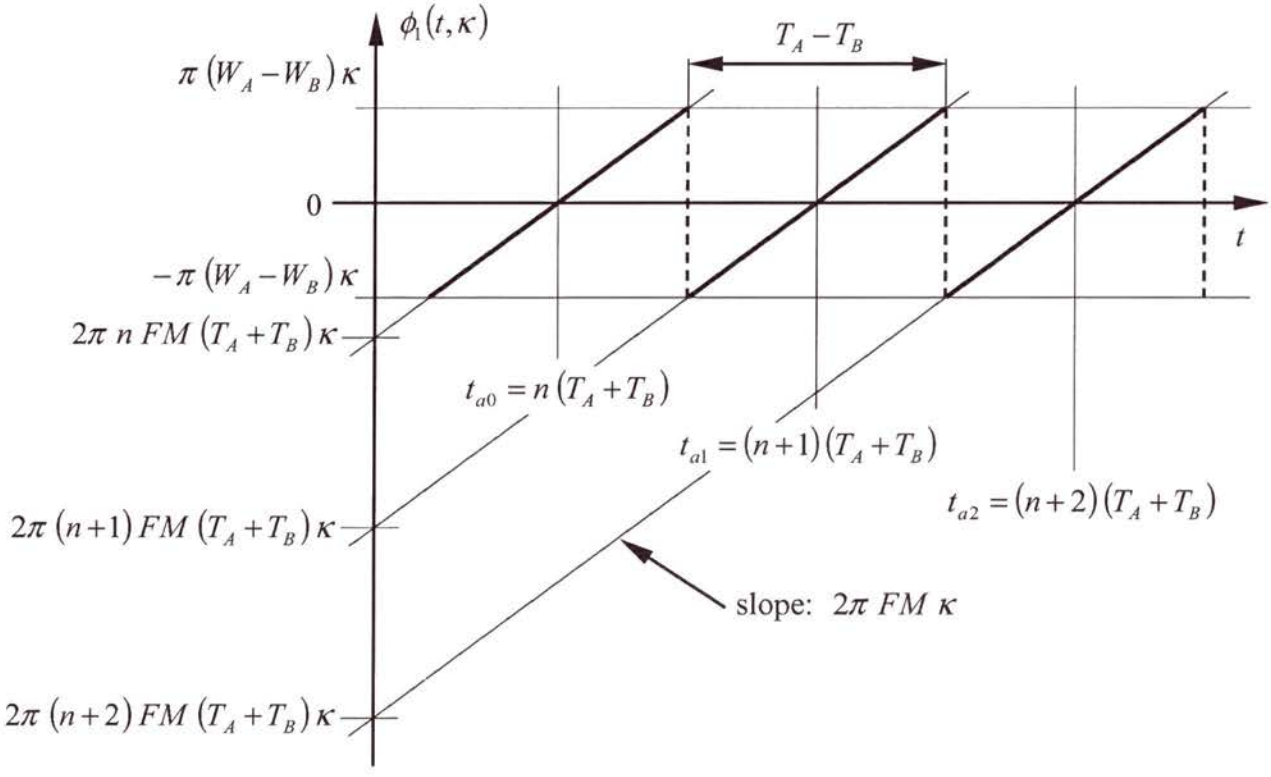

Figure 3.12: Phase course of a single look sub-swath interferogram. The phase jumps originate from the acquisition time dependent phase offset in the presence of a mis-registration κ.

A full phase cycle over the burst extent $T_A - T_B$ is obtained for a mis-registration κ of

$$\kappa = \frac{1}{(T_A - T_B)FM} \approx \rho_A , \qquad (3.40)$$

that is the strip-map SAR resolution cell which is slightly larger than the acquisition PRF (Scheiber and Moreira 2000). On the other hand, when a co-registration of $\rho_A/10$ is assumed the phase change over the burst image extend amounts to approximately $2\pi/10$ which is still significant.

The phase offset ϕ_0 in (3.39) depends on the burst acquisition time $t_a = nT_P$ (equation (3.8)). It does not appear in the interferogram ACF (appendix A3) since the interferogram is azimuth time-invariant. However, it arises in the phase of the interferogram sample expectation value (equation (3.39), appendix A3):

$$\arg\left(\mathrm{E}\{i(t)\}\right) = \arg\left(\mathrm{R}_{uu,n}(t,\kappa)\right) = 2\pi\ FM\ (nT_P - t)\,\kappa \qquad (3.41)$$

where the quadratic term κ^2 has been neglected. Figure 3.12 illustrates the phase behaviour of a single look interferogram after concatenating the individual bursts to give a contiguous interferogram sub-swath. In contrast to the high sensivity, the interferogram phase with respect to a mutual mis-registration of the burst-images, coherence drops slowly following a sinc-like function (equation (3.19)). Total decorrelation occurs at its first zero-crossing at $1/W_B$. This effect is illustrated using simulated data from ERS in figure 3.13. A mis-registration of 5 image samples (approximately half the single burst look image resolution cell) was introduced which resulted in a linear phase pattern with $3.3 \cdot 10^{-3}$ cycles/ sample.

These results were also obtained by (Scheiber and Moreira 2000) using a different approach. Phase jumps in the differential interferogram as reported in the same article are a consequence of (3.41) (figure 3.14).

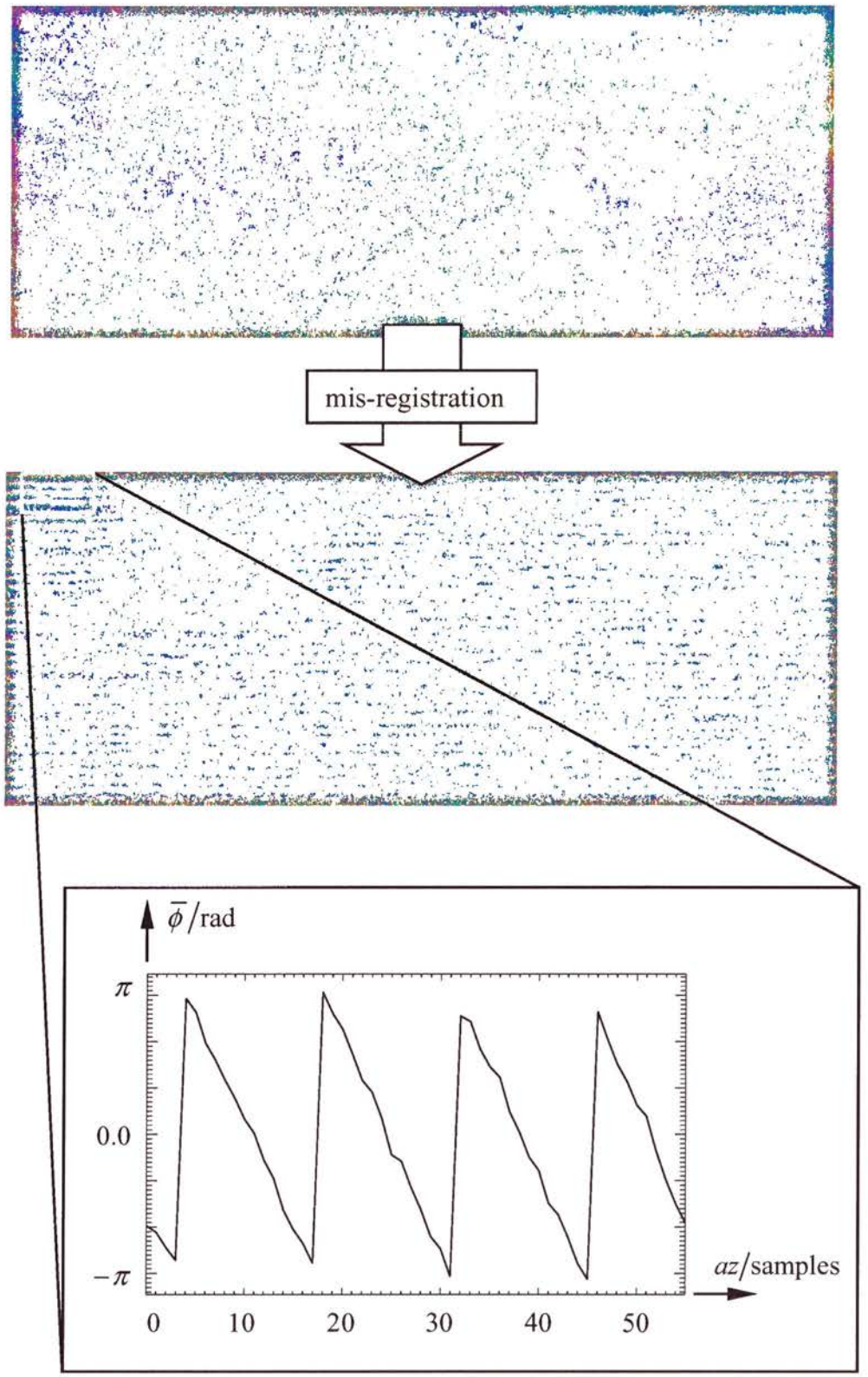

Figure 3.13: Single burst look interferogram for a mis-registration of 5 samples. The data is simulated from ERS raw data ($N_L = 2$, $W_B/PRF = 0.092$, $W_P/PRF = 0.32$, $PRF = 1679$ Hz, multi-looking (range x azimuth): 4 x 20).

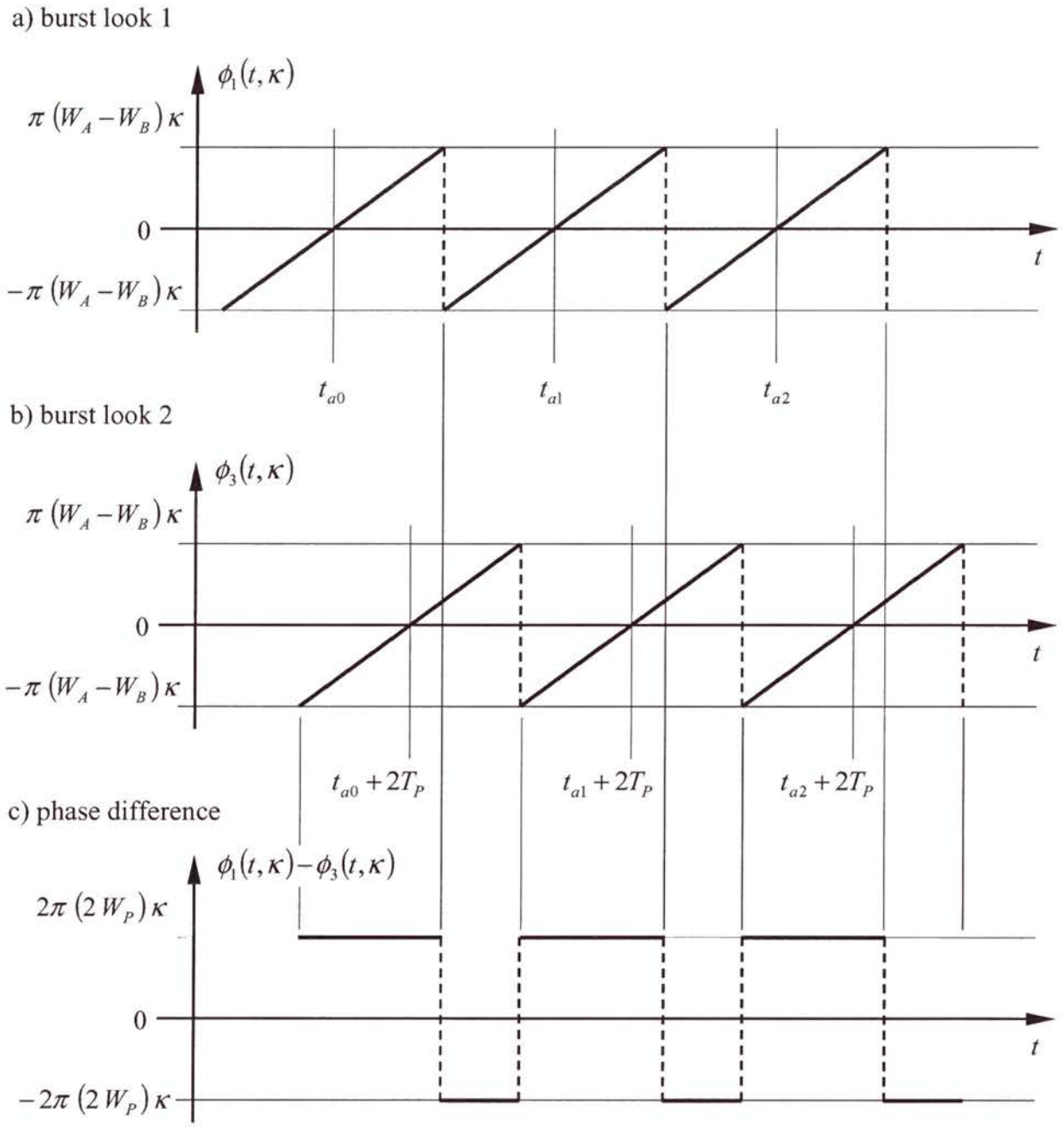

Figure 3.14: Difference phase of two burst looks given a mis-registration κ. Phase course of the single look sub-swath interferograms with burst-number n (a), n+2 (b), and of their difference phase (c).

When the single burst interferograms are multi-looked to obtain a swath interferogram the linear phase ramp remains, since:

$$
\begin{aligned}
i_B(t) &= \sum_{N_L} i_n(t) \\
&= \sum_{N_L} \exp\left(j\, 2\pi\, FM\, (nT_P - t)\,\kappa\right) \\
&= \exp\left(-j\, 2\pi\, FM\, \kappa\, t\right) \sum_{N_L} \exp\left(j\, 2\pi\, n\, FM\, T_P\, \kappa\right)
\end{aligned}
\qquad (3.42)
$$

where unit amplitude of the interferogram samples was assumed. The sum of exponentials determines the amplitude of the multi-looked single burst interferogram sample.

Total decorrelation occurs for values outside $-T_B < \kappa < T_B$, equation (3.18). Apart from the technique reported in (Scheiber and Moreira 2000), the fact that the phase (3.41) directly reflects the mis-registration may be used for estimation of the mutual shift. Note that the FM rate is range dependent and a sufficiently flat terrain or a DEM should be available. Moreover, robust estimation requires moderate to high coherence otherwise a large number of range samples can be used for phase noise reduction.

The interferogram PSD for a mutual shift Δt_{SP} of the burst-scanning patterns shows an effect not occurring in the above functions. The spectral line is then centred around zero frequency and the tri-function is shifted off this position (figure 3.15):

$$
\overline{S}_{ii,B}(f) = \frac{1}{N_L}\frac{1}{W_B}\,\mathrm{tri}\left(\frac{f - FM\,\Delta t_{SP}}{W_B}\right) + \left|\gamma_T\,\mathrm{tri}\left(\frac{FM\,\Delta t_{SP}}{W_B}\right)\right|^2 \delta(f)\ . \qquad (3.43)
$$

In figure 3.16 this effect is illustrated using data simulated from ERS data (cf. figures 3.10 and 3.13) for a burst-scanning pattern shift of 50% of the burst length. The pedestal is shifted by half the burst bandwidth off the zero frequency position.

This outstanding characteristic may be used for estimation of the shift Δt_{SP} by determining the centre of gravity of the spectrum's main lobe. Since this shift does not affect the spectral line position the estimate may even be obtained for very low coherence. If the measured burst scanning pattern misalignment modulo T_P is equal to (2-beam) or larger T_B the interferogram carries no phase information.

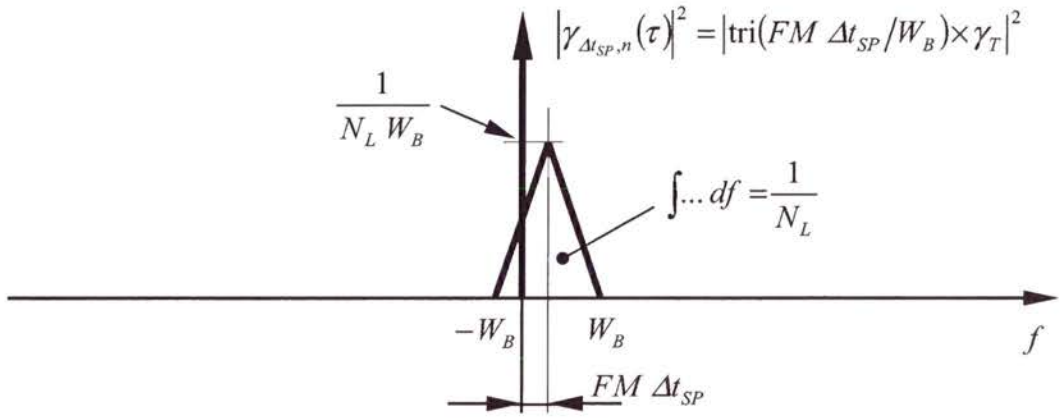

Figure 3.15: Burst interferogram power spectrum for non-zero burst scanning pattern misalignment.

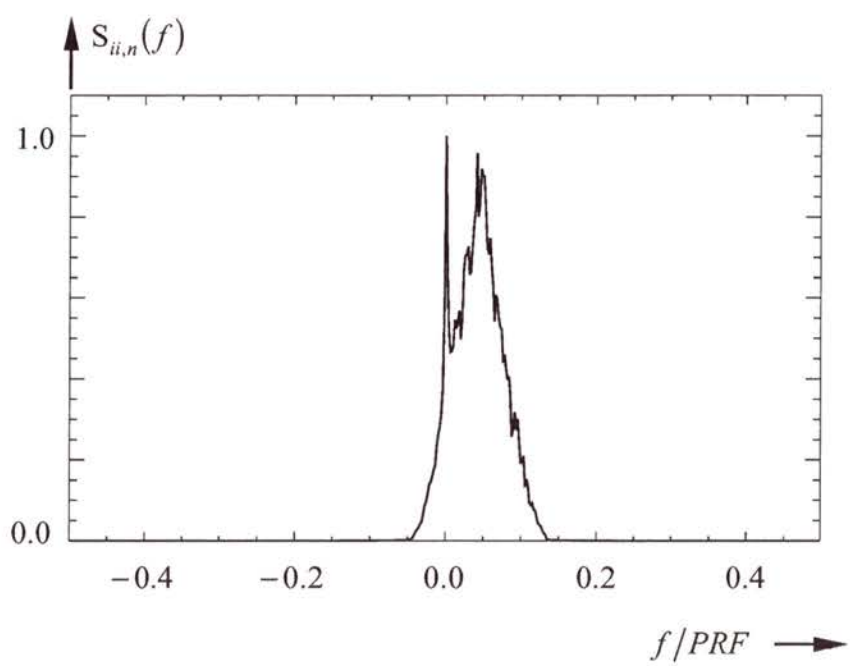

Figure 3.16: Interferogram azimuth power spectrum for a burst pattern misalignment of 50% of the burst length. The burst-mode data is based on ERS raw data: $N_L = 2$, $W_B/PRF = 0.092$, $W_P/PRF = 0.32$.

3.2.3 Multiple Burst Interferograms

Multiple burst interferograms are formed from burst images of a single beam that are coherently added before interferogram formation. If the burst looks are not individually focussed but as a train of raw data bursts with zeros inserted when the antenna beam was switched to other beams or polarisations, then the multiple burst images are the output of the SAR processor (Bamler and Eineder 1996). The signal has a bandwidth of approximately W_A and has properties as described in section 3.1.1 and 3.1.3. For the normalised interferogram PSD the following equation can be found:

$$\overline{S}_{ii,C}(f) = \sum_{k=-N_L}^{N_L} \frac{(N_L - |k|)}{N_L^2 W_B} \operatorname{tri}\left(\frac{f - kW_P}{W_B}\right) + \left|\gamma_T \operatorname{tri}\left(\frac{f_\phi}{W_B}\right)\right|^2 \delta(f + f_\phi) \qquad (3.44)$$

This PSD is illustrated in figure 3.9 c) where the side-lobes are indicated by the dotted lines. The side lobes are the reason that the multiple coherent interferogram has single look phase statistics. By applying a low pass filter $H_{LP}(f)$, i.e. averaging of neighbouring pixels, only the main lobe of the interferogram PSD is kept:

$$\overline{S}_{ii,C,LP}(f) = \overline{S}_{ii,C}(f)\, H_{LP}(f). \qquad (3.45)$$

The oscillations of the point response (section 3.1.1, figure 3.4) are removed, and the interferogram has N_L-look phase character. Since this resulting interferogram is of low pass type down-sampling reduces the data rate by a factor of $2 \times W / PRF$ without introducing aliasing effects.

If a filter is used that only picks out the centre triangle, e.g. $H_{LP}(f) = \operatorname{rect}\left(\frac{f}{2W_B}\right)$ the interferogram PSDs of the single- and multi-look are equivalent.

Apart from the previously discussed particularities of mis-registration in the single burst interferogram case, a mutual shift of the multiple coherent burst images introduces a modulation into the coherence in analogy to the modulation of the impulse response of equation (3.10), the expectation value in (3.42), and figure 3.4 (for the derivation cf. appendix A3):

$$\gamma_{\kappa,C}(\kappa) \approx \operatorname{sinc}(W_B\, \kappa) \exp(-j\, 2\pi\, FM\, t\, \kappa) \sum_n \exp(-j\, 2\pi\, n\, W_P\, \kappa). \qquad (3.46)$$

This modulation, may be used for improving co-registration accuracy as outlined in section 4.2.1.

3.3 Equivalence of the Interferogram Formation Options

Within this thesis equivalence of the burst-mode interferogram formation options (multiple single burst interferogram and multiple coherent burst interferogram) is examined by means of selected statistical expectation values. In particular, the interferogram formation options are considered equivalent if the interferogram sample expectation value and the normalized power spectral density are supplying identical values. The identity of the expectation values of the interferogram formation options was shown in appendix A3 with equations (A3.46) and (A3.54). These equations provide identical values for both interferogram formation options. The equivalence of the power spectral densities (see also A3.5) is shown with equations (A3.49), (A3.58), and (A3.62). The conditions that have to be met for the power spectral densities to be identical are 1) the interferogram pedestals (tri-function in figure 3.9) due to the convolution of the burst image power spectra, equation (3.33), do not exceed a support covering an extend of W_P, i.e. $W_P \leq 2\,W_B$, and 2) a rect-shaped lowpass filter $H_{LP}(f)$ is used with an amplitude of 1. Condition 1, however, is met for every reasonable burst-mode system. A suitable normalization of the interferogram power spectra as proposed in section A3.4 does not change the equality of the results and, hence, the equivalence is shown. Note, by comparison of equations (3.36) and (3.44) the identity was illustrated in the last section for the normalized power spectra of a special case. It is the case when the burst image power spectra are rect-shaped.

The assessment by means of the above expectation values allows the comparison of interferogram in a statistical sense. In practice numerical equivalence on a sample by sample basis is impossible to show due to noise introduced in the differing processing steps applied within the burst formation options (see chapter 4).

3.4 Summary

This section gave a complete overview of the signal characteristics of burst-mode signals: end-to-end impulse response and transfer function, auto-correlation properties, sampling of burst-mode signal, and interferometric characteristics of single and multiple coherent burst interferograms. In order to highlight the particular properties of burst-mode data they were contrasted to strip-map mode signals. The parameter cases of existing mis-registration, burst scanning mis-alignment, and fringe frequency were summarised. Moreover, this section comprises the proof of the equivalence of the single burst and multiple coherent burst interferogram processing techniques. Thus this part of the thesis provides the foundations for the understanding of interferometric burst-mode data processing.

... we accept the idea that the task of science is the search for truth, that is, for true theories (...). Yet we also stress that truth is not the only aim of science. We want more than mere truth: what we look for is interesting truth - truth which is hard to come by. And in the natural sciences (...) what we look for is truth which has a high degree of explanatory power, in a sense which implies that it is logically improbable truth.

- Truth, Rationality, and the Growth of Scientific Knowledge (Popper 1963).

Chapter 4

Burst-Mode and RADARSAT ScanSAR Interferometric Processing

This section addresses issues of ScanSAR and burst-mode interferometric processing. In addition to the individual interferometric processing steps for burst-mode and ScanSAR data the first part explains required pre-processing steps. Pre-processing of the data is addressed, since complex burst images are not available as standard products today. Moreover, the individual processing steps of ScanSAR and burst-mode interferometric processing are discussed. In the second part of the chapter the two principle ScanSAR interferometric data and processing structures are outlined and an optimal processing scheme is proposed. Examples and illustrations originate from the data set described in section 5.1. In this way, this section gives a recipe-like description of ScanSAR interferometric processing, requirements, and experience obtained from processing the data set in section 5.1.

4.1 Pre-processing

4.1.1 Phase Preserving Processing

In SAR and ScanSAR processing the matched filter principle is commonly adopted. A matched filter is the time-reversed complex conjugate reference signal:

$$h_{matched}(t) = h_{ref}^{*}(-t) \tag{4.1}$$

In the case of a SAR, the filter is matched to the transmitted range chirp and to the azimuth phase history. Thus, the SAR image data is reconstructed from the SAR raw data.

Azimuth signal focussing can also be viewed as an answer to the question: What is the response of an antenna of azimuth extent $L_A = v_S\, T_A$, the 'small' SAR antenna of length L is synthesising? Then the operation can be viewed as correcting the phase of each individual echo acquired by the SAR antenna and adding all these corrected echoes up in order to obtain an image with resolution of about $L/2$ (Elachi 1988; Bamler and Schättler 1993).

There are several burst-mode and ScanSAR focussing algorithms that operate in the time-domain, range time-Doppler frequency domain (range-Doppler processors), or apply the spectral analysis principle (SPECAN). All these algorithms are phase preserving (which is important for interferometry) and may be optimised with respect to computational complexity. Implementations of the SPECAN algorithm for ScanSAR processing are outlined in (Moreira et al. 1996; Lanari et al. 1998) and the adaptation of the range-Doppler algorithm are presented in (Monti Guarnieri and Prati 1996; Cumming et al. 1997; Cumming et al. 1997). Another approach, although not computationally efficient, is described in (Bamler and Eineder 1996) where standard SAR processors are utilised for phase preserving ScanSAR processing. Note that strip-map and burst-mode data require the same range processing (range compression, range cell migration correction, and secondary range compression) only the azimuth processing is different for ScanSAR data adapted (optimised) algorithms.

For processing the data sets described in section 5.1 the following approach adopted was adopted. Each burst of range lines is range processed separately by a standard chirp scaling processor whose azimuth compression has been disabled ((Breit et al. 1997)). Since the bursts are usually short, in particular after azimuth scanning pattern synchronisation, a straightforward time domain azimuth correlation was used for final azimuth compression as an alternative to frequency domain methods.

4.1.2 Doppler Centroid Estimation

Doppler centroid (DC) estimation determines the centre frequency of the azimuth spectrum for SAR image processing. The Doppler centroid information is important for focussing of the SAR data, interferometric processing, and radiometric correction including scalloping correction (section 2.2). In focussing, the Doppler centroid determines which part of the

azimuth phase history of the scatterer was recorded, since Doppler centroid is a measure for the squint angle.

Doppler centroid accuracy requirements for radiometric correction of ScanSAR images are known to be rather stringent (Jin 1996; Mittermayer et al. 1996; Lancashire 1998). For ScanSAR interferometry radiometric correction is not essential (section 4.2.3) and the Doppler centroid only determines which part of the raw data spectrum is chosen. Thus, requirements with respect to Doppler centroid estimation accuracies may be relaxed if azimuth ambiguities at the edges of the Doppler bandwidth are still negligible.

Doppler centroid estimation is usually divided into two steps: determination of the base-band DC and determination of the PRF band of the absolute Doppler centroid. This two-step procedure is indispensable for RADARSAT-1 data since no yaw steering is applied.

Data spectra algorithms determine the 'centre of gravity' of the SAR azimuth power spectrum (Bamler 1991) and may be also utilised for the estimation of the Doppler centroid of ScanSAR data since the DC of space borne systems is very stable in along track direction (Eldhuset 1993) and large numbers of data records can be averaged. It can be shown that the average power spectrum of ScanSAR raw data resembles the one of conventional SAR data for homogenous targets and that the spectrum of one burst reflects the convolution of the target intensity profile with the transfer function of a single scatterer (appendix 4). Hence, the described Doppler centroid estimation methods can be applied. Sufficiently large estimation windows are required to average out spectral 'distortions' of the azimuth spectra as a result of scene intensity variations.

For the ScanSAR data used in the thesis, the individual raw data bursts were concatenated in order to obtain a contiguous sequence of echo lines. Then these were input into an implementation of Madsen's Doppler centroid estimator (Madsen 1989). In order to avoid disturbing phase effects, one range line of zeros was inserted in-between subsequent bursts. The DC estimates and a second order polynomial fit for the investigated ScanSAR data set (section 5.1) are illustrated in figure 4.1. Since the Doppler centroids differences of the data set are quite small with maximum deviations of about 23 Hz and 46 Hz for beam 1 and beam 2. Estimation windows sizes of 10,000 range lines by 150 range samples were chosen. A number of 45 and 53 estimates were obtained for beam 1 and beam 2, respectively. Standard deviations of the estimates with respect to the quadratic fit amount to about 20 Hz for beam 1 and 10 Hz for beam 2. For the values from the fit a remaining error of about 3 Hz may be

assumed which is by far accurate enough. The interferometric image pairs were focussed with the mean value of the two estimated DC frequency fits. This approach avoids decorrelation and, hence, interferometric phase noise due to non-overlapping azimuth spectra (section 2.1.3).

4.1.3 PRF Ambiguity Resolution

PRF ambiguity resolution determines the absolute Doppler centroid value as the sum of the base-band Doppler centroid (see above) and a multiple n_{PRF} of the PRF. If the data is processed using a wrong PRF band the SAR or ScanSAR image will appear blurred due to mis-compensated range cell migration and geolocation is off by a multiple of the synthetic aperture length. For the data set considered, this index was estimated using a modified version of the azimuth look correlation technique (Cumming et al. 1986). With this technique, parts of the azimuth spectrum are focussed individually with trial n_{PRF} settings. When the data is processed to a DC with a wrong ambiguity, targets in the two looks appear at slightly different range positions. This mutual displacement is proportional to the DC ambiguity necessary to correct the initial focussing setting (appendix A5). In the used implementation, the range distance is determined by cross-correlation of image chips or from the position of objects that appear as strong point-like targets. In case of image chip correlation, only image contrast serves for co-registration of the image patches, since the azimuth looks have non-overlapping frequency support and, hence, their speckle patterns are completely different.

ScanSAR images cover areas at least 10 times as large as strip-map images (ERS/ENVISAT: 100 km x 100 km). Therefore, objects that appear as strong point-like targets are very likely to be imaged (cities, man-made features, rocky terrain). Such point targets may be detected automatically and applied to the determination of n_{PRF} as described above. The diagram in figure 4.2 illustrates the range position offset of the two looks versus a range of PRF bands. A safe determination of the PRF ambiguity was possible since the chosen target appeared equally strong in both bursts. Otherwise the results from several point-targets or high contrast areas must be averaged. For the data set under investigation the PRF band index $n_{PRF} = -5$ was found.

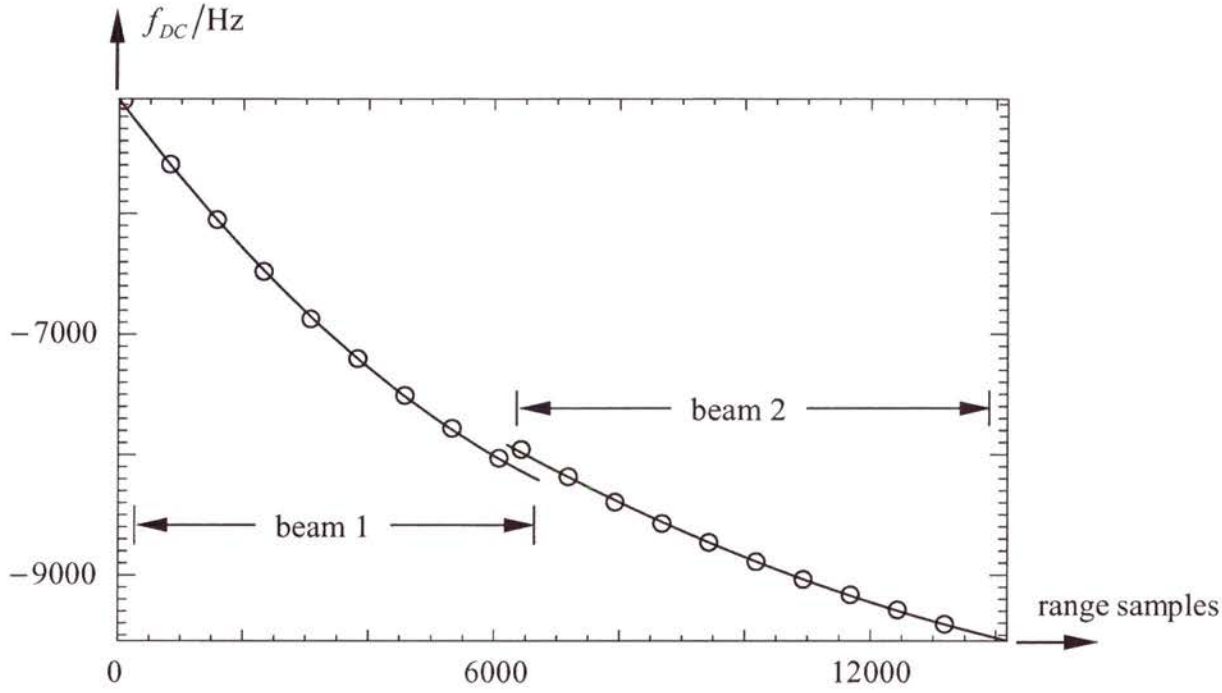

Figure 4.1: Doppler centroid estimates (circles) and fitted 2nd order polynomial (ScanSAR Narrow A, orbit 10969). The estimates are plotted using the correct *PRF* band found from figure 4.2.

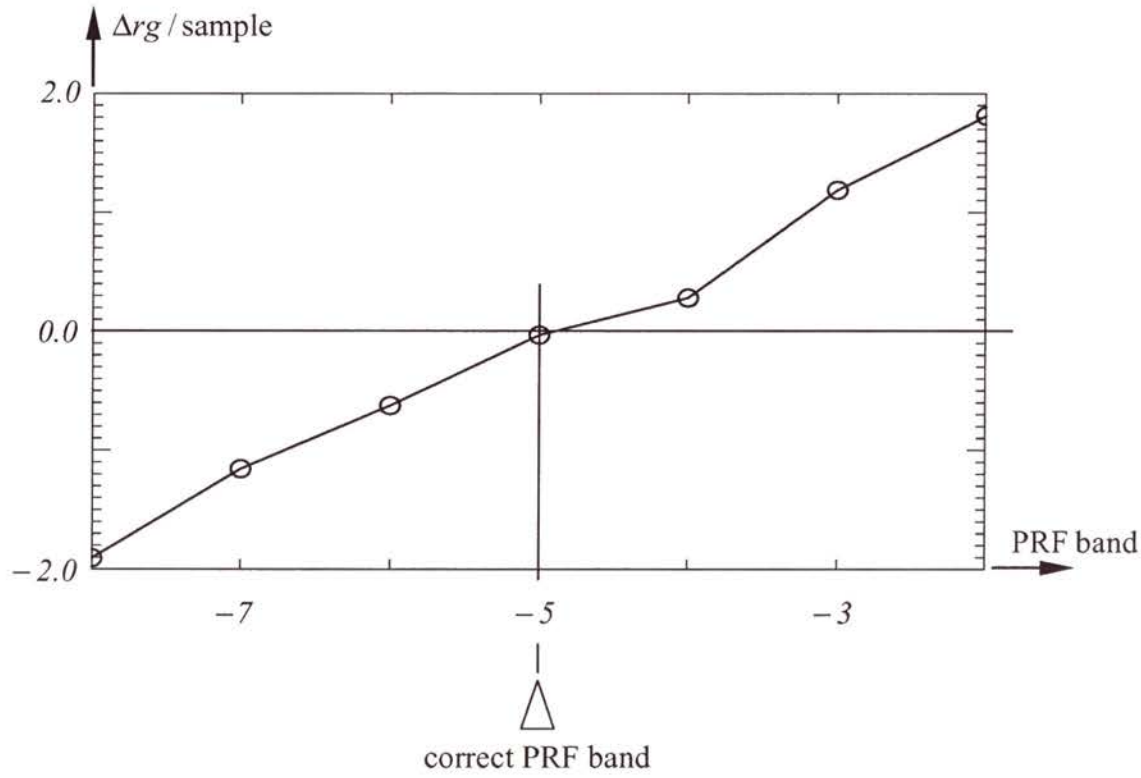

Figure 4.2: Range position difference of the two looks of a point-like scatterer for the ScanSAR Narrow A data set used with orbit 10969 (section 5.1). The correct PRF band has index -5.

4.1.4 Azimuth Scanning Pattern Synchronisation (ASPS)

Burst-mode interferometry requires synchronisation of the antenna switch on cycles (azimuth scanning pattern synchronisation: ASPS) (Bamler and Eineder 1996; Monti Guarnieri and Prati 1996; Cumming 1998). For optimal coherence only the spectral components of a target that are also imaged in the companion image are kept. There are two options available to discard the non-common spectral information. Either only those raw data lines are kept that have counterparts in the interferometric partner or an azimuth variant filter is used after focussing. In order to measure the mutual scanning pattern shift Δt_{SP}, a simple correlation approach has been chosen (Bamler et al. 1998). Figure 4.3 illustrates the ASPS concept. Several bursts of the master and slave data sets are processed and coherently added (multiple burst look image). A small image section at mid range from master and slave image is then cross-correlated. The mutual shift is measured by determining the spectrum peak of the interferogram versus mutual azimuth lag. Thus, the azimuth shift can be determined to an accuracy of at least one range line which is sufficient for ASPS requirements.

Figure 4.4 shows the result of the cross-correlation after ASPS for the data set in section 5.1. The interferogram spectral peak maximum is shown versus mutual shift of the image patches. A strong peak at around zero suggests sufficient accuracy of the ASPS. The observed modulation originates from the properties of the multiple burst image data (section 3.2.3). The maximum of the interferogram spectrum is the magnitude of the cross-correlation function of the multiple burst data (appendix A6).

The number of remaining burst lines and the corresponding burst bandwidths are given in section 5.1. For the bursts a bandwidth of $W_B - |FM|\Delta t_{SP} = 95Hz$ remains for interferometry. This bandwidth implies an azimuth resolution of approximately 75 m and, hence, is better than the 100 m pixel spacing of DTED-1 data (1993).

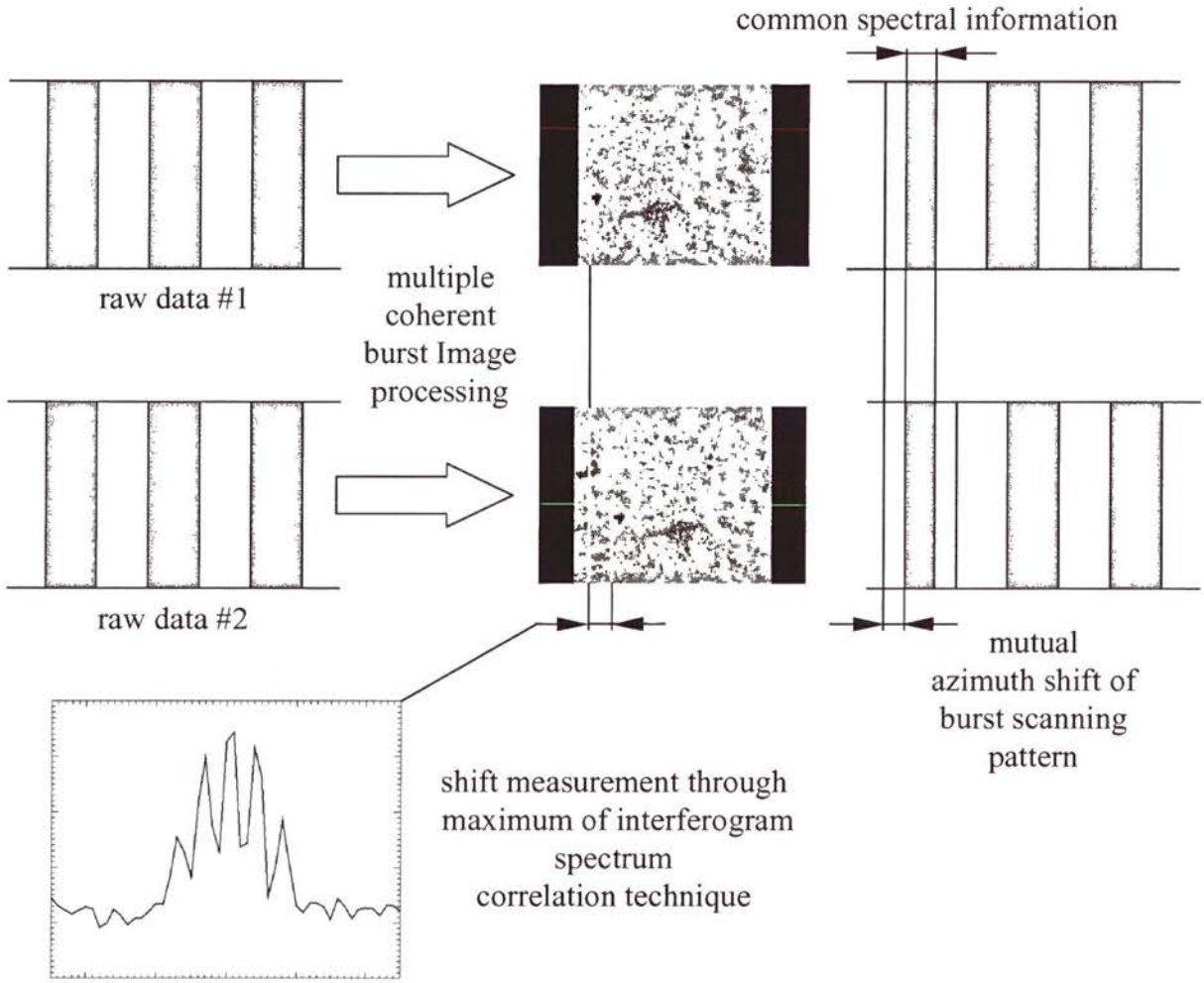

Figure 4.3: Concept for asynchronous burst scanning pattern synchronisation (ASPS).

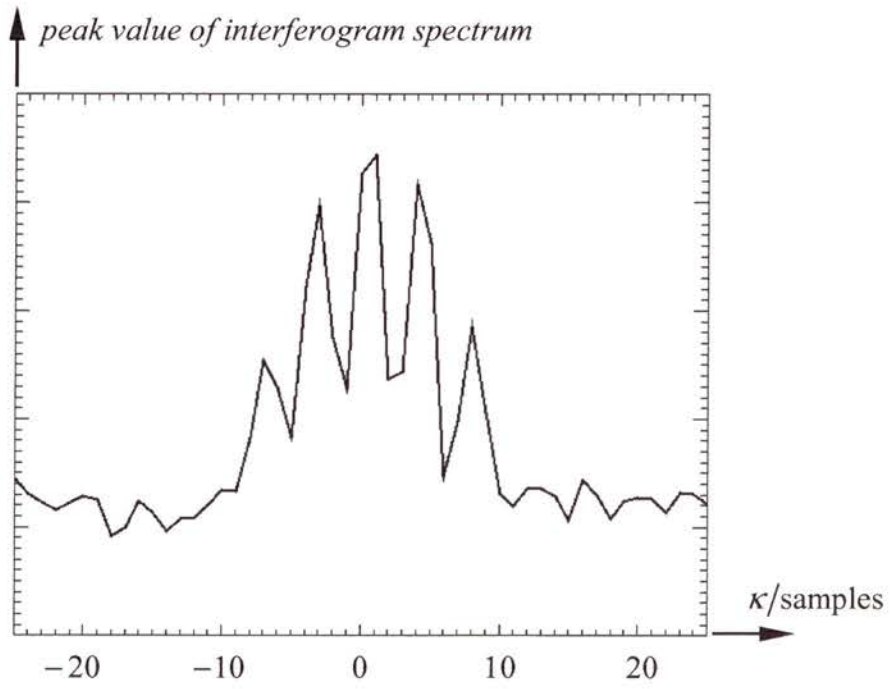

Figure 4.4: Cross-correlation result after azimuth scanning pattern synchronisation. As cross-correlation measure the peak value of interferogram spectrum vs. mutual azimuth shift is used.

4.2 Components of Interferometric ScanSAR Processing

4.2.1 Estimation of Co-Registration Parameters

Accurate co-registration of the SAR image partners is required for optimum phase quality (section 2.1.3). Phase errors as a result of remaining mis-alignments introduce phase noise and systematic phase errors in case of large DC values (Just and Bamler 1994; Bara et al. 2000) and for the considered burst-mode data properties (section 3.2.2). The achievable accuracy for shift estimates depends on the similarity of the image patches used (coherence) and the resolution of the signals (Bamler 2000).

Co-registration options for burst-mode data

With the burst images at hand there are two options for deriving the co-registration shifts. Option one retrieves the shifts from all available burst images by the cross-correlation of single look patches. The procedure for option two involves the coherent addition of the burst-looks before correlation of companion signal patches.

When single burst images are correlated the achievable co-registration accuracy is proportional to $\rho_B/\sqrt{N_L}$, since for every image position N_L (number of burst looks) independent estimates can be obtained. Figure 4.5 a) depicts the two dimensional (range lag: υ and azimuth lag: τ) autocorrelation function of a detected single burst-mode signal $|u|^2$.

Interpretation of co-registration results from multiple burst images requires some care but offers the chance to obtain a better registration parameter accuracy. The modulation of the impulse response (equation (3.10)) is the reason that the autocorrelation function, cross-correlation function, and coherence (complex cross-correlation coefficient) show multiple maxima (figure 4.5 b) and c); sections 3.1.2 and 3.2.3). This means there is a chance, depending on the local coherence, that false hits occur positioned at the side-lobe maxima of the cross-correlation function (figure 4.5d). On the other hand, the main lobe has a width significantly smaller than the burst resolution which provides better co-registration results. Note, the azimuth cross cut in figure 4.5 c) of two dimensional autocorrelation function is the square magnitude of the ACF as given in equation (3.19). Its width at amplitude 0.5 corresponds approximately to the burst signal resolution ρ_B (section 3.1.1).

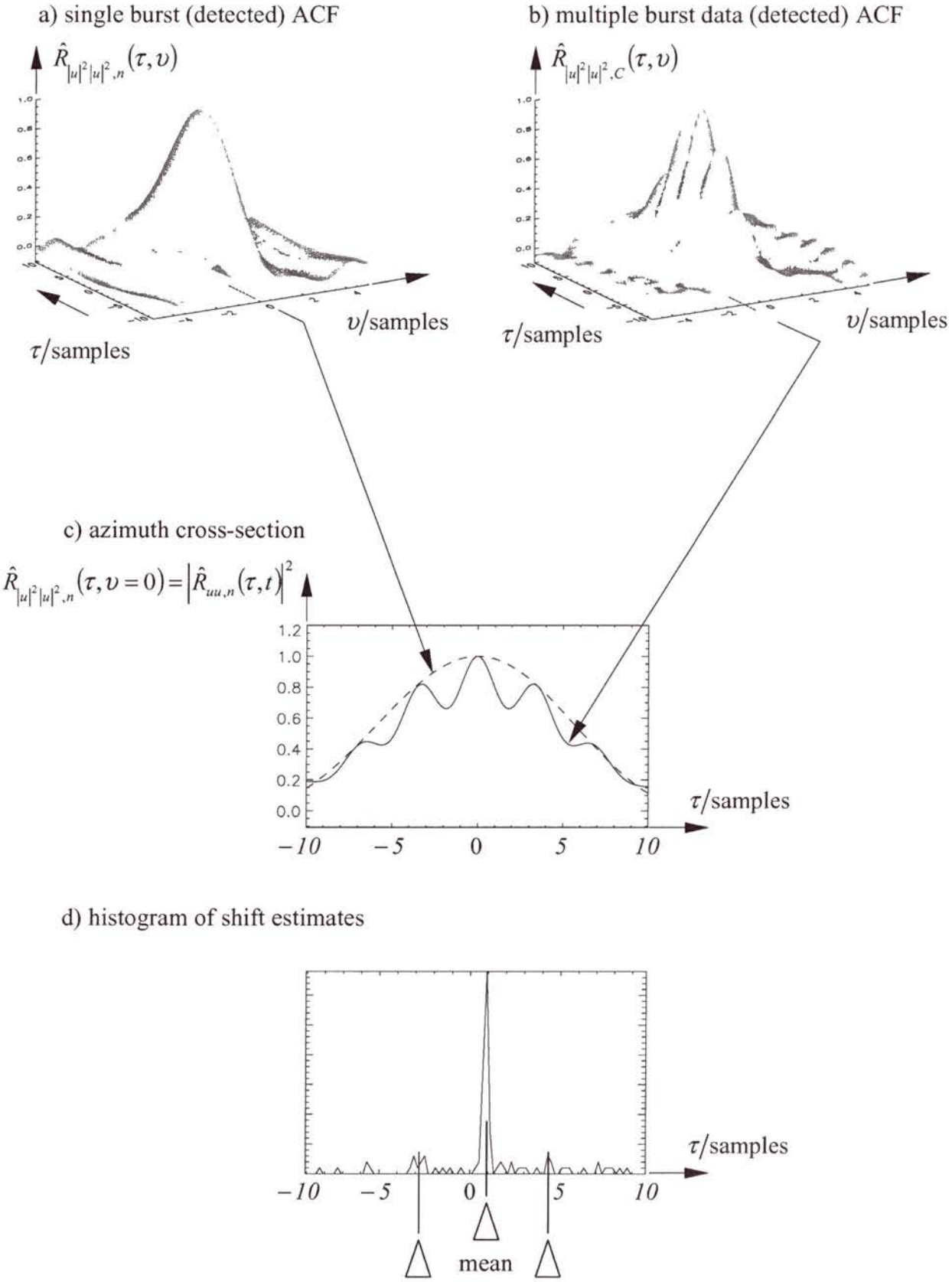

Figure 4.5: Measured ACF of ScanSAR single look (a), multiple (coherent) look (b), comparison of both (c), and histogram of 121 co-registration estimates (d).

In appendix A2, section A2.3, it is shown that for large estimation window sizes the resolution of the autocorrelation function and, hence, also for the cross-correlation function is determined by the extent T_E of the estimation window. Then the achievable accuracy may be in the order of $\rho_E \approx \rho_A = 1/(|FM|\, T_A)$ for both single burst and multiple burst data. A lot more computational effort is required for calculation of the estimates, since the window contains $N_L\ N_S$ more samples than for the above approaches (where T_E may be smaller or in the order of T_B).

Figure 4.6 shows the results of an experiment where the first two correlation options are assessed. Beam 1 of the example data in section 5.1 was evaluated and cross-correlation was carried out on detected image patches $|u|^2$, i.e. the square of the magnitude image was the input data into the correlation process. For the experiment 21 by 21 patches were equally distributed over the subswath with azimuth window size extents of 44 pixel or 33 ms, i.e. T_E does not determine the cross-correlation function main lobe width. The results are illustrated after subtraction of a resampling polynomial obtained from geometry (see below). An offset was subtracted to compensate for possible orbit errors and, thus, to centre the histograms around zero. Plate c) illustrated the histogram of the co-registration shifts after averaging 2 single look displacement estimates and the reduction in standard deviation of the shift distribution. As expected from the above considerations, a significantly narrower distribution is obtained by coherently averaging the burst images in advance of cross-correlation (figure 4.6 d)). Since for the results in this illustration the square amplitude patches where used an improvement factor of $\sigma_{L,1+L,2}/\sigma_{C(L,1+L,2)} = 1.76/0.41 = 4.29$ is obtained. This outcome may be verified by plotting the function in equation (A2.21), section A2.3, to the power of four and finding the ordinate where the obtained function is 0.5.

A fundamentally different but computationally also very efficient approach for shift determination was proposed in (Scheiber and Moreira 2000). It evaluates the phase difference of two interferograms generated from non-overlapping spectral SAR image looks ('spectral diversity') and exploits the fact that a non-zero centre frequency $f_{C,1}$ [cycles/sample] of one look introduces a phase offset ϕ_1 into the interferogram in the case of a mutual mis-registration κ:

(4.2) $$\phi_1 = 2\pi\, f_{C,1}\, \kappa .$$

For a second look with centre frequency $f_{C,2}$ [cycles/sample] the phase offset will be:

(4.3) $$\phi_2 = 2\pi\, f_{C,2}\, \kappa .$$

Since the centre frequencies are known and the mis-registration Δt is the same for both spectral looks the difference phase allows the retrieval of the mutual shift of the SAR images:

(4.4) $$\kappa = \frac{\phi_2 - \phi_1}{f_{C,2} - f_{C,1}} .$$

This means that after formation of the differential interferogram a mis-registration map is obtained that may be smoothed for noise reduction.

For ScanSAR and burst-mode data the individual azimuth spectral looks are readily available. The centre frequencies of the burst looks are azimuth dependent sweeping the whole processed Doppler bandwidth between $-W_A/2$ and $W_A/2$ (equation (3.8)):

(4.5) $$f_{C,n} = FM\,(nT_P - t_0)$$

(4.6) $$f_{C,m} = FM\,(mT_P - t_0)$$

where m and n refer to two looks acquired for a target at position t_0. Inserting these equations into (4.4) yields:

(4.7) $$\Delta t = \frac{\phi_2 - \phi_1}{FM\,(m-n)\,T_P} .$$

In this case, Mis-registration only depends on the difference in frequency of the two spectral looks. Note that the phases ϕ_1 and ϕ_2 are assumed to be absolute phases.

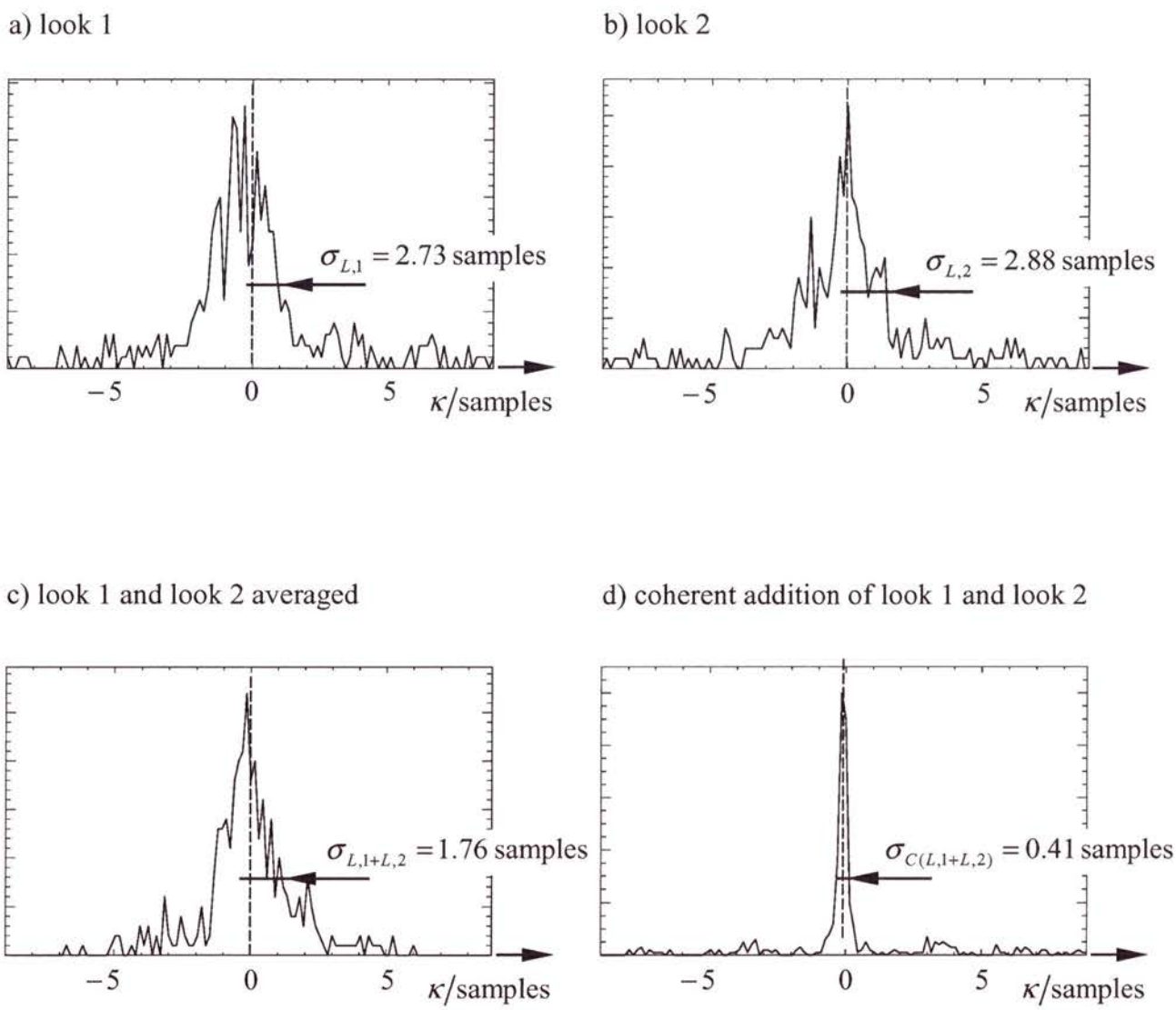

Figure 4.6: Histograms of cross-correlation measurments (2-look, data set section 7.1): a) look 1, b) look 2, c) look 1 and look 2 results averaged, and d) after coherent addition of the two looks.

Signal processing

For burst-mode data processed by the full aperture multiple coherent burst method described in (Bamler and Eineder 1996) the following approach for oversampling the image patches may be chosen. It is illustrated in figure 4.7 for 2-look burst-mode data. For the subsequent cross-correlation operation the squared amplitude of the image patches is used for higher sensivity and robustness. However, the detected signal demands twice the bandwidth which is required to the complex signal. This means the data have to be oversampled before detection and, in contrast to range, azimuth oversampling requires knowledge of the Doppler centroid. However, for the 2-look multiple coherent burst images oversampling may be conducted *after* detection since the detected signal's bandwidth is still smaller than PRF. This means, Doppler centroid information is not required since the spectrum of the detected signal is centred around zero frequency. The only requirement is that the sampling frequency of the complex data PRF_o is large enough to accommodate the bandwidth of the detected signal, i.e. for a N_L-look burst-mode signal $PRF_o \geq W_D = 2\left(N_L - 1\right)W_P + 2\,W_B$. For the example 2-look ScanSAR Narrow mode (section 5.1) this requirement is easily met since $W_A \geq N_L\,W_P = 2\,W_P$ and the bandwidth of the detected signal is $W_D = 2\left(W_P + W_B\right)$. The respective multiple coherent burst images represented at the acquisition PRF may be conveniently applied to for co-registration information retrieval.

Derivation of the Resampling Model

For RADARSAT-1 accurate co-registration is essential due to the very high Doppler centroid values. In particular when it comes to beam combination as described in section 4.2.7 co-registration accuracy must be high and a smooth transition between beams is desired. Unfavourable coherence conditions may hinder a robust fit of resampling polynomials (section 4.2.7, figure 4.14) using cross-correlation data alone. For this reason geometrical and cross-correlation measurements were combined to provide the most accurate and robust resampling information (Holzner et al. 2001).

The geometric co-registration parameters can be obtained by geolocation using zero Doppler iteration (Meier et al. 1993). This means for a point on ground the times for the primary and secondary channel were calculated when it was 'seen' by the antenna at the individual repeats. The differences in times provide the co-registration information when converted into pixel units. This zero-Doppler geolocation was done for several positions equally distributed over

the area covered by the ScanSAR scenes and a second order azimuth and range resampling polynomials for were fitted to the samples. Geolocation was conducted using positions on the WGS84 Reference-Ellipsoid since topographic effects are negligible. For the data set baseline of 167 m a difference in mis-registration of about 0.05 pixel at midrange ($\theta \approx 30^\circ$) was obtained for a height variation of 3000 m. Hence, topographic influences in the mutual co-registration relationship of the SAR images can be considered as additional noise. The impact of orbit errors on resampling polynomial accuracy was investigated and is outlined in appendix A7. For RADARSAT-1 orbit data it is recommendable to check the applicability of geometrically derived resampling information in each individual case.

Hence, the co-registration polynomials obtained from geometry were compared to cross-correlation measurements of the individual beams. For this reason the polynomials were converted into polynomials valid for each individual beam pixel co-ordinate system. The standard deviations of the differences (measurement minus geometry) are in the order of 0.16 (0.26) pixel for beam 1 (beam 2). A second order polynomial fit to the cross-correlation measurements supplied the same standard deviations. Therefore, it was decided to use the registration information from geometry corrected by the offsets measured from the cross-comparison due to the coherence constraints of the data set (Figure 4.16) and robustness of fit. In contrast to the range offsets which are almost negligible – 0.05 pixel and 0.07 pixel for beam 1 and beam 2, respectively – the azimuth offsets amount to –5.27 and –3.11 pixels equivalent to 3.95 msec and 2.33 msec for beam 1 and beam 2. The large difference of the azimuth offsets is caused by from the different alignment of the images within the beam-co-ordinate systems.

Since mis-registrations in the individual beams are very sensitive to azimuth mis-alignments (section 4.2.7), the beams were resampled individually. A possible remaining mutual phase difference of the beams showing up in the beam overlap area was corrected during beam combination (section 4.2.7).

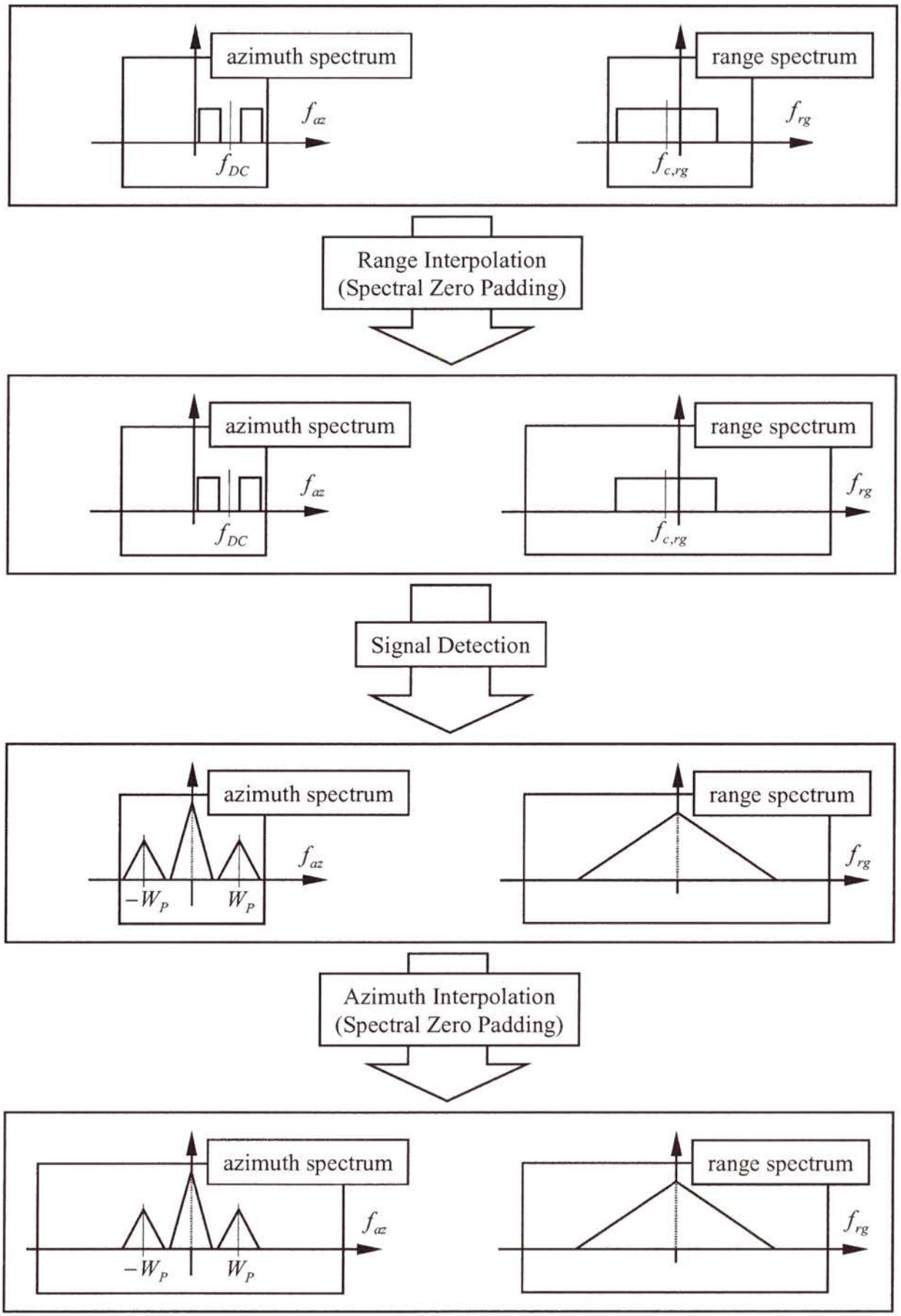

Figure 4.7: Signal interpolation for co-registration of 2-look multiple burst images.

4.2.2 Interpolation for Image Co-Registration

Co-registration of interferometric data pairs involves the interpolation of the secondary channel image. Multiple coherent burst images and single burst images sampled at acquisition PRF can be resampled using conventional interpolation algorithms since the average spectral density is $|A(f)|^2$ and resembles that of strip-map mode data:

$$
\begin{aligned}
\tilde{S}_{u_1 u_1}(f) &\approx \int_{-\frac{T_A}{2}}^{\frac{T_A}{2}} dt_0 \, |H_C(f,t_0)|^2 \\
&= \sum_{N_L} |A(f)|^2 \int_{-\frac{T_A}{2}}^{\frac{T_A}{2}} dt_0 \, \mathrm{rect}\left(\frac{f + n W_P + FM\, t_0}{W_B} \right) \\
&= N_L \, W_B \, |A(f)|^2 \\
&\propto |A(f)|^2
\end{aligned}
\qquad (4.8)
$$

In this equation, the approximation of the burst-mode power spectral density in section 3.1.2 was utilised and equation (3.9) in section 3.1.1 was extended with the spectral weighting of strip-map data $A(f)$ ("$\propto$" denotes proportionality).

If the single-burst-mode images are sampled at a frequency lower than the processed Doppler bandwidth W of the equivalent strip-map mode images, burst interpolation requires an adapted resampling approach. In contrast to strip-map data where the spectrum is centred around the Doppler centroid, the centre frequency of the burst spectrum varies linearly with azimuth. Hence, an azimuth variant interpolation kernel must be used.

There are two methods of carrying out the single burst signal interpolation. First, an azimuth-variant bandpass may be applied to resample the images. Second, the burst-mode data is deramped and then the obtained low-pass signal is resampled using a standard interpolation module; after interpolation the quadratic phase is re-established. This latter efficient approach is derived in more detail in the following.

The phase of the single burst impulse response $h_n(t,t_0)$ (equation (3.8)) is linear and depends on the scatterer position t_0 as strongly amplified in Figure 4.8. Since every single point scatterer has a position t_0 dependent phase slope, the burst signal's spectrum shows the previously described azimuth-varying behaviour (figure 4.9 a) and section 3.1.1). When the

burst signal is sampled at a PRF_n lower than the acquisition PRF (sections 3.1.3 and 4.3.1) then the signal components appear wrapped in the time-frequency diagram (figure 4.9 b) and section 4.2.4). The illustration suggests that the overall signal phase variation may be compensated by a quadratic phase function. Applying such a phase function generates a low-pass signal.

In terms of formulas let us consider a burst of index $n = 0$ without loss of generality. Then the impulse response is (equation (3.8)):

$$(4.9)\quad h_0(t;t_0) = \mathrm{sinc}(W_B\,(t-t_0))\exp(-j\,2\pi\,FM\,t_0\,(t-t_0))\ .$$

After application of the quadratic phase $\exp(j\,\pi\,FM\,t^2)$ the following signal is obtained:

(4.10)

$$\mathrm{sinc}(W_B\,(t-t_0))\exp(j\,\pi\,FM\,(t^2-2\,t_0\,(t-t_0)))=$$

$$\mathrm{sinc}(W_B\,(t-t_0))\exp(j\,\pi\,FM\,(t-t_0)^2)\exp(j\,\pi\,FM\,{t_0}^2)\ .$$

It has no linear phase component anymore, and, hence, its spectrum is of low-pass type (figure 4.9 c)). A slight broadening of the spectrum occurs as a result of the residual quadratic phase $\pi\,FM\,(t-t_0)^2$. It is in the order of $\Delta W_B = |FM|/\,W_B$, assuming a burst response resolution of $\rho_B = 1/W_B$ and applicability of the principle of stationary phase. This bandwidth increase has to be taken into account in the case of the burst image sampling frequency PRF. For the RADARSAT example ($FM \approx -2000\ Hz/\mathrm{sec}$) and a burst bandwidth in the order of 100 Hz, a bandwidth increase of 20 Hz can be found. In the comparison of the bandwidths of the signals in figures 4.9 b) and c), no significant bandwidth increase was observed for the considered configuration. However, the reason for this may be the limited time-frequency resolution of the periodogram. After the described down-modulation, the signal may be resampled using standard resampling algorithms. The time co-ordinate is then mapped to the one of the master image $t \rightarrow t'$. It may be considered a constant shift within a sufficiently small regions. In order to re-establish the gross quadratic phase (properly mapped to the master co-ordinates) the resampled image is multiplied with $\exp(-j\,\pi\,FM\,t'^2)$. The burst deramp resampler was implemented using a 4-point FIR resampling kernel (FIR: finite impulse response function) (Hanssen and Bamler 1999) and tested.

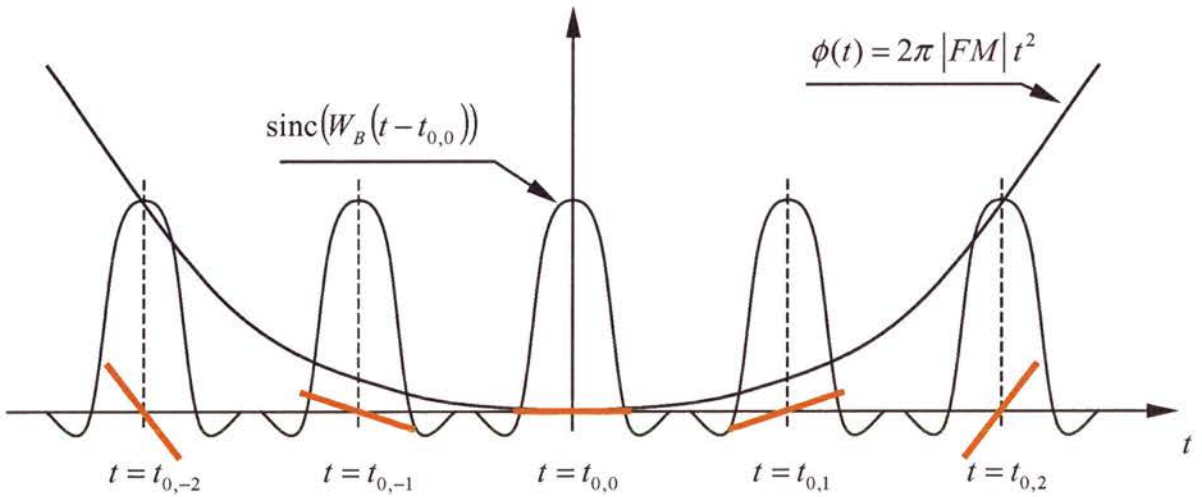

Figure 4.8: Phase behavior of point-scatterer responses at various time positions.

a) burst at (acquisition) *PRF*

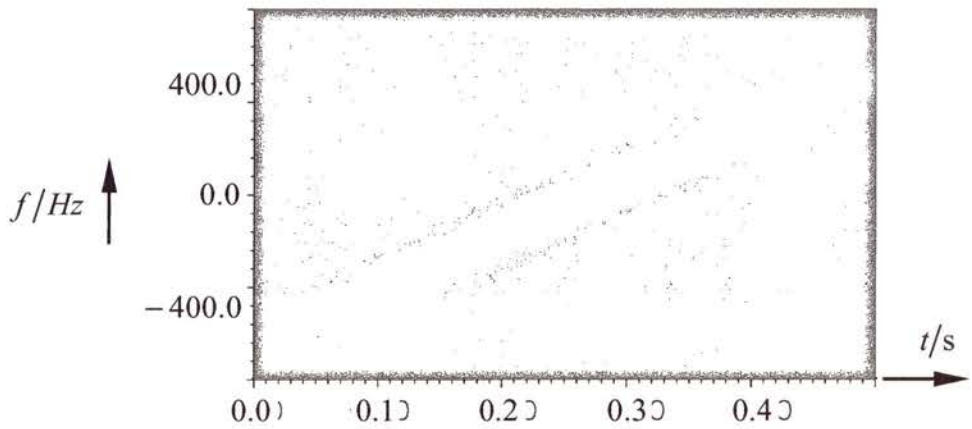

b) burst at *PRF* / 5

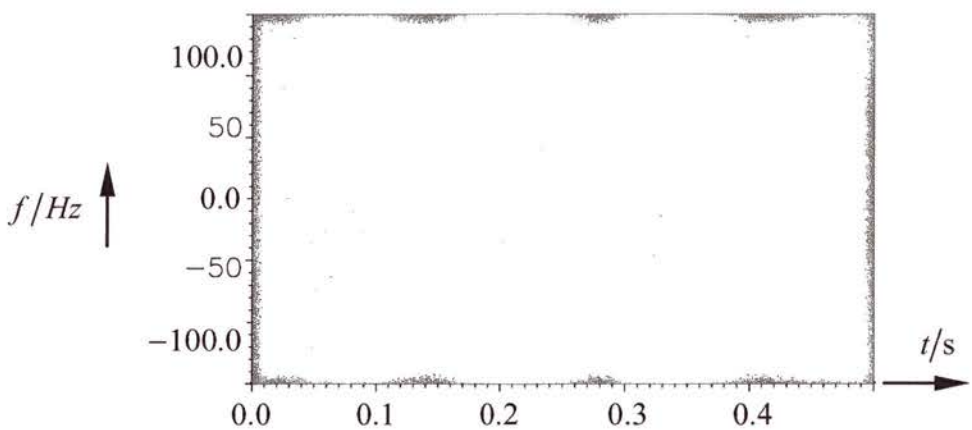

c) deramped burst (*PRF* / 5)

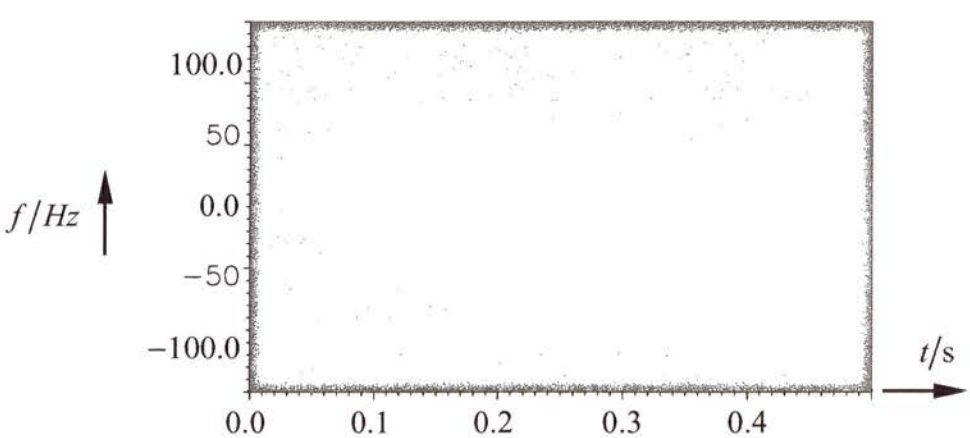

Figure 4.9: Time-frequency diagram of a) a burst at acquisition *PRF* b) at PRF_n=*PRF* / 5, and c) the deramped burst of illustration b). The periodograms where obtained from real data in a clutter area (section 5.1: ScanSAR Narrow data set 11312).

Illustration 4.10 demonstrates the phase preserving character of the resampler (red indicates zero phase difference) for the data of figure 4.9 and a mis-registration of 0.4 samples at $PRF_n = PRF/5$. For this sampling frequency the phase noise errors originating from resampling are negligible since the data is still oversampled by a factor of about 2.8 and aberrations caused by the resampling kernel occur mainly in the vicinity of the $\pm PRF_n/2$ limits. This algorithm is also very efficient compared to a bandpass FIR. When using the above approach, two complex multiplications per sample become necessary. However, for the use of a bandpass FIR with N samples, N complex multiplications per data sample are conducted (The number of required operations to calculate one interpolated data sample in the base band are identical).

4.2.3 Variation of Coherence with Varying CNR

Scalloping may introduce an azimuth-varying clutter-to-noise ratio (CNR) that can be corrected (Bamler 1995). Moreover, as a result of the CNR variation the interferometric phase and coherence may be affected (Zebker and Goldstein 1986; Bamler and Hartl 1998) according to:

$$\frac{\Delta\gamma}{\gamma} \approx \frac{1}{1+CNR}\frac{\Delta CNR}{CNR}, \qquad (4.11)$$

which is the relative variation of the coherence with the relative variation of the clutter-to-noise ratio. From this equation it is clear that the coherence pattern depends on the local SNR values. Figure 4.11 shows the conditions for the data set considered with parameters from section 5.1. This pattern is obtained as the convolution of the azimuth antenna pattern with the burst scanning pattern profile (Mittermayer et al. 1996). The ratio as illustrated in figure 4.11 is given by the following equation:

$$\frac{CNR_{burst}}{CNR_{strip}} = \frac{\sum_N A^2\left(FM\left(t-\frac{n}{PRF}\right)\right)\left|B(n)\right|^2}{\sum_N \left|B(n)\right|^2}\frac{N}{E_G} \qquad (4.12)$$

with

$$B(n) = \sum_{\ell=-\infty}^{\infty} \mathrm{rect}\left(\frac{\left(\frac{n}{PRF}-\ell\,T_p\right)}{T_B}\right). \qquad (4.13)$$

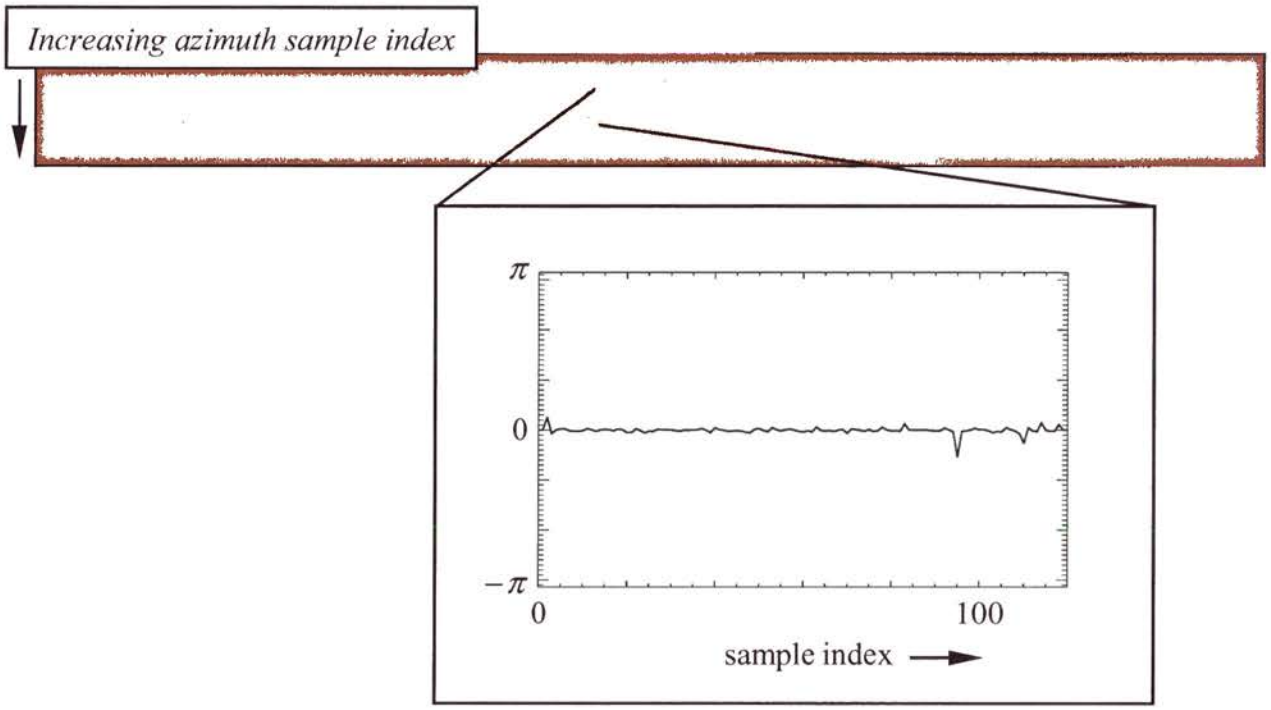

Figure 4.10: Results obtained for the resampler based on burst deramping. The difference phase between original and resampled burst image for a mis-registration of 0.4 (PRF_n=PRF / 5) is illustrated.

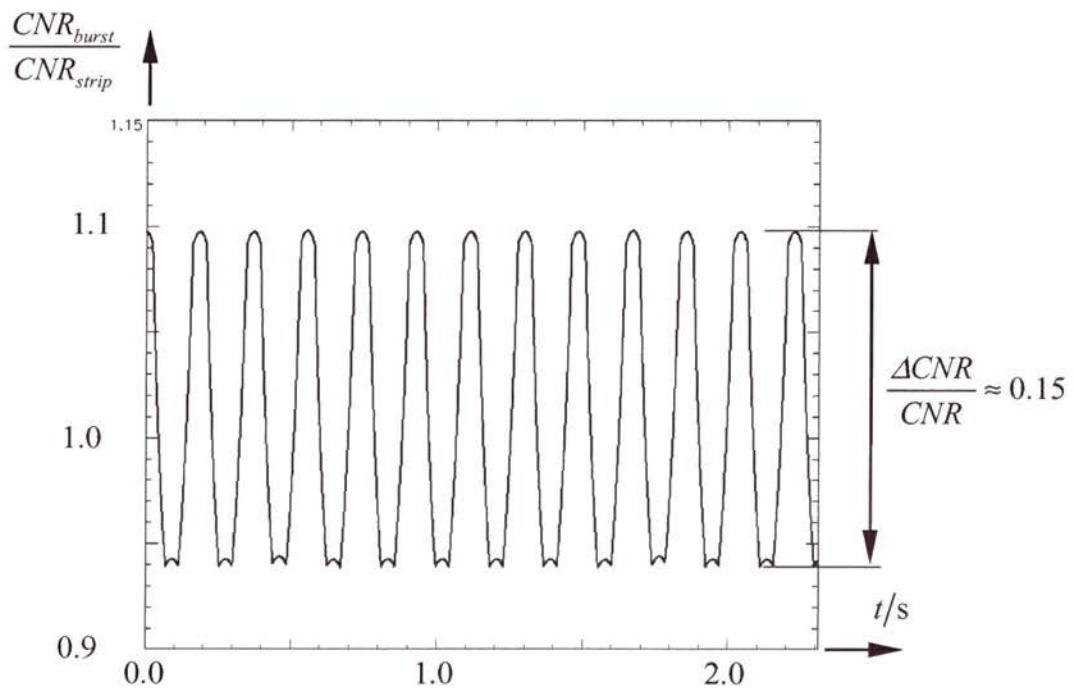

Figure 4.11: Clutter-to-noise ratio (CNR) comparison of strip map and noise data. The quotient of burst over strip-map data CNR is shown for the data set parameters in section 5.1.

The burst scanning pattern and $A(.)$, N, and P_G are the spectral weighting, the number of samples integrated, and the energy of the spectral weighting:

$$E_G = \sum A^2\left(FM \frac{n}{PRF} \right), \quad (4.14)$$

respectively.

It can be observed from the illustration that the CNR varies approximately by 15 %. This means that, for example, in a low CNR area ($CNR = 2$) a coherence modulation of 5% may be expected in contrast to a modulation of about 2% when $CNR = 10$. However, such effects were not observed for the considered interferometric RADARSAT data set due to the dominating temporal decorrelation.

4.2.4 Common Band Filtering and Azimuth Spectral Shift

Range Common Band Filtering

A possible range spectral shift is accounted for during common band filtering. The amount of usable overlapping bandwidth is determined by the gross range fringe frequency (section 2.1.3). Usually for ERS and the fine beam and standard beam modes of RADARSAT-1 this shift may be assumed constant over range due to their small swath width of 50 km (fine beam) and 100 km (ERS and standard beam). The gross range fringe frequency of the 'ScanSAR Narrow A' data set varies considerably from near to far range. For beam 1 (beam 2), a variation of -3.1 MHz to -1.6 MHz (-1.6 MHz to -1.05 MHz) was found. Compared to the bandwidth the variation amounts to 13 % (5 %). Hence, the spectral shift filtering operation has to account for this significant variation of the overlap bandwidth. In the used implementation the signal parameters were adapted on a block-by-block basis where blocks of extent 1024 x 1024 were used.

Azimuth Common Band Filtering

In this section the case is considered when the burst images were focussed with differing Doppler centroid frequencies. This situation occurs when two interferometric partners are focussed independently which is, for example the case when standard complex burst image products are available. Azimuth common band filtering chops off the non-common Doppler frequency components of the azimuth signal as a result of differences in Doppler centroid (section 2.1.3). Figure 4.12 shows the situation for an interferometric pair of single burst

images. As can be seen from the illustration for single and multiple coherent burst-mode data represented at $PRFs$ higher than the (strip-map) processing bandwidth W_A, standard interferometric modules may be utilised (section 3.1.3 and 2.1.3). A different approach must be considered for the single burst-mode images sampled at lower frequencies. Either the signal is interpolated to the acquisition PRF and common band filtered using standard azimuth spectral filters, or the data is filtered using an azimuth varying bandpass filter that has to account for the wrap back behaviour of the burst-mode data in the frequency interval $\pm PRF_n/2$ (section 4.3.1) as illustrated in figure 4.13. The secondary channel burst image bandwidth at time t_0 is wrapped back to the centre frequency $FM\left(t_0 - t_{c,2}\right) + f_{DC,2} - \ell\, PRF_n$ where ℓ denotes the index of the PRF_n band where the original centre frequency of the bandpass signal was located.

It is apparent in figure 4.12 that only the signal components at the end of the primary channel burst extent and the beginning of the secondary channel burst extent have to be filtered. Evidently, the pixels within the time spans $\Delta f_{DC}/|FM|$ as indicated in the figure may simply be set to zero. After azimuth common band filtering the bursts are centred around t_c, the centre time of the burst images.

A third option is to focus both ScanSAR data sets to the mean Doppler centroid with reduced azimuth bandwidth as was done for the data set in section 5.1.

In the case of large Doppler centroid deviations between repeated passes the interferogram swath may not be contiguous anymore. Figure 4.14 shows a situation when after azimuth common band filtering gaps in the interferogram will occur. The condition to be met is:

$$\Delta f_{DC} \le W_A - |FM|\, T_P \qquad (4.15)$$

where Δf_{DC} is the difference of the Doppler centroid values. This conditions stems from the fact that per for the remaining bandwidth at least one burst look must be available (see section 2.2). For the current data set the Doppler centroid difference is in the order of 50 Hz which is much smaller than the required 641 Hz on the right hand side of equation (4.15).

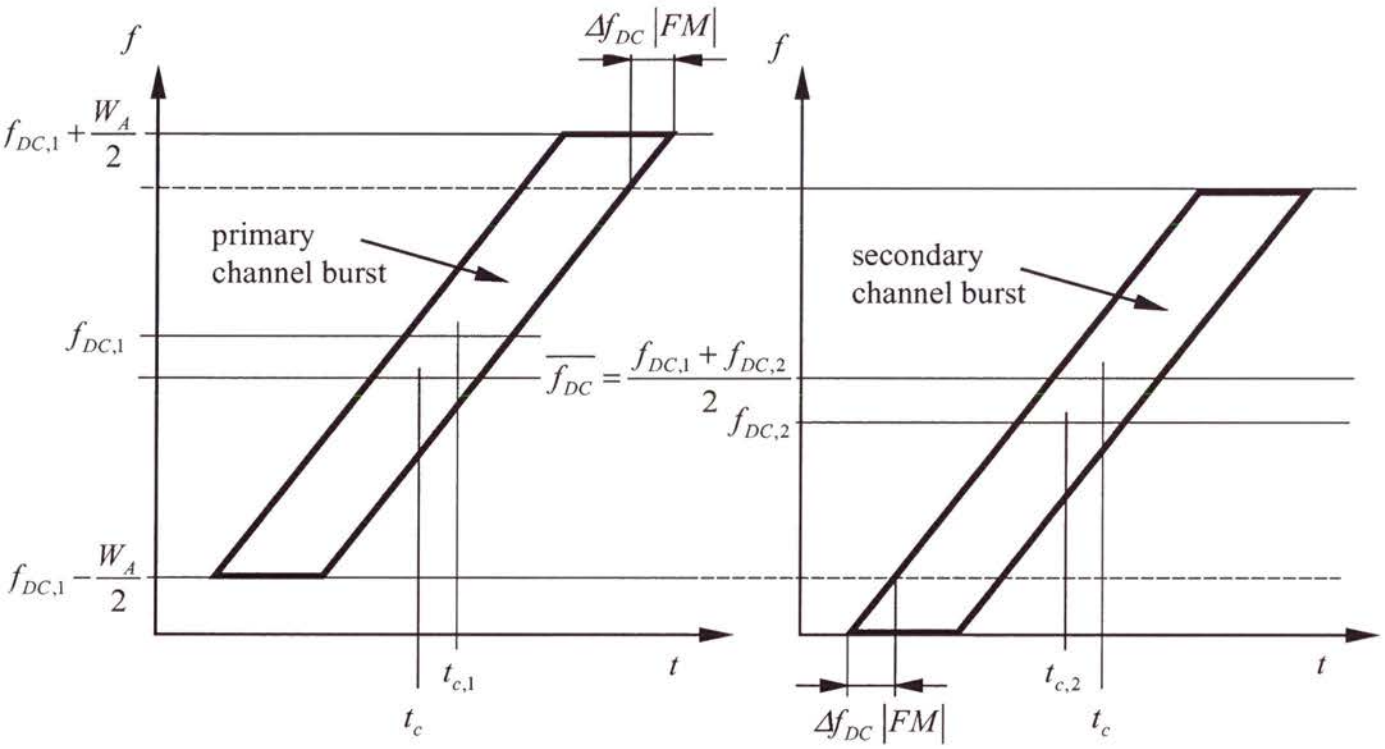

Figure 4.12: Azimuth common band filtering of an interferometric pair of single burst images (Example for $f_{DC,1} > f_{DC,2}$.) The indicated parts of the burst images with extent $\Delta f_{DC}\,|FM|$ may be discarded simply by setting the respective pixel of the burst image signals to zero. After common band filtering both bursts are centered around t_c.

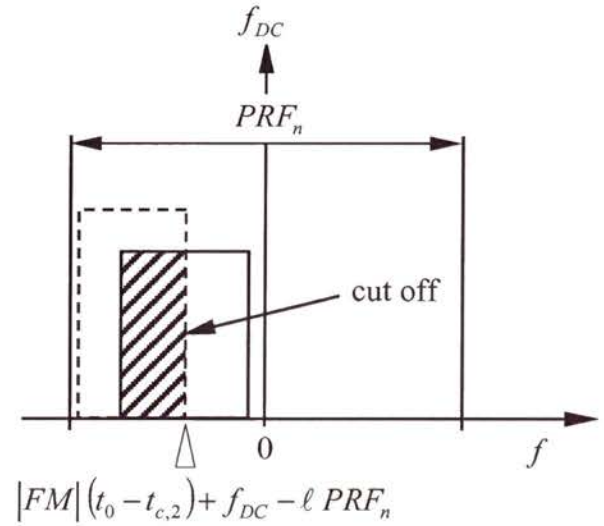

Figure 4.13: Wrap back of ScanSAR burst image spectrum for a scatterer at t_0. An example cut off section and filter for establishing azimuth common bands are indicated.

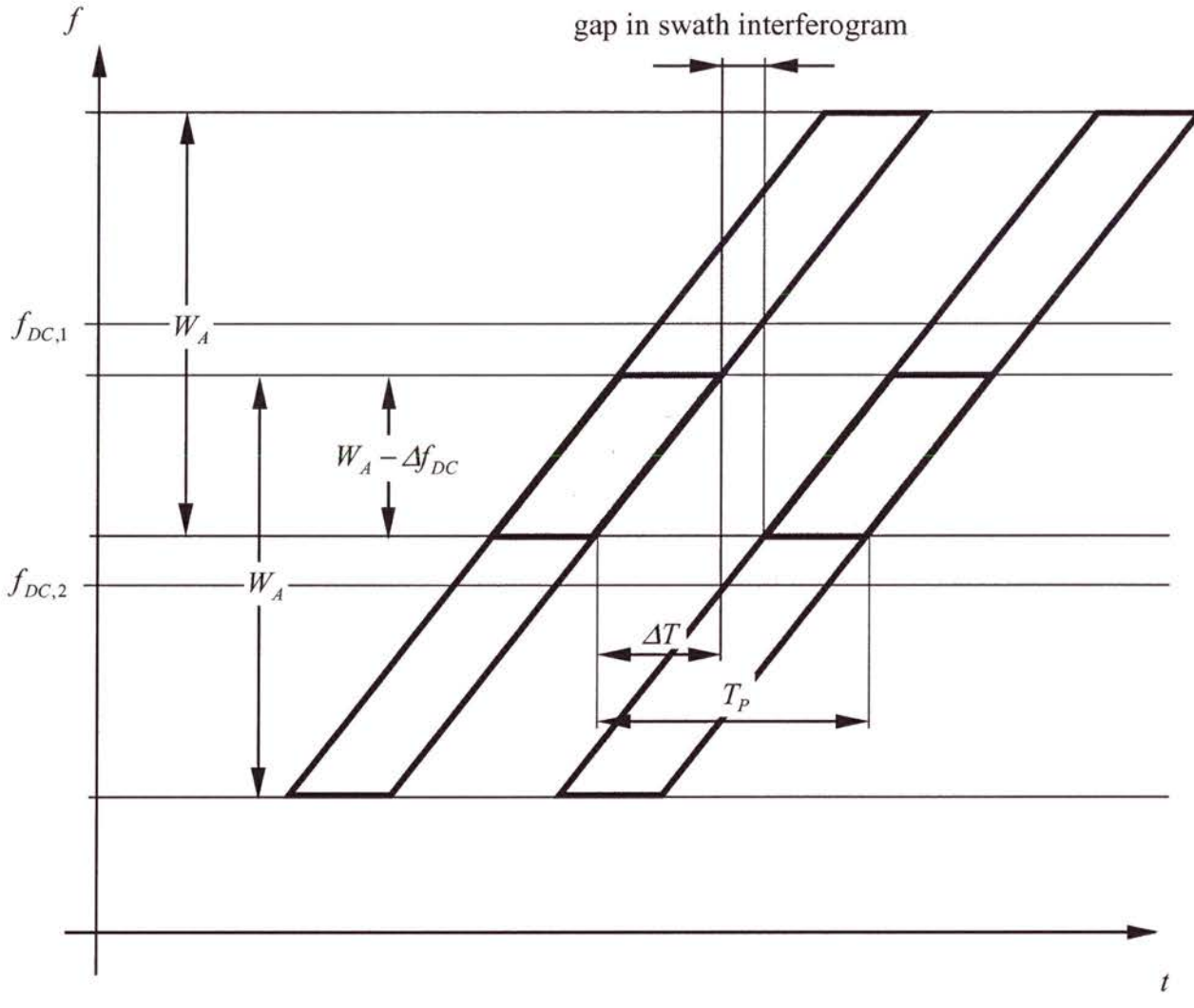

Figure 4.14: Large Doppler centroid differences may cause non-contiguous burst-mode swath interferograms. The gap occurs, since the remaining burst support (ΔT) does not cover the burst cycle period T_P.

Azimuth Spectral Shift

Terrain angles and converging orbits introduce mutual spectral shifts in interferometric data. This means companion spectral components are mapped to slightly different frequency positions and a fringe frequency f_ϕ is introduced into the interferogram (Zebker and Villasenor 1992; Gatelli et al. 1994; Monti Guarnieri and Prati 1996). In the case of terrain angles, this frequency displacement may be quantified as (Monti Guarnieri and Prati 1996):

$$f_\phi = -\frac{2}{\lambda}\frac{B_\perp v_S}{R_0}\sin\theta\tan\alpha \qquad \text{[Hz]} \tag{4.16}$$

As an example, consider interferometric burst-mode data acquired at a look angle of 40° and with perpendicular baseline of 167 m. The terrain angles must be above 22° for the fringe frequency to exceed one tenth of the burst bandwidth (RADARSAT-1 conditions, section 5.1). The effect is thus negligible for the data set considered.

Azimuth spectral shifts become significant only when very small burst bandwidth are available as for the RADARSAT Wide A and B modes ($W_B \approx 60\ Hz$), the ENVISAT Wide Swath ($W_B \approx 60$ Hz), and in particular for the ENVISAT Global Monitoring mode ($N_B \approx 7$ range lines). Then the coherence may be significantly improved by suitable azimuth spectral shift filtering.

4.2.5 Range Spectrum Shift of RADARSAT data

RADARSAT-1 is not yaw steered and, hence, its SAR data is characterised by large-squint angles and, consequently, high Doppler centroid values (Raney et al. 1991; Geudtner 2001). A complex SAR image can be considered a 2-D bandpass excerpt of the full scatterer spectrum (section 2.1.3). If this image was acquired at a high squint angle its average range spectrum appears to be shifted off-zero frequency. This frequency shift can be given as (cf. equation (2.19)):

$$\Delta f_{c,rg} = f_{c,rg} - f_0 \approx -\frac{c}{2\cdot\lambda}\left(\frac{f_{DC}}{v_S}\cdot\frac{\lambda}{2}\right)^2 \tag{4.17}$$

(Rocca et al. 1989; Bamler and Holzner 2000; Bara et al. 2000; Geudtner 2001).

For the data set considered this frequency offset changes from –0.95 MHz in near range to –3.8 MHz in far range caused by the high Doppler centroid variation (figure 4.1). With respect

to the signal's bandwidth this variation is significant and involves adaptations of interpolation and spectral shift filtering algorithms.

4.2.6 Mosaicking of the Single Burst Interferograms

Sub-swath interferogram formation requires coherent addition of the single burst interferograms. The representation of the burst interferogram on a common reference grid is favourable for this task. The native sampling of the burst data is not a continuos one since the PRF of the swaths differ (section 2.2). In the best-case scenario, the ScanSAR processor should take care of the processing of the data to a common grid across swaths. Differential interferograms in the overlap area of the bursts help to identify phase and sampling errors. After multi-looking a N_L-look swath interferogram is obtained (section 3.2.2).

4.2.7 Beam Alignment

Current and future missions offer ScanSAR data consisting of 2 to 5 beams (Raney et al. 1991; Karnevi et al. 1994; Thompson et al. 2001). Either the ScanSAR beams are treated individually or the swath images or interferograms are stitched together prior to subsequent processing. For the generation of the ScanSAR DEM (section 7), the interferogram subswaths were combined in advance of filtering, phase unwrapping, phase-to-height conversion, and geo-coding.

Usually the ScanSAR beams show significant overlap. These overlap regions are exploited for radiometric calibration of ScanSAR images (Luscombe 1993; Hawkins et al. 2001). When swath interferograms are combined, the common area provides valuable information for inter-beam co-registration verification and mutual phase offset determination.

Phase deviations in the interferogram overlap area originate from several error sources. These phase errors are either already contained in the interferograms or result from mutual mis-alignments of the sub-swath interferograms. The first group includes phase errors as a result of remaining tiny azimuth and range mis-registrations scaled with the azimuth and range spectrum centre frequencies, i.e. Doppler centroid and an off-zero range spectrum centre frequency (sections 2.1.3, 4.2.1 and 4.2.5). The phenomena are very well known and an extensive discussion can be found in (Bara et al. 2000). In accordance with the phase errors from Doppler centroid, the error phase from mis-aligned interferograms arises from a slight deviation in the sampling of the main interferometric phase ramp. The slope of the phase ramp is the gross (flat-earth) azimuth or range fringe frequency (Bamler and Holzner 2000).

All phase effects may be compactly represented by the following equations. Phase errors originating from azimuth displacements are quantified according to:

$$\Delta\phi_{az} = 2\pi\left(\frac{f_{DC,2}}{PRF}\delta az_{b2} - \frac{f_{DC,1}}{PRF}\delta az_{b1} + f_{\phi,az}\,\delta az_i\right) \qquad (4.18)$$

with $f_{DC,1}$ ($f_{DC,2}$) [Hz] - Doppler centroid value for beam 1 (beam 2), δaz_{b1} (δaz_{b2}) [samples] remaining azimuth registration errors for beam 1 (beam 2), $f_{\phi,az}$ [cycles/sample] - azimuth fringe frequency, and δaz_i [samples] - azimuth interferogram mis-alignment. Likewise, the phase impact as a result of range shifts is obtained from:

$$\Delta\phi_{rg} = 2\pi\left(\frac{f_{c,rg,2}}{RSF}\delta rg_{b2} - \frac{f_{c,rg,1}}{RSF}\delta rg_{b1} + f_{\phi,rg}\,\delta rg_i\right) \qquad (4.19)$$

where $f_{c,rg,1}$ ($f_{c,rg,2}$) [Hz], δrg_{b1} (δrg_{b2}) [samples], $f_{\phi,rg}$ [cycles/sample], and δrg [sample] denote the range spectrum centre for beam 1 (beam 2), residual range mis-registrations for beam 1 (beam 2), and the mutual range interferogram mis-alignment. The total phase error in the overlap area is then the sum of the phase error contributions from equations (4.18) and (4.19).

The predominating phase error contribution for the data set considered are the high Doppler centroid values ($f_{,1}/PRF \approx f_{,2}/PRF \approx 6.0$ cycles/sample) followed by the range frequencies which are in the order of 0.2 cycles/sample. Phase errors due to azimuth fringe frequencies, however, are negligible: $f_{\phi,az} = 6\cdot10^{-4}$ cycles/sample. Slight differences of the Doppler centroid values scale interferometric mis-registrations in the order of the range frequencies ($\Delta f_{DC} / PRF \approx 0.3$ cycles/sample) while the contributions from the differing range spectrum centre frequencies are very low ($\Delta f_{rg,c} / PRF \approx 0.02$ cycles/sample). The difference in Doppler centroid comes from slightly different look directions of the antenna beam for adjacent swaths. This difference – as can be seen in the above value – has only a minor effect on the range spectrum offset frequency deviation (equation (4.17)).

Potential mis-alignments may be verified by cross-correlation measurements in the overlap area of the interferograms. In order to guarantee a smooth phase transition remaining phase errors have to be estimated and compensated before beam combination.

Note that for single beam modes phase errors as a result of the high Doppler centroids may be accounted for by suitable orbit trimming. This can only be recommended if the swath interferograms are geocoded individually.

In contrast to the considered repeat-pass case an additional error source may occur for bi-static interferometers (Jordan et al. 1996; Lee and James 2001). Phase offsets may differ for each individual beam caused by beam-varying electronic delays of the instruments and contribute to phase deviations in the overlap area.

Mutual beam mis-alignments of the particular RADARSAT data set were measured by cross-correlation of detected image patches in the overlap area. Only image contrast helps to measure mutual shifts since the spectra of the complex valued beam signals are non-overlapping. Detected multiple coherent burst images of a high contrast section (mountainous terrain) were used in order to improve the co-registration results. A shift of 0.15 ± 0.02 samples in range was measured from several hundred image chips distributed over the considered overlap region. The far range beam interferogram was resampled and a phase offset of –3.11 radians (Standard deviation of offset measurement: 1.47 radians) was reduced for a smooth phase transition between the interferogram beams. Then the individual interferograms were combined and the interferogram samples were coherently added in the area overlap.

Figure 4.15 shows the differential phase in the overlap area. There are no systematic effects apparent that indicate remaining mis-registrations or phase errors as a reason of high Doppler centroid values (see above). Errors from mutual shifts of the interferograms would appear as topography-correlated phase patterns and tiny interferometric mis-registrations would generate slowly varying phase errors, e.g. linear phase trends.

a) difference phase of overlap area

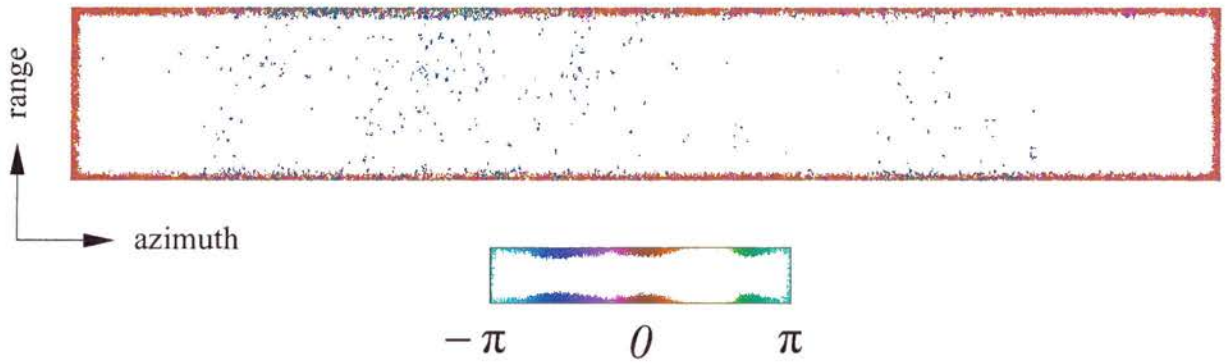

b) range mean of difference phase

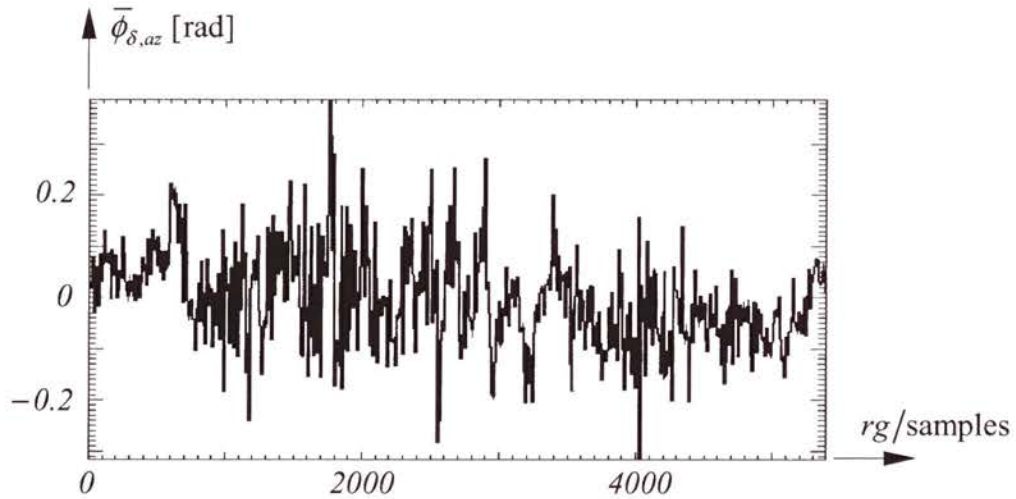

Figure 4.15: Differential phase (a) of the beam 1 and beam 2 interferogram in the overlap area after reduction of a phase offset of -3.11 radians. The range mean of the phase versus azimuth in (b) shows no systematic effects. Zero phase is indicated in red.

The combined interferogram amplitude and phase is shown in figure 4.16. The data cover an area of about 110 km x 350 km in azimuth and range, respectively.

After burst interferogram formation coherence information as defined in equation (2.1) is no longer available. Instead, the following phase stability measure serves for statements on the phase quality:

$$\hat{\gamma}' = \frac{\left| \sum_{N} i_n \right|}{\sqrt{\sum_{N} |i_n|^2}} \qquad (4.20)$$

Figure 4.17 shows the phase stability map for the RADARSAT-1 data set. Apart from the apparent sources of phase noise (layover, water surfaces, snow fall, and temperature effects) phase stability increases in the beam overlap area. This phase stability increase implies that there are no additional phase ramps that cancel out in the differential interferogram of figure 4.15. In addition, the coherent addition of the independent swath-interferogram reduce phase noise equivalent to coherently averaging two N_L-look interferogram samples.

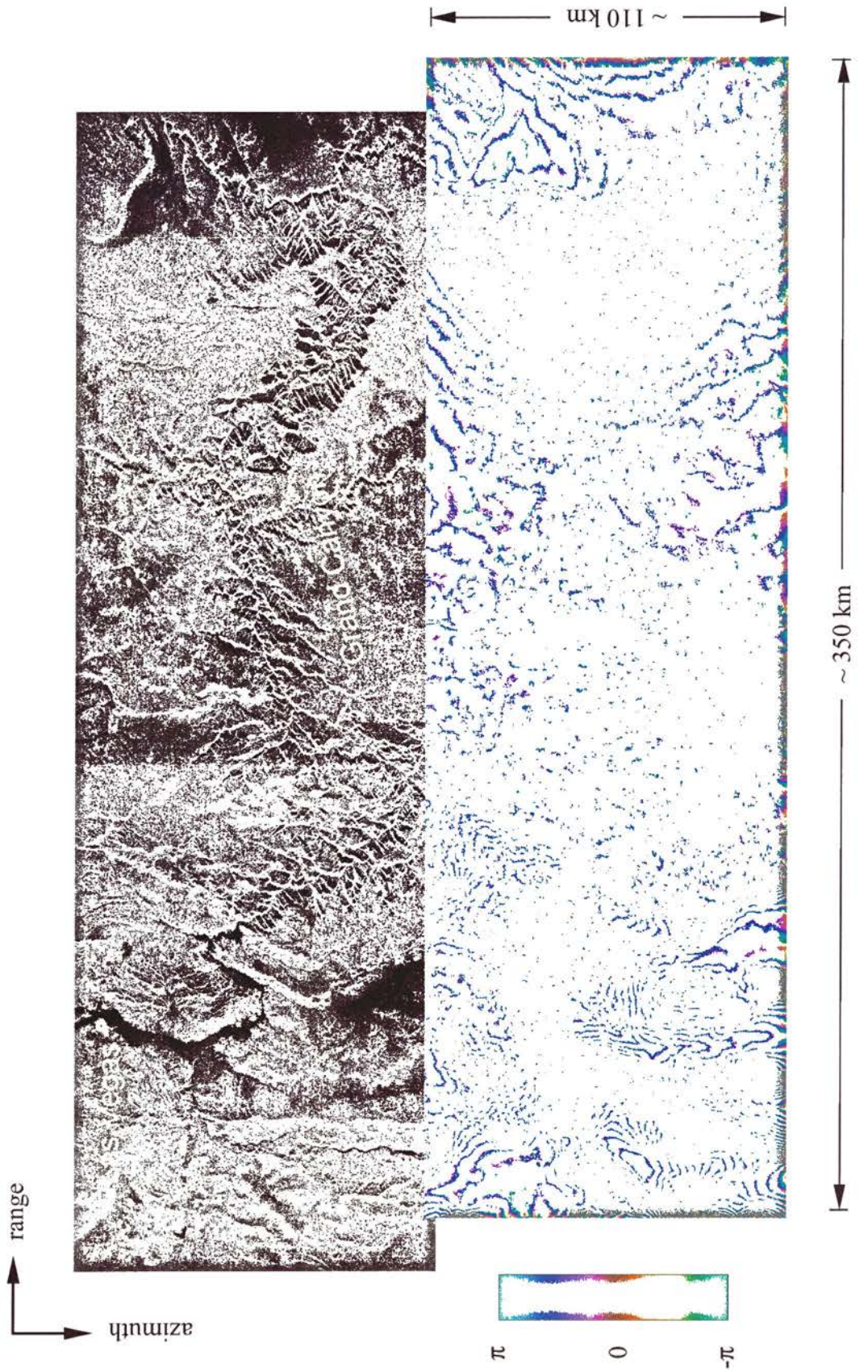

Figure 4.16:Phase and amplitude of the two-beam RADARSAT-1 ScanSAR interferogram.

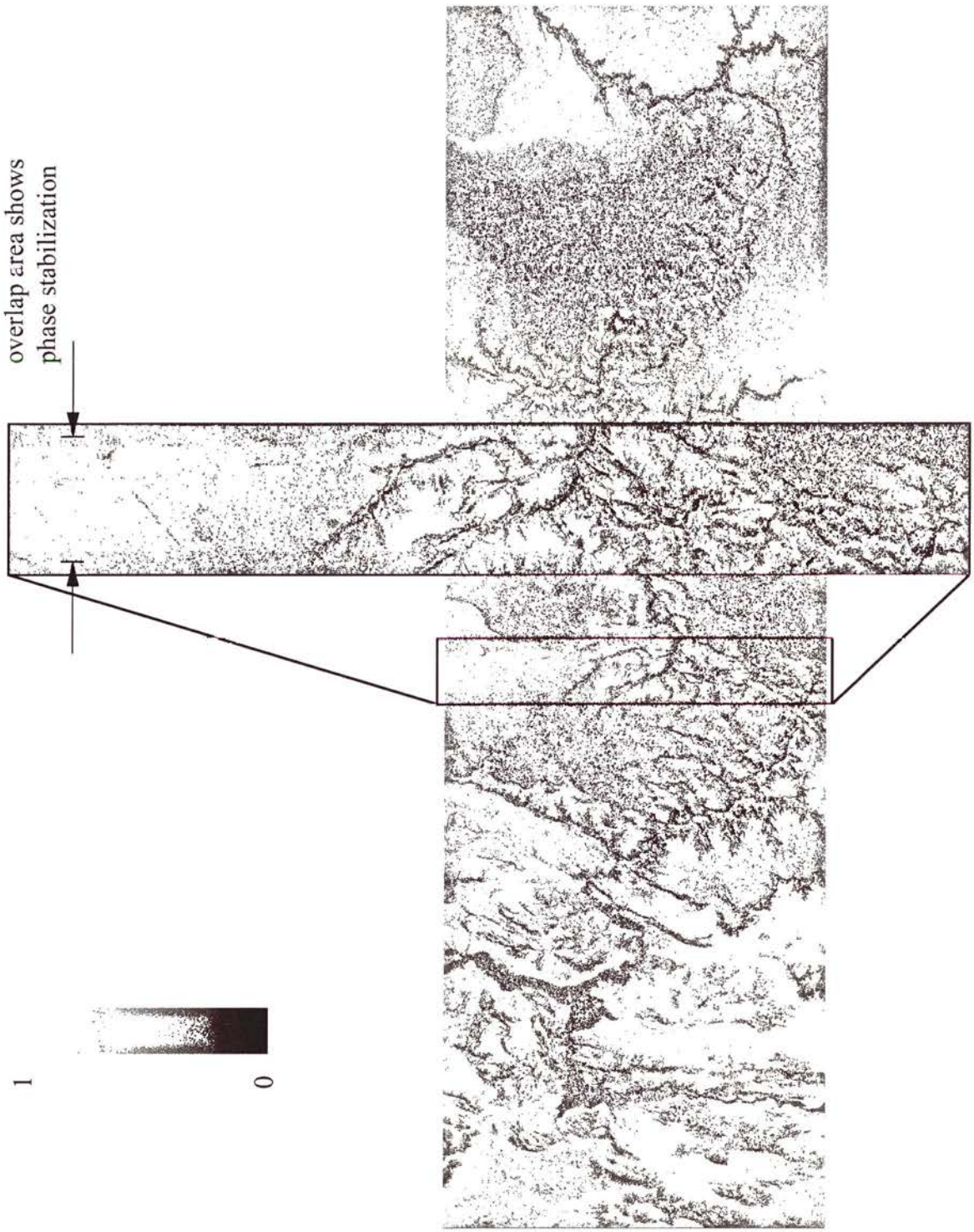

Figure 4.17: Stability of the complex interferogram phase. The phase stability increases (brighter values) in the beam overlap area.

4.2.8 Orbit Correction

Orbit information for the RADARSAT-1 spacecraft are only available at low accuracy (Rufenacht et al. 1997; Geudtner 2001). The along and circular across track accuracies amount to 100 m and 20 m, respectively (Rufenacht et al. 1997). Orbit errors show up in the difference phase (measured - simulated) as fringe pattern and disturb the final DEM result (Figure 4.18 a)). From the difference phase about 49 phase cycles over the full range can be observed resulting in a height ramp of about 6200 m over the full ground range extent of 350 km. To a first approximation, neglecting the effect of baseline length, this is equivalent to a baseline tilt of 0.0175 rad or 1°. The initial baseline configuration is specified within the depicted co-ordinate system by baseline length $B_0 = 167$ m and angle $\xi_0 = -159°$. Note that the phase distortion due to Doppler centroid variation is negligible. A maximum possible phase variation of about 0.3 cycles can be assumed for a given Doppler centroid variation of $\Delta f_{DC} = 4.5$ kHz (section 5.1) and an upper accuracy limit of $\sigma_\Delta \leq 0.1$ samples for the co-registration estimates incorporated in the azimuth resampling polynomials (section 4.2.1).

Orbit correction was carried out in two subsequent steps: timing correction of the master-slave orbit configuration and adjustment of the interferometric baseline.

Timing correction takes care of absolute positioning errors, i.e. orbit shifts in range and along track direction. Orbit timing correction is addressed first since the subsequent step of baseline estimation cannot account for overall shifts of the interferometer configuration, since within the process only the secondary channel orbit is corrected. Moreover, across track shifts introduce range phase ramps in the differential ScanSAR interferogram, since for the wide range extent the gross fringe frequency changes considerably (for the data set considered the fringe frequency varies from 0.23 cycles/sample in near range to 0.077 cycles/sample in far range.) Such phase ramps would distort the baseline estimation process and should be compensated beforehand.

Second, adjusting the baseline adapts the orbit parameter information in a way such that it fits to the measured interferogram phase. Accurate orbit parameters are important since the information is utilised for phase-to-height conversion and geocoding of the DEM. Errors in the orbit parameters would introduce height ramps and terrain scaling errors into the topographic data. These effects can be already observed in the differential or flattened interferogram phase as fringe pattern (Figure 4.18 a) and topography related phase errors. The

differential phase is a direct measure for the baseline or orbit data quality provided with the data set and is the basis for optimisation of the orbit parameters.

ScanSAR data with its wide swath width supports baseline estimation, since it limits the space of possible result vectors for baseline length B and angle ξ. Within the optimisation process, for several baseline length and angle parameters in the vicinity of the initial interferometer configuration (B_0, ξ_0), differential interferograms are calculated. The optimum is obtained when the differential phase is within a one or two phase cycles (atmospheric effects may have additional impact on the differential phase (Hanssen 1998).) For ScanSAR data this criterion must be met for a very wide range extent – representing about three times the ERS/ ENVISAT SAR range imaging extent –, thus, constituting a more rigorous constraint.

Orbit timing parameter correction for the master image was performed using a high quality DEM (DTED2, 25 m sampling grid,) since ground control points were not available. From the height information an interferogram phase was simulated and subtracted from the measured interferogram. In areas of rough topography, the difference phase contains fine structured misalignment errors. This effect may be applied to timing optimisation. As optimisation criterion serves the peak of the differential interferogram spectrum. For perfectly constant or linear phase the peak in the spectrum has a maximum. Any fluctuation however generates Fourier components at higher frequencies. This means when the phase is very smooth the spectrum is concentrated around the frequency representing the phase slope. The misalignment of the interferograms is minimum. Additionally, by allowing for a remaining linear phase in the differential interferogram, this method is independent with respect to existing orbit uncertainties or smooth atmospheric distortions. Several interferogram patches were used for optimisation and an overall optimum was obtained for shifts of 310 nsec in range and 4.87 msec in azimuth. Following the above discussion on phase ramps originating from timing shifts, the range shift – equivalent to about 4 range samples – reduced a phase ramp of 0.6 cycles over range equivalent to about 80 m over the full range extent of the data set.

a) differential phase and baseline configuration before orbit correction

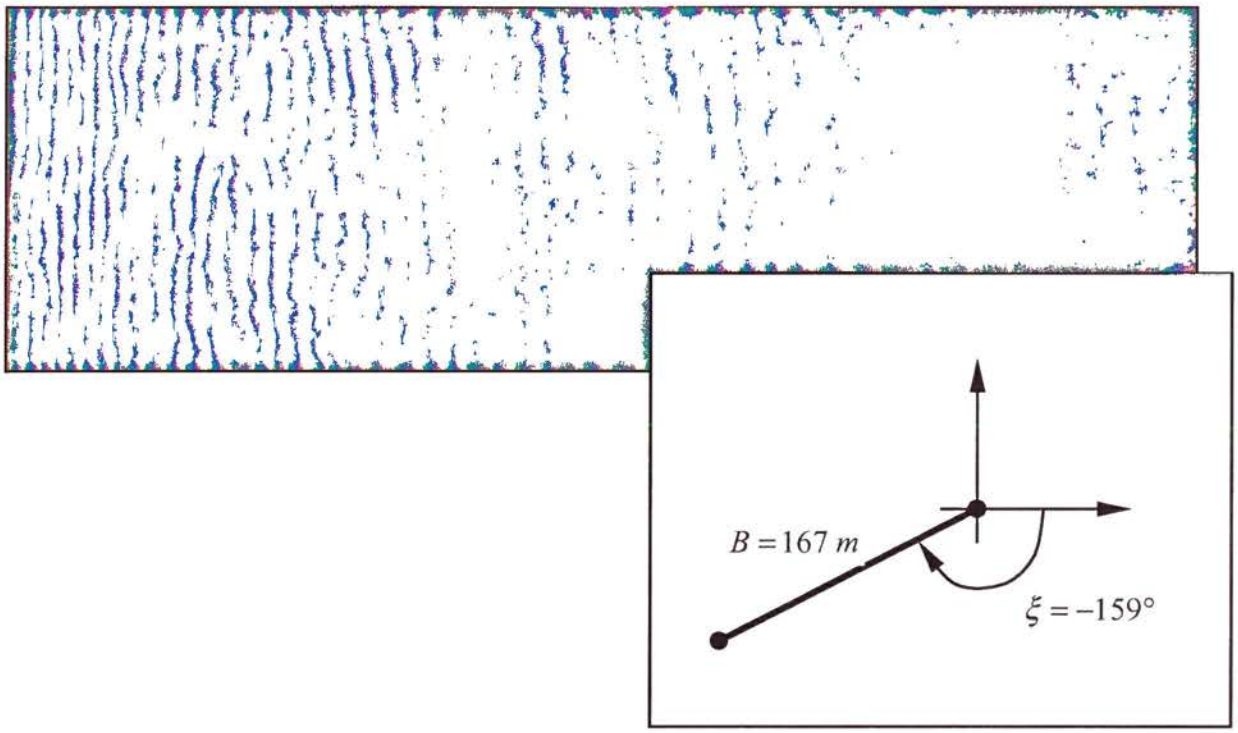

b) differential phase and baseline configuration after orbit correction

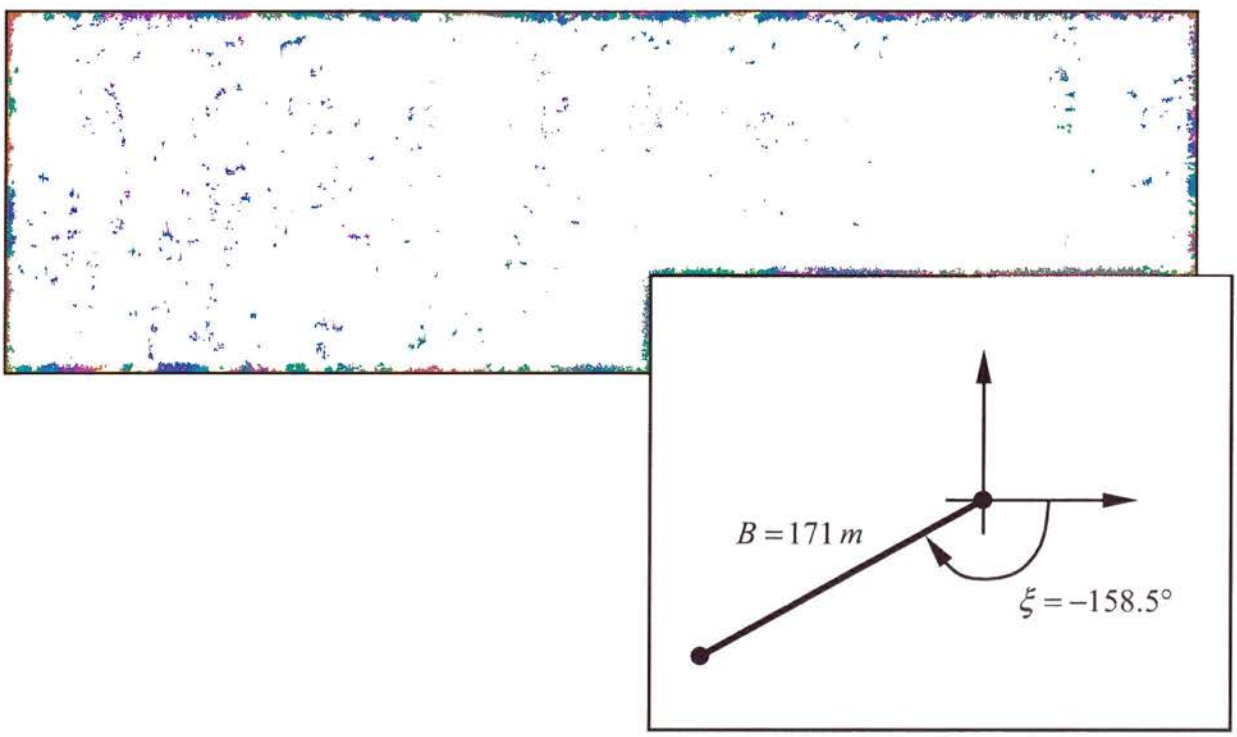

Figure 4.18: Difference phase and baseline configuration before a) and after b) baseline optimisation. The simulated phase was generated from a DTED-2 DEM.

Baseline adjustment was carried out before phase unwrapping due to the low overall coherence and severe topographic conditions (Grand Canyon and mountainous areas). For correction of the secondary channel (slave) orbit parameters a DTED-2 (25 m sampling grid) was utilised since ScanSAR interferometry is examined independently of the enormous RADARSAT-1 orbit errors. As described above, the deviation of simulated and measured interferogram was minimised, i.e. the overall residual range fringe frequency should become zero. For this reason, a matrix of differential phases was calculated for several combinations of $\Delta B = B - B_0$ and $\Delta\xi = \xi - \xi_0$ around the initial baseline configuration. Optimum baseline parameters were obtained by subsequent refinement of the sampling steps for ΔB and $\Delta\xi$ (zoom-in). This refinement process was carried out until no difference between neighbouring phase images was visible anymore. Thus, an error estimate of $\left(\Delta\hat{B}, \Delta\hat{\xi}\right) = (4.22\,\text{m}, 0.0075\,\text{rad})$ was chosen. Figure 4.18 b) illustrates the new orbit configuration and differential phase after baseline correction. Besides, this illustration suggests tropospheric phase effects which may be observed in the middle part of the differential interferogram (Goldstein 1995; Hanssen 1998).

4.3 Data and Processor Structures

This section discusses data structures and processing schemes for ScanSAR interferometry. First two basic burst-mode data or image structures are described that may be input into the interferometric ScanSAR processor. In a second part, two basic processing schemes are outlined that are derived from the discussed interferogram formation methods in section 3.2.2 and 3.2.3. An optimal processing procedure is then proposed combining the advantages of both basic processing options. In this way this section addresses the lack of interferometric ScanSAR and burst-mode products in the product lists of today's sensors and gives layouts for operational interferometric processors on the basis of the interferometric processing steps discussed in the preceding section. The descriptions allow to choose the interferometric processing scheme that may be readily integrated into existing strip-map processors.

4.3.1 Single Burst Images

Single burst images are complex SAR images from individual (raw data) bursts. The ScanSAR processing result or product is then the collection of all the burst images. Since each scatterer is represented by a bandwidth of W_B, a significantly lower azimuth sampling frequency may be used to represent the burst images (section 3.1.3). Allowing for an over-sampling factor of PRF/W_A – being the over-sampling factor of the equivalent strip-map data – the burst-image product azimuth sampling frequency is

$$PRF_n = \frac{W_B}{W_A} PRF \,. \qquad (4.21)$$

Representing the burst images at this sampling frequency results in a number of:

$$N_n = (T_A - T_B)\, PRF_n = \left(1 - \frac{T_B}{T_A}\right) T_B \; PRF \qquad (4.22)$$

range lines per burst image.

In case the burst duration T is sufficiently small with respect to the synthetic aperture time T_A, for the number of image lines the following relationship can be found:

$$N_n = \frac{T_A - T_B}{T_A} T_B \; PRF = \frac{T_P}{T_P} \frac{T_A - T_B}{T_A} T_B \; PRF \overset{T_B \ll T_A}{\approx} \frac{N_A}{N_S \; N_L} \qquad (4.23)$$

with N_S the number of swaths (or polarisation modes in case of ENVISAT/ASAR) and N the number of burst looks. Equation (4.23) shows that a burst image product (a set of several individual burst images) may be represented with the same data amount as a strip-map image if both image products have the same number of range samples.

As a result of the azimuth dependent bandpass characteristic of burst images (section 3.1.1) the burst-mode spectrum wraps several times within the available spectral band $\pm PRF_n/2$. Therefore, special algorithms are required for the interpolation steps (section 4.2.2) within the interferometric processing chain (see below).

4.3.2 Multiple Burst Images

A coherent superposition of the single burst images and, hence, providing multiple coherent burst images, is another possibility of supporting ScanSAR interferometry. With this option, only two complex images per swath have to be handled, visual browsing would be easier, and conventional interferometric processing modules may be applied since the average azimuth spectrum resembles the one of strip-map data (section 4.2.2). The complex image, however, shows a highly modulated point response (section 3.1.1). This point response has no impact on the final (detected) image or interferogram result as has been shown in (Bamler and Eineder 1996) and in section 3.2.3.

Since the strip-map data acquisition bandwidth W_A is used, the images have to be represented at the acquisition PRF. This excess sampling increases the amount of data input to the interferometric processor by a factor of $N_S = T_P/T_B$, the number of ScanSAR swaths. Formation of the multiple coherent burst images from single burst images represented at PRF_n requires interpolation (section 4.2.2) to $PRF \geq W_A$.

4.3.3 Interferometric Processor Structures

There are two basic processing structures for interferometric ScanSAR data according to the interferogram formation methods outlined in section 3.2.2 and 3.2.3. From these two known processing options a hybrid interferometric processor is presented incorporating the advantages of the single burst and multiple coherent burst interferogram formation options.

Table 4.1 gives an overview of the basic and hybrid variants available for burst-mode and ScanSAR processing. The options are evaluated with respect to the criteria: fast prototyping, data volume requirements, computational effort, use of existing components, support of ScanSAR interferometry applications, and the suitability towards operational demands. The criteria of ScanSAR interferometry refers to the ability of the processing system to process long data takes.

Figure 4.19 describes the processor following the single burst interferogram formation method (variant I in table 4.1). In this method, burst interferograms from each interferometric burst pair (single burst images as described above) are formed after common band filtering and co-registration. Swath interferograms are obtained by arranging and coherently multi-looking the burst interferograms. With the swath interferograms at hand further processing can be

conducted as described in section 4.2.7. The data amount input to the ScanSAR interferometric processor matches the one of strip-map data acquired at the same range bandwidth. However, the utilised interpolation (section 4.2.2) and common band filtering algorithms have to be adapted to the azimuth dependent bandpass behaviour of the data (section 4.2.4). Standard strip-map processing components can be used if each individual burst is oversampled to the acquisition PRF.

The second method is based on the multiple coherent burst interferogram formation method (figure 4.20, variant II in table 4.1). These images are then common band filtered and co-registered using standard strip-map algorithms (section 2.1.3). After swath interferogram formation, further processing can be conducted as described in section 4.2.7. The advantages of this processing option is the higher co-registration accuracy (section 4.2.1) and that standard interferometric processing modules for common band filtering, co-registration, and resampling may be applied. Disadvantages arise from the high amount of data input to the interferometric processor (section 4.3.2).

When both variants, I and II, are implemented using standard strip-map mode processing modules they may serve as a reference prototype towards operational system implementations.

An optimal interferometric processor comprising the low data space requirements of the single burst interferogram formation method and the co-registration accuracy of the multiple coherent burst interferogram formation method is described in the following (figure 4.21). After common band filtering, the co-registration parameters are estimated from one of the efficient techniques proposed in section 4.2.1. A suitable co-registration model is generated using the shift estimates (section 4.2.1) and the single bursts of the secondary channel are efficiently resampled (section 4.2.2) according to this model. Single burst interferogram formation and mosaicking is then implemented as for the single burst interferogram processor.

Therefore, variant III combines the low data space requirements of variant I with the high co-registration accuracy of variant II. Using dedicated burst-mode algorithms high throughput is obtained as required for operational system implementations.

The listed options refer to complex burst-mode images. If burst-mode or ScanSAR interferometry is conducted using raw data products, (azimuth) common band filtering and co-registration may be carried out by the SAR processor. Since ScanSAR is only operated on spaceborne systems, azimuth mis-registration properties will be very stable and, hence,

parameters may be obtained by trial processing small parts of the whole data set as was shown, for example, for ASPS (section 4.1.4).

For beam combination similar flexibility exists. The individual interferogram or DEM swaths may be either geo-coded individually or aligned in advance of further processing (section 4.2.7). In case the beams are geo-coded individually, existing standard mosaicking components may be applied. For orbit correction purposes the beams should reside on the same reference grid, then the beams may jointly contribute to optimisation as described approach in 4.2.8, since a mutual offset of the beam phases does not affect the algorithm result.

Table 4.1: Comparison of burst-mode and ScanSAR processing options.

Variant	I single burst	II multiple coherent burst	III hybrid
Processing Components	▪ Adapted standard processor ▪ Burst mosaicker ▪ Burst interpolator	▪ Adapted standard processor ▪ Burst mosaicker	▪ Burst mosaicker ▪ Burst interpolator ▪ Azimuth common band filtering ▪ Co-registration module
Fast Prototyping	+	++	-
Data Volume Requirements	++	--	++
Computational Effort	--	-	+
Use of Existing Components	+	++	-
Applications	+	-	++
Operational System	-	--	++

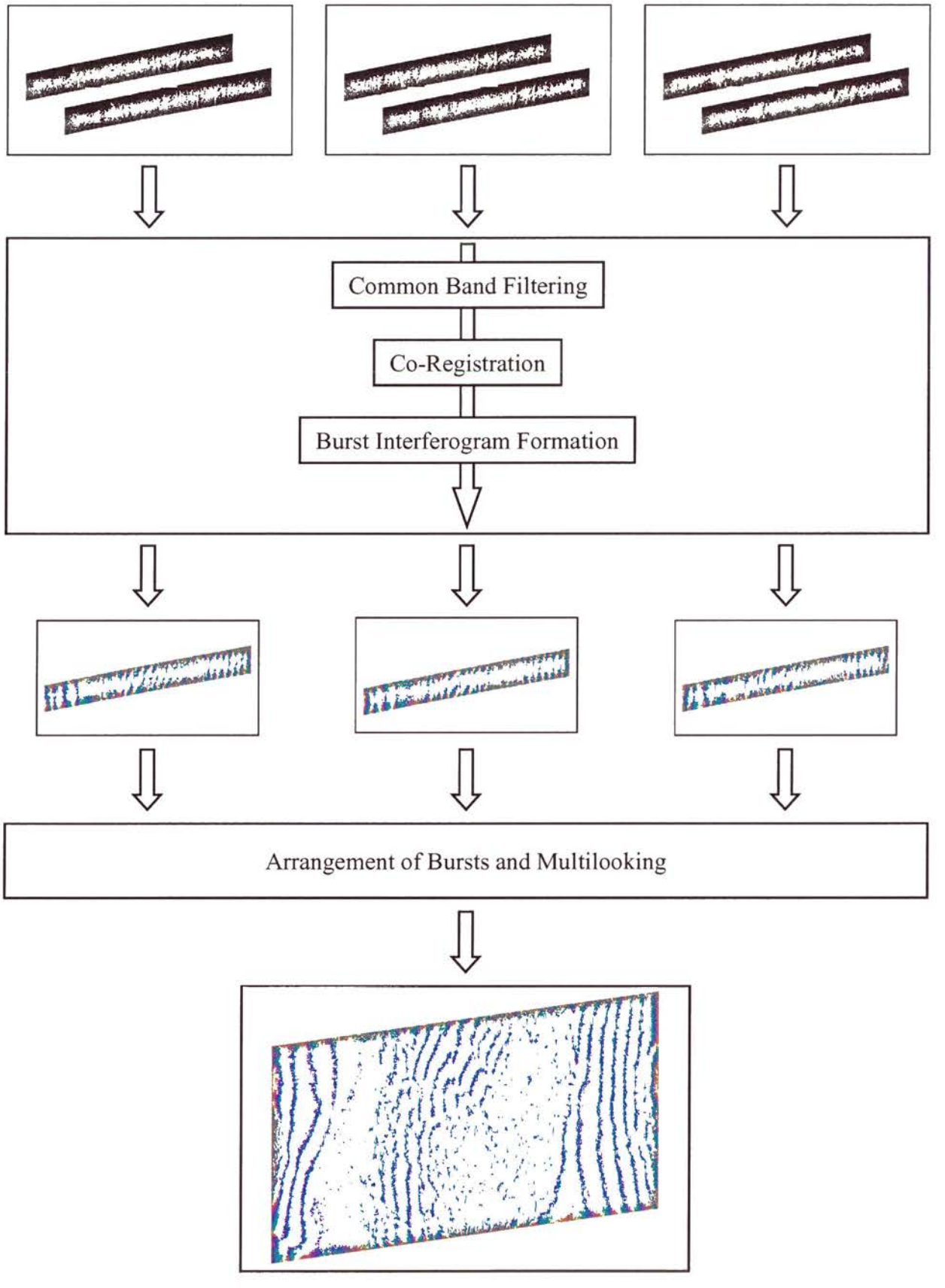

Figure 4.19: Single burst processing flow diagram.

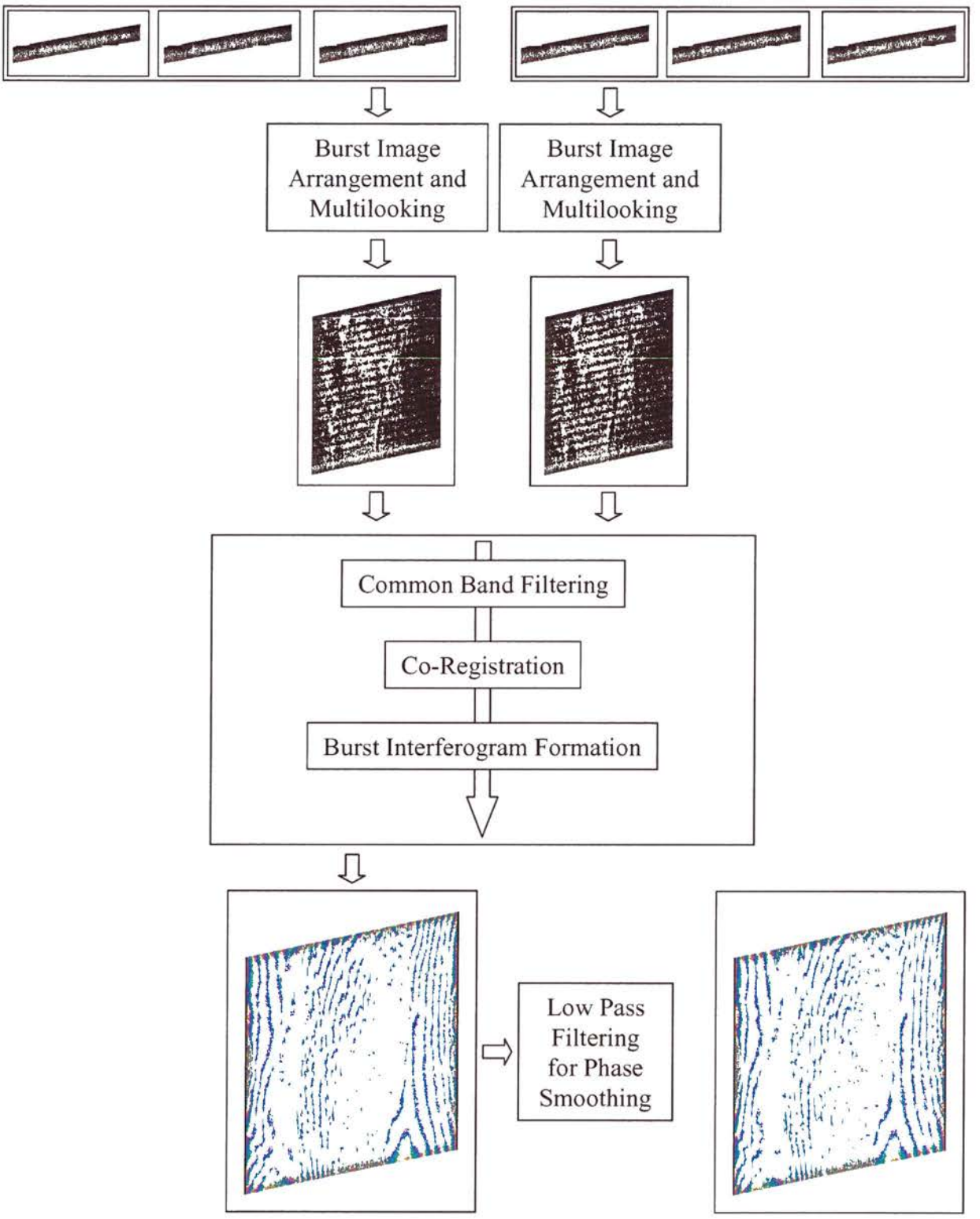

Figure 4.20: Multiple burst processing flow diagram.

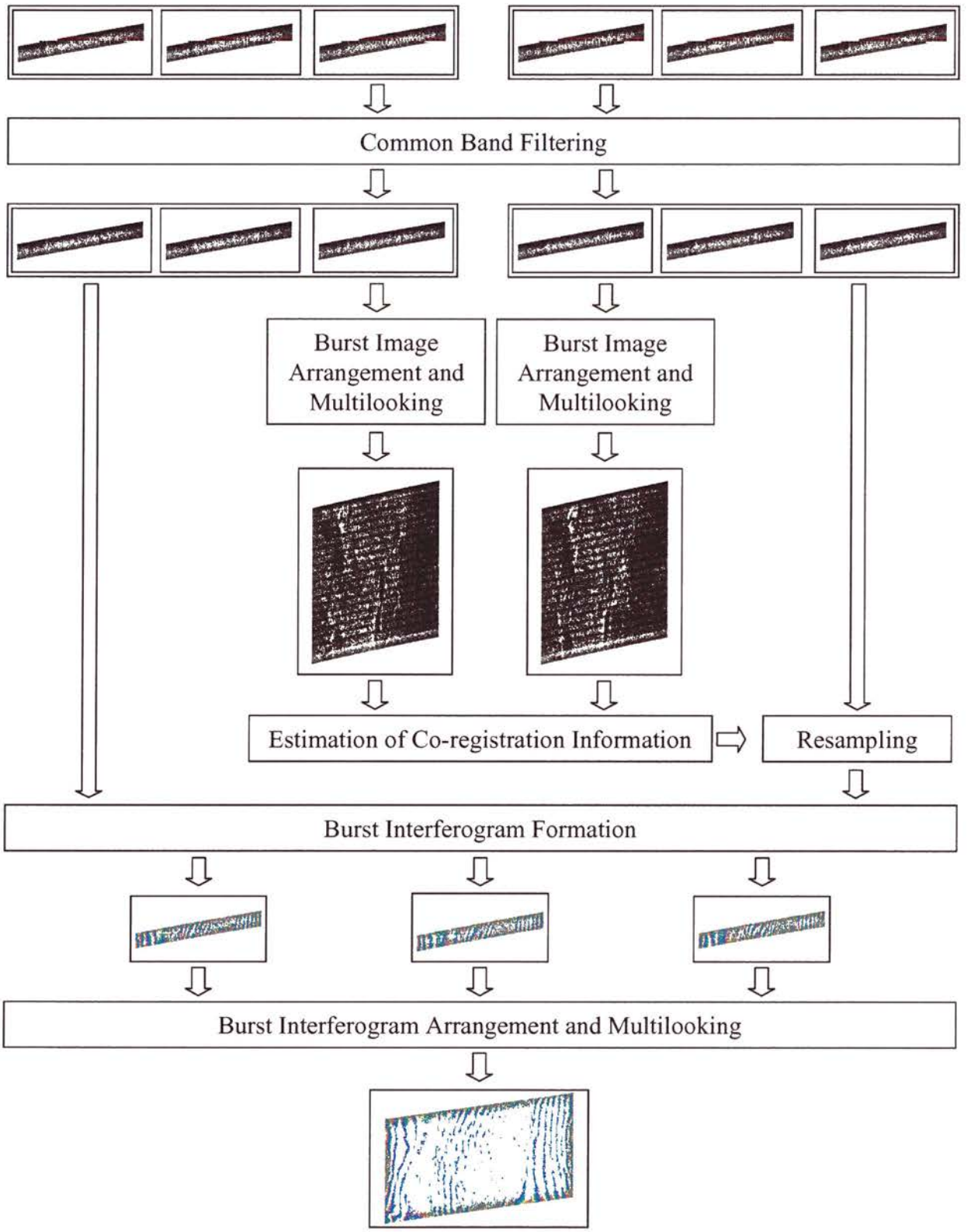

Figure 4.21: Proposed processing scheme flow diagram.

4.4 Summary

This section provided a complete overview of the individual processing steps required for interferometric burst-mode and ScanSAR processing including pre-processing of the data, retrieval of co-registration parameters, interpolation, common band filtering and azimuth spectral shift, and beam alignment. For the individual processing steps several algorithms were outlined and compared. Aspects of RADARSAT-1 interferometry comprised orbit correction and range spectrum shifts due to the very high Doppler centroid values. The aim of these algorithms is to maximise coherence taking into account the particular properties of burst-mode data. The result finally resembles a low-resolution strip-map interferogram.

Options to integrate these steps into efficient interferometric processors were provided. The advantages of the two basic burst-mode processors (single burst and multiple coherent burst) were synthesised into a third, hybrid processor. It combines the data volume efficient representation of the single burst processor and the unique co-registration properties of the multiple coherent burst data. The three burst-mode processing options were compared with respect to the major criteria: fast prototyping, data volume, and computational efficiency. Hence, the processor may be chosen that meets the requirements of the individual application, either scientific/ exploratory or operational/ high throughput. A prototype of the combined processor was implemented. Its test was the processing of the sample RADARSAT-1 ScanSAR Narrow data set to a digital elevation model as described in the next section.

For indeed, the most interesting experiments and observations were carefully designed by us in order to test our theories, especially our new theories.

- *Truth, Rationality, and the Growth of Scientific Knowledge (Popper 1963).*

Chapter 5

ScanSAR DEM Example

This part of the thesis describes the data set used and the remaining interferometric processing steps for generating a digital elevation model from ScanSAR data. The evaluation of the ScanSAR DEM includes a comparison to other available DEMs for the test site. For the processing of the data a prototype implementation of the optimal burst-mode processor as described in the last section was utilised. Thus, the results document the test of the proposed processing scheme and demonstrates the feasibility of repeat-pass ScanSAR interferometry for wide-swath topographic mapping.

5.1 Data set description

Among several strip-map modes the RADARSAT-1 SAR instrument provides four ScanSAR modes. These ScanSAR modes are grouped in 'ScanSAR Narrow' and 'ScanSAR Wide' with swath widths in the order of 300 km and 500 km, respectively. Each group has a near range and a far range configuration. The sample data set is a 'ScanSAR Narrow Near' mode (table 5.1). It is combined from two wide swath modes: W1 and W2 (Raney et al. 1991). The range bandwidth of the mode is 11.58 MHz, giving a critical baseline in the order of 600 m in contrast to the one of ERS which is in the order of 1100 m (figure 5.1). The resolution for the single look complex ScanSAR data set is in the order of 12 m x 40 m in slant range and azimuth respectively. After burst pattern synchronisation (section 4.1.4) only half of the burst echo lines remain and the resolution in azimuth reduces to about 70 m.

Acquisition requests for the RADARSAT-1 data were based on predicted orbit ground track drifts as provided from the Canadian Space Agency (CSA). An example equatorial ground track drift of RADARSAT-1 is shown in figure 5.2. The westward drift is in the order of ±4 km and at the most eastward positions orbit boosts (approximately every 35 days) keep the satellite within orbit specifications. Most favourable for ScanSAR interferometry are the positions around the drift maximum when the drift *rate* is minimum. Then baselines lower than the critical baseline can be expected within the 24 day repeat cycle (Armour et al. 1997; Geudtner 2001).

Based on definitive orbit information (Rufenacht et al. 1997) the data sets with the lowest baselines were chosen. Among the 12 ScanSAR interferometric data sets acquired, finally 2 data pairs remained with baselines lower than the critical one. For the thesis the data pairs with the higher azimuth scanning pattern overlap was chosen. Its parameters are listed in table 5.1. The test site is the area around Las Vegas (figure 5.3).

The land surface can be assumed temporally stable within the 24-day repeat-cycle of RADARSAT-1. However, snowfall and thunderstorms occur in autumn and winter. During the winter months temperatures may fall well below freezing point in the areas around the Grand Canyon and the Colorado Plateau.

Table 5.1: RADARSAT data set used for ScanSAR interferometry in the thesis. Variations from near to far range indicated by "...".

PARAMETER		MASTER DATASET	SLAVE DATASET
orbits		10969	11312
equator crossing direction		ascending	
acquisition dates		11-DEC-97	04-JAN-98
mode		SNA (ScanSAR - W1 + W2)	
incidence angle range	[deg]	20 ... 40	
range sampling frequency	[MHz]	12.93	
range bandwidth	[MHz]	11.58	
Doppler centroid fDC	[Hz]	-5000 ... -10000	
no. of bursts per aperture		2.5	
PRF (acquisition)	[Hz]	1298 / 1335	
PRF (after processing)	[Hz]	1335	
processed Doppler bandwidth	[Hz]	1000	
no. of range lines per burst before ...	[lines]	121 / 121	
... after ASPS	[lines]	64 / 63	
burst duration	[ms]	93/ 91	
burst bandwidth after ASPS	[Hz]	96 / 92	
burst cycle time	[s]	0.1839	
FM rate (mid swath)	[Hz/s]	-1950	
effective baseline	[m]	130 ... 83	
critical baseline	[m]	670 ... 1212	
height conversion factor (mid range)	[m/cycle]	64	

The imaged area is 100 km by 350 km large (section 4.2.7). It ranges from Lake Powell in the East to Las Vegas in the West and covers large parts of the Colorado Plateau. This test site covers a large range of topographic features, including flat to moderately rugged regions as well as very steep and mountainous terrain with the Grand Canyon and along Colorado River valley from Lake Mead towards the South.

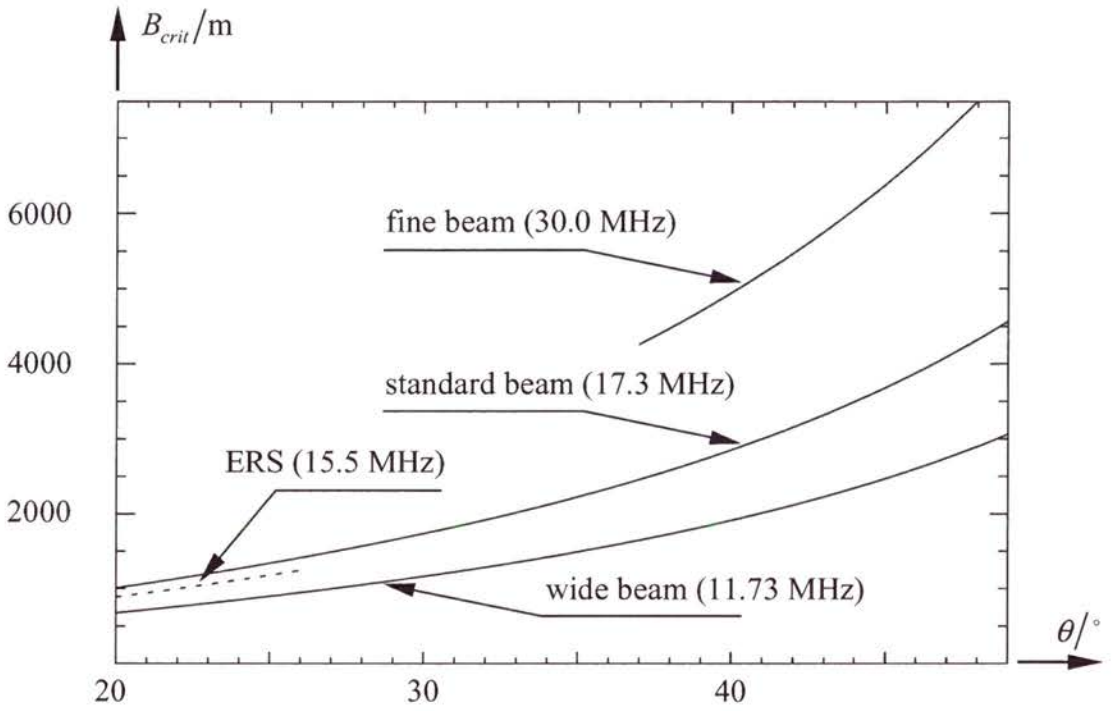

Figure 5.1: Critical baseline of different RADARSAT modes and ERS as a function of incidence angle. The bandwidths of the SAR modes are 11.73 MHz, 17.3 MHz, 30.0 MHz, and 15.5 MHz for wide, standard, fine beam mode, and ERS, respectively.

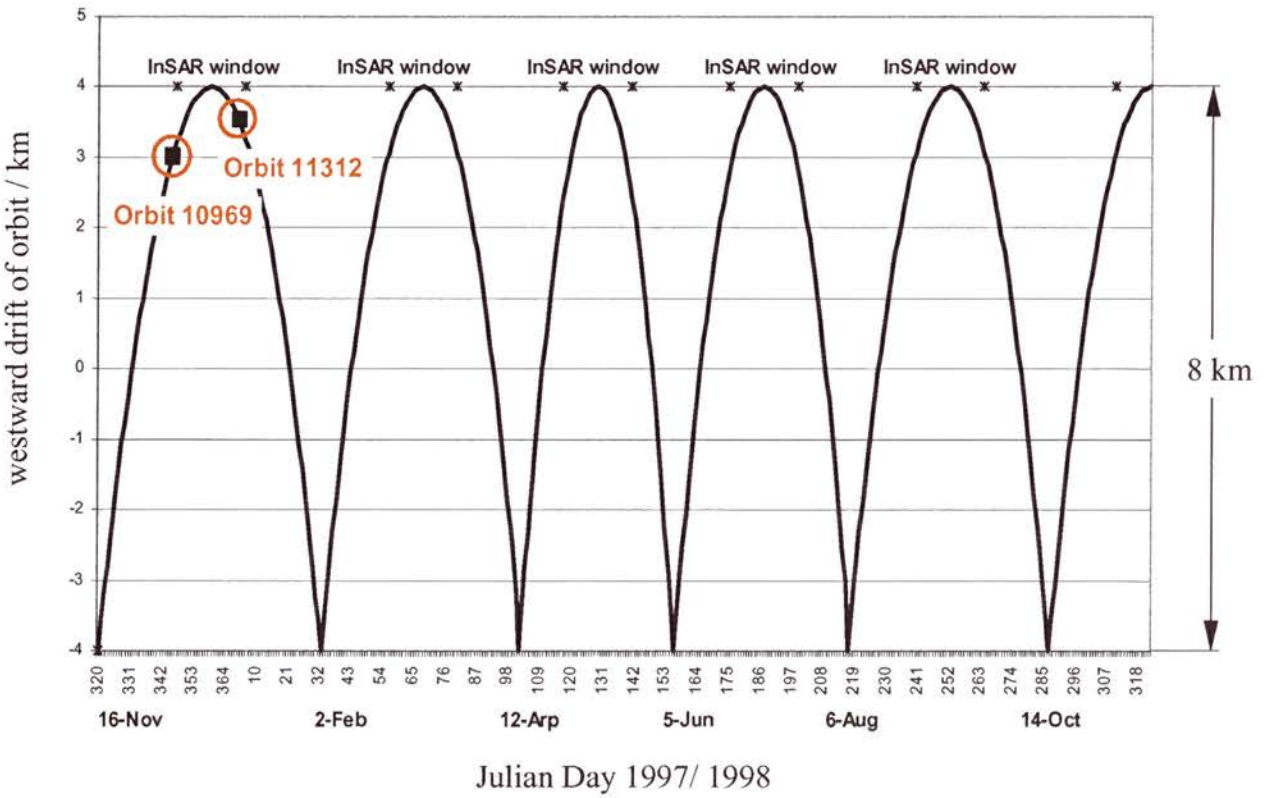

Figurre 5.2: The RADARSAT-1 orbit drift ranges ±4 km. Orbit boosts occuring approximately every 35 days at the east-most border keep the orbit within specifications. Data sets for interferometric evaluation are favourably acquired within the time frames indicated when the drift rate is minimum.

5.2 Interferometric processing and geocoding procedure

Interferometric processing for the RADARSAT-1 data was performed according to the single burst interferogram formation technique as described in section 4.3.3. This means each pair of companion bursts was spectral shift filtered (section 4.2.5) and co-registered (section 4.2.1) before the burst interferogram was formed (Eineder and Adam 1997). Then the individual burst interferograms were mosaicked (section 4.2.6) so that the two subswath interferograms were obtained. After careful beam alignment (section 4.2.7), the interferograms were combined and coherently added in the area of overlap. Orbit and baseline were optimised as outlined in section 4.2.8 and a simulated phase from the 1 km GLOBE DEM was subtracted from the interferogram. This flattening of the interferogram phase (Seymour and Cumming 1998; Seymour 1999) supports the subsequent processing steps. In particular, phase filtering and unwrapping benefit from reducing the number of topographic residues and phase gradients. The flattened phase was smoothed using a Gaussian low-pass filter. Its bandwidth was matched to the fringe frequency distribution of a representative area of the interferogram. Reduction of phase noise significantly improves unwrapping performance – quality and duration – of the applied minimum cost flow algorithm (Costantini 1997). The differential phase was then added to the simulated GLOBE phase and, finally, geocoding (Roth 1999) generated the ScanSAR DEM result.

5.3 Evaluation of the ScanSAR DEM

Figure 5.4 depicts the ScanSAR DEM result. Since the ScanSAR interferogram phase was flattened by GLOBE the result is expected to contain to some extent information from the coarse DEM. This effect is restricted to low coherence areas (dark in figure 4.14), i.e. regions of steep and rugged terrain slopes and parts of the signal where temporal decorrelation dominates interferometric phase information.

The result was compared to a high quality DTED-2 DEM (25 m grid) and found a local height standard deviation of about 3 to 5 m for flat terrain. This height error distribution agrees well with the expectations from coherence that varies from 0.72 to 0.85 in such regions. In areas of low and medium coherence height deviations increase to 20 m and in regions of layover, shadow, and temporal decorrelation the result is not expected to be better than the coarse reference DEM (GLOBE). Meteorological data suggests that the low coherence patches at mid and far range are due to snowfall and temperatures around freezing point.

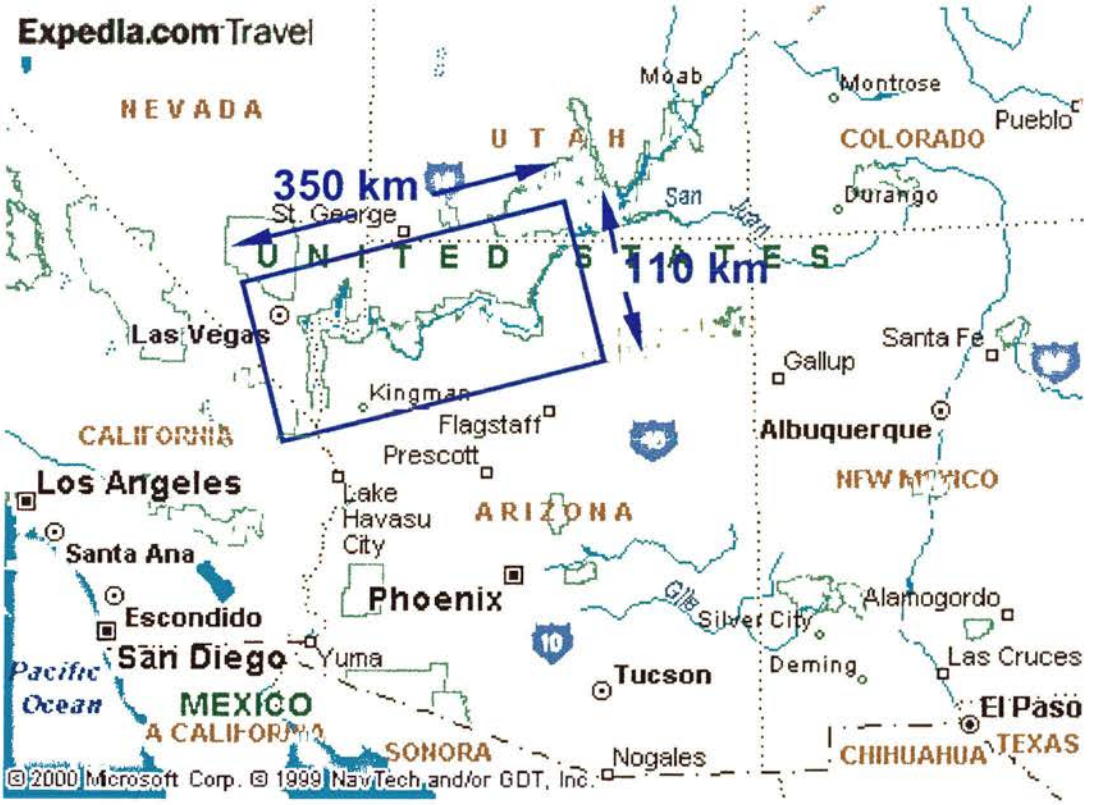

Figure 5.3: The covered area by the data set extends 350 km in eastward and 110 km in northward direction. It includes the city of Las Vegas, the Colorado river, and the Grand Canyon (map: © www.expedia.com/dayily/home/default.asp).

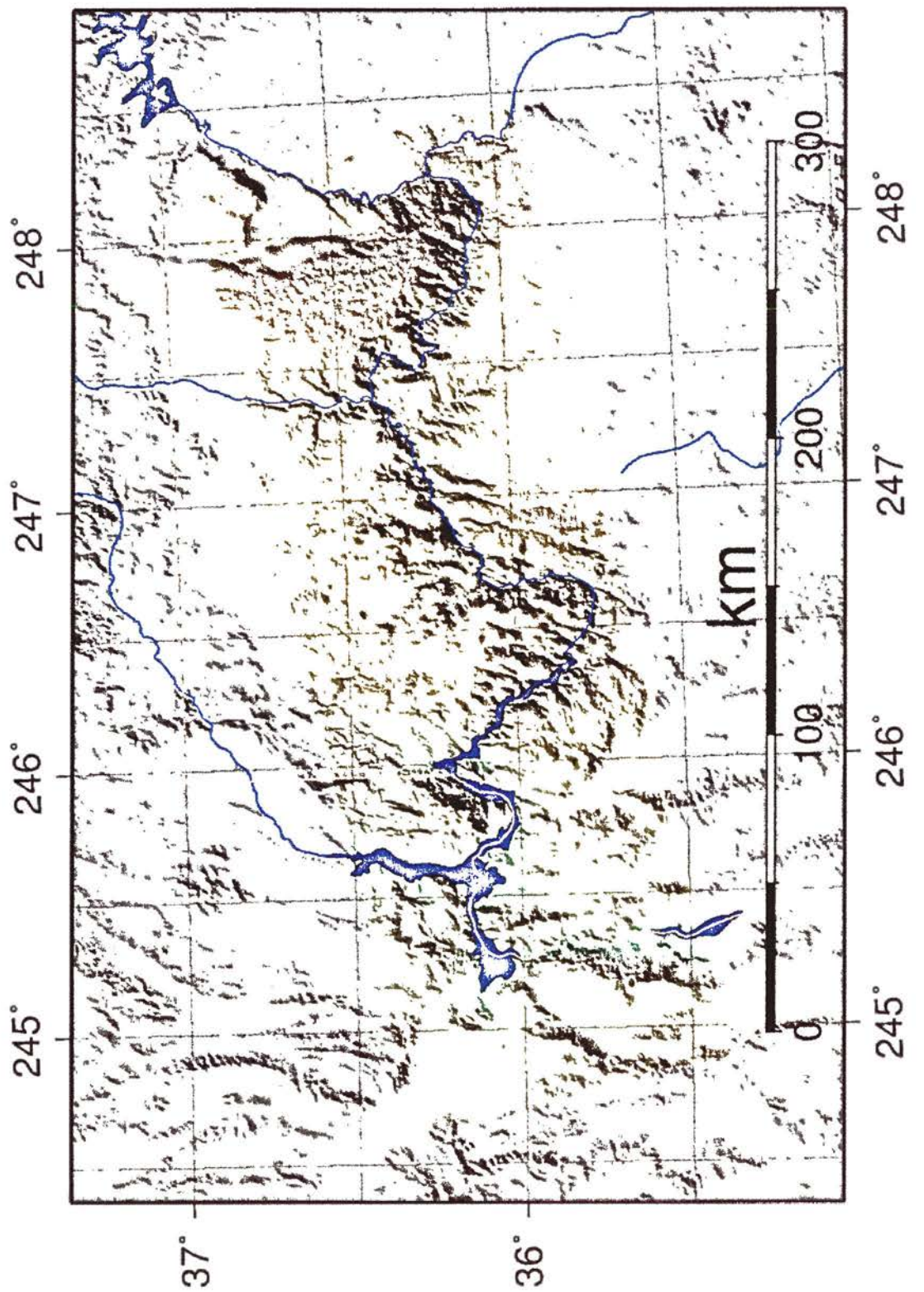

Figure 5.4: The resulting two-beam ScanSAR DEM covers an area of 350 km in range and 110 km in azimuth. Colored: ScanSAR DEM, grey: GLOBE DEM.

For further evaluation, the ScanSAR DEM was compared it to several other DEMs available for the test site. Figure 5.5 illustrates the various elevation data – GLOBE, DTED-1, and DTED-2 at sampling grids of 1 km, 100 m, and 25 m – available for the area. A patch covering 35 km × 35 km with heights ranging from 640 m to 1860 m (DTED-2) serves for the comparison. Simple visual inspection suggests that the ScanSAR DEM with nominal resolution of 75 m shows much more detail than the 100 m grid DTED-1 data. The ScanSAR DEM evidently improves the GLOBE data and even has the potential to add detail to the DTED-1 height information. For the area around Las Vegas, it is remarkable how distorted the DTED-1 data is.

In order to arrive at a quantitative statement on the resolution, the power spectra of the DEMs are compared. The individual DEMs' power spectra of the area depicted in figure 5.5 are illustrated in figure 5.6 in a double logarithmic diagram. From the illustration it can be found that for the three reference DEMs the power spectrum has an almost linear behaviour versus frequency. At some point this linearity is lost and a more or less fast drop-off is apparent. The kind of drop-off and the drop-off frequency depends on the type of DEM. For the GLOBE the drop-off is (as expected) at the lowest frequency, followed by the DTED-1 and the DTED-2. This result compares well with the visual comparison indicating that the DTED-2 has the best resolution or largest bandwidth compared to the other two DEMs. The form of the drop-off is also different for the individual DEMs. Whereas the DTED DEMs have an almost linear drop-off which only differ in slope, the GLOBE shows a curved fast drop-off. On the other hand, the DEM obtained from ScanSAR interferometry follows the linear behaviour as known from the reference DEMs, however, instead of a drop-off the spectrum forms a plateau for frequencies above 10^{-2} m^{-1}. For all of the DEMs it appears that for frequencies lower than 10^{-4} m^{-1} the slope differs from the slope of the second linear spectrum behaviour section for each DEM.

The linear behaviour of the terrain was explored before and commonly a $1/f$ or fractal model is assumed (Polidori 1991; Datcu et al. 1996). The above results for the various DEMs verify this model (The DEMs are probably obtained from three different sources where the GLOBE seems to be derived from any of the DTED DEMs.) Based on this model an interpretation of figure 5.6 with respect to resolution or 'detailed-ness' will be given. The $1/f$-line defined for frequencies above 10^{-4} m^{-1} serves as the reference line. The 'detailed-ness' or resolution of the reference DEMs is defined as the frequency where the power spectrum has departed by 3 dB

from the fractal model slope. In contrast, the ScanSAR DEM is evaluated differently (figure 5.7). It is assumed that for higher frequencies noise dominates the spectrum. The expected resolution (section 5.1) is 70 m, i.e. the DEM should contain terrain information to a resolution of $1/70 \approx 1.4 \cdot 10^{-2}$ m^{-1}. Figure 5.6 confirms this expectation.

Based on figure 5.6 and the described method a measure for the 'detailed-ness' or resolution for each individual DEM is obtained as indicated in the illustration. In addition, the nominal sample spacing is given. From the point of view of the spectral behaviour and the resolution measure as defined above, the ScanSAR DEM obviously exceeds the quality of DTED-1 and compares well with the DTED-2 DEM for frequencies lower than $3 \cdot 10^{-3}$ m^{-1}. Hence, the results from the power spectrum correspond well with the results from the visual inspection.

Figure 5.8 shows difference height histograms for an example area as illustrated. The histograms were obtained from the difference heights of the individual DEMs with respect to the DTED-2 serving as reference. For the GLOBE, a seemingly good result is obtained since the area contains sufficiently large areas of flat terrain. The histogram of the DTED-1 is bimodal suiting the artefacts observable from figure 5.5. For the ScanSAR DEM the deviations are in the order of the DTED-1 DEM. Together with the higher resolution it resembles more DTED-2 than DTED-1.

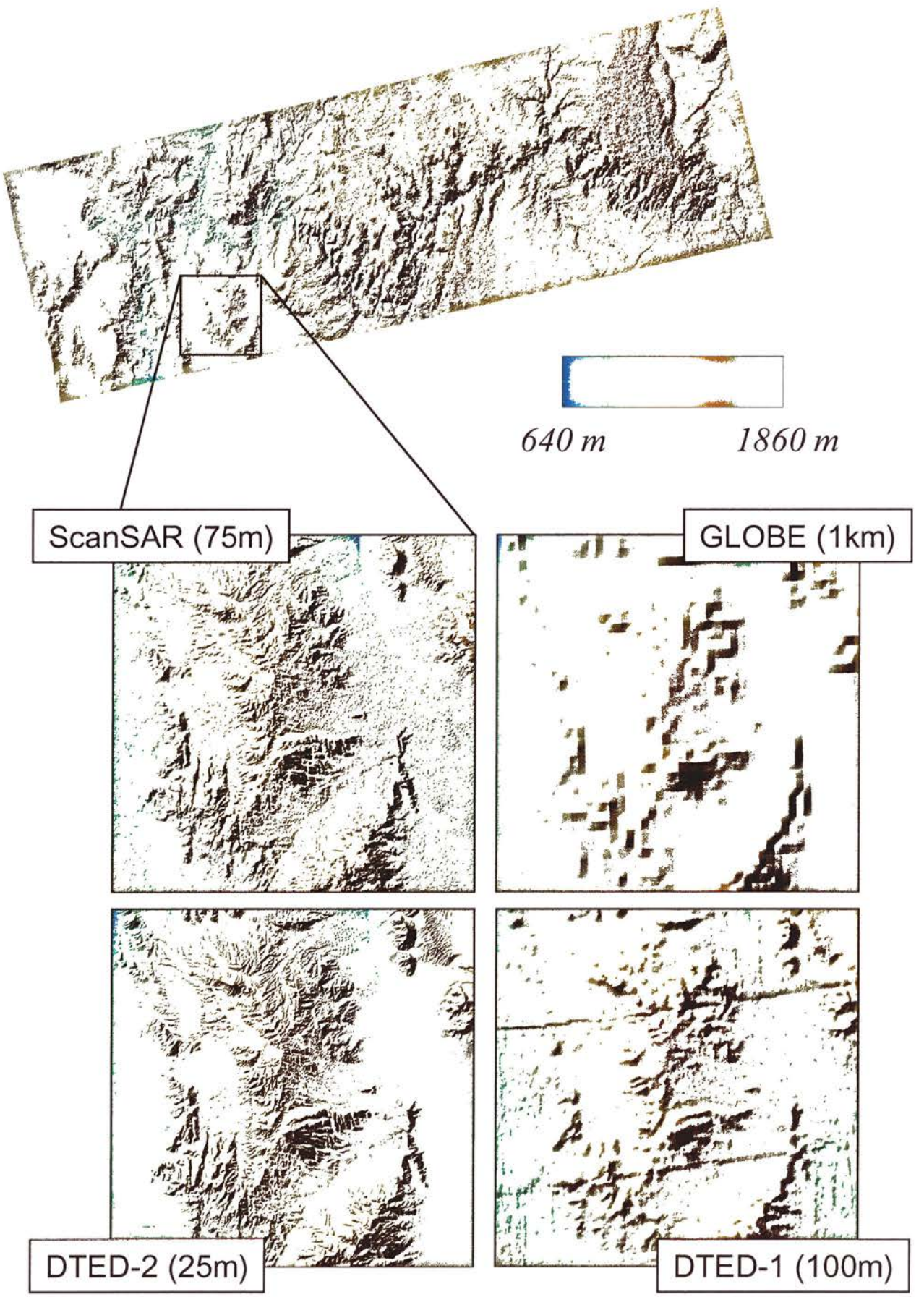

Figure 5.5: Comparison of different DEMs: GLOBE, DTED-1, DTED-2, and ScanSAR.

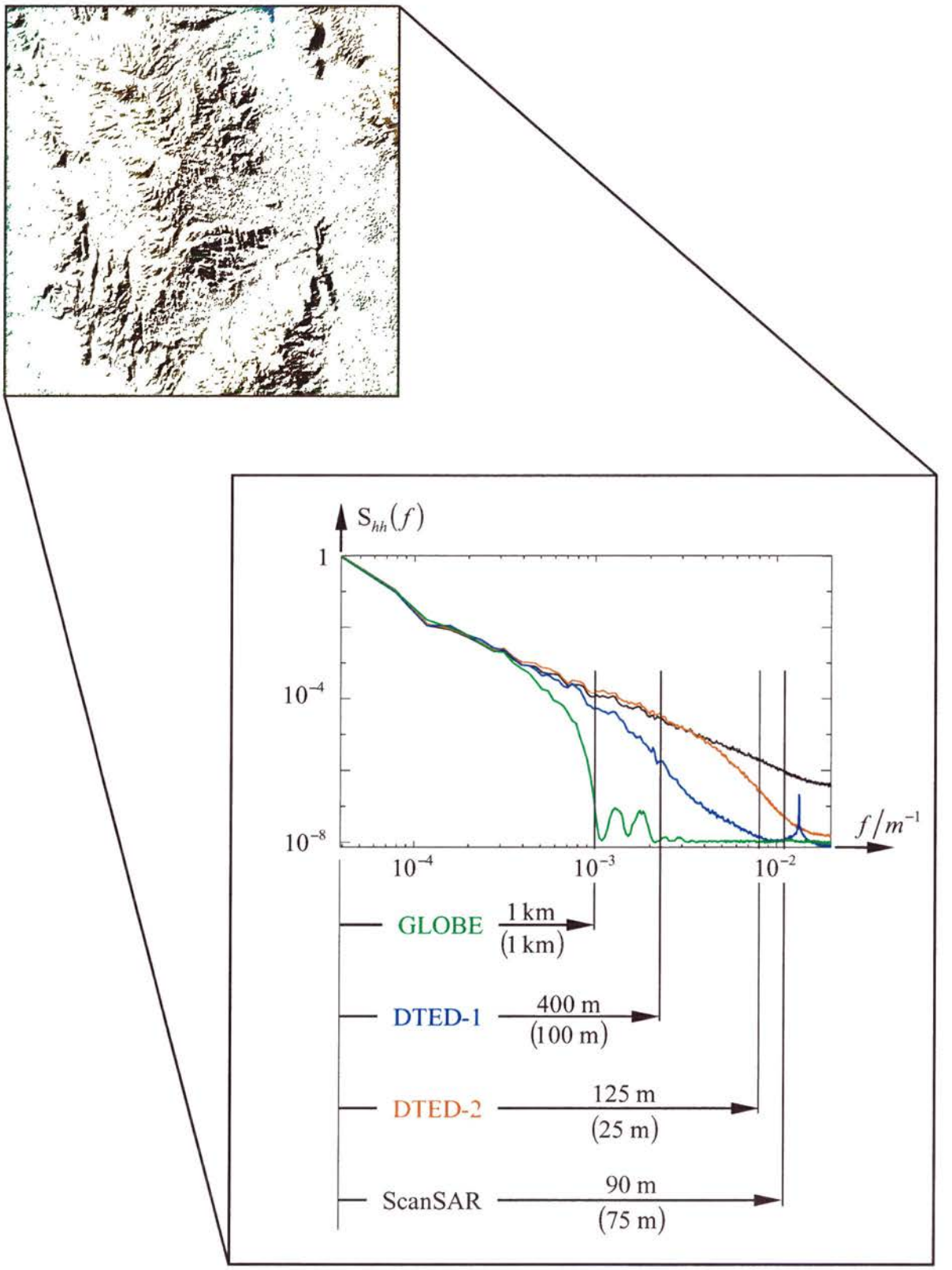

Figure 5.6: Power spectrum of the available DEMs in a double logarithmic diagram for the area illustrated in figure 5.5. The resolutions interpreted from the power spectra and the nominal resolutions (in brackets) are indicated.

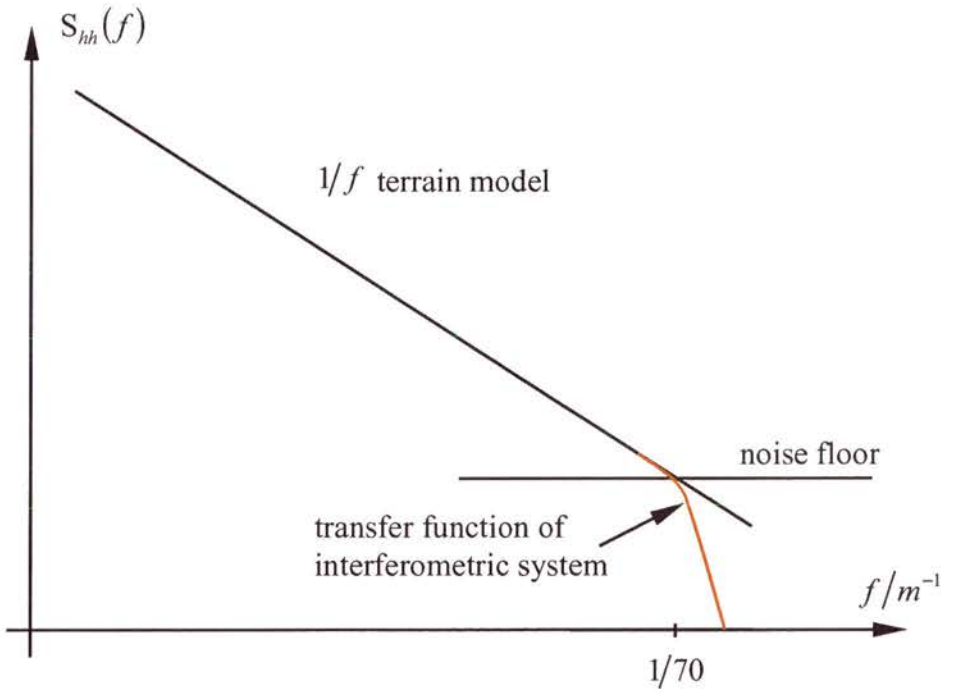

Figure 5.7: Expected behaviour of terrain power spectrum from SAR interferometry taking into account a 1/ f terrain model. The red line indicates the resolution of the DEM from ScanSAR interferometry.

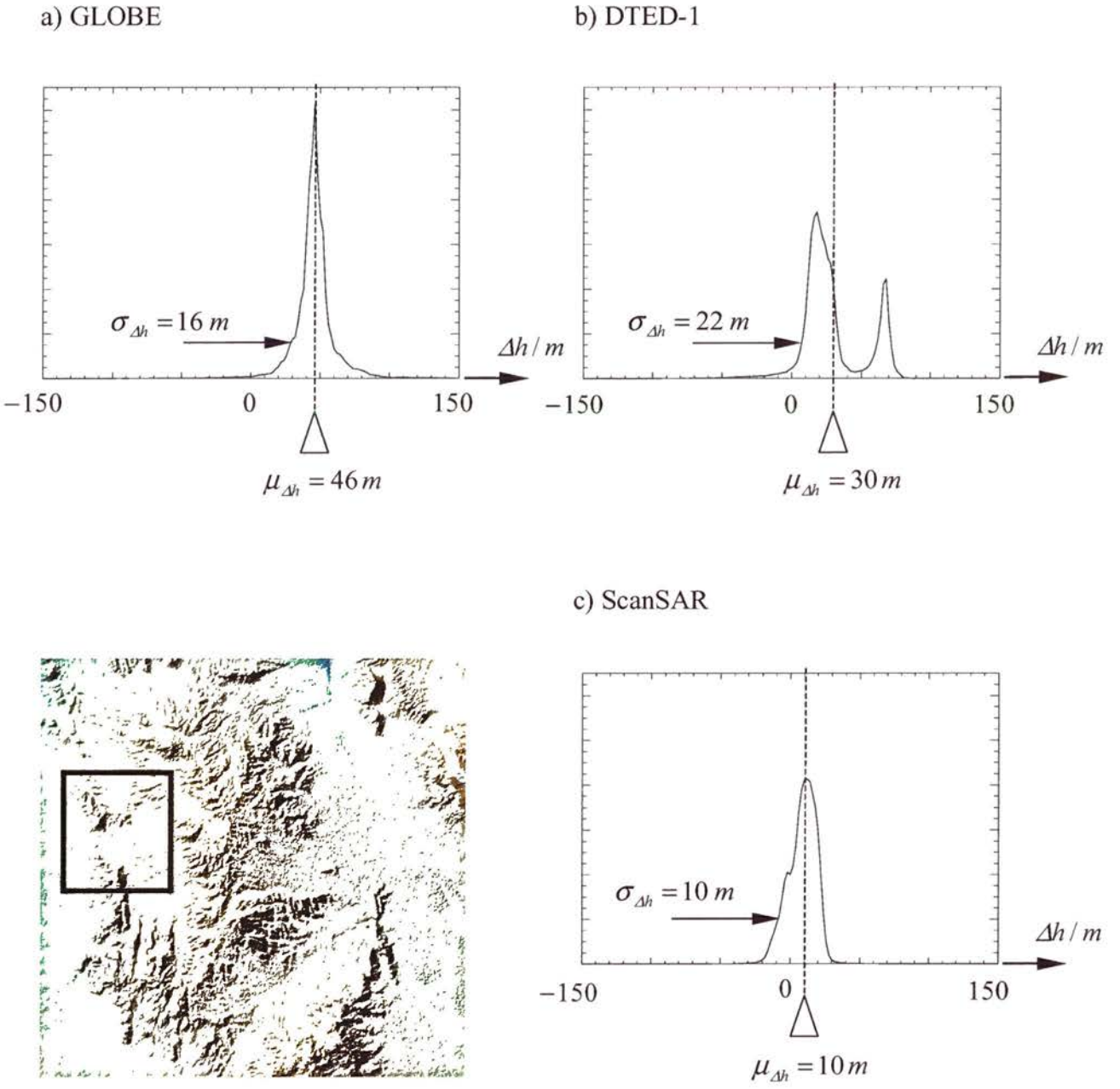

Figure 5.8: Histograms of the height differences a) GLOBE – DTED-2, b) DTED-1 – DTED-2, and c) ScanSAR – DTED-2.

5.4 Summary

This section comprised the remaining processing steps of the RADARSAT-1 ScanSAR Narrow data set and evaluation of the resulting ScanSAR DEM. After interferometric processing of the data set as described in the last section, an interferogram was obtained that resembles a wide area low resolution strip-map interferogram. Hence, for the further interferometric processing, i.e. interferogram flattening, filtering, and phase unwrapping, standard methods may be applied. Generation of the ScanSAR DEM also provided a test for the prototype processor proposed in the last section. The ScanSAR DEM result covers a ground range extent of 350 km at a resolution of approximately 75 m. High height accuracies may be obtained for moderate terrain and temporally stable areas. A comparison of several DEMs for the test site showed that the ScanSAR DEM has potential to improve the DTED-1 reference DEM.

The next section shows that ScanSAR and burst-mode data is available from all main current and future SAR missions. The next part of the thesis provides recommendations for the order and acquisition of interferometric ScanSAR and burst-mode data sets and takes the particularities of the signal into account.

... we ought not to aim at theories which are mere instruments for the exploration of facts, but we ought to try to find genuine explanatory theories: we should make genuine guesses about the structure of the world.

- Truth, Rationality, and the Growth of Scientific Knowledge (Popper 1963).

Chapter 6

Preconditions and Particularities for ScanSAR Interferometry

This section provides an overview over the conditions for the use of ScanSAR interferometry from a parameter, system, and mission point of view. First a range of sources of interferometric repeat-pass ScanSAR and burst-mode data is provided. It lists the main parameters for the RADARSAT-2/3, ENVISAT/ASAR, and the ALOS/PALSAR instruments. In the second part of this section recommendations are given related to the conditions for ScanSAR interferometry to work well and what improvements in ScanSAR system design will provide better conditions for this special type of SAR interferometry.

6.1 Current and Future ScanSAR Missions

The ScanSAR mode has become a standard mode on current and future missions (Table 6.1). It was first operated on the Canadian RADARSAT-1 mission (Raney et al. 1991) and is now followed by ENVISAT/ ASAR (Karnevi et al. 1994; ESA 1997). RADARSAT-2 operates the same modes as RADARSAT-1 and added some new modes and has, in contrast to RADARSAT-1, multi-polarisation capability (Brûlé and Baeggli 2002; Brûlé and Baeggli 2002). ENVISAT, however, operates not only ScanSAR modes for wide swath coverage but also has added a new burst-mode to its operation called alternating polarisation (AP) mode. In

contrast to ScanSAR, the antenna beam is not steered to swaths parallel to the first one but the polarisation is changed with each burst. In this way two polarisations are acquired in quasi-simultaneous fashion.

Both, the Canadian and the European mission, are operated in C-Band whereas the Japanese PALSAR instrument on board the ALOS satellite operates in L-Band (NASDA; Shimada et al. 2002). It will be launched in 2003 and will also provide 3 ScanSAR modes with 3, 4, and 5 beams (Frick et al. 2000).

6.2 Data Order Recommendations

6.2.1 Baseline and Range Bandwidth

ScanSAR interferometry requires short baselines as a result of the limited range bandwidth (Table 6.1, figure 5.1 in section 5, section 2.1.1). This bandwidth limit originates either from data rate requirements or from the intention to balance range and azimuth resolutions. Consequently, based on a priori orbit data, ScanSAR data pairs should be chosen with sufficiently small baselines. Basic parameters are the orbit repeatability of a specific mission, the range bandwidth of the individual ScanSAR modes and the resulting critical baseline, and predicted or actual orbit data (Table 6.1). For the orbit repeatability of RADARSAT-1 ±4 km is specified, however, for the Canadian Interferometric mission a requirement of ±1 km could be met (Mahmood et al. 2001). A similar situation will exist for RADARSAT-2, in (Brûlé and Baeggli 2002) an orbit repeatability of ±5 km is specified with the goal of ±1 km. In case of ENVISAT, a repeat orbit should be within a range of 1 km with respect to the first pass (ESA 1997).

For the example data set predicted orbit drifts and actual orbit data supplied by CSA were evaluated for ordering the data products (section 5.1). Data were required for the positions along the orbit were the drift rate is minimum (section 5.1, figure 5.2). Hence, baseline changes in-between the 24 day repeat cycle were also minimum.

A remarkable service was provide for the ERS data. Baseline information is available on the web (ESA) for ERS-1/2 tandem and for the following phases. Hopefully this baseline support will continue for ENVISAT (ESA 2002).

Table 6.1: Current and future missions operating ScanSAR modes. RADARSAT-2 operates the same ScanSAR modes as RADARSAT-1. Unknown information is indicated by '-'.

mission		RADARSAT-1		RADARSAT-2		ENVISAT-ASAR		ALOS-PALSAR
comments		In Operation		Launch in 2004		Launched March 2002		Launch in 2003
yaw steering		No		Yes		Yes		Selective
wavelength		C-Band				C-Band		L-Band
radar frequency	[GHz]	5.3		5.405		5.331		1.270
repeat cycle	[d]	24				35		46
orbit repeatability	[km]	± 4 (± 1 possible)		± 5 (± 1 goal)		± 1		-
modes		ScanSAR Narrow		ScanSAR Wide		Wide Swath	AP Mode **)	-
		A	B	A	B			
full coverage	[d]	6		12		-		-
range bandwidth	[MHz]	12				26-15 *)	16-8 *)	14 / 28
incidence angle range	[°]	20-40	31-47	20-49	20-47		18-39	18-43
swath width	[km]	300	300	500	450	400	100	250-350
resolution	[m]	50	50	100	100	150	30	100 (range)
critical baseline	[m]	600	1000	600	600	1300	800	2900/8900
number of beams/ looks (burst lines)		2 / 2 (120)	3 / 2 (100)	4 / 4 (40)	4 / 4 (40)	5 / 2 (50-80*))	2 ***)/ 2 (200-300 *))	3 to 5 / - (-)

*) swath dependent, personal communication with ESA

**) alternating polarisation mode

***) two polarisations

6.2.2 Burst Pattern Alignment

In order to have the azimuth ScanSAR image resolution also available for interferometry, the burst scanning patterns had to be synchronised at repeated acquisitions. For the example data set, half of the burst range echo lines have to be discarded (section 4.1.4) which corresponds to a burst pattern shift along the orbit of about 340 m (assuming a satellite velocity of $v_S = 7500$ m/s). In order to have at least 90 % of the burst lines available, a maximum mutual shift of 68 m corresponding to 9 ms of the burst patterns is required. All current missions do not allow such a synchronisation of the burst scanning patterns at repeated acquisitions and, hence, the available azimuth interferometric resolution is lower than the available SAR azimuth resolution. In order to maximise the probability of obtaining sufficient burst overlap, ScanSAR data sets with maximum duty cycle per beam are recommended, this means 2-beam 2-look burst- or ScanSAR modes should be preferred, e.g. the 300 km range 'ScanSAR Narrow A' mode Table 6.1. In this way the inter-burst pauses are smallest and the burst lengths still provide suitable interferometric azimuth resolutions even when a major part of the burst bandwidth has to be discarded.

From a mission point of view the burst pattern synchronisation can be realised by a latitude based start of the ScanSAR frames. This solution may be implemented using a GPS that can determine the latitude and longitude positions of the satellite to within millisecond accuracy when measured along the orbit.

6.2.3 Yaw Steering

Except for RADARSAT-1 all mission in Table 6.1 are yaw steered or may be operated in yaw steering mode. For these SAR data sources, the azimuth spectrum will mainly reside in the baseband which considerably facilitates interferometric processing as described in section 4.2. Due to lower Doppler centroids the phase errors originating from mis-registration are smaller which relaxes co-registration precision requirements. This allows to independently derive resampling polynomials for each individual swath in advance of beam alignment (sections 4.2.1 and 4.2.7). Since the Doppler centroid variation depends on the absolute value of the Doppler centroid, common band filtering and resampling become easier. In particular, the experienced range spectrum shift for RADARSAT-1 data is then negligible (section 4.2.5). Baseline estimation is supported since range varying phase errors as a result of mis-registrations do not mix with phase effects due to imprecise orbit data (section 4.2.8).

In addition, yaw steering of the instrument should provide sufficiently small Doppler centroid differences between repeated passes. Otherwise, the swath interferograms may not be contiguous after coherence maximisation by azimuth spectral shift filtering (section 4.2.4). The reason for this effect is the coupling of azimuth time and azimuth frequency as illustrated in figure 4.14. The more azimuth bandwidth is cut-off the less is the time extend of the individual burst. If the time extend corresponding to the remaining burst bandwidth is less than the burst cycle period then gaps occur in the swath interferogram. This additional condition for continuos interferometric mapping using ScanSAR or burst-modes should be checked for all repeat-pass instruments and modes, e.g. also for the alternating polarisation mode driven by ENVISAT/ ASAR.

6.3 Summary

This section outlined the profile of the ScanSAR and burst-modes on current and future satellite missions. The Canadian RADARSAT-1 and the European ENVISAT/ ASAR instrument are the current main sources for ScanSAR data. RADARSAT-1 provides 2-, 3-, and 4-beam ScanSAR modes covering ground ranges from 300 km to 500 km. From the instrument ENVISAT/ ASAR wide swath mode data covering 400 km and a multi-polarisation burst-mode, the so-called alternating polarisation mode, is available. In the near future, RADARSAT-2 and ALOS/ PALSAR will provide ScanSAR data. RADARSAT-2 will resemble the design of RADARSAT-1 with respect to the scanned mode. In contrast to the Canadian and European instruments, ALOS/ PALSAR is operated in L-Band and is planned to provide ScanSAR modes with swath widths of 250 km to 350 km.

The second part of this section gave recommendations for data order and acquisition, taking the special properties of burst-mode and ScanSAR data into account. Given a temporally stable test site, the main constraints are the baseline limit and the burst scanning pattern alignment. However, taking predicted orbit data for deriving expected baselines into account and choosing ScanSAR modes with large burst extends (e.g. the ScanSAR Narrow mode operated by RADARSAT-1) maximises the probability of obtaining interferometric ScanSAR data.

The conscious task before the scientist is always the solution of a problem through the construction of a theory which solves the problem; for example, by explaining unexpected and unexplained observations. Yet every worthwhile new theory raises new problems; problems of reconciliation, problems of how to conduct new and previously unthought-of observational tests. And it is mainly through the new problems which it raises that it is fruitful.

- *Truth, Rationality, and the Growth of Scientific Knowledge (Popper 1963).*

Chapter 7

Discussion and Conclusion

This thesis provides an exhaustive description of burst-mode and ScanSAR signal characteristics, algorithms for ScanSAR interferometric processing, and options for the efficient utilisation of the wide-swath data. Section 3 discussed the necessary theoretical background by providing expectation values for the coherence and power spectra of the interferometric burst-mode signals for non-zero mis-alignment and scanning pattern mis-alignment of the interferometric partners. The relationship between interferogram power spectral density and coherence was derived. Section 4 addressed all aspects of interferometric processing of RADARSAT-1 ScanSAR data including Doppler centroid estimation, azimuth scanning pattern synchronisation, common band filtering and resampling in the presence of high squint, beam alignment, and interferogram formation. A new fast time-variant interpolator for burst-mode data was implemented and tested which is the key module to the efficient processing of burst-mode data. Several processing options were described that are based on the flexibility of burst-mode and ScanSAR data. Based on the two known processing options, a hybrid processor prototype that is optimal from a data space and computational point of view was proposed and tested. The processing approach was evaluated by generating a digital elevation model from a RADARSAT-1 ScanSAR Narrow data set.

In this way, not only the processor was validated but also RADARSAT-1 repeat-pass ScanSAR interferometry was demonstrated. In section 5 it was found that the DEM produced from the RADARSAT-1 ScanSAR data set has quality better than DTED-1.

After interferometric processing the ScanSAR interferogram resembles a coarse resolution strip-map interferogram. Thus, existing procedures for baseline optimisation, interferogram filtering, and phase unwrapping can be applied. Interpretation of the resulting interferogram phase can then be conducted as for strip-map interferograms. From all the interferometric applications, those applications benefit that require wide swath extent, fast revisit times, or additional information, for example provided by the alternating polarisation mode, as on ENVISAT/ ASAR.

The following discussions outlines the original contributions of the thesis in detail and describes arising areas of future research.

7.1 Burst-mode Theory

7.1.1 ScanSAR Interferogram Expectations and Power Spectral Densities

In section 3.2 the interferogram power spectral densities for single and multiple coherent look burst-mode signals were derived. During this process the key step was to find the autocorrelation function (ACF) for burst-mode data. The ACF may be approximated using the ScanSAR impulse response for both the single burst technique and the multiple burst interferogram formation options. Thus, within this present study the approximate analytical derivation of the ScanSAR interferogram power spectral density (PSD) was possible. In studying the properties of the interferogram expectation values and of the power spectral density, several properties of ScanSAR interferograms became evident that cannot be observed in strip-map interferograms. Approaching the interferometric signal characterisation with the methodology developed in this study provided not only qualitative but also quantitative insights into the properties of interferometric burst-mode signals that are either new or had only been published using different, less holistic, approaches. Among these are the co-registration properties of ScanSAR data, the interferogram properties in the case of existing asynchronous scanning patterns, and the properties for the case of non-zero fringe frequency. In examining the single burst interferograms first, the properties of multiple coherent burst interferograms could be inferred analogously. Only for the case of mis-registration significant deviations between single and multiple coherent burst interferogram

signal characteristics were found. The solution to the problem of proving the equivalence of the two basic interferometric processing options was finally found by suitably normalising the signal ACFs (section 3.2.3).

7.1.2 Relationship of Coherence and Interferogram Spectrum

Analysing the properties of the strip-map mode and burst-mode interferograms yielded a to my knowledge new relationship between interferogram power spectral density and coherence (section 3.2.1). In essence, the power spectral density of an interferogram consists of a spectral line and a pedestal with a form which depends on the SAR signal spectral weighting window. The ratio between the mass of the spectral line and the integral of the pedestal (component of the power spectrum that is generated by cross-correlation of the power spectra of the individual SAR signals) provides a measure of the coherence of the interferometric signal, that is, the phase stability of the interferogram. Thus, implying that conclusions can be drawn from the power spectral density of the interferometric signal with respect to the first order phase statistics of the interferogram. This conclusion promises to directly relate the physical properties of the interferometer (strip-map, burst-mode, Spotlight), represented by its interferogram power spectrum, to the phase statistics of the interferogram.

7.2 Burst-mode and ScanSAR Data Properties and Processing Algorithms

The flexibility of burst-mode and ScanSAR data allows the development of efficient algorithms for their processing. A complete overview of the available range of processing methods is given in section 4.2. In particular, this section includes contributions and detailed discussions on burst-mode data co-registration, resampling, beam alignment, and the selection of a suitable processing concept for burst-mode and ScanSAR data.

7.2.1 Revision of Standard SAR Interferometry Assumptions

ERS, with its well maintained orbit and precise orbit information, its operation in yaw steering mode, and its swath width of 100 km, allowed for several assumptions leading to the rapid development of SAR interferometry and the opening up for its wide use for the retrieval of bio- and geophysical parameters and the monitoring of long term effects (e.g. topographic reconstruction and subsidence monitoring using the permanent scatterers technique). However, these assumptions are no longer valid for RADARSAT-1 repeat-pass interferometry: there is no yaw steering and orbit maintenance is poor. (Geudtner 2001)

reported that, as a result of the high Doppler centroids, a range spectrum centre offset occurs that requires the adaptation of existing resampling and spectral shift filtering implementations so far applied to ERS interferometry (see also section 4.2.5). For RADARSAT-1 ScanSAR interferometry another difficulty arises. During the processing of this study's ScanSAR Narrow data set, significant variations of the Doppler centroid (section 4.1.2) and of the gross range fringe frequency (section 4.2.4) became evident. This problem was tackled by extending the interpolation and spectral shift filtering operations. Range varying filters were applied to both signal processing steps in order to adapt to the particular signal characteristics.

7.2.2 Co-registration

There are several possible options for co-registering burst-mode data depending on the interferometric processing approach utilised (sections 3.2.2, 3.2.3, 4.3.1, and 4.3.2). For the co-registration of burst-mode data it seems, however, to be most efficient – from a data volume and computational complexity point of view – to combine multiple burst looks within small estimation windows before shift estimation via cross-correlation. A similar level of efficiency may be obtained by the spectral diversity approach (Scheiber and Moreira 2000) after averaging sufficiently large number of samples in order to obtain shift estimates at the desired precision.

The use of geometrical parameters enabled the robust co-registration of the data sets which is particularly difficult under low coherence conditions. Given such circumstances the resampling polynomials tend to be less reliable at the edges of the image. A comparison of the correlation measurements and geometrically derived resampling polynomials allowed the combination of different sources of data for improved co-registration performance (section 4.2.1). This approach has additionally allowed the co-registration of the SRTM/ X-band data using only geometric information, since the orbit is known with millimetre precision (Holzner et al. 2001). The measured offset between the geometrically derived resampling model and cross-correlation data indicates mutual orbit errors of the primary and secondary satellite in line of sight. Hence, the offset may be used as an estimate for baseline errors of the considered orbits.

7.2.3 Resampling

Complex strip-map SAR images are bandpass excerpts around the Doppler centroid frequency. The Doppler centroid is relatively stable over the azimuth scene extent for space-

borne systems and can be assumed to be constant. Hence, during resampling the (baseband) interpolation kernel is readily adapted to the bandpass character of the signal by application of a linear phase ramp with slope constant over the whole azimuth extent. This approach may also be applied to burst-mode data represented at the acquisition *PRF* (section 3.1.3 and 4.2.2).

The ability to resample burst-mode images represented at their Nyquist sampling frequency (section 3.1.3) is essential for the design of efficient and operational burst-mode processing systems (section 4.3). In addition, if standard interferometric processing modules are to be adopted, an efficient resampling module is a key processing step (see section 4.3). Several resampling options are available for burst-mode data. In section 4.2.2 a new algorithm was described, implemented, and tested using real data. This algorithm has been first described in (Holzner and Bamler 2001). It deramps the burst data in advance of applying existing resampling kernels and, thereafter, reramping the signal so that the azimuth time variant bandpass character is re-established. This study showed that it performs well in all relevant tests, it was easily implemented compared to linear azimuth variant bandpass filters, and was found to be computationally very efficient. Due to the bandpass characteristics of Spotlight data (Mittermayer 2000; Lanari et al. 2001) it is also a candidate for the interpolation of Spotlight mode data for Spotlight SAR interferometry.

7.2.4 Beam Alignment, Timing and Baseline Optimisation

ScanSAR imagery is usually represented as a single product, possibly geo-coded, spanning 300 km to 500 km ground range extent (RSI 1995). However, during the interferometric processing the beams are individually accessible. They may be either geocoded individually or combined before further evaluation. In the case of ScanSAR interferometry, geocoding of the individual beams (e.g. DEM generation or geocoding of differential phases for subsidence monitoring) prevents the analysis of the beam overlap which is sensitive to phase errors (section 4.2.7). Combination of the beams in a geo-referenced co-ordinated system may be easier, since existing modules for mosaicking can be applied. All new generation satellite sensors (section 6.1) will be yaw steered and hence phase errors as a result of mis-alignment are expected to be lower and, as a result, beam alignment would be easier. Mutual range mis-registrations of the swaths may be circumvented by adjusting the electronic delay offsets during a preceding calibration phase and the joint use of both beams for baseline optimisation allows accurate orbit and timing verification (section 4.2.8). If a baseline optimisation

approach resembling the one in section 4.2.8 is chosen, mutual phase offsets of the beams have no impact on the baseline estimation result after timing optimisation. Which option is finally chosen also depends on the application requirements (required baseline and timing precision, co-ordinate system, and geo-coding procedure), data volume requirements, and available standard components for baseline estimation and mosaicking of geocoded products.

In ScanSAR imaging the beam overlap area is analysed for image calibration and parameter estimation (Luscombe 1993; Hawkins et al. 2001). In ScanSAR interferometry and interferometric processing, the examination of the beam overlap provides valuable information on the mutual relationship of the subswath interferograms. The examination of the possible phase errors (section 4.2.8) identified two effects. Phase errors originating from remaining tiny mis-registrations in range and azimuth introduce phase errors into the individual beam interferograms. Secondly, mutual mis-alignments of the beam interferograms introduce significant phase errors as a result of the gross range fringe frequency. The main contributions originate from the gross range fringe frequency, the Doppler centroid, and off-zero centre frequency of the range spectrum. Topography correlated errors appear when the interferograms are mutually mis-registered. These effects may allow conclusions as to the remaining mis-registrations components within and across the individual beams. Additional information on beam-alignment is obtained by amplitude cross-correlation in high contrast areas (rough terrain, man made features, cities) within the beam overlap.

During the course of timing optimisation (section 4.2.8) and beam alignment, a very useful method for co-registration was applied. It is based on the previously described correlation of the differential interferogram phase with topography in the case of a mutual mis-alignment. If this effect is minimised, optimal alignment of two given interferograms can be assumed. A suitable measure for the alignment of the interferograms is the spectral line of the differential interferogram in rough terrain. When there is little or no mutual shift, the terrain effect will be minimal and, hence, the peak will be at a maximum; the signal's energy is concentrated within one spectral line. Thus, this approach may also be applied to co-register two SAR interferograms when they contain areas of highly modulating or fine structured topography, indicating mutual mis-registrations as fine structure. A similar approach and interpretation of the differential interferogram's spectrum was described by (Seymour 1999). (Seymour and Cumming 1998) applied the same approach to co-register a DEM in slant-range geometry with respect to the SAR imagery used. Coherence or the cross-correlation coefficient was chosen to optimise the DEM-to-interferogram co-registration and baseline. In order to

investigate the equivalence of coherence and the maximum interferogram spectral peak method, the relationship derived in appendix A6 between cross-correlation function and interferogram spectral peak is of importance. However, the application to co-registration of two measured interferograms was not made explicit in the (Seymour and Cumming 1998) study.

7.2.5 Selection of the Suitable Interferometric Processing Concept

Two processing schemes were described that build up the basic processing schemes for ScanSAR data. The single burst interferogram formation option comprises the formation of interferograms from the individual burst images. The multiple coherent burst interferogram technique coherently arranges and superimposes the single burst images so that swath SAR images are obtained. The interferogram is formed from these swath burst-mode images. The single burst interferogram processing option is optimal with respect to its data volume requirements. However, examining burst-mode signal properties showed that the multiple coherent interferogram formation option has significant advantages for the co-registration of the interferometric signals. This study then went one step further by combining both methods to a new hybrid processing scheme proposed in section 4.3.3. It is primarily based on the single burst interferogram formation option for the data space efficient representation of the signals and temporarily forms coherent multiple burst-look patches for co-registration, retrieving high precision co-registration estimates. The high efficiency in data volume requirements and computational effort makes this processor a candidate for operational processing systems. Within this study this processor was implemented and tested using an example RADARSAT-1 data set.

Finally, all three processing options were compared in table 4.1, section 4.3.3, with respect to the criteria: fast prototyping, data volume and computational efficiency, and application of existing strip-map processing components. This assessment helps, depending on the individual requirements (scientific, exploratory to operational, high throughput), in the selection of the most suitable processing concept.

7.3 ScanSAR DEM Example

As expected, DEMs produced from ScanSAR data perform well for moderate terrain relief and where high coherence is available (figure 5.5, section 5.3). The given drawbacks of the RADARSAT-1 24 day repeat-pass data set – atmospheric effects and low coherence –

generate the problems already experienced when computing ERS-1/2 interferograms and DEMs (Zebker et al. 1994). Phase unwrapping errors occur which distort the DEM result, in mountainous areas (steep incidence angles and low range bandwidth) and areas of low coherence. Consequently, several interferometric acquisitions of an area are necessary to generate reliable height information (Roth 1999).

Despite these effects, ScanSAR interferometry has the capability to add detail to available DEM. This was evident from a comparison of the resolution characteristics of the DEM products. The ScanSAR DEM performed significantly better than the DTED-1 reference for the considered area. This suggests that repeat-pass ScanSAR interferometry may be utilised as an efficient mapping technique providing geo-information at sampling grids of the order of hundreds of meters in areas where only GLOBE data is available.

7.4 Efficient Application of Burst-mode and ScanSAR Data for Interferometry

In the following it will be argued that ScanSAR interferometry may be applied efficiently to interferometric applications that require fast monitoring and wide swath coverage capability at the expense of resolution.

Following the recommendations in section 6.2 and the overview of current and planned satellite missions in table 6.1, suitable repeat-pass interferometric ScanSAR or burst-mode data sets may be acquired on a routine basis in the future.

This study showed two things. Firstly, efficient and accurate algorithms are available for ScanSAR interferometric processing (section 4.2). Secondly, during the interferometric processing the main parameter effects (mutual mis-alignment, burst scanning pattern mis-alignment, differing Doppler centroids of the data sets) are corrected so that after generation of the ScanSAR interferograms the interferometric phase has the same properties as that of a of strip-map interferogram with the only one difference: coarser resolution and wider swath. Hence, the standard approaches to interferogram filtering, baseline optimisation, and phase unwrapping can be applied.

Within this project a prototype of an optimal processor was implemented and tested using an example repeat-pass RADARSAT-1 data set. From this data a digital elevation model was generated. The results of this experiment both verified the expectations from the theory that, after suitable processing, ScanSAR interferograms resemble strip-map interferograms, and demonstrated the feasibility of repeat-pass ScanSAR interferometry using real data.

One approach for the efficient application of ScanSAR data would be the set-up of a background mission, for example, with the RADARSAT-2 instrument. For this mission several suitable long term stable test sites of interest would be selected. Then these test sites would be continuously monitored using ScanSAR wide swath modes. In the event of a major land slide or earthquake the mode could be switched to a finer resolution operation focussing on the particular area of interest. Then the cross-interferometric data ScanSAR/Fine could be evaluated. This has several practical advantages: 1) high resolution image data is available for the test site, 2) the wide band fine beam mode facilitates the retrieval of interferometric data even in case of very high baselines (section 5), and 3) the problem of burst scanning pattern synchronisation is addressed by combining a strip-map mode and a burst-mode, the interferometric data will thus have the resolution of the ScanSAR mode data. A slightly different concept for utilising the strip-map/ ScanSAR combination was described in (Monti Guarnieri and Rocca 1999). The authors proposed the acquisition of a data base of high resolution strip-map mode data and then to switch to a monitoring in ScanSAR mode. The advantage of the previous mode over the one proposed by (Monti Guarnieri and Rocca 1999) is that the data base has relaxed data volume requirements. Both methods, however, require the permanent possibly real time evaluation of the currently acquired data.

ScanSAR interferometry also provides data for the evaluation with the permanent scatterers technique (Monti Guarnieri and Ferretti 2000). The advantage of applying ScanSAR interferometry using this new technique is that many more potential permanent scatters can be imaged within one scene. Thus, the subsidence of city areas can be examined on a regional scale and mutual relationships in the subsidence behaviour may be revealed. However, there are basically two problems that have to be tackled before applying ScanSAR interferometry with this new technique: low resolution and a missing data base of ScanSAR data. The coarse resolution of ScanSAR implies that besides several strong scatterers many more weaker scatterers as in the case of ERS are integrated in the same resolution cell. Then an effect analogous to the baseline decorrelation effect occurs. Slight changes in look angle would already decorrelate the phase. Hence, it is to be expected that the effective number of permanent scatterers per square kilometre is lower for ScanSAR than it is for ERS interferometry. Secondly, the rich ERS data base available for the permanent scatterer technique is not available for ScanSAR data. Such a data base has to be built up first which is unlikely due to the multimode capability of ENVISAT/ASAR, the successor of ERS-1 and -2,

in the near future. This suggests that only a dedicated mission could provide data which would be available to its full extent after the course of only a few years.

Apart from a repeat-pass interferometer, ScanSAR mode can be favourably applied in a single-pass fully polarimetric or multi-frequency configuration. Such an instrument constitutes an efficient vegetation cover or biomass assessment and monitoring tool. Interferometric evaluation of the phase difference of available SAR channels provide, depending on the vegetation itself, average ground, and in the case of forests, canopy heights (Askne et al. 1997; Papathanassiou et al. 2000). Since the data rate for fully polarimetric SAR data is four times the data rate of single polarisation SAR mode, the swath width is considerably restricted for spaceborne sensors. However, the operation of the antenna in a ScanSAR mode may considerably increase the swath width at the expense of resolution. Lower resolution appears tolerable since the aim is to cover and monitor wide areas, possibly on a global scale. When designing such a systems the following parameters are of importance: revisit time, swath width and number of swaths, resolution, and phase quality which is a function of the number of burst looks and the available range bandwidth.

7.5 Future Work

7.5.1 Interferometer Mode Exploration and Characterisation

In chapter 3 the burst-mode interferometer signal data was contrasted to an interferometric strip-map signal. As an exploration tool, coherence and the interferogram power spectra were used. A comparison based on this two expectation values may also provide insights into the properties of other interferometric configurations like Spotlight SAR interferometry (Mittermayer 2000; Lanari et al. 2001), along track interferometry (Bao et al. 1997), or into the interferometric use of extraordinary SAR configurations (Runge et al. 2001).

For Spotlight signals with their bandpass character similar to burst-mode signals (section 3.1.1), some of the results obtained for burst-mode data may be directly applied to tackle questions of Spotlight SAR interferometry. For example, a linear phase ramp in the case of mis-registration as observed in (Mittermayer 2000) originates from a frequency sweep of the bandpass Spotlight SAR signal and, hence, has its grounds in the same physical phenomenon as the linear phase ramp in burst-mode interferometry discussed in section 3.2.2.

Spotlight interferometry is an interesting option providing high resolution interferometric data for height map generation and subsidence monitoring. Its exploration, in particular with the availability of the derived signal theoretical tools, will be subject to further research.

7.5.2 Phase Stability Estimator

The relation of power spectrum and coherence (see section 3.2.1) supports the interpretation and analysis of interferogram phase and signal characteristics when the SAR images are no longer accessible. In this respect, the measure applied to statements on the phase stability in section 4.2.7 is of importance, since its basis is the interferogram samples within the given estimation window and, hence, it constitutes an efficient tool for interferogram quality assessment. To this author's knowledge, this estimator has not previously been published (Ridha Touzi and Urs Wegmüller: personal communication). Its nature is expressed using the relationship between interferogram spectrum and coherence described above.

When the measure (section 4.2.7)

$$(7.1) \qquad \hat{\gamma}' = \frac{\left| \sum_N i_n \right|}{\sqrt{\sum_N |i_n|^2}}$$

is seen as an estimate of (appendix A8)

$$(7.2) \qquad \gamma' = \frac{|\mathrm{E}\{ i \}|}{\sqrt{\mathrm{E}\{|i|^2\}}}$$

and the result of section A3.1:

$$(7.3) \qquad \int \overline{\mathrm{S}}_{ii}(f)\, df = 1 + |\gamma|^2$$

is applied, then the following relationship to coherence is identified (appendix A8):

$$(7.4) \qquad |\gamma'|^2 = \frac{|\gamma|^2}{1 + |\gamma|^2} \quad .$$

The statistics, i.e. the probability density function and moments of (7.1), is the subject of further research. This phase stability estimator constitutes a very useful tool for the determination of the interferogram quality. Example applications are the assessment of interferograms that are obtained from an integrated airborne interferometer system readily providing the SAR interferogram phases.

7.5.3 Correction of Burst Pattern Effects

In section 4.2.3 the impact of the burst pattern on the variation of the coherence was discussed. For the RADARSAT-1 ScanSAR data set, the effect was found to be negligible given the scanning pattern configuration and the dominating temporal decorrelation. Burst pattern variation may, however, have more significance for single-pass interferometer configurations where the signal-to-noise ratio instead of the temporal decorrelation determines phase quality. A special burst combination approach which attempts to correct for the variation in signal-to-noise ratio at the single burst interferogram level then becomes necessary. An approach for SNR balancing was suggested by (Bamler 1995). The examination and adaptation of the outlined balancing approach to the combination of single burst interferograms is the subject of forthcoming research.

7.5.4 Application of DEMs from ScanSAR Interferometry

DEMs from ScanSAR interferometry can find their application as a reference and as an efficient source for ground control points for the generation and mutual alignment of higher resolution DEMs. Sample higher resolution data sources include the fine and standard beam modes of RADARSAT-1/ 2 and the ERS tandem phase data. Multi-resolution and wavelet techniques appear to be very well suited (Mallat 1997) for this task. This suggests that the DEMs from different resolutions can be expanded in a 2D wavelet transform and compared on a wavelet coefficient basis. Based on the concept of self-similarity of terrain (Polidori 1991; Datcu et al. 1996) the wavelet transform operates as a whitening operation (Wornell 1993) and, hence, the coefficients may be evaluated with respect to resolution or information content, mutual registration of the DEMs, or error effects (e.g. atmospheric influences). This further suggests that algorithms for DEM data fusion that optimally combine the available height data can be found, for example, (Ferretti et al. 1998; Ferretti et al. 1999). After the SRTM a height data set is available with consistency and accuracy unknown to this date. However, there still are the known problems of interferometric data when steep terrain is to be imaged and height errors increase in mountainous regions. In such areas optical DEM data promise favourable quality (Ferretti et al. 1998). Hence, the combination of different sources of DEM data, i.e. optical, radar, and existing, is an interesting area of further research.

7.6 Conclusion

During this study the following original work was contributed to the understanding of interferometric burst-mode and strip-map mode signal characteristics, burst-mode and ScanSAR interferometric processing, and to the understanding of repeat-pass RADARSAT-1 ScanSAR data:

1) Interferometric burst-mode and strip-map mode signal characteristics – contributions to the theoretical background:

   - A means of exploring the properties of interferometric SAR signals (strip-map mode, burst-mode, Spotlight) was developed. It includes the characterisation of the interferometric signal by its coherence and power spectrum. Using these two expectation values, the signal can be studied under several parameter conditions.
   - Burst-mode interferogram signal properties were studied in terms of this approach for the parameter conditions of non-zero
     - fringe frequency,
     - mis-registration,
     - azimuth scanning pattern mis-alignment.
   - In the same way the properties of the multiple coherent burst-mode interferogram were examined. Most of the expectation values for the given parameter conditions can be directly inferred from the single burst interferogram case. The most prominent deviation from the single burst interferogram case are:
     - coherence for non-zero mis-registration,
     - power spectral density for non-zero fringe frequency.
   - As a conclusion it was found that strip-map and burst-mode interferograms have significantly different signal characteristics for the case of mis-registration and for the multiple coherent burst image case.
   - Another important result was the equivalence of single burst and multiple coherent burst formation method under all previously listed parameter conditions.

- The systematic derivation of the interferogram power spectral density quantified the relationship of the interferogram power spectral density and coherence. Interferogram power spectral densities consist of a spectral line with a mass directly corresponding to the coherence and a pedestal that is the cross-correlation of the individual SAR autocorrelation functions. It was finally found that the ratio of the spectral line mass and the energy of the pedestal is the square of the coherence value.
- An efficient measure for the phase quality of the full swath interferogram was applied that, as could be shown in this study, directly relates to coherence by applying the relationship between coherence and interferogram power spectral density.
- In order to obtain the burst-mode interferogram power spectral density the calculation of the azimuth time varying auto-correlation function was necessary. The examination of the signals showed that it is possible to derive the autocorrelation of the burst-mode signals.
- An additional outcome of this exploration was the derivation of the various correlation properties of burst-mode data contributing to the proposed processing scheme for interferometric ScanSAR data.

2) Contributions to the understanding of processing interferometric burst-mode and ScanSAR data:

- This thesis provides a complete overview of interferometric processing of burst-mode and ScanSAR data including particularities of RADARSAT-1 interferometry.
- The co-registration properties derived in the theoretical part were verified in several experiments. An approach was proposed and tested integrating signal and geometric information for the derivation of a robust co-registration model.
- A fast and efficient resampling algorithm was found to be easily implemented and experiments confirmed the theoretical expectations with respect to the performance of the algorithm.
- A deeper insight was gained into the properties of the beam interferograms in the overlap area. It was found that mutual phase offsets of the beams originate from remaining tiny mis-registrations of the interferometric partners or from the mutual mis-alignment of the beams in conjunction with azimuth and range fringe frequencies. These phase offsets have to be measured and corrected before beam combination.

- Based on the two known burst-mode processing options: single burst and multiple coherent burst a new hybrid interferometric processor was proposed and verified. It is based on the data volume effective representation of the single burst processing technique and on the favourable co-registration properties of the multiple coherent burst processing options. This optimal processor is a candidate to be utilised within an operational environment.

3) Contributions from the evaluation of the RADARSAT-1 ScanSAR Narrow data set.

- The proposed hybrid processor for interferometric ScanSAR and burst-mode processing was verified with RADARSAT-1 interferometric data.
- It was verified that after processing of the ScanSAR data set the interferogram characteristics resemble the one of low resolution strip-map interferograms.
- From the combined ScanSAR swath interferograms a digital elevation model was derived and evaluated.
- Thus, this study demonstrated the feasibility of repeat-pass ScanSAR interferometry.

This thesis holds the following two arguments:

1. *ScanSAR interferometry is available for wide range of interferometric applications.*

   This argument is supported by the observations from the theoretical study, results from the processing, and from evaluation of the actual ScanSAR data. Theoretical explorations revealed the special properties of burst mode interferograms which differ from the well-known strip-map interferogram properties. However, it was shown that efficient algorithms and procedures are available which provide ScanSAR interferograms that resemble low resolution strip-map interferograms. Furthermore, the evaluation of the repeat-pass RADARSAT-1 ScanSAR data proved that for moderate terrain and temporarily stable regions interferogram phase quality can be obtained which enables the monitoring geo- and biophysical information on a global scale. This was shown during the SRTM where the C-Band ScanSAR mode provided almost global coverage.

2. *This thesis is a significant contribution to the signal theory and processing in ScanSAR interferometry with the aim of making this efficient mapping and monitoring tool more easily available to the remote sensing community.*

In order to support this argument this thesis provides a complete description of burst-mode interferogram signal properties. The particular burst-mode interferogram properties were made explicit by a comparison to strip-map mode data characteristics. An important milestone was the proof of the equivalence of the two available burst-mode interferogram formation options. This result makes it possible to freely choose the processing option that is best adapted to the individual needs: either scientific/ exploratory or operational/ high throughput.

The achievements within the area of interferometric burst-mode and ScanSAR processing are a further significant contribution to this argument. This thesis provides a complete overview of the various options of interferometric burst-mode and ScanSAR processing: co-registration parameter retrieval, resampling, spectral shift and common band filtering, beam alignment. Based on a comparison of the available burst-mode processing alternatives, a hybrid processing approach was proposed integrating the advantages of each individual algorithm.

The third key component comprises the processing and evaluation of the interferometric RADARSAT-1 ScanSAR data set. This thesis provides a recipe-like description of the interferometric processing, hence, giving a practical tour of ScanSAR interferometry. Moreover, this study encompasses the reconstruction of a digital elevation model from the wide-swath interferograms obtained. Thus, it demonstrated the feasibility of repeat-pass ScanSAR interferometry. From the evaluation of the height data it became evident that DEMs from interferometric ScanSAR data have the potential to improve DTED-1 standard DEMs.

Establishing the above three achievements and providing the availability of ScanSAR data for a wide range of applications (argument 1) makes this thesis a significant contribution to making ScanSAR interferometry more easily available within the remote sensing community as a standard tool for efficient mapping and monitoring.

Appendix 1

SAR and ScanSAR Data Model

A1.1 SAR Data

In the following the azimuth time, range time, and zero Doppler range distance variables are denoted as t [s], ϑ [s], and r [m], respectively. SAR raw data $d(t,\tau)$ is represented as the following integral (Bamler and Schättler 1993):

$$d(t,\vartheta) = \iint dt'\,dr'\,h_{raw,A}\left(t-t', \vartheta - \frac{2r'}{c}; r'\right)\chi(t',r') \qquad (A1.1)$$

with $\chi(.)$ the complex reflectivity function (section 3.1.2). In equation (A1.1) the acquisition impulse response function (IRF) $h_{raw,A}(t,\vartheta)$ is defined as:

$$h_{raw,A}(t,\vartheta;r) = A(t-t_c)\,g\left(\vartheta - \frac{2}{c}\Delta R(t,r)\right)\exp\left(-j\frac{4\pi}{\lambda}\sqrt{r^2+(v_S\,t)^2}\right) \qquad (A1.2)$$

with

$$\begin{aligned}\Delta R(t,r) &= \sqrt{r^2+(v_S\,t)^2} - r \\ &= r\left(\sqrt{1+\left(\frac{v_S\,t}{r}\right)^2} - 1\right)\end{aligned} \qquad (A1.3)$$

where a rectangular geometry was assumed, c [m/s] is the speed of light, λ [m] is the radar's wavelength, v_S [m/s] is the satellite velocity, $A(.)$ is the antenna pattern of the SAR, t_c [s] denotes the acquisition centre time, and $g(.)$ is the chirp function of the form $\mathrm{rect}\left(\frac{\tau}{W_R/K_R}\right)\exp\left(j\,\pi\,K_R\,\tau^2\right)$ (W_R [Hz]: range bandwidth, K_R [Hz/s]: range chirp rate, $\tau_p = W_R/|K_R|$ [s]: pulse duration).

For example, a point scatterer at (t_0, R_0) has the complex reflectivity function $\chi(t,r) = \delta(t - t_0, r - R_0)$, with $\delta(.)$ the Dirac distribution. Hence, we obtain from the integral in (A1.1) as the response of the scatterer:

(A1.4)

$$\begin{aligned} d(t,\vartheta) &= h_{raw,A}\left(t - t_0, \vartheta - \frac{2R_0}{c}; R_0 \right) \\ &= A(t - t_0 - t_c)\, g\left(\vartheta - \frac{2}{c}(R_0 + \Delta R(t - t_0, R_0)) \right) \exp\left(-j\frac{4\pi}{\lambda}\sqrt{R_0{}^2 + (v_S(t - t_0))^2} \right) \end{aligned}$$

with

(A1.5) $$\Delta R(t - t_0, R_0) = \sqrt{R_0{}^2 + (v_S(t - t_0))^2} - R_0$$

In order to focus or reconstruct the SAR image from the SAR raw data, the data is correlated with the matched filter (Bamler and Schättler 1993):

(A1.6) $$h_r(t,\vartheta;r) = h^*_{raw,A}(-t,-\vartheta;r),$$

that is, the complex conjugate of the SAR acquisition kernel plus time reversal. The SAR image is then obtained from the integral:

(A1.7) $$u(t,r) = \int dt'\, d\vartheta\, d(t',\vartheta)\, h^*_{raw,A}\left(t'-t, \vartheta - \frac{2r}{c}; r \right)$$

By inserting (A1.1) and reordering the resulting integral, the SAR end-to-end system IRF $h_A(.)$ is won as a correlation of the acquisition IRF with the matched filter:

(A1.8)

$$\begin{aligned} u(t,r) &= \int d\upsilon\, d\vartheta\, d(\upsilon,\vartheta)\, h_r\left(t - \upsilon, \frac{2r}{c} - \vartheta; r \right) \\ &= \int d\upsilon\, d\vartheta\, h_r\left(t - \upsilon, \frac{2r}{c} - \vartheta; r \right) \int dt'dr'\, h_{raw,A}\left(\upsilon - t', \vartheta - \frac{2r'}{c}; r' \right) \chi(t',r') \\ &= \int dt'dr'\, \chi(t',r') \int d\upsilon\, d\vartheta\, h_{raw,A}\left(\upsilon - t', \vartheta - \frac{2r'}{c}; r' \right) h_r\left(t - \upsilon, \frac{2r}{c} - \vartheta; r \right) \\ &= \int dt'dr'\, \chi(t',r')\, h_A(t,t';r,r') \end{aligned}$$

(A1.9) $$h_A(t,t';r,r') = \int d\upsilon\, d\vartheta\, h_{raw,A}\left(\upsilon - t', \vartheta - \frac{2r'}{c}; r' \right) h_r\left(t - \upsilon, \frac{2r}{c} - \vartheta; r \right)$$

The above relationships are complex since they refer to the 2 dimensional representation of SAR data. However, ScanSAR data processing (see below) differs only in its azimuth compression step. From the processing of SAR data for example, it is possible to fill the gaps in-between the bursts with zeros and input this data stream into a standard high precision SAR processor (Bamler and Eineder 1996)).

Hence, a one dimensional model of SAR and ScanSAR data concentrating on azimuth co-ordinates only is sufficient to satisfy the aims of the thesis.

To come to a suitable data description, the three main processing steps of SAR focussing are outlined in the following: range focussing, range cell migration correction, and azimuth focussing.

Range processing compresses the received data using a filter matched to the chirp function $g(.)$ (equation (A1.2)):

$$h_{raw,A}(t,\vartheta;r) = A(t-t_c)\,q\left(\vartheta - \frac{2}{c}\Delta R(t,r)\right)\exp\left(-j\frac{4\pi}{\lambda}\sqrt{r^2+(v_S\,t)^2}\right) \qquad (A1.10)$$

with $q(.)$ the inverse Fourier transform of a window $Q(.)$ that was used for side-lobe suppression in range. The range IRF has now a range resolution of about $\rho_R = 1/B_R$ [s].

Range cell migration corrects for the term $2/c\,\Delta R(.)$ in the argument of $q(.)$. This means the azimuth history of the target is 'placed', e.g. through resampling, onto a straight line for simplification of the subsequent azimuth compression step. After range compression and range cell migration correction, the target history is separable in azimuth time t and range time τ :

$$h_{raw,A}(t,\vartheta;r) = A(t-t_c)\,q(\vartheta)\exp\left(-j\frac{4\pi}{\lambda}\sqrt{r^2+(v_S\,t)^2}\right) \qquad (A1.11)$$

Hence, azimuth focussing can be considered independently for a certain range position r using:

$$h_{raw,A}(t) = h_{raw,A}(t,r) = A(t-t_c)\exp\left(-j\frac{4\pi}{\lambda}\sqrt{r^2+(v_S\,t)^2}\right) \qquad (A1.12)$$

The azimuth phase history may be represented using a Taylor series expansion truncated after the second order term:

$$
\begin{aligned}
h_{raw,A}(t,r) &= A(t-t_c)\exp\left(-j\frac{4\pi}{\lambda}r\left(1+\frac{1}{2}\left(\frac{v_S\,t}{r}\right)^2\right)\right) \\
&= A(t-t_c)\exp\left(-j\frac{4\pi}{\lambda}r\right)\exp\left(-j\frac{2\pi}{\lambda}\frac{(v_S\,t)^2}{r}\right) \\
&= A(t-t_c)\exp\left(-j\frac{4\pi}{\lambda}r\right)\exp\left(j\pi FM\,t^2\right)
\end{aligned}
\qquad (A1.13)
$$

with FM the frequency modulation rate:

$$
FM = -\frac{2}{\lambda}\frac{{v_S}^2}{r} \qquad (A1.14)
$$

In equation (A1.13) the term $\exp\left(-j\frac{4\pi}{\lambda}r\right)$ represents the propagation delay of the travelling pulse and is reduced into the complex reflectivity function so that we finally arrive at:

$$
h_{raw,A}(t) = A(t-t_c)\exp\left(j\pi FM\,t^2\right) \qquad (A1.15)
$$

for the SAR azimuth acquisition kernel.

The SAR raw data and the reconstruction of the SAR image can then be represented by:

$$
d(t) = \int dt'\, h_{raw,A}(t-t')\,\chi(t') \qquad (A1.16)
$$

$$
\begin{aligned}
u(t) &= \int ds\; d(s)\,h_r(t-s) \\
&= \int ds\; h_r(t-s)\int dt'\, h_{raw,A}(s-t')\,\chi(t') \\
&= \int dt'\,\chi(t')\int ds\; h_{raw,A}(s-t')\,h_r(t-s)
\end{aligned}
\qquad (A1.17)
$$

with

$$
\begin{aligned}
h_A(t,t') &= \int ds\; h_{raw,A}(s-t')\,h_r(t-s) \\
&= \int ds\; h_{raw,A}(\alpha)\,h_r((t-t')-\alpha) \\
&= h_A(t-t')
\end{aligned}
\qquad (A1.18)
$$

All in all, the SAR end-to-end impulse response is the convolution of the acquisition IRF with the reconstruction kernel and the reconstructed data is the convolution with the SAR end-to-end impulse response:

(A1.19) $$u(t) = \int dt' \, \chi(t') \, h_A(t - t')$$

A1.2 ScanSAR Data

From the above considerations, the ScanSAR raw data is:

(A1.20) $$\begin{aligned} d(t) &= \int dt' \, h_{raw,C}(t - t') \, \chi(t') \\ &= \int dt' \sum_n \text{rect}\left(\frac{t - nT_P}{T_B} \right) h_{raw,A}(t - t') \, \chi(t') \end{aligned}$$

where $h_{raw,C}(t)$ stands for the acquisition impulse response of a full aperture SAR and the train of rectangular-function (short a rect-function) models to the switch-on-off cycle when the antenna is switched to a different polarisation or beam. In the sense of the above integral, the ScanSAR acquisition function may be represented as:

(A1.21) $$h_{raw,C}(t,t') = \sum_n \text{rect}\left(\frac{t - nT_P}{T_B} \right) h_{raw,A}(t - t')$$

and the acquisition IRF of the nth burst is then:

(A1.22) $$h_{raw,n}(t,t') = \text{rect}\left(\frac{t - nT_P}{T_B} \right) h_{raw,A}(t - t')$$

From equations (A1.20) and (A1.22) the burst image is reconstructed from:

(A1.23) $$\begin{aligned} u_n(t) &= \int dt' \, \chi(t') \int ds \, \text{rect}\left(\frac{s - nT_P}{T_B} \right) h_{raw,A}(s - t') \, h_r(t - s) \\ &= \int dt' \, \chi(t') \, h_n(t,t') \end{aligned}$$

where

(A1.24) $$h_n(t,t') = \int ds \, \text{rect}\left(\frac{s - nT_P}{T_B} \right) h_{raw,A}(s - t') \, h_r(t - s)$$

is the ScanSAR end-to-end processing system response for burst number n. It depends on the utilised reconstruction kernel $h_r(t)$. Further considerations on the end-to-end burst-mode impulse response are given in sections 3.1.1.

Appendix 2

Autocorrelation Properties of Burst-mode Data

A2.1 Derivation of the Exact Burst-mode Autocorrelation Function (ACF)

For complex data the autocorrelation function (ACF) is defined as

(A2.1) $$R_{uu,n}(t,\tau) = E\{u_n^*(t)\, u_n(t+\tau)\}$$

where $u_n(.)$ are the complex single burst images and τ is the lag of the considered image pixels $u_n(t)$ and $u_n(t+\tau)$; the asterisk '*' denotes the conjugate complex of a complex variable. The burst mode images are obtained from the integral (section A1.2, equation (A1.23))

(A2.2) $$u_n(t) = \int dt_0\; h_n(t,t_0)\chi(t_0)$$

with

(A2.3) $$h_n(t;t_0) = \mathrm{sinc}(W_B\,(t-t_0))\exp(j\,2\pi\,FM\,(n\,T_P - t_0)(t-t_0))$$

and the complex reflectivity function $\chi(t)$ models a distributed scatterer by a complex, zero mean, unit variance Gaussian process, hence:

(A2.4) $$E\{\chi(t)\,\chi^*(s)\} = \delta(t-s)$$

with $\delta(t)$ the Dirac (delta) function.

From equation (A2.1), the ACF of the ScanSAR data is:

(A2.5) $$\begin{aligned} R_{uu,n}(t,\tau) &= E\{u_n^*(t)\, u_n(t+\tau)\} \\ &= \iint dt'\, ds'\, E\{\chi^*(t')\,\chi(s')\}\, h_n^*(t,t')\, h_n(t+\tau,s') \end{aligned}$$

Inserting (A2.3) and integration with respect to s' we have for the ACF:

(A2.6)

$$\begin{aligned} R_{uu,n}(t,\tau) &= \int dt' \, h_n^*(t,t') \, h_n(t+\tau,t') \\ &= \int dt' \, \mathrm{sinc}(W_B(t-t')) \, \mathrm{sinc}(W_B(t+\tau-t')) \exp(j\,2\pi\,FM[(nT_P-t')\tau]) \\ &= \exp(j\,2\pi\,FM\,(nT_P-t)\tau) \int du\ \mathrm{sinc}(W_B\,u) \, \mathrm{sinc}(W_B(u+\tau)) \exp(j\,2\pi\,FM\,u\,\tau) \end{aligned}$$

Finally, Parseval's theorem is applied so that:

(A2.7)

$$R_{uu,n}(t,\tau) = \exp(j\,2\pi\,FM\,(nT_P-t)\tau) \int df\ \mathrm{rect}\left(\frac{f+FM\tau}{W_B}\right) \mathrm{rect}\left(\frac{f}{W_B}\right) \exp(j\,2\pi\,f\,\tau)$$

Figure A2.1 shows the support of the integrand of the function and an example of the integrand for a special value of the parameter τ. From this sketch, the integral in (A2.6) can be easily evaluated. It is given in equation (A2.8). The quadratic dependence of the phase of the exponential comes from the frequency shift $\frac{FM\,\tau}{2}$ of the function displayed in grey shade in the lower half of figure A2.1. Figure A2.2 sketches the azimuth time variant phase behaviour of the ACF.

(A2.8) $$R_{uu,n}(t,\tau) = W_B\ \mathrm{tri}\left(\frac{\tau}{T_B}\right) \mathrm{sinc}((W_B - |FM\,\tau|)\tau) \exp(j\,\pi\,FM[2\,(nT_P-t)\tau - \tau^2])$$

Note, that equation (A2.8) and figure 2.1 implies that a mis-registration introduces a mutual frequency shift of the burst-data of $FM\,\tau$ and that the ACF is non-zero for values of τ in the range of $-T_B \le \tau \le T_B$ only.

A2.2 Autocorrelation Function of Multiple Coherent Burst Data

Multiple coherent burst data according to equation (3.10) in section 3.1 has the impulse response (scatterer position: $t = t'$):

(A2.9) $$h_C(t,t') = \sum_{N_L} \mathrm{sinc}(W_B\,(t-t')) \exp(j\,2\pi\,(nT_P-t')(t-t')).$$

A multiple coherent burst image is obtained from the integral and is the coherent sum of the individual burst images:

$$u_C(t) = \int dt' \, h_C(t,t') \, \chi(t') = \sum_{N_L} u_n(t) \qquad (A2.10)$$

Inserting these equations into the standard definition for the ACF yields:

(A2.11)

$$\begin{aligned} R_{uu,C}(t,\tau) &= E\left\{ u_C^*(t) \, u_C(t+\tau) \right\} \\ &= E\left\{ \sum_m u_m^*(t) \sum_n u_n(t+\tau) \right\} \\ &= \sum_m \sum_n E\left\{ u_m^*(t) \, u_n(t+\tau) \right\} \\ &= \sum_m \sum_n \int du \, \mathrm{sinc}(W_B \, u) \, \mathrm{sinc}(W_B \, (u+\tau)) \exp(j \, 2\pi \, FM \, ([(n-m)T_P + \tau]u + (nT_P - t)u)) \end{aligned}$$

By application of Parseval's theorem the following relationship for the ACF arises:

$$R_{uu,C}(t,\tau) = \sum_m \sum_n \int df \, \mathrm{rect}\left(\frac{f}{W_B} \right) \mathrm{rect}\left(\frac{f + FM[(n-m)T_P + \tau]}{W_B} \right) \exp(j \, 2\pi \, f \, \tau) \qquad (A2.12)$$

The integral is only non-zero when the rect-functions have common support, i.e. with f_p the offset frequency of the second rect-function:

$$f_p = FM \, [(n-m)T_P + \tau] \qquad (A2.13)$$

the following condition must be met:

$$-W_B \le f_p \le W_B . \qquad (A2.14)$$

implying that

$$-T_B - (n-m)T_P \le \tau \le T_B - (n-m)T_P . \qquad (A2.15)$$

This means, for shifts in the range $-T_B \le \tau \le T_B$ that only bursts of common index, i.e. frequency support contribute to the ACF and, hence:

$$R_{uu,C}(t,\tau) = \sum_n R_{uu,n}(t,\tau) . \qquad (A2.16)$$

This means the ACF of the multiple coherent burst data is the sum of the ACFs of the individual bursts and has similar properties to the point response of the multiple coherent burst data in equation (3.10) in section 3.1.1.

A2.3 Autocorrelation Estimator

In order to derive the properties of the auto-(cross) correlation estimator:

(A2.17) $$\hat{\mathrm{R}}_{uu,n}[\tau] = \sum_{N_E} u_1^*[i]\, u_2[i+\tau]$$

for single burst data where N_E is the number of samples within an estimation window with size T_E, the following expectation value is examined:

(A2.18) $$\breve{\mathrm{R}}_{uu,n}(\tau) = \mathrm{E}\left\{ \int_{-\frac{T_E}{2}}^{\frac{T_E}{2}} dt\; u_n^*(t)\, u_n(t+\tau) \right\}$$

where $u_n(t)$ is given in (A2.2) and the continuous valued ordinate variables allow easier computations and interpretations. Inserting equation (A2.2) and use of equations (A2.5) and (A2.8) yields:

(A2.19)

$$\begin{aligned}
\breve{\mathrm{R}}_{uu,n}(\tau) &= \int_{-\frac{T_E}{2}}^{\frac{T_E}{2}} dt\; \mathrm{R}_{uu,n}(t,\tau)\, dt \\
&= \int_{-\frac{T_E}{2}}^{\frac{T_E}{2}} dt\; W_B\, \mathrm{tri}\left(\frac{\tau}{T_B}\right) \mathrm{sinc}\left(\left(W_B - |FM\,\tau|\right)\tau\right) \exp\left(j\,\pi\, FM\left[2\,(nT_P - t)\,\tau - \tau^2\right]\right) \\
&= T_E\, W_B\, \mathrm{tri}\left(\frac{\tau}{T_B}\right) \mathrm{sinc}\left(\left(W_B - |FM\,\tau|\right)\tau\right) \mathrm{sinc}\left(FM\, T_E\, \tau\right) \exp\left(j\,\pi\, FM\left[2\, nT_P\, \tau - \tau^2\right]\right)
\end{aligned}$$

This means that the auto-(cross)-correlation estimate for $T_E > T_B$ has a resolution ρ_E that is determined by:

(A2.20) $$\rho_E \approx \frac{1}{|FM|\, T_E}$$

since the functions $\mathrm{tri}(\tau/T)$ and $\mathrm{sinc}\left(\left(W_B - |FM\,\tau|\right)\tau\right)$ are much broader or 'smoother' than $\mathrm{sinc}(FM\, T_E\, \tau)$ in the vicinity of 0.

In analogy the case of multiple coherent burst data may be examined. In this case the result is:

$$\breve{\mathrm{R}}_{uu,C}(\tau) = \mathrm{E}\left\{ \int_{-\frac{T_E}{2}}^{\frac{T_E}{2}} dt\; u_C^*(t)\, u_C(t+\tau) \right\}$$

$$= \sum_n \breve{\mathrm{R}}_{uu,n}(\tau)$$

$$= T_E\, W_B\, \mathrm{tri}\left(\frac{\tau}{T_B}\right)$$

(A2.21)

$$\mathrm{sinc}\left(\left(W_B - |FM\;\tau|\right)\tau\right)$$

$$\mathrm{sinc}\left(FM\; T_E\; \tau\right)$$

$$\exp\left(j\,\pi\; FM\; \tau^2\right)$$

$$\sum_n \exp\left(j\; 2\pi\; FM\; nT_P\; \tau\right)$$

where again the sum of the exponentials is responsible for a modulation of the function similar to the point response in equation (3.10) in section 3.1.1. However, for large enough T_E the width of the main lobe is determined by the estimation window size and has approximately the same extent as for the single burst case discussed above:

(A2.22)

$$\rho_E \approx \frac{1}{|FM|\, T_E}$$

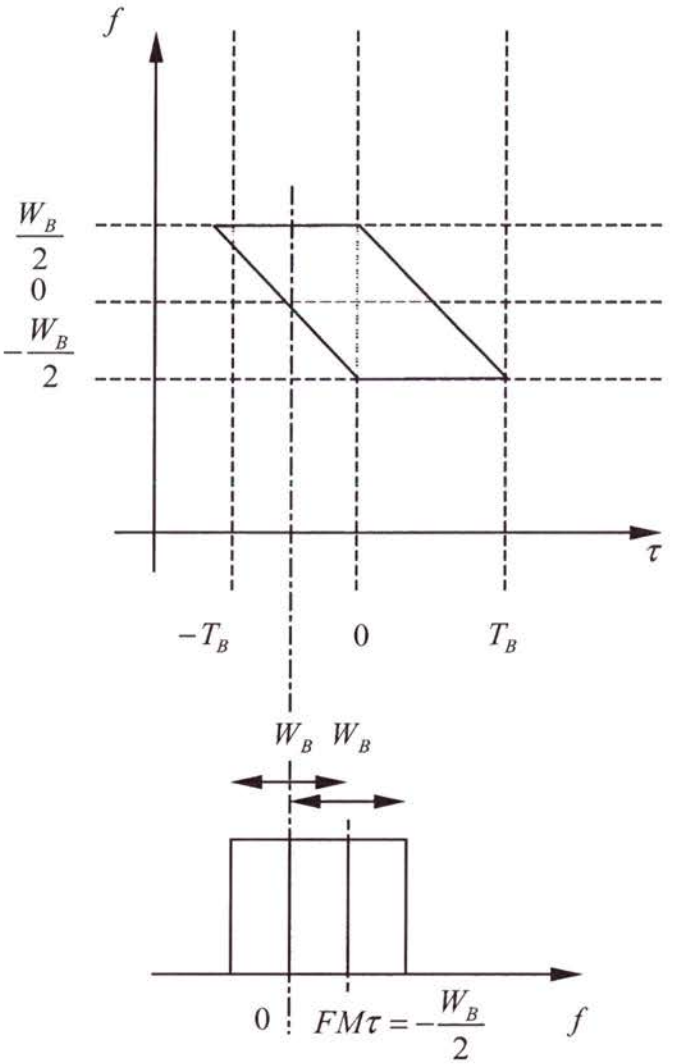

Figure A2.1: Sketch for derivation of the auto-correlation of ScanSAR data: equation (A2.7).

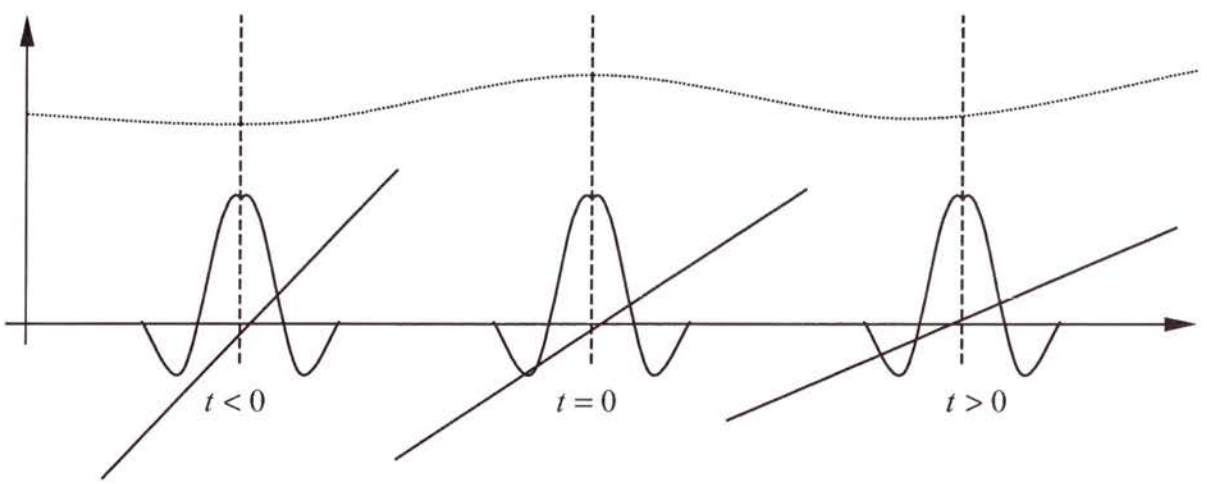

Figure A2.2: ACF of a burst signal for different positions where the burst index n is not zero. The dotted line indicateds the focussed burst. Its extent (T_A - T_B) is larger then the burst ACF extent.

Appendix 3

Derivation of the Properties of Burst-mode Interferogram Signals

A3.1 Single Burst Interferograms

A3.1.1 Expectation Value and Coherence of the Interferogram Pixel

The expectation value ($\mathrm{E}\{.\}$) and coherence of a burst interferogram pixel $i_n(t) = u_{1,n}(t)\,u_{2,n}^*(t)$ is:

(A3.1) $$\mathrm{E}\{i_n(t)\} = \mathrm{E}\{u_{1,n}(t)\,u_{2,n}^*(t)\}$$

and

(A3.2) $$\gamma_n = \frac{\mathrm{E}\{i_n(t)\}}{\sqrt{\mathrm{E}\{|u_{1,n}(t)|^2\}\mathrm{E}\{|u_{2,n}(t)|^2\}}}$$

where the burst image pixels are obtained by the following integral (appendix A1):

(A3.3) $$u_{i,n}(t) = \int dt_0\; h_{i,n}(t,t_0)\,\chi_i(t_0)$$

with i denoting the channel: $i = 1$ (master), $i = 2$ (slave) and

(A3.4) $$h_{i,n}(t;t_0) = \mathrm{sinc}(W_B\,(t-t_0))\exp(j\,2\pi\,FM\,(n\,T_P - t_0)(t-t_0))$$

is the burst-mode impulse response function. For clarity the antenna weighting and burst weighting are neglected.

For interferometry the following complex Gaussian model of a partially correlated process is used (section 4.1):

$$\begin{aligned} \chi_1(t) &= \sqrt{1-\gamma_T}\; a(t) + \sqrt{\gamma_T}\; c(t) \\ \chi_2(t) &= \left(\sqrt{1-\gamma_T}\; b(t) + \sqrt{\gamma_T}\; c(t)\right)\exp\left(-j\,2\pi\, f_\phi\, t\right) \end{aligned} \qquad (A3.5)$$

where χ_1 and χ_2 are the complex reflectivity functions for either interferometric channel with correlated part $c(t)$ and uncorrelated components $a(t)$ and $b(t)$. All input processes $a(t)$, $b(t)$, and $c(t)$ are independent zero-mean circular complex Gaussian processes. Temporal coherence is denoted by γ_T and a mutual shift of the frequency components is modelled by the fringe frequency f_ϕ.

For the subsequent calculations the expectation values

$$\mathrm{E}\left\{\chi_1(t)\chi_2^{*}(s)\right\} = \delta(t-s)\exp\left(-j\,2\pi\, f_\phi\, s\right) \qquad (A3.6)$$

$$\mathrm{E}\left\{\chi_i(t)\,\chi_i^{*}(s)\right\} = \delta(t-s),\quad i\in\{1,2\} \qquad (A3.7)$$

are of importance where $\delta(.)$ is the Dirac or delta distribution.

From the above equations (A3.3), (A3.4), and (A3.7), the basic relationships

$$\begin{aligned} \mathrm{E}\left\{\left|u_{1,n}(t)\right|^2\right\} &= \mathrm{E}\left\{\left|\int dt'\,\chi(t')\,h_{1,n}(t,t')\right|^2\right\} \\ &= \mathrm{E}\left\{\int dt'\,\chi_1(t')\,h_{1,n}(t,t')\int ds'\,\chi_1^{*}(s')\,h_{1,n}^{*}(t,s')\right\} \\ &= \int\int dt'\,ds'\,E\left\{\chi_1(t')\chi_1^{*}(s')\right\}h_{n,1}(t,t')\,h_{1,n}^{*}(t,s') \\ &= \int dt'\left|\mathrm{sinc}\left(W_B(t-t')\right)\right|^2 \\ &= \int df\ \mathrm{rect}\left(\frac{f}{W_B}\right)rect\left(\frac{f}{W_B}\right) \\ &= W_B \end{aligned} \qquad (A3.8)$$

in analogy,

$$\mathrm{E}\left\{\left|u_{2,n}(t)\right|^2\right\} = W_B, \qquad (A3.9)$$

and

$$\begin{aligned} \mathrm{E}\left\{i_n(t)\right\} &= \gamma_n\sqrt{\mathrm{E}\left\{\left|u_{1,n}(t)\right|^2\right\}\mathrm{E}\left\{\left|u_{2,n}(t)\right|^2\right\}} \\ &= \gamma_n\, W_B \end{aligned} \qquad (A3.10)$$

are obtained.

A3.1.1.1 Coherence of the Burst-mode Interferogram for Non-zero Mis-registration

A mis-registration of the interferometric partners is realised by shifting one signal with respect to the other by κ [s]:

(A3.11) $$u_{1,n}(t) = u_{2,n}(t+\kappa)$$

Apart from the shift both signals are assumed to be identical. Then the expectation value of the interferogram pixel is the autocorrelation function ACF of the burst-image, $f_\phi = 0$ (cf. appendix A2):

(A3.12)

$$\begin{aligned}
\mathrm{E}\left\{ u_{1,n}(t)\, u_{2,n}^{*}(t)\right\} &= \gamma_T \; \mathrm{R}_{u_1 u_1, n}(t,\kappa) \\
&= \gamma_T \; \mathrm{R}_{u_2 u_2, n}(t,\kappa) \\
&= \gamma_T \; \mathrm{R}_{uu,n}(t,\kappa) \\
&= \gamma_T \; \exp(-j\,2\pi\; FM\,(nT_P - t)\,\kappa) \int df \; \mathrm{rect}\left(\frac{f}{W_B}\right) \mathrm{rect}\left(\frac{f + FM\,\kappa}{W_B}\right) \exp(j\,2\pi\; f\;\kappa) \\
&= \gamma_T \; W_B \; \mathrm{tri}\left(\frac{\kappa}{T_B}\right) \mathrm{sinc}\left(\left(W_B - |FM\;\kappa|\right)\kappa\right) \exp\left(j\,\pi\; FM\left[2\,(nT_P - t)\,\kappa - \kappa^2\right]\right)
\end{aligned}$$

.

Consequently, the coherence is (equation (A3.10)):

(A3.13)

$$\begin{aligned}
\gamma_{\kappa,n}(t) &= \gamma_T \; \frac{\mathrm{R}_{uu,n}(t,\kappa)}{W_B} \\
&= \gamma_T \left(\mathrm{tri}\left(\frac{\kappa}{T_B}\right) \mathrm{sinc}\left(\left(W_B - |FM\;\kappa|\right)\kappa\right) \exp\left(j\,\pi\; FM\left[2\,(nT_P - t)\,\kappa - \kappa^2\right]\right)\right).
\end{aligned}$$

There are two major differences between this burst-mode result and the result:

(A3.14) $$\gamma_{\kappa,A} = \mathrm{sinc}(\kappa)$$

for a conventional strip-map SAR (with transfer function $H_1(f) = H_2(f) = \mathrm{rect}\left(\frac{f}{W_A}\right)$.)

Firstly, the burst interferogram will show a linear frequency component $\exp(j\,2\pi\,FM\,(nT_P - t)\kappa)$ neglecting the small quadratic phase component in (A3.13). Secondly, in principle the magnitude of the coherence reduces like a sinc-function (as for conventional SAR) but with an argument proportional to κ^2. This dependency is a result of the mutual frequency shift $FM\,\kappa$ of the channels introduced by the mis-registration κ.

A3.1.1.2 Coherence of the Burst-mode Interferogram for Non-zero Burst-scanning Pattern Mis-alignment

A mis-alignment of the burst-patterns actually implies that a different part of the ground was imaged and, hence, a different part of the azimuth scatterer spectrum was acquired. (Figure A3.1 illustrates the configuration in a scatterer-time – frequency diagram.) This mutual mis-alignment of the burst patterns introduces a shift of the centre frequencies of the companion bursts. For the following derivations the burst pattern mis-alignment denoted by Δt_{SP} of the second channel bursts with respect to the first channel bursts, i.e. nT_P in (A3.4), is replaced by $nT_P - \Delta t_{SP}$. The second channel impulse response is then:

(A3.15) $$h_{2,n}(t,t') = \mathrm{sinc}(W_B(t-t'))\exp(j\,2\pi\,FM(nT_P - \Delta t_{SP} - t')(t-t'))$$

Using this equation, the expectation value of the interferogram pixel may be obtained by:

(A3.16)

$$\begin{aligned}
\mathrm{E}\{u_{1,n}(t)\,u_{2,n}^*(t)\} &= \mathrm{E}\Big\{\int dt'\,\chi_1(t')\,h_{1,n}(t,t')\int ds'\,\chi_2^*(s')\,h_{2,n}^*(t,s')\Big\} \\
&= \gamma_T \int dt'\,h_{1,n}(t,t')\,h_{2,n}^*(t,t') \\
&= \gamma_T \int \begin{aligned}[t] & dt'\,\mathrm{sinc}(W_B\,(t-t'))\,\mathrm{sinc}(W_B\,(t-t')) \\ & \exp(j\,2\pi\,FM[\,(nT_P - t')(t-t') - (nT_P - \Delta t_{SP} - t')(t-t')])\end{aligned} \\
&= \gamma_T \int \begin{aligned}[t] & du\,\mathrm{sinc}(W_B u)\,\mathrm{sinc}(W_B u) \\ & \exp(j\,2\pi\,FM[\,(nT_P - t)\,u - (nT_P - \Delta t_{SP} - t)\,u])\end{aligned}
\end{aligned}$$

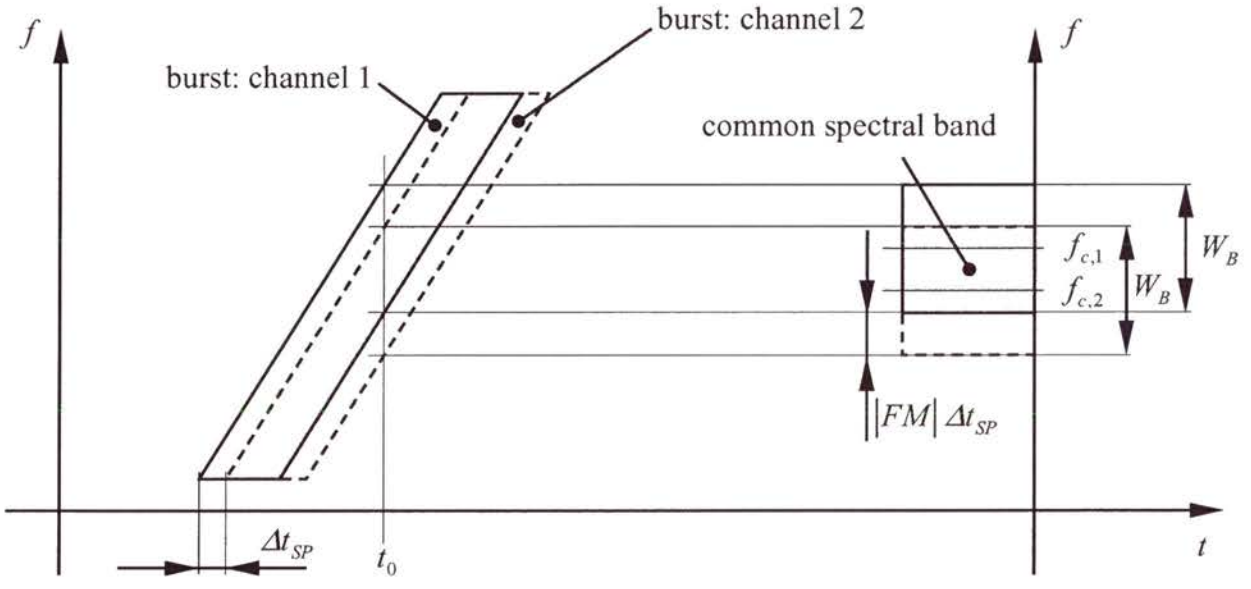

Figure A3.1: Visualisation of scanning pattern misalignment. The support of an interferometric burst pair in a scatterer – time versus focussed frequency domain diagram is shown. The overlap area contains interferometric information.

The last line in the derivation is expressed more succinctly using Parseval's theorem:

(A3.17)

$$\mathrm{E}\left\{ u_{1,n}(t)\, u_{2,n}^{*}(t) \right\} = \gamma_T \int df \ \mathrm{rect}\left(\frac{f_\tau - FM\left[nT_P - t\right]}{W_B} \right) \mathrm{rect}\left(\frac{f_\tau - FM\left[nT_P - \Delta t_{SP} - t\right]}{W_B} \right)$$
$$= \gamma_T \, W_B \ \mathrm{tri}\left(\frac{FM \ \Delta t_{SP}}{W_B} \right).$$

and consequently, the coherence is:

(A3.18) $$\gamma_{\Delta t_{SP},n} = \gamma_T \ \mathrm{tri}\left(\frac{FM \ \Delta t_{SP}}{W_B} \right).$$

This result suggests that no systematic phase distortion is introduced into the interferogram in the case of a mutual mis-registration of the burst images. The effect is more similar to the phenomenon in conventional SAR when the Doppler centroids differ. This analogy becomes evident in figure A3.1 when a single scatterer at time $t = t_0$ is considered. In order to increase coherence the non-overlapping frequency domain amplitudes have to be removed (Monti Guarnieri and Prati 1996).

Note that the data is perfectly registered in t-dimension (scatterer time dimension). However, a different time and frequency domain excerpt of the scene is rendered (figure A3.2).

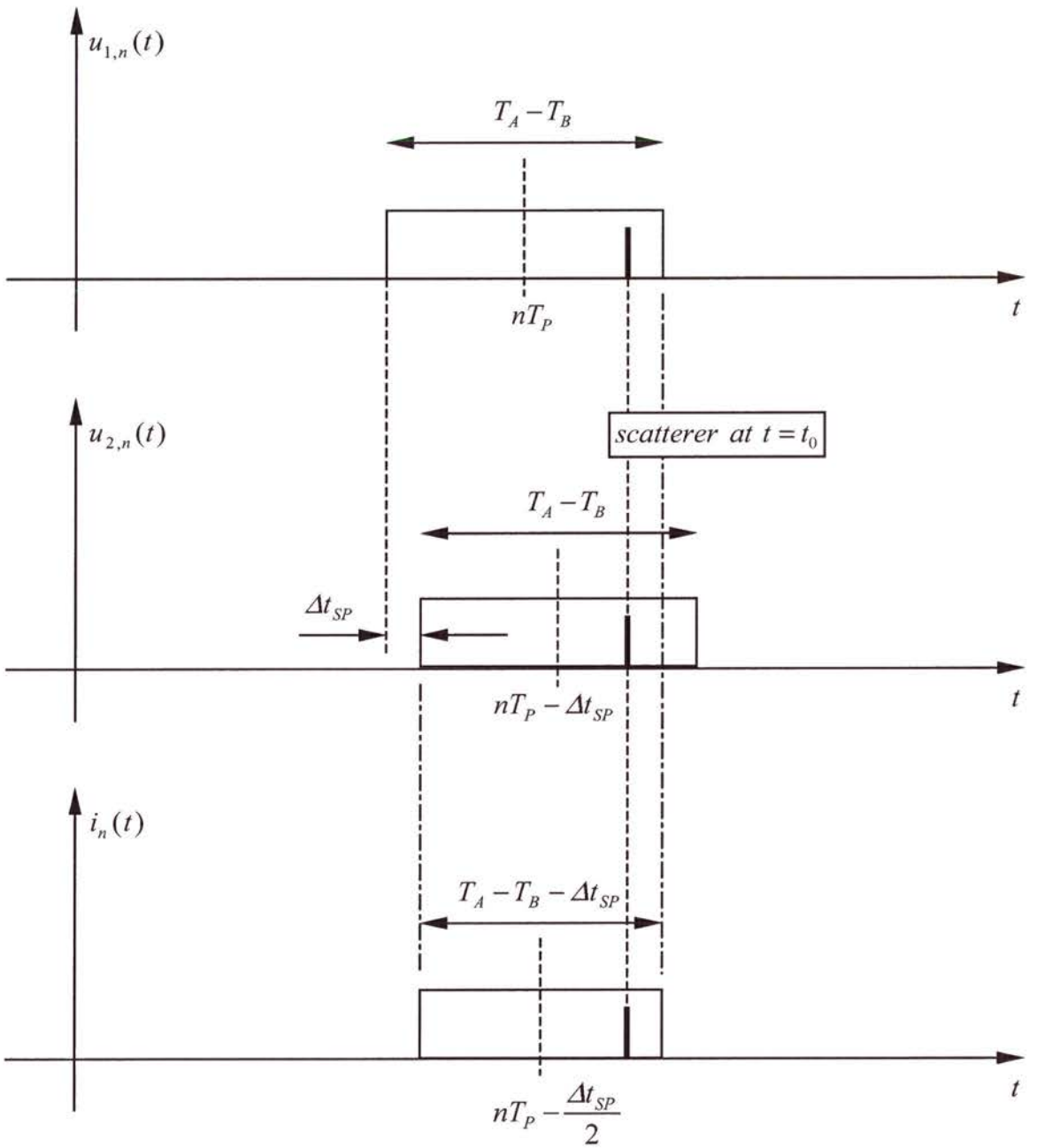

Figure A3.2: Interferogram formation from two interferometric ScanSAR bursts with mutual shift in acquisition scanning pattern. The horizontal axis shows focussed time t. The topmost two diagrams show interferometric channel 1 and 2, the bottom diagram shows the result for the interferogram.

A3.1.1.3 Coherence of the Burst-mode Interferogram for Non-zero Fringe Frequency

In this case, the expectation value of the interferogram pixel is obtained from:

(A3.19)

$$\begin{aligned}
\mathrm{E}\left\{u_{1,n}(t)\,u_{2,n}^{*}(t)\right\} &= \mathrm{E}\left\{\int dt'\,\chi_1(t')\,h_{1,n}(t,t')\int ds'\,\chi_2^{*}(s')\,h_{2,n}^{*}(t,s')\right\} \\
&= \gamma_T \int dt'\,h_{1,n}(t,t')\,h_{2,n}^{*}(t,t')\exp\left(j\,2\pi\,f_\phi\,t'\right) \\
&= \gamma_T \int^{dt'} \operatorname{sinc}\left(W_B\,(t-t')\right)\operatorname{sinc}\left(W_B\,(t-t')\right) \\
&\qquad \exp\left(j\,2\pi\left(FM[\,(nT_P-t')\,(t-t')-(nT_P-t')\,(t-t')]+f_\phi\,t'\right)\right) \\
&= \gamma_T \int^{du} \operatorname{sinc}\left(W_B u\right)\operatorname{sinc}\left(W_B u\right) \\
&\qquad \exp\left(-\,j\,2\pi\left(FM[\,n(T_P-(t-u))\,u-(nT_P-(t-u))\,u]+f_\phi\,(t-u)\right)\right) \\
&= \gamma_T\,\exp(j\,2\pi\,f_\phi\,t)\int^{du} \operatorname{sinc}\left(W_B\,u\right)\exp\left(j\,2\pi\,FM\,(nT_P-t)\,u\right) \\
&\qquad \operatorname{sinc}\left(W_B\,u\right)\exp\left(-\,j\,2\pi\left[\,FM\,(nT_P-t)\,u-f_\phi\,u\right]\right)
\end{aligned}$$

The application of Parseval's theorem yields:

(A3.20)

$$\begin{aligned}
\mathrm{E}\left\{u_{1,n}(t)\,u_{2,n}^{*}(t)\right\} &= \gamma_T\,\exp\left(j\,2\pi\,f_\phi\,t\right)\int df\,\operatorname{rect}\left(\frac{f-FM\,(nT_P-t)}{W_B}\right)\operatorname{rect}\left(\frac{f-\left[FM\,(nT_P-t)-f_\phi\right]}{W_B}\right) \\
&= \gamma_T\,\exp\left(j\,2\pi\,f_\phi\,t\right)\int df\,\operatorname{rect}\left(\frac{f}{W_B}\right)\operatorname{rect}\left(\frac{f-f_\phi}{W_B}\right)
\end{aligned}$$

.

Hence, the effect of the fringe frequency is perfectly consistent with the outcome for conventional SAR interferometry. A linear phase with frequency f_ϕ is introduced into the interferogram and coherence drops linearly if the mutual fringe frequency increases:

(A3.21) $$\gamma_{f_\phi,n}(t) = \gamma_T\,\exp\left(j\,2\pi\,f_\phi\,t\right)\operatorname{tri}\left(\frac{f_\phi}{W_B}\right)$$

A3.1.2 Autocorrelation and Power Spectral Density of the Single Burst Interferogram

A3.1.2.1 Interferogram Autocorrelation Function

The autocorrelation of the burst interferogram is defined as:

$$\begin{aligned} R_{ii,n}(\tau,t) &= E\{ i_n^*(t)\, i_n(t+\tau)\} \\ &= E\{ u_{1,n}^*(t)\, u_{2,n}(t)\, u_{1,n}(t+\tau)\, u_{2,n}^*(t+\tau)\} \end{aligned} \qquad (A3.22)$$

with equation (A3.3) and Reed's Theorem (Reed 1962):

$$E\{ z_1^* z_2^* z_3 z_4 \} = E\{ z_1^* z_3 \} E\{ z_2^* z_4 \} + E\{ z_1^* z_4 \} E\{ z_2^* z_3 \} \qquad (A3.23)$$

a relationship between the ACFs of the individual burst images and the interferogram ACF is obtained:

(A3.24)

$$\begin{aligned} R_{ii,n}(\tau) &= E\{ i_n^*(t)\, i_n(t+\tau)\} \\ &= \iiint dv\, dx\, dy\, dz\; h_{1,n}^*(t,v)\, h_{2,n}(t,x)\, h_{1,n}(t+\tau,y)\, h_{2,n}^*(t+\tau,z) \\ &\qquad E\{ \chi_1^*(v)\, \chi_2(x)\, \chi_1(y)\, \chi_2^*(z)\} \\ &= \iiint dv\, dx\, dy\, dz\; h_{1,n}^*(t,v)\, h_{2,n}(t,x)\, h_{1,n}(t+\tau,y)\, h_{2,n}^*(t+\tau,z) \\ &\qquad \left(E\{ \chi_1^*(v)\, \chi_1(y)\} E\{ \chi_2^*(z)\, \chi_2(x)\} + E\{ \chi_1^*(v)\, \chi_2(x)\} E\{ \chi_2^*(z)\, \chi_1(y)\} \right) \\ &= E\{ u_{1,n}^*(t)\, u_{1,n}(t+\tau)\} E\{ u_{2,n}^*(t)\, u_{2,n}(t+\tau)\}^* + E\{ u_{1,n}(t)\, u_{2,n}^*(t)\}^*\, E\{ u_{1,n}(t+\tau)\, u_{2,n}^*(t+\tau)\} \\ &= R_{u_1u_1,n}(t,\tau)\, R_{u_2u_2,n}^*(t,\tau) + E\{ i^*(t)\} E\{ i(t+\tau)\} \end{aligned}$$

The interferogram ACF will only depend on the variable τ since in equations (A3.4), (A3.5), and section A2.1 (A2.8) only the phase term exhibits the azimuth time t (t') dependence. This phase term is linear in all cases (non-zero fringe frequency, burst pattern mis-alignment, mis-registration) and as a result of the conjugate multiplications in (A3.24) the dependence on the variable t is discarded. This means that apart from a linear phase term in the interferogram or a frequency shift of the interferogram spectrum, the interferogram ACF and the PSD (see below) are time-invariant. Moreover, the interferogram ACF is positive definite (the PSD is positive for all f, see results below) and of finite energy. Since the expectation values are also time-invariant (ignoring the phase term) the interferogram process may be considered wide sense stationary.

A3.1.2.2 Interferogram Power Spectral Density

In order to obtain the interferogram PSD, the Fourier transform $\mathrm{F}_{\tau}\{.\}$ of (A3.24) with respect to τ is formed. Hence, the interferogram PSD is:

$$
\begin{aligned}
\mathrm{S}_{ii,n}(t,f) &= \mathrm{F}_{\tau}\left\{ R_{ii,n}(t,\tau)\right\} \\
&= \mathrm{S}_{u_1u_1,n}(t,f) *_f \mathrm{S}^{*}_{u_2u_2,n}(t,-f) + \mathrm{F}_{\tau}\left\{ \mathrm{E}\left\{ i^{*}(t)\right\}\mathrm{E}\left\{ i(t+\tau)\right\}\right\} \\
&= \mathrm{S}_{u_2u_2,n}(t,f) \otimes_f \mathrm{S}_{u_1u_1,n}(t,f) + \mathrm{F}_{\tau}\left\{ \mathrm{E}\left\{ i^{*}(t)\right\}\mathrm{E}\left\{ i(t+\tau)\right\}\right\}
\end{aligned}
\qquad \text{(A3.25)}
$$

where '$*_f$' is the convolution operator and '$\otimes_f$' is the cross-correlation operator with respect to f. Equation (A3.25) expresses the fact that the interferogram PSD consists of a spectral line and a component or pedestal given by the cross-correlation of the image's ACF.

For comparability of the individual interferograms (see also section appendix A3.4) the following normalised PSD (NPSD) is used:

$$
\begin{aligned}
\overline{\mathrm{S}}_{ii,n}(f_{\tau}) &= \frac{\mathrm{S}_{ii,n}(f)}{\int df\, \mathrm{S}_{u_1u_1,n}(t,f)\int df\, \mathrm{S}_{u_2u_2,n}(t,f)} \\
&= \frac{\mathrm{S}_{u_2u_2,n}(t,f)\otimes_f \mathrm{S}_{u_1u_1,n}(t,f)}{\int df\, \mathrm{S}_{u_1u_1,n}(t,f)\int df\, \mathrm{S}_{u_2u_2,n}(t,f)} + \mathrm{F}_{\tau}\left\{ \frac{\mathrm{E}\left\{ i^{*}(t)\right\}\mathrm{E}\left\{ i(t+\tau)\right\}}{\mathrm{E}\left\{ \left| u_{1,n}(t)\right|^2\right\}\mathrm{E}\left\{ \left| u_{2,n}(t)\right|^2\right\}}\right\}
\end{aligned}
\qquad \text{(A3.26)}
$$

since:

$$
\begin{aligned}
\int df\, \mathrm{S}_{u_1u_1,n}(t,f)\int df\, \mathrm{S}_{u_2u_2,n}(t,f) &= \mathrm{R}_{u_1u_1,n}(t,0)\,\mathrm{R}_{u_2u_2,n}(t,0) \\
&= \mathrm{E}\left\{ \left| u_{1,n}(t)\right|^2\right\}\mathrm{E}\left\{ \left| u_{2,n}(t)\right|^2\right\}
\end{aligned}
\qquad \text{(A3.27)}
$$

The last term of equation (A3.26) is related to the coherence:

$$
\frac{\mathrm{E}\left\{ i_n^{*}(t)\right\}\mathrm{E}\left\{ i_n(t+\tau)\right\}}{\mathrm{E}\left\{ \left| u_{1,n}(t)\right|^2\right\}\mathrm{E}\left\{ \left| u_{2,n}(t)\right|^2\right\}} = \gamma_n^{*}(t)\,\gamma_n(t+\tau). \qquad \text{(A3.28)}
$$

This term may linearly depend on τ or it is constant, i.e. the NPSD is either a Dirac distribution that is centred around zero (mis-alignment of the burst scanning pattern) or it is a Dirac distribution that is centred around a frequency that is determined by the amount of mis-registration or by the fringe frequency. Consequences of the two cases are outlined in the following:

1) $\gamma_n^*(t)\gamma_n(t+\tau)=|\gamma_n|^2$ - not a function of τ :

$$S_{ii,n}(f_\tau)=\frac{S_{u_2u_2,n}(t,f)\otimes_f S_{u_1u_1,n}(t,f)}{\int df\, S_{u_2u_2,n}(t,f)\int df\, S_{u_1u_1,n}(t,f)}+|\gamma_n|^2\,\delta(f) \qquad (A3.29)$$

and

$$\int df\, S_{ii,n}(f)=1+|\gamma_n|^2 \qquad (A3.30)$$

since

$$\int df\, S_{u_2u_2,n}(t,f)\otimes_f S_{u_1u_1,n}(t,f)=\int df\, S_{u_1u_1,n}(t,f)\int df\, S_{u_2u_2,n}(t,f) \qquad (A3.31)$$

with $|\gamma_n|^2$, the square of the coherence magnitude.

2) $\gamma_n(t)\gamma_n^*(t+\tau)=(\gamma_n\ \gamma_n^*)(\tau)$ - has a linear phase function of τ :

$$S_{ii,n}(f)=\frac{S_{u_2u_2,n}(t,f)\otimes_f S_{u_1u_1,n}(t,f)}{\int df\, S_{u_1u_1,n}(t,f)\int df\, S_{u_2u_2,n}(t,f)}+|\gamma_n|^2\,\delta(f-f_p) \qquad (A3.32)$$

where f_p is determined by mis-registration or fringe frequency. The integral of the NPSD yields (sampling property of the Dirac distribution):

$$\int df\, S_{ii,n}(f)=1+\gamma_n(0)\gamma_n^*(0) \qquad (A3.33)$$

where γ_n is a function of t.

A3.1.2.3 Approximation of the Interferogram Power Spectral Density

The interferogram ACF is composed of two terms, equation (A3.24). For the last term the Fourier transform is trivial in contrast to the first term, the conjugate complex multiplication of the individual burst-image ACFs. A numerical solution is possible as well as an algebraic solution using the principle of stationary phase. Both approaches are inconvenient for the representation of the results and a suitable approximation using equation 3.6 in section 3.1.2 is favoured. Inserting this approximation for the burst-image ACF in equation (A3.25) yields a so-called triangular (short: tri-) function or pedestal for the first term of the interferogram ACF:

(A3.34) $$W_B \, \mathrm{tri}\left(\frac{f}{W_B}\right) \qquad \text{where}$$

$$\mathrm{tri}\left(\frac{f}{W}\right) = \begin{cases} 1 - f/W & \textit{for} \quad 0 < f < W \\ 1 + f/W & \textit{for} \quad -W < f < 0 \\ 0 & \textit{elsewhere} \end{cases}$$

In order to support this approximation, it is compared to a numerical solution in the following. Two example burst-mode configurations are examined (figure A3.3 and A3.4; parameters of the ScanSAR data set in section 7.1 for burst durations $T_B = 0.09$ sec and $T_B = 0.045$ sec). The comparison of the representations by evaluating the relative difference in energy:

(A3.35) $$\frac{\Delta E}{E} \qquad \text{with} \qquad \Delta E = \int dt \, |g(t) - h(t)|^2 = \int df \, |G(f) - H(f)|^2$$

$$\text{and} \qquad E = \int dt \, |g(t)|^2 = \int df \, |G(f)|^2$$

yields deviations in the order of 1 to 2 percent and is, hence, negligible. Therefore, equation (A3.34) is utilised for representing the first term of the interferogram ACF according to equation (A3.25) in the following.

The 'nominal' PSD and NPSD (perfectly registered interferometric partners, no scanning pattern mis-alignment, flat phase, i.e. zero fringe frequency) are:

(A3.36) $$S_{ii,n}(f_\tau) = W_B \, \mathrm{tri}\left(\frac{f}{W_B}\right) + |W_B \, \gamma_T|^2 \, \delta(f)$$

and

(A3.37) $$\overline{S}_{ii,n}(f_\tau) = \frac{1}{W_B} \, \mathrm{tri}\left(\frac{f}{W_B}\right) + |\gamma_T|^2 \, \delta(f) .$$

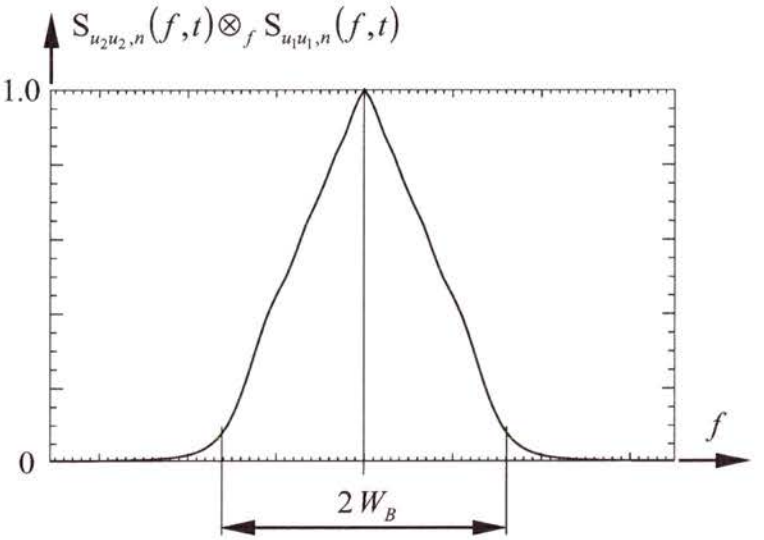

Figure A3.3: Normalized Fourier transform of the triangular pedestal of the burst interferogram ACF for $T_B = 0.09$ s and parameters as in section 7.1.

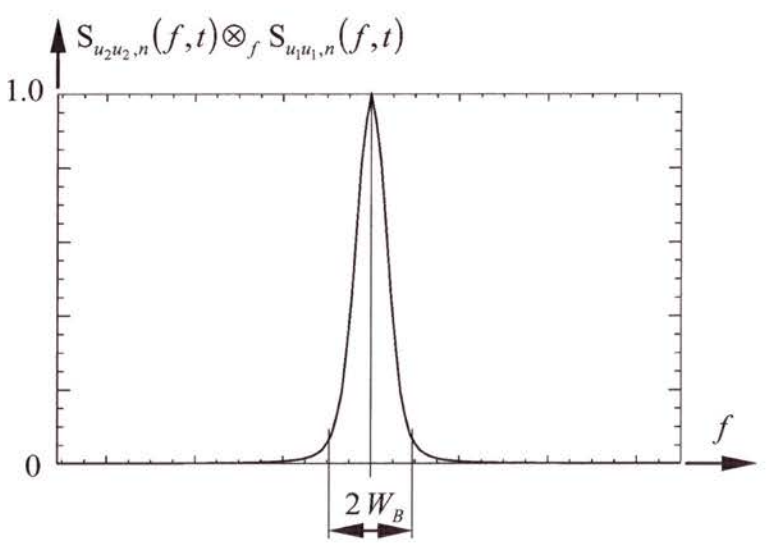

Figure A3.4: Normalized Fourier transform of the triangular pedestal of the burst interferogram ACF for $T_B = 0.045$ s and parameters as in section 7.1.

In the following, normalised single burst interferogram power spectral densities are derived for:

1. Non-zero fringe frequency ($f_\phi \neq 0, \kappa = 0, \Delta t_{SP} = 0$).
2. Non-zero mis-registration ($f_\phi = 0, \kappa \neq 0, \Delta t_{SP} = 0$).
3. Non-zero mis-alignment of burst scanning patterns ($f_\phi = 0, \kappa = 0, \Delta t_{SP} \neq 0$).

A3.1.2.4 Power Spectral Density of the Burst-mode Interferogram for Non-zero Fringe Frequency ($f_\phi \neq 0, \kappa = 0, \Delta t_{SP} = 0$).

In this case, the interferogram ACF is readily obtained from (A3.24), section A2.1, (A2.8), and (A3.21) is:

(A3.38)
$$\begin{aligned} \mathrm{R}_{ii,n}(\tau) &= \mathrm{R}_{u_1u_1,n}(t,\tau)\,\mathrm{R}^{*}_{u_2u_2,n}(t,\tau) + \gamma^{*}_{f_\phi,n}(t)\,\gamma_{f_\phi,n}(t+\tau) \\ &= W_B^2\ \mathrm{tri}^2\left(\frac{\tau}{T_B}\right)\mathrm{sinc}^2\left(\left[W_B - |FM|\right]\tau\right) + \exp\left(-j\,2\pi\,f_\phi\,\tau\right)\left|\gamma_T\ \mathrm{tri}\left(\frac{f_\phi}{W_B}\right)\right|^2 \end{aligned}$$

and the NPSD is obtained from equations (A3.26), (A3.34), and (A3.38) (figure A3.5):

(A3.39)
$$\overline{\mathrm{S}}_{ii,n}(f) = \frac{1}{W_B}\,\mathrm{tri}\left(\frac{f}{W_B}\right) + \left|\gamma_T\ \mathrm{tri}\left(\frac{f_\phi}{W_B}\right)\right|^2 \delta\left(f - f_\phi\right)$$

A3.1.2.5 Power Spectral Density of the Burst-mode Interferogram for Non-zero Burst Pattern Mis-alignment ($f_\phi = 0, \kappa = 0, \Delta t_{SP} \neq 0$).

For the derivation of the interferogram power spectral density in the presence of a burst scanning pattern mis-alignment Δt_{SP} (section A3.1.1.2) the following relation is helpful (equation (A3.3), (A3.15) and the findings of appendix A2):

(A3.40)
$$\mathrm{E}\left\{u^{*}_{2,n}(t)\,u_{2,n}(t+\tau)\right\} = \mathrm{R}_{u_2u_2,n}(t,\tau) = \mathrm{R}_{u_1u_1,n}(t+\Delta t_{SP},\tau)$$

Then, the interferogram ACF is obtained (section A 2.1 (A2.8); (A3.17) and (A3.24)):

(A3.41)
$$\begin{aligned} \mathrm{R}_{ii,n}(\tau) &= \mathrm{R}_{u_1u_1,n}(t,\tau)\,\mathrm{R}^{*}_{u_2u_2,n}(t,\tau) + \gamma^{*}_{\Delta t_{SP},n}(t)\,\gamma_{\Delta t_{SP},n}(t+\tau) \\ &= W_B^2\ \mathrm{tri}^2\left(\frac{\tau}{T_B}\right)\mathrm{sinc}^2\left(\left[W_B - |FM|\,\tau\right]\tau\right)\exp\left(j\,2\pi\,\Delta t_{SP}\,FM\,\tau\right) + \left|\gamma_T\,W_B\ \mathrm{tri}\left(\frac{FM\Delta t_{SP}}{W_B}\right)\right|^2 \end{aligned}$$

This autocorrelation of the interferogram yields an interferogram NPSD composed of a triangular pedestal $\mathrm{tri}\left(\frac{f_\tau - FM\ \Delta t_{SP}}{W_B}\right)$ and a Dirac distribution with weight $\left|\gamma_T\ \mathrm{tri}\left(\frac{FM\ \Delta t_{SP}}{W_B}\right)\right|^2$. However, in contrast to the NPSD in equation (A3.37) the triangular function is shifted by $FM\ \Delta t_{SP}$ and the Dirac distribution is centred at zero frequency (figure A3.6):

(A3.42) $$\overline{S}_{ii,B}(f) = \frac{1}{W_B}\mathrm{tri}\left(\frac{f - FM\ \Delta t_{SP}}{W_B}\right) + \left|\gamma_T\ \mathrm{tri}\left(\frac{FM\ \Delta t_{SP}}{W_B}\right)\right|^2 \delta(f)$$

A3.1.2.6 Power Spectral Density of the Burst-mode Interferogram for Non-zero Mis-registration ($f_\phi = 0, \kappa \neq 0, \Delta t_{SP} = 0$)

For non-zero mis-registration: (A3.11), the coherence is given according to equation (A3.13) and, consequently, the autocorrelation function of the interferogram is (cf. appendix A2):

(A3.43)

$$\begin{aligned} R_{ii,n}(\tau) &= R_{u_1u_1,n}(t,\tau)\, R^*_{u_2u_2,n}(t,\tau) + \gamma^*_{\kappa,n}(t)\,\gamma_{\kappa,n}(t+\tau) \\ &= R_{u_2u_2,n}(t+\kappa,\tau)\, R^*_{u_2u_2,n}(t,\tau) + \gamma^*_{\kappa,n}(t)\,\gamma_{\kappa,n}(t+\tau) \\ &= \exp(-j\,2\pi\ FM\ \tau\ \kappa) \\ &\quad \left(W_B^2\ \mathrm{tri}^2\left(\frac{\tau}{T_B}\right)\mathrm{sinc}^2\left(\left[\,W_B - |FM|\,\tau\right]\tau\right) + \left|\,\gamma_T\ W_B\ \mathrm{tri}\left(\frac{\kappa}{T_B}\right)\mathrm{sinc}\left(\left(W_B - |FM\ \kappa|\right)\kappa\right)\right|^2 \right) \end{aligned}$$

The NPSD of the interferogram can be calculated as follows (figure A3.7):

(A3.44) $$\overline{S}_{ii,n}(f) = \frac{1}{W_B}\mathrm{tri}\left(\frac{f - FM\ \kappa}{W_B}\right) + \left|\gamma_T \frac{R_{uu,n}(t,\kappa)}{W_B}\right|^2 \delta(f - FM\ \kappa)$$

This means that the whole (N)PSD of the interferogram is shifted by $FM\ \kappa$. It is an effect that does not occur with conventional SAR interferometry and makes it, in this way, a special property of burst-mode data.

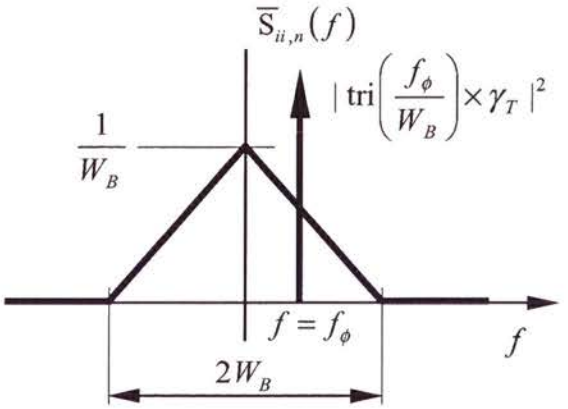

Figure A3.5: Sketch of the approximate normalized power spectrum of a single burst interferogram for non-zero fringe frequency f_ϕ.

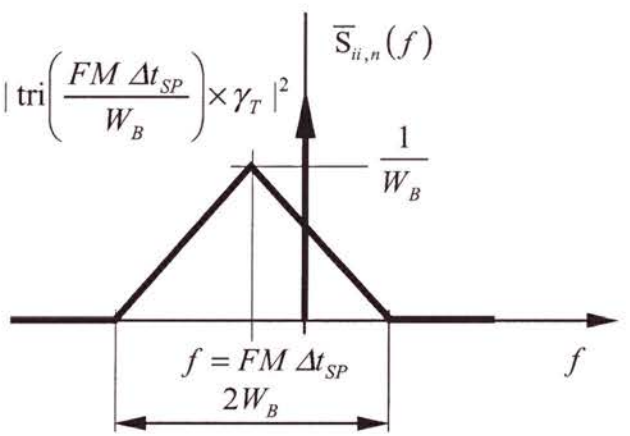

Figure A3.6: Sketch of the approximate normalized power spectrum of a single burst interferogram for non-zero burst pattern alignment Δt_{SP}.

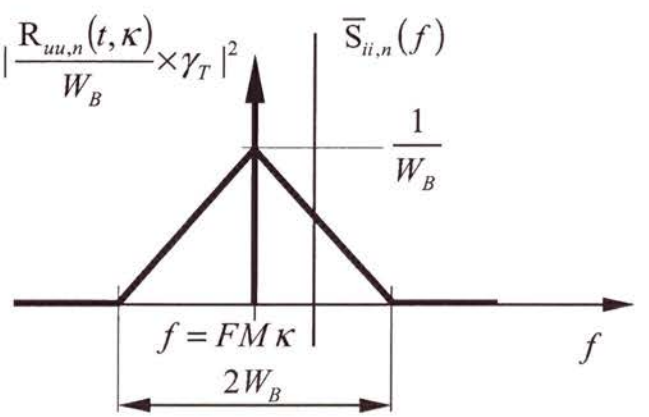

Figure A3.7: Sketch of the approximate normalized power spectrum of a single burst interferogram for non-zero mis-registration κ.

A3.2 Multiple Single Burst Interferogram

A multiple single burst interferogram (MSBI) is obtained by the mosaicking of the single burst interferograms. This means, the single burst interferograms that contribute to a single time or pixel are added up:

(A3.45) $$i_B(t) = \sum_n i_n(t) = \sum_n u_{1,n}(t)\, u_{2,n}^{*}(t)$$

A3.2.1 Expectation Value of an Multiple Single Burst Interferogram Pixel

Since the expectation operator is linear, the expectation value of a MSBI pixel is the sum of the expectation values of the individual single burst interferogram pixels:

(A3.46) $$\mathrm{E}\{ i_B(t)\} = \sum_n \mathrm{E}\{ i_n(t)\}$$

A3.2.2 Autocorrelation Function and Power Spectral Density

For the ACF of the multiple single burst interferogram the following intermediate result is obtained:

(A3.47)

$$\mathrm{E}\left\{ i_B^{*}(t)\, i_B(t+\tau)\right\} = \mathrm{E}\left\{ \sum_n i_n^{*}(t) \sum_m i_m(t+\tau)\right\} = \sum_n \sum_m \mathrm{E}\left\{ u_{1,n}^{*}(t)\, u_{2,n}(t)\, u_{1,m}(t+\tau)\, u_{2,m}^{*}(t+\tau)\right\}$$

From this representation an expression for the MSBI ACF is found using equation (A3.3) and Reed's theorem:

(A3.48) $$\mathrm{E}\left\{ i_B^{*}(t)\, i_B(t+\tau)\right\} = \sum_n \mathrm{R}_{u_1 u_1,n}(\tau,t)\, \mathrm{R}_{u_2 u_2,n}^{*}(\tau,t) + \sum_n \mathrm{E}\left\{ i_n^{*}(t)\right\} \sum_m \mathrm{E}\{ i_m(t+\tau)\}$$

Hence, the MSBI ACF is not the sum of the individual burst interferogram ACFs. It is stationary for all considered parameter cases ($f_\phi \neq 0$: (A3.38), $\Delta t \neq 0$: (A3.41), $\kappa \neq 0$: (A3.43)) since the phase term of the burst image's ACFs disappears due to the Hermitian product and since the second term depends on τ only.

After Fourier transforming the MSBI ACF, the PSD of the interferogram is obtained:

(A3.49) $$\begin{aligned} \mathrm{S}_{,B}(f) &= \sum_n \mathrm{S}_{1\,1,n}(t,f) *_f \mathrm{S}^{*}_{2\,2,n}(t,-f) + \mathrm{F}_\tau\left\{ \sum_n \mathrm{E}\left\{ i_n^{*}(t)\right\} \sum_m \mathrm{E}\{ i_m(t+\tau)\}\right\} \\ &= \sum_n \mathrm{S}_{2\,2,n}(t,f) \otimes_f \mathrm{S}_{1\,1,n}(t,f) + \sum_n \sum_m \mathrm{F}_\tau\left\{ \mathrm{E}\left\{ i_n^{*}(t)\right\} \mathrm{E}\{ i_m(t+\tau)\}\right\} \end{aligned}.$$

This PSD is similarly built up as for the PSD of the single burst interferogram (Figure A3.8). The first term is the sum of the cross-correlation functions of the single burst image PSDs and the spectral line has the mass of the second term of the MSBI ACF. Since the support of the interferogram PSD is the same for all burst indices n, the support of the MSBI has the support of the single burst interferogram.

For example, the normalised MSBI PSD for the case ($f_\phi \neq 0, \kappa = 0, \Delta t_{SP} = 0$) is:

(A3.50) $$\overline{S}_{ii,B}(f) = \frac{1}{N_L W_B} \operatorname{tri}\left(\frac{f}{W_B}\right) + \left|\gamma_T \operatorname{tri}\left(\frac{f_\phi}{W_B}\right)\right|^2 \delta(f - f_\phi) .$$

A3.3 Multiple Coherent Burst Interferogram

For the formation of the multiple coherent burst interferogram (MCBI), the individual SAR bursts are added up coherently for either interferometric channel:

(A3.51) $$u_{1,C}(t) = \sum_n u_{1,n}(t)$$

(A3.52) $$u_{2,C}(t) = \sum_m u_{2,m}(t)$$

and then the interferogram $i_C(t) = u_{1,C}(t)\, u_{2,C}^*(t)$ is formed.

A3.3.1 Autocorrelation Function of Multiple Coherent Burst Images

Since bursts of different indices are not correlated (appendix A2), the ACF of the multiple coherent burst data is the sum of the individual burst ACFs, e.g.:

(A3.53) $$\begin{aligned} \mathrm{R}_{u_1 u_1, C}(t, \tau) &= \mathrm{E}\left\{ u_{1,C}{}^*(t)\, u_{1,C}(t+\tau) \right\} \\ &= \sum_n \mathrm{R}_{u_1 u_1, n}(t, \tau) \end{aligned}$$

A3.3.2 Expectation Value of the Multiple Coherent Burst Interferogram

The MCBI pixel expectation value is obtained from:

(A3.54)
$$\begin{aligned} \mathrm{E}\{ i_C(t)\} &= \mathrm{E}\left\{ \sum_n u_{1,n}(t) \sum_m u^*_{2,m}(t) \right\} \\ &= \sum_n \mathrm{E}\{ i_n(t)\} \end{aligned}$$

as a result of the mutual independence of the burst image pixels $u_{n,1}(t)$ and $u_{m,2}(t)$ for $m \neq n$:

(A3.55)
$$\begin{aligned} \mathrm{E}\left\{ u_{1,n}(t)\, u^*_{2,m}(t) \right\} &= \int dt' \operatorname{sinc}(W_B\,(t-t'))\,(\operatorname{sinc}(W_B\,(t-t'))\exp(j\,2\pi\,(n-m)\,W_P\,(t-t'))) \\ &= \int df\ \operatorname{rect}\left(\frac{t}{W_B} \right) \operatorname{rect}\left(\frac{t-(n-m)W_P}{W_B} \right) \end{aligned} ,$$

i.e. if the burst window width $W_B < W_P$, which is given for any reasonable ScanSAR system, then the integral yields zero for non-overlapping bursts. Hence, this expectation value is the same as for the MSBI.

A3.3.3 Coherence of the Multiple Coherent Burst Interferogram for a Mis-registration κ

For a mutual mis-registration the MCBI coherence shows a remarkable feature. When the individual expectation values are summed up according to (A3.54) the coherence exhibits a modulation similar to the multiple coherent burst impulse response function (section 3.1.1, equations 12 and 14, figure 3.2: $t \rightarrow \kappa$):

(A3.56)
$$\begin{aligned} \gamma_{\kappa,C}(t) &= \sum_n \gamma_{\kappa,n}(t) \\ &= \operatorname{tri}\left(\frac{\kappa}{T_B} \right) \operatorname{sinc}\left((W_B - |FM\ \kappa|)\,\kappa \right) \exp\left(-j\,\pi\ FM\ \left[2\,t\,\kappa + \kappa^2 \right] \right) \sum_n \exp(-j\,2\pi\,n\,W_P\,\kappa) \\ &\approx \operatorname{sinc}(W_B\,\kappa) \exp(-j\,2\pi\ FM\ t\,\kappa) \sum_n \exp(-j\,2\pi\,n\,W_P\,\kappa) \end{aligned}$$

In analogy to the multiple coherent burst image impulse response, the outcome is an interference pattern: the low-pass envelope is determined by burst bandwidth W_B and the high frequency modulation depends on the distance of the burst spectra W_P.

a) single burst

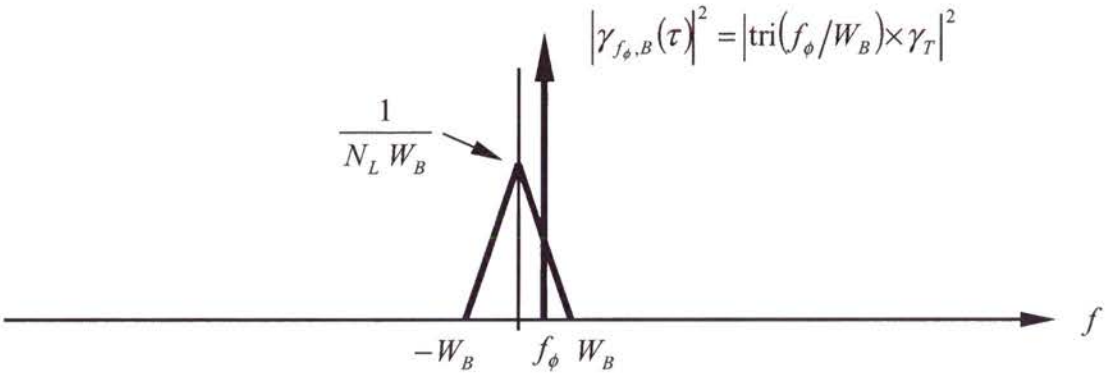

b) multiple burst

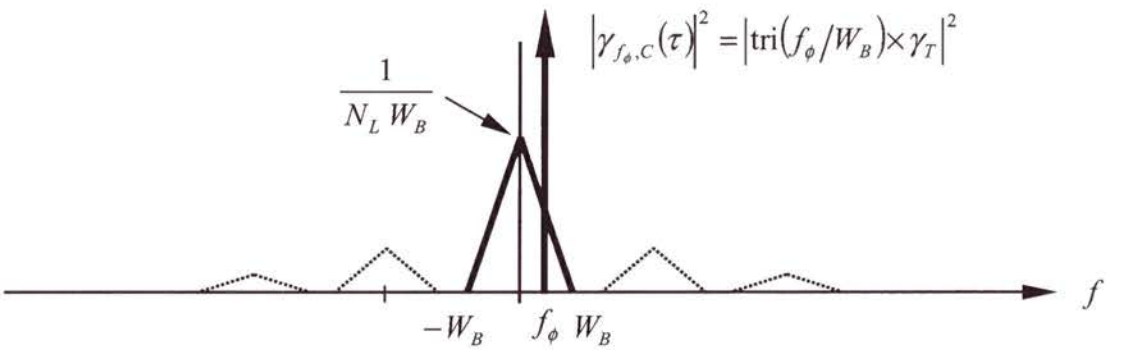

Figure A3.8: Multiple single burst interferogram a) and multiple coherent burst interferogram b) PSD before (dotted) and after low pass filtering.

A3.3.4 Auto-Correlation Function and Power Spectral Density of the Multiple Coherent Burst Interferogram

Application of Reed's theorem yields the MCBI ACF:

$$\begin{aligned} \mathrm{R}_{ii,C}(\tau) &= \mathrm{E}\left\{ i_C^*(t)\, i_C(t+\tau) \right\} \\ &= \mathrm{E}\left\{ \sum_n u_{1,n}{}^*(t) \sum_m u_{2,m}(t) \sum_k u_{1,k}(t+\tau) \sum_\ell u_{2,\ell}{}^*(t+\tau) \right\} \\ &= \sum_n \mathrm{R}_{u_1u_1,n}(t,\tau) \sum_m \mathrm{R}_{u_2u_2,m}{}^*(t,\tau) + \sum_n \mathrm{E}\left\{ i_n{}^*(t) \right\} \sum_m \mathrm{E}\left\{ i_m(t+\tau) \right\} \end{aligned} \qquad (\text{A3.57})$$

This result is obtained from the assumption that the spectral weightings of the individual bursts have non-overlapping frequency support for $n \neq m$. This ACF is also time invariant for the above parameter cases ($f_\phi \neq 0$: (A3.38), $\Delta t_{SP} \neq 0$: (A3.41), $\kappa \neq 0$: (A3.43)) since the azimuth time t dependent contributions of the phase disappear after formation of the conjugate complex product. Moreover, the second term is equivalent to the second term of the MSBI ACF.

The Fourier transform of (A3.57) is the MCBI PSD:

$$\begin{aligned} \mathrm{S}_{ii,C}(f) &= \sum_n \mathrm{S}_{u_1u_1,n}(t,f) *_f \sum_m \mathrm{S}^*_{u_2u_2,n}(t,-f) + \mathrm{F}_\tau \left\{ \sum_n \mathrm{E}\left\{ i_n{}^*(t) \right\} \sum_m \mathrm{E}\left\{ i_m(t+\tau) \right\} \right\} \\ &= \sum_m \mathrm{S}_{u_2u_2,n}(t,f) \otimes_f \sum_n \mathrm{S}_{u_1u_1,n}(t,f) + \mathrm{F}_\tau \left\{ \sum_n \mathrm{E}\left\{ i_n{}^*(t) \right\} \sum_m \mathrm{E}\left\{ i_m(t+\tau) \right\} \right\} \end{aligned} \qquad (\text{A3.58})$$

This means that the PSD is built up from a Dirac component and a cross-correlation of the train of single burst image ACFs. This cross-correlation will give a series of triangular pedestals when the bursts have a rect-shaped envelope; for the case $f_\phi \neq 0, \kappa = 0, \Delta t_{SP} = 0$ the PSD is (Figure A3.8):

$$\mathrm{S}_{ii,C}(f) = \sum_{k=-N_L}^{N_L} \left(N_L - |k| \right) W_B \, \mathrm{tri}\left(\frac{f - kT_P}{W_B} \right) + \left| \gamma_T \, N_L \left(W_B - f_\phi \right) \right|^2 \delta\left(f - f_\phi \right) \qquad (\text{A3.59})$$

A3.4 Normalisation of Multiple Single Burst Interferograms

The last terms of equations (A3.49) and (A3.58) are identical. Hence, the PSDs are normalised so that the masses of the Dirac distributions are still comparable. In order to obtain comparability of the MSBI and MCBI, the MSBI is also normalised by the multiple coherent burst image's energy:

$$E_C = \mathrm{E}\left\{\left|\sum_n u_{n,1}(t)\right|^2\right\}\mathrm{E}\left\{\left|\sum_n u_{n,2}(t)\right|^2\right\} = \int df \sum_n \mathrm{S}_{u_1u_1,n}(f)\int df \sum_n \mathrm{S}_{u_2u_2,n}(f) \quad \text{(A3.60)}$$

For the rect-shaped burst window case the MCBI energy is:

$$E_C = (N_L\, W_B)^2 \quad \text{(A3.61)}$$

In this way all relevant interferograms (strip-map, set: $E_A = {W_A}^2$, single burst, set: $E_B = {W_B}^2$, MSBI, MCBI) may be compared with respect to the mass of the spectral line component. Moreover, this normalisation is beneficial when considering the equivalence of the MSBI and the MCBI in the following section.

A3.5 Equivalence of Multiple Single Burst and Multiple Coherent Burst Interferogram Power Spectral Densities

The side lobes of the MCBI PSD are the only difference between the two PSDs (equations (A3.49) and (A3.58)). These side-lobes can be removed by a suitable low pass filter $H_{LP}(f)$, e.g. with bandwidth $2\,W_B$. For the equivalence, a burst period equivalent bandwidth W_P larger than $2\,W_B$ is required (which is the case for every realistic ScanSAR or burst-mode). Furthermore, the energy of the cross-correlation of the autocorrelation functions of the single burst interferograms has to be sufficiently concentrated within a frequency support smaller than the bandwidth W_P. These conditions are necessary in order to obtain equivalence between the two interferometric processing options for burst mode data. A suitable weighting of the bursts input into the ScanSAR processor may implement this constraint.

The PSD of the low pass filtered multiple coherent burst interferogram is then:

(A3.62)

$$\begin{aligned} S_{ii,C,LP}(f) &= H_{LP}(f)\left(\sum_m S_{u_2u_2,m}(t,f) \otimes_f \sum_n S_{u_1u_1,n}(t,f) + F_\tau\left\{ \sum_n E\{ i_n^*(t)\} \sum_m E\{ i_n(t+\tau)\} \right\} \right) \\ &= H_{LP}(f)\, S_{ii,C}(f) \end{aligned}$$

This means, either a suitably weighted rect-function for the low pass filter is required or both interferograms are filtered with a suitably weighted low pass filter of shape $H_{LP}(.)$ in order to obtain the anticipated equivalence (Figure A3.8).

Appendix 4

Average Raw Data Burst Spectrum

A4.1 Average Spectrum of a Raw Data Burst for Homogenous Target

The power spectral density (PSD) of raw data of uniform target is calculated from:

$$S_{dd,n}(f) = \mathrm{F}_\tau\left\{ \mathrm{E}\left\{ d^*(t)\, d(t+\tau)\right\}\right\} = \mathrm{E}\left\{ d^*(t)\, \mathrm{F}_\tau\left\{ d(t+\tau)\right\}\right\} \qquad (A4.1)$$

with $\mathrm{F}_\tau\{.\}$ the Fourier transform operator with respect to τ and $d(t)$ the burst-mode raw data:

$$\begin{aligned} d(t) &= \int dt'\, \chi(t')\, h_{raw,n}(t,t') \\ &= \int dt'\, \chi(t')\, A(FM[t-t'])\, \mathrm{rect}\left(\frac{t-nT_P}{T_B}\right) \exp\left(j\,\pi\, FM\,(t-t')^2\right) \end{aligned} \qquad (A4.2)$$

where the target is modelled as a zero mean, complex Gaussian process with unit variance.

After reordering the integration sequence and evaluation of the expectation value operator the following expression is obtained:

(A4.3)

$$\begin{aligned} S_{dd,n}(f) &= \int dt'\, A(FM[t-t'])\, \mathrm{rect}\left(\frac{t-nT_P}{T_B}\right) \exp\left(j\,\pi\, FM\,(t-t')^2\right) F_\tau\left\{ h_{raw,n}(t+\tau,t')\right\} \\ &= A(f) \exp\left(-j\,\pi\,\frac{f^2}{FM}\right) \mathrm{rect}\left(\frac{t-nT_P}{T_B}\right) \exp(j\,2\pi\, f\, t) \\ &\quad \int dt'\, A(FM[t-t'])\, \mathrm{rect}\left(\frac{FM\,t'+f+nW_P}{W_B}\right) \exp\left(-j\,\pi\, FM(t-t')^2\right) \exp(-j\,2\pi\, f\, t')\, dt' \end{aligned}$$

The integral can be solved using the principle of stationary phase, assuming a sufficiently high time bandwidth product, and the PSD of the raw data is:

$$S_{dd,n}(f) = A^2(f)\, \mathrm{rect}\left(\frac{t-nT_P}{T_B}\right). \qquad (A4.4)$$

This means that the raw data PSD is a function of f and t. Its time extent is determined by the burst duration T_B and the full SAR bandwidth is covered with weight $A^2(f)$, the PSD of the conventional SAR data Figure A4.1.

A4.2 Spectrum of a Raw Data Burst for Non-homogenous Target

For non-homogenous targets the raw data is spectrum is

(A4.5)

$$\mathrm{F}_t\{d(t)\} = D(f)$$

$$\int dt' \chi(t') \mathrm{F}_t\{h_{raw,n}(t,t')\}$$

$$\int dt' \chi(t') A(f) \mathrm{rect}\left(\frac{t' - (nT_P + f/|FM|)}{T_B}\right) \exp\left(-j\pi \frac{f^2}{FM}\right) \exp(-j\,2\pi\, t' f)$$

$$= \int dt' \chi(t') \; A(f) \exp(-j\pi f (nT_P + f/|FM|)) \; \mathrm{rect}\left(\frac{(nT_P + f/|FM|) - t'}{T_B}\right) \exp(j\,2\pi f [(nT_P + f/|FM|) - t'])$$

$$= (\chi(t) *_t H_{raw,n}(f,t))(t = nT_P + f/|FM|)$$

with $F_t\{.\}$ and '$*_t$' the Fourier transform and convolution in t dimension, respectively. The Fourier pair $h_{raw,n}(t,t') \rightarrow H_{raw,n}(f,t')$ represents the ScanSAR raw data system behaviour (section 3.1.1.). Equation (A4.5) expresses the fact that the Fourier transform of the raw data is the convolution of the scene reflectivity function and the ScanSAR raw data transfer function.

For example, consider $T_A/T_B = T_A/T_P \; N_S = N_L \; N_S$ point scatterer:

(A4.6) $$\chi(t) = \sum_{N_S \, N_L} a_m \, \delta(t - m\, T_B)$$

then the raw data spectrum is:

(A4.7)

$$D(f) = \sum_{m=-\lceil N_S N_L/2 \rceil}^{\lfloor N_S N_L/2 \rfloor} a_m \; A(f)\,\mathrm{rect}\left(\frac{f + nW_P + FM\; mT_B}{T_B} \right) \exp\left(-j\,\pi\,\frac{f^2}{FM} \right) \exp\left(j\,2\pi\; f\; mT_B \right)$$

where $\lfloor . \rfloor$ and $\lceil . \rceil$ are operators yielding the lower or upper integer value. The spectrum is depicted in figure A4.2 for $N_S\; N_L = 5$ and $a_m = 1$ for $m \neq 1$ and $a_m = 2$ for $m = 1$. The strong scatterer with $a_m = 2$ 'distorts' the raw data spectrum in contrast to the spectrum in figure A4.1 obtained for homogenous targets. Hence, Doppler estimation which is based on the estimation of the power spectral density of the raw data requires a larger number of azimuth samples to average out the effect of strong targets (section 4.1.2). This problem is not an issue for conventional SARs, since all targets are represented with the full SAR bandwidth. Difficulties only appear at the estimation window and raw data matrix edges (partially covered chirps)(Bamler 1991) and in areas where a sudden change in intensity occurs, e.g. at land/sea boundaries (Cumming 2001).

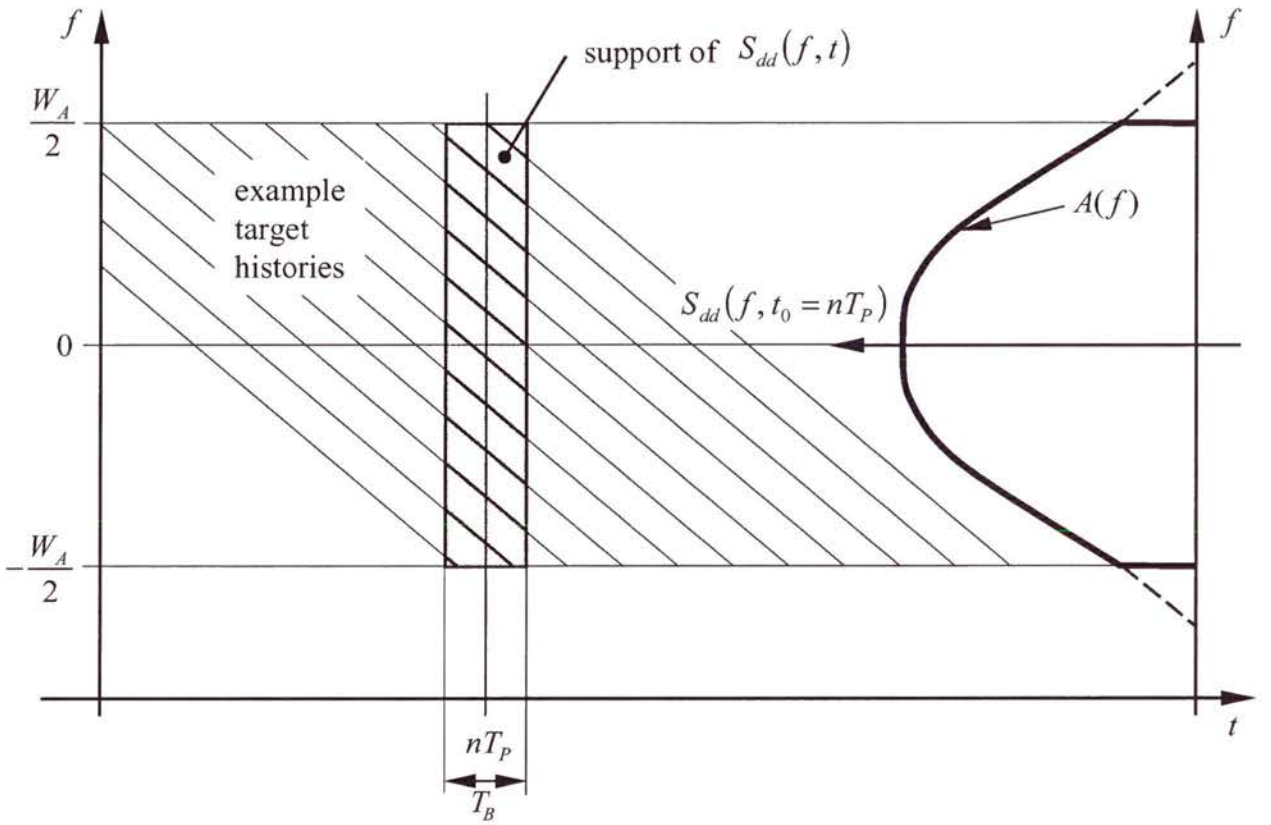

Figure A4.1: Support and frequency envelope of the raw data power spectral density $S_{dd}(f,t)$.

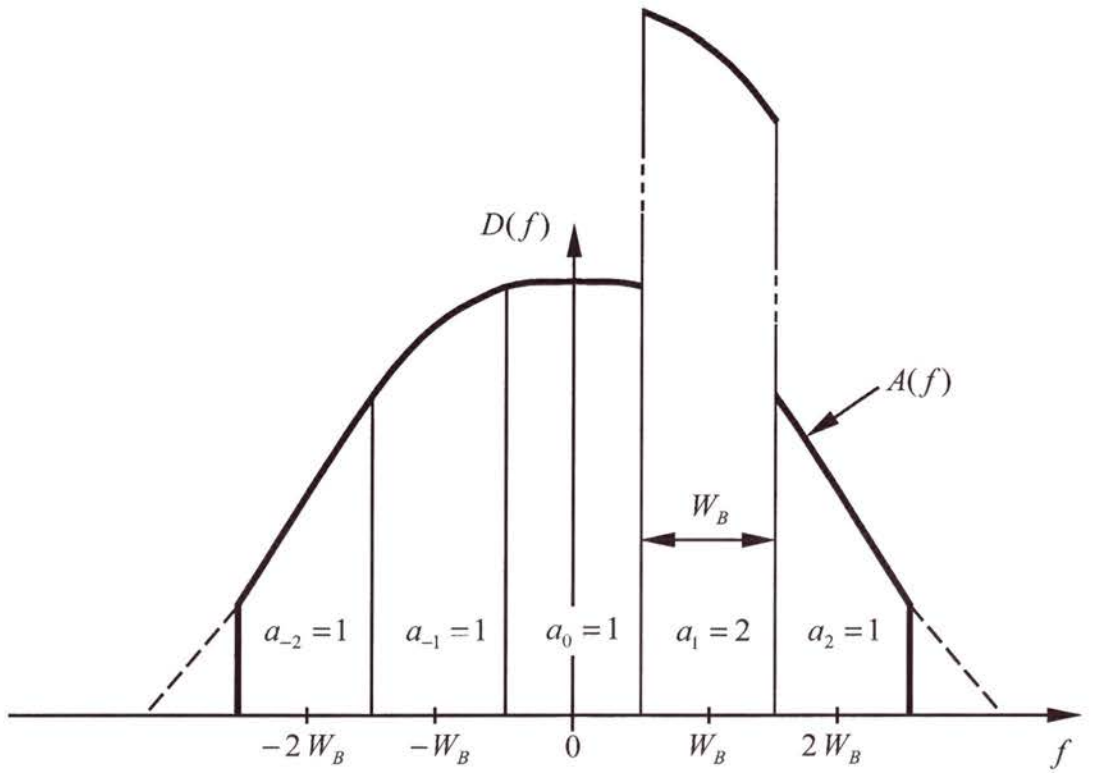

Figure A4.2: Example burst-mode raw data spectrum for a train of point scatterers with distance T_B. One of the scatterers (m=1) has double the amplitude compared to the remaining four scatterers and introduces a considerable deviation from the original envelope $A(f)$.

Appendix 5

PRF Band Determination Using the Range Look Correlation Technique for ScanSAR Signals

Figure A5.1 shows the integration path of the SAR processor in a range versus raw data time co-ordinate system:

$$R(t,R_0)=\sqrt{R_0^2+[v_S\,(t-t_0-t_c)]^2} \approx R_0\left(1+\frac{1}{2}\left(\frac{v_S\,(t-t_0-t_c)}{R_0}\right)^2\right) \quad (A5.1)$$

where t_0, v_S, t_c, and R_0 are the time of the point scatterer, the satellite's velocity, the Doppler centroid equivalent offset time ($f_{DC} = FM\,t_c$), and the range of closest approach, respectively. The Taylor series expansion (A5.1) is utilised for the following derivations. In the illustration the segments at $t_{c,1}$ and $t_{c,2}$ represent two bursts acquired with burst cycle time $T_P = \Delta t_c = t_{c,2} - t_{c,1}$. Two further integration paths are depicted which indicate the integration trajectories of the SAR processor for a wrong PRF band setting. The loci of the two 'wrong' parabolas indicate that the focussing positions are offset by a multiple of the PRF equivalent time $T_{PRF} = PRF/|FM|$ and that the target will be focussed at different range positions in the two bursts. This distance is calculated from the range position difference $\Delta R(n_{PRF,1}\,T_{PRF})$ of positions P_{11} and P_{12} for the 'correct' PRF band index $n_{PRF,1}$ and $\Delta R(n_{PRF,2}\,T_{PRF})$ of positions P_{11} and P_{21} for the 'wrong' PRF band index $n_{PRF,2}$:

$$\delta\Delta R = \Delta R_{\Delta tc}(n_{PRF,2}\,T_{PRF}) - \Delta R_{\Delta tc}(n_{PRF,1}\,T_{PRF}) \quad (A5.2)$$

where the differences $\Delta R(n_1 t_{PRF})$ and $\Delta R(n_2 t_{PRF})$ may be obtained from:

$$\Delta R_{\Delta tc}(n_{PRF}\, T_{PRF}) = \left.\frac{\partial R}{dt}\right|_{t=t_{c,1}} \Delta t_c = \frac{v_S{}^2 \left(t_{c,1} - t_0 - \left[n_{PRF}\, t_{PRF} + t_{c,b}\right]\right)}{R_0} T_P \qquad (A5.3)$$

where $t_{c,b}$ denotes the base band Doppler centroid time equivalent; the Taylor expansion of (A5.1) was adopted. Then, the difference in range position is:

$$\delta\Delta R = \frac{v_S{}^2}{R_0} \frac{PRF}{|FM|} \left(n_{PRF,2} - n_{PRF,1}\right) T_P . \qquad (A5.4)$$

Hence, from measuring the difference in range position $\delta\Delta R$ of, e.g. a point-like strong target, in two bursts that were focussed using an initial setting $n_{,2}$ for the PRF band index, the correct PRF band can be found by:

$$n_{PRF,1} = n_{PRF,2} - \frac{R_0 |FM|}{v^2\, PRF\, T_P} \delta\Delta R . \qquad (A5.5)$$

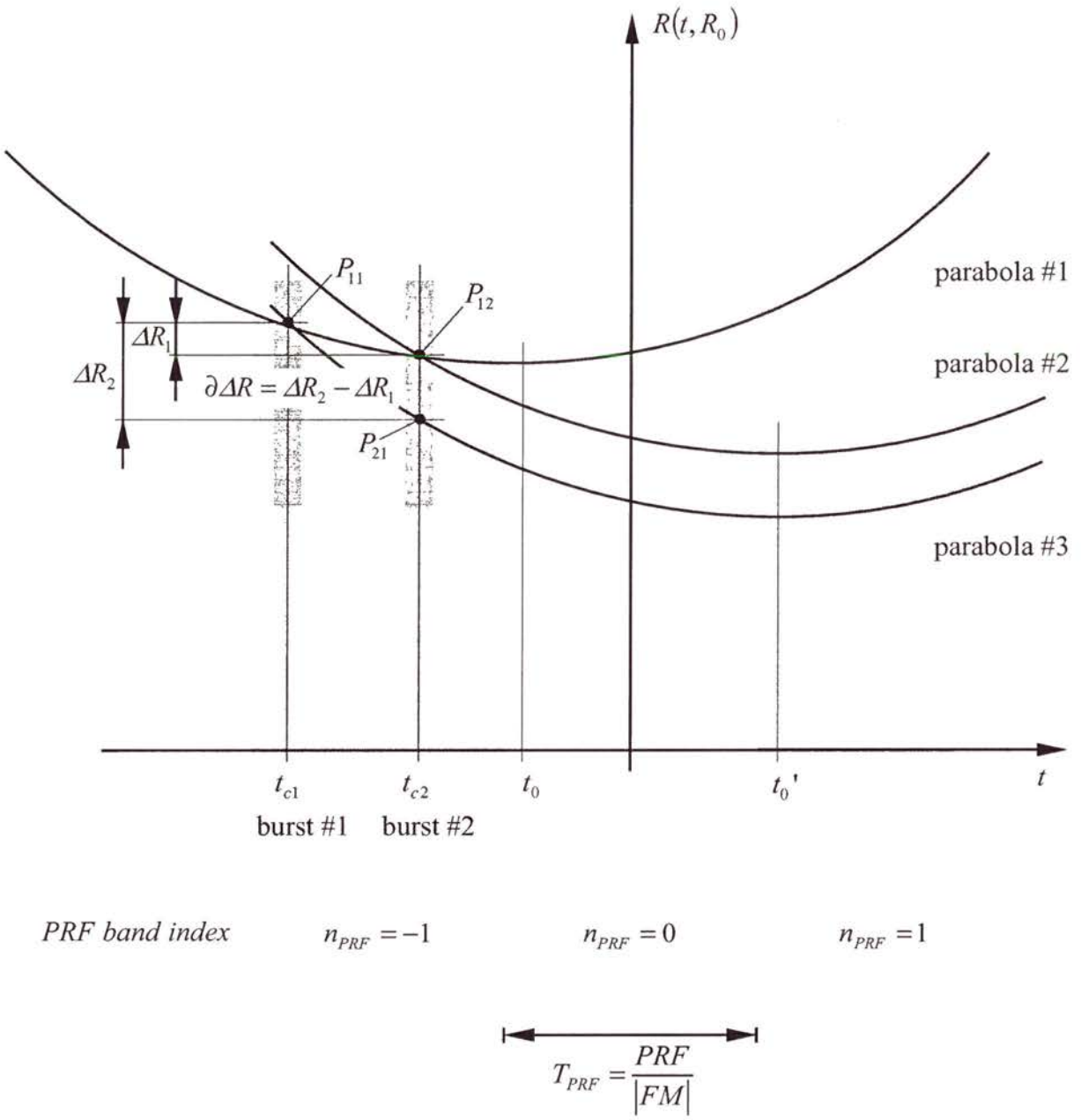

Figure A5.1: Range displacement $\delta\Delta R$ of a target appearing in two individually focussed bursts for a wrong PRF band index n_{PRF} = - 2 (parabolas #2 and #3). It is the range offset between parabolas #2 and #3. The target history of burst #1 (#2) is focussed along parabola #3 (#2) and the response appears at $t_0' = t_0 + T_{PRF}$. The correct PRF band index is n_{PRF} = -1 when the target is focussed along parabola #1 and positioned at t_0.

Appendix 6

Maximum of Interferogram Spectrum Correlation Technique

This technique works as follows: the discrete Fourier transform of an interferogram patch with N samples is calculated where the interferogram was formed from SAR images that are mutually mis-registered by a (sample) lag κ. Here, only one dimension is considered but the extension to the two dimensional case is straight forward. Then the maximum is determined from the magnitude of the spectrum. This is done for several shifts κ and the optimum registration is found where the maxima of the interferogram spectra have a maximum (figure 4.3 and 4.4).

The algorithm can be described as follows:

(A6.1) $$\kappa = \arg\max_{(\kappa)} \left| \mathrm{DFT}\left\{ u_1[i+\kappa]\, u_2^*[i] \right\} \right|$$

or explicitly

(A6.2) $$\kappa = \arg\max_{(\kappa)} \left| \sum_N u_1[i+\kappa]\, u_2^*[i] \exp\left(-j\, 2\pi \frac{i\, \ell_0(\kappa)}{N} \right) \right|$$

with $\ell_0(\kappa)$ the frequency index of the individual spectrum's maximum that depends on the current mis-registration κ and on the terrain phase that may be modelled as a linear phase within the estimation window. Equation (A6.2) is, however, the cross-correlation function of u_1 and u_2 where a linear phase is reduced before summation in order to obtain an uncorrupted estimate.

Appendix 7

Co-registration Errors due to the use of Non-optimal Orbits

Resampling polynomials (section 2.1.3) may be derived from geometry, i.e. with the use of orbit data and a reference ellipsoid. The first section of this appendix discusses the effect of orbit errors on the rotational parts of the resampling polynomials and the second part explores the effect of orbit errors on the determination of the range co-registration polynomial.

A7.1 Azimuth

Figure 7.1 illustrates a crossing orbits configuration leading to mutually rotated SAR images. This mutual rotation may be represented by the following equations:

$$\begin{aligned} x_2 &= \Delta x + \cos\varepsilon\ R_1 + \sin\varepsilon\ x_1 \\ R_2 &= \Delta R - \sin\varepsilon\ R_1 + \cos\varepsilon\ x_1 \end{aligned} \qquad (A7.1)$$

where x_1 (x_2) and R_1 (R_2) are the master (slave) azimuth and range co-ordinate, respectively (resampling model of section 2.1.3.) The angle ε can be approximately calculated from:

$$\varepsilon \approx \operatorname{atan}\left(\frac{D}{L}\right) \qquad (A7.2)$$

where D denotes the distance of the orbits at scene centre and L denotes the distance to an imaginary intersection position far away from the scene. For the following discussion it is assumed that the orbits are located within the same plane and that all individual orbit errors are bundled into along and across track errors of orbit 2. For the two errors to be negligible their individual impact:

$$\Delta\varepsilon_D = \frac{\partial\varepsilon}{\partial D}\sigma_D = \frac{1}{1+\left(\frac{D}{L}\right)^2}\frac{\sigma_D}{L} \overset{D\ll L}{\approx} \frac{\sigma_D}{L} \qquad (A7.3)$$

$$\Delta\varepsilon_L = \left|\frac{\partial\varepsilon}{\partial L}\right|\sigma_L = \frac{D\,\sigma_L}{L^2+D^2} \overset{D\ll L}{\approx} \frac{D\,\sigma_L}{L^2} \qquad (A7.4)$$

on the error of the inter orbit angle should be lower 0.01:

(A7.5) $\Delta\varepsilon < 0.01$ rad.

For equation (A7.4), it was assumed that the intersection position varies due to an azimuth orbit shift. From the nominal RADARSAT-1 along and across track orbit errors of 100 m and 20 m, respectively (section 4.2.8), the generous along and across track errors $\sigma_D = 40$ m and $\sigma_L = 200$ m are assumed. For the angle error according to equation (A7.3) and the condition (A7.5) we obtain that L must be larger than 4 km. This requirement is easily met for common azimuth scene extents of 100 km to 300 km when it may be assumed that the point of the orbits' intersection is located far from the scene centre (this assumption is met for the example baseline configuration of the data set in section 7.1.) In the case the along track errors are examined a lower bound of 20 km is found for the distance L of the scene centre to the orbit intersection position. In this case a maximum orbit distance D at scene centre of 7 km is assumed which approximates the largest critical baseline allowed for any RADARSAT-1 mode (section 7.1). Hence, the accuracy requirements for the along track errors are easily met if standard scene extents are assumed.

A7.2 Range

A7.2.1 Introduction

Slant range resampling is carried out according to the following polynomial (section 2.1.3):

(A7.6) $$R_2 = a_0 + a_1 R_1 + a_2 x_1 + a_3 R_1 x_1 + a_4 R_1^2 + a_5 x_1^2$$

where R_1 (R_2), and x_1 are the primary (secondary) interferometric channel range distance to the target and the primary channel azimuth co-ordinate, respectively. For the error propagation of the orbit information errors into the resampling polynomial only the range dependent components are considered, since errors in the rotational component of the resampling polynomial were discussed in the previous section on azimuth mis-registration. Moreover, a rect-linear acquisition geometry, flat earth – i.e. constant height, and zero Doppler data representation are assumed. The resampling polynomial provides the answer to the question as to what distance or range of the secondary satellite position to a target is, given the range between primary satellite and target.

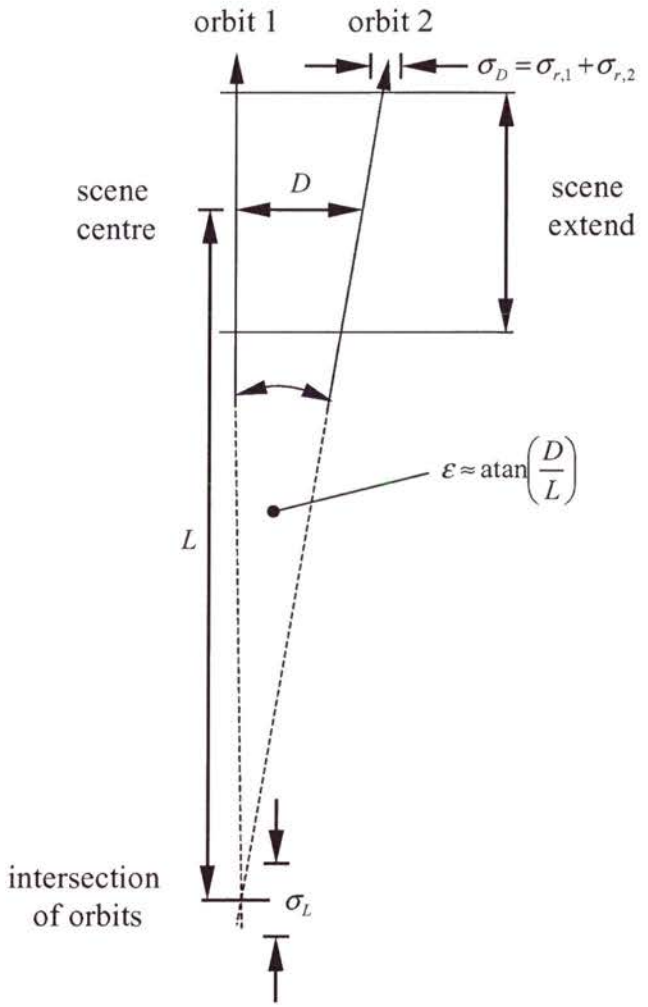

Figure A7.1: Propagation of the orbit errors into azimuth dependent resampling errors. orbit 1 is considered error free and the individual along and across track orbit errors are bundeled into the orbit 2 error variances σ_L and σ_D. The orbits are considered to reside in the same plane.

In most cases a second order polynomial of the form:

(A7.7) $$\Delta R = R_2 - R_1 = b_0 + b_1(R_1 - R_0) + b_2(R_1 - R_0)^2$$

is sufficient (R_0 is a reference range) and it may be obtained from a quadratic Taylor series expansion of the range displacement ΔR :

(A7.8) $$\Delta R = \Delta R\big|_{R=R_0} + \frac{\partial \Delta R\big|_{R=R_0}}{\partial R_1}(R_1 - R_0) + \frac{1}{2!}\frac{\partial^2 \Delta R\big|_{R=R_0}}{\partial R_1^{\,2}}(R_1 - R_0)^2 .$$

A comparison of the coefficients in (A7.7) and (A7.8) yields for the coefficients b_i, $i \in \{0, 1, 2\}$:

$$b_0 = \Delta R\big|_{R=R_0}$$

(A7.9) $$b_1 = \frac{\partial \Delta R\big|_{R_1=R_0}}{\partial R_1}$$

$$b_2 = \frac{1}{2!}\frac{\partial^2 \Delta R\big|_{R_1=R_0}}{\partial R_1^{\,2}} .$$

The total error Δb_i of the coefficients b_i is calculated as the total derivative:

(A7.10) $$\Delta b_i \approx \mathrm{grad}_{\vec{S}_1}(b_i)\,\vec{\sigma}_{\vec{S}_1} + \mathrm{grad}_{\vec{S}_2}(b_i)\,\vec{\sigma}_{\vec{S}_2}$$

where $\vec{S}_1 = (x_1 \quad y_1 \quad z_1)^T$, $\vec{S}_2 = (x_2 \quad y_2 \quad z_2)^T$ and $\vec{\sigma}_{\vec{S}_1} = (\sigma_{x_1} \quad \sigma_{y_1} \quad \sigma_{z_1})^T$, $\vec{\sigma}_{\vec{S}_2} = (\sigma_{x_2} \quad \sigma_{y_2} \quad \sigma_{z_2})^T$ ($\vec{S}^T$ the transpose of a vector $\vec{S}$) are the satellite positions and their respective error vectors, $\mathrm{grad}_{\vec{S}}(\ )$ denotes the gradient of b_i with respect to the satellite position $\vec{S}$.

Within the next section the coefficients b_i and their deviations Δb_i due to uncertainties in knowledge of the geometry are discussed. As an example the equations are evaluated for RADARSAT-1 nominal orbit conditions.

A7.2.2 Calculation of the coefficients b_i, $i = 0, 1, 2$, from orbit and target position information

Figure A7.2 shows the assumed geometry for the following deliberations. The satellite positions are represented by the vectors $\vec{S}_1$ and $\vec{S}_2$ referenced from the Earth's centre, $\vec{B} = \vec{S}_2 - \vec{S}_1$ being the baseline vector. The lengths of the vectors $\vec{B}$, $\vec{R}_1$, and $\vec{R}_2$ are referred to as B, R_1, and R_2, respectively. A target at position $\vec{T} = (x_T \quad y_T \quad z_T)^T$ imaged from satellite positions $\vec{S}$ and $\vec{S}_2$ appears at slightly different range positions with distance:

(A7.11) $$\Delta R = R_2 - R_1 \approx \frac{\vec{B}\,\vec{R}_1}{R_1},$$

that is the projection of the Baseline onto the vector $\vec{R}_1$, corresponding to the well-known approximation $\Delta R \approx B \cdot \sin(\xi - \theta)$ with θ the look angle and ξ the baseline angle.

Using the above definitions, the range difference is calculated from:

(A7.12) $$\Delta R = \frac{(x_2 - x_1)(x_1 - x_T) + (y_2 - y_1)(y_1 - y_T) + (z_2 - z_1)(z_1 - z_T)}{\sqrt{(x_1 - x_T)^2 + (y_1 - y_T)^2 + (z_1 - z_T)^2}}.$$

Both acquisitions are assumed to have taken place with zero-Doppler and, hence, the baseline vector is an element of the x-z-plane. When the range position R_1 increases (decreases), the considered target x-component x_T increases (decreases) – assuming a terrain surface with constant height.

Hence, in order to differentiate (A7.12), the partial derivative $\partial \Delta R / \partial x_T$ is formed first and via the chain rule of differentiation the derivatives $\partial \Delta R / \partial R_1$ and $\frac{\partial}{\partial R_1}\frac{\partial \Delta R}{\partial R_1}$ are obtained:

(A7.13) $$\frac{\partial \Delta R}{\partial R_1} = \frac{\partial \Delta R}{\partial x_T}\frac{\partial x_T}{\partial R_1}$$

(A7.14)
$$\begin{aligned}\frac{\partial}{\partial R_1}\frac{\partial \Delta R}{\partial R_1} &= \left(\frac{\partial}{\partial r_1}\frac{\partial \Delta R}{\partial x_T}\right)\frac{\partial x_T}{\partial R_1} + \frac{\partial \Delta R}{\partial x_T}\left(\frac{\partial}{\partial R_1}\frac{\partial x_T}{\partial R_1}\right) \\ &= \left(\frac{\partial^2 \Delta R}{\partial {x_T}^2}\frac{\partial x_T}{\partial R_1}\right)\frac{\partial x_T}{\partial R_1} + \frac{\partial \Delta R}{\partial x_T}\frac{\partial^2 x_T}{\partial {R_1}^2} \\ &= \frac{\partial^2 \Delta R}{\partial {x_T}^2}\left(\frac{\partial x_T}{\partial R_1}\right)^2 + \frac{\partial \Delta R}{\partial x_T}\frac{\partial^2 x_T}{\partial {R_1}^2}\end{aligned}$$

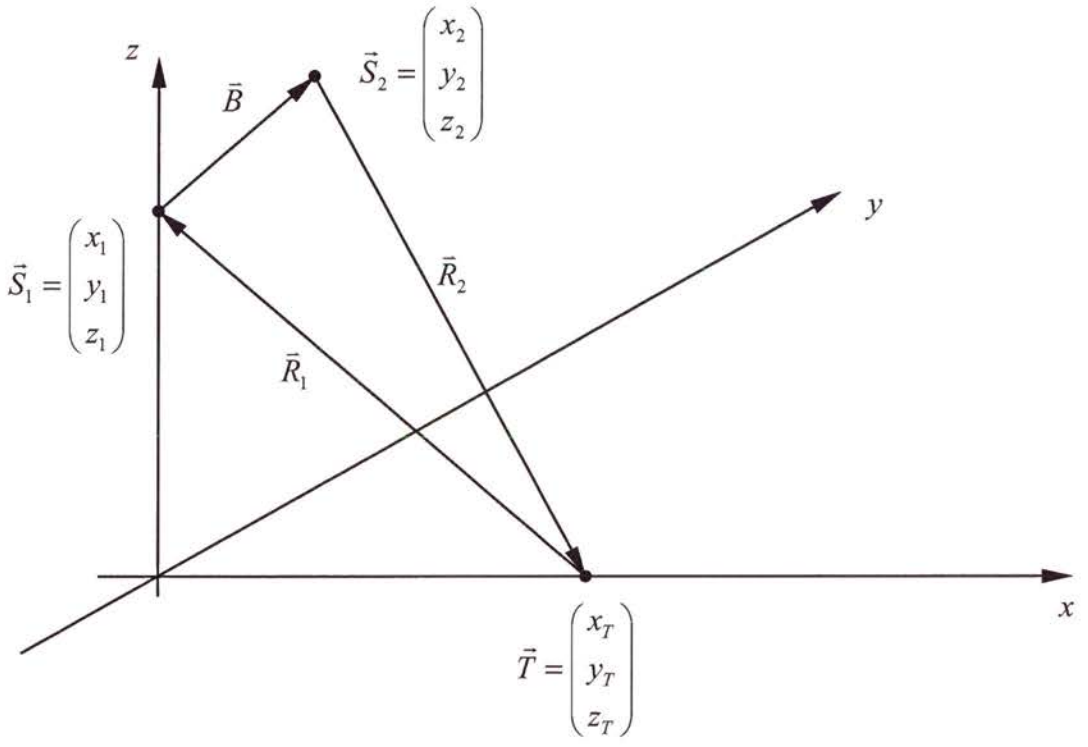

Figure A7.2: Geometry for the calculation of the range co-registration polynomial coefficients b_i, $i=\{0,1,2\}$, and their errors Δb_i. S_1, S_2, R_1, R_2, B, denote the primary and secondary satellite position, the ranges of the primary and secondary satellite to the target position T, and the baseline vector, respectively.

This means the derivatives $\frac{\partial \Delta R}{\partial x_T}$, $\frac{\partial^2 \Delta R}{\partial {x_T}^2}$, $\frac{\partial x_T}{\partial R_1}$, and $\frac{\partial^2 x_T}{\partial {R_1}^2}$ are of importance:

$$\frac{\partial \Delta R}{\partial x_T} = \frac{-(x_2 - x_1) R_1}{\sqrt{(x_1 - x_T)^2 + (y_1 - y_T)^2 + (z_1 - z_T)^2}^2} + \frac{\frac{(x_1 - x_T)}{R_1}[(x_2 - x_1)(x_1 - x_T) + (y_2 - y_1)(y_1 - y_T) + (z_2 - z_1)(z_1 - z_T)]}{\sqrt{(x_1 - x_T)^2 + (y_1 - y_T)^2 + (z_1 - z_T)^2}^2} \qquad \text{(A7.15)}$$

$$= \frac{-(x_2 - x_1) R_1 + (x_1 - x_T)\Delta R}{{R_1}^2}$$

$$= \frac{-(x_2 - x_1)}{R_1} + \frac{(x_1 - x_T)}{R_1}\frac{\Delta R}{R_1}$$

$$\frac{\partial^2 \Delta R}{\partial {x_T}^2} = \frac{\partial}{\partial x_T}[-\frac{(x_2 - x_1)}{R_1} + (x_1 - x_T)\frac{\Delta R}{{R_1}^2}]$$

$$= \frac{(x_2 - x_1)}{{R_1}^2}\frac{(x_1 - x_T)}{R_1} + [-\frac{\Delta R}{{R_1}^2} + (x_1 - x_T)\frac{\partial}{\partial x_T}\frac{\Delta R}{{R_1}^2}]$$

$$= \frac{(x_2 - x_1)(x_1 - x_T)}{{R_1}^3} - \frac{\Delta R}{{R_1}^2} + (x_1 - x_T)\frac{\frac{\partial \Delta R}{\partial x_T}{R_1}^2 - \Delta R\frac{\partial {R_1}^2}{\partial x_T}}{{R_1}^4}$$

$$= \frac{(x_2 - x_1)(x_1 - x_T)}{{R_1}^3} - \frac{\Delta R}{{R_1}^2} + (x_1 - x_T)\left((\frac{(x_2 - x_1)}{{R_1}^3} + \frac{(x_1 - x_T)}{{R_1}^2}\frac{\Delta R}{{R_1}^2}) + \frac{2\Delta R(x_1 - x_T)}{{R_1}^4}\right)$$

$$= (3\frac{(x_1 - x_T)^2}{{R_1}^2} - 1)\frac{\Delta R}{{R_1}^2} + \frac{2(x_2 - x_1)(x_1 - x_T)}{{R_1}^3} \qquad \text{(A7.16)}$$

where $\frac{\partial R_1}{\partial x_T} = -\frac{x_1 - x_T}{R_1}$ and $\frac{\partial {R_1}^2}{\partial x_T} = -2(x_1 - x_T)$.

The target positions depend on the range distance R_1 by:

$$x_T = x_1 - \sqrt{R_1^2 - [(y_1 - y_T)^2 + (z_1 - z_T)^2]} \qquad (A7.17)$$

with first and second derivatives:

$$\frac{\partial x_T}{\partial R_1} = -\frac{R_1}{(x_1 - x_T)} \qquad (A7.18)$$

$$\frac{\partial^2 x_T}{\partial R_1^2} = -\frac{(x_1 - x_T) - \frac{R_1^2}{(x_1 - x_T)}}{(x_1 - x_T)^2} = \frac{R_1^2}{(x_1 - x_T)^3} - \frac{1}{(x_1 - x_T)} \qquad (A7.19)$$

The first and second order derivative with respect to r_1 is then:

$$\frac{\partial \Delta R}{\partial R_1} = \frac{\partial \Delta R}{\partial x_T}\frac{\partial x_T}{\partial R_1} = \frac{\Delta R}{R_1} - \frac{(x_2 - x_1)}{(x_1 - x_T)} \qquad (A7.20)$$

and

$$\frac{\partial}{\partial R_1}\frac{\partial \Delta R}{\partial R_1} = \frac{\partial^2 \Delta R}{\partial x_T^2}\left(\frac{\partial x_T}{\partial R_1}\right)^2 + \frac{\partial \Delta R}{\partial x_T}\frac{\partial^2 x_T}{\partial R_1^2} = \frac{2\Delta R}{R_1^2} + \frac{3(x_2 - x_1)}{R_1 (x_1 - x_T)^2} - \frac{R_1 (x_2 - x_1)}{(x_1 - x_T)^3} \qquad (A7.21)$$

For a more suitable representation the results, the formulae are summarised in table 7.1. The errors for the coefficients are calculated and shown in table 7.3 (RADARSAT-1 parameters were assumed as listed in table 7.2.) The impact of orbit knowledge uncertainties on the higher order coefficients seems to be less than for the constant term. Finally, from the values in Table 7.3, the orbit data of RADARSAT-1 should be evaluated carefully and its application for co-registration of the interferometric data set is to be decided for each individual case.

Table A7.1: Collection of the partial derivatives of the coefficients b_i, $i \in \{0, 1, 2\}$.

i	0	1	2
$b_i = \frac{\partial^i \Delta R}{\partial R_1^{\,i}}$ *)	$= \Delta R$ $= \frac{(x_2 - x_1)(x_1 - x_T)}{\sqrt{(x_1 - x_T)^2 + (y_1 - y_T)^2 + (z_1 - z_T)^2}}$ $+ \frac{(y_2 - y_1)(y_1 - y_T)}{\sqrt{(x_1 - x_T)^2 + (y_1 - y_T)^2 + (z_1 - z_T)^2}}$ $+ \frac{(z_2 - z_1)(z_1 - z_T)}{\sqrt{(x_1 - x_T)^2 + (y_1 - y_T)^2 + (z_1 - z_T)^2}}$	$\frac{\Delta R}{R_1} - \frac{(x_2 - x_1)}{(x_1 - x_T)}$	$\frac{2\Delta r}{R_1^{\,2}} + \frac{3(x_2 - x_1)}{R_1 (x_1 - x_T)^2} - \frac{R_1 (x_2 - x_1)}{(x_1 - x_T)^3}$
$\frac{\partial b_i}{\partial u}$, $u \in \{x_1, y_1, z_1, z_T\}$	$\frac{-2u_1 + u_2 + u_T}{R_1} - \frac{\Delta R(u_1 - u_T)}{R_1^{\,2}}$ $u \in \{x, y, z\}$	$\frac{-2x_1 + x_2 + x_T}{R_1^{\,2}} - \frac{2\Delta r(x_1 - x_T)}{R_1^{\,3}}$ $+ \frac{1}{x_1 - x_T} + \frac{x_2 - x_1}{(x_1 - x_T)^2}$	$\frac{2(-2x_1 + x_2 + x_T)}{R_1^{\,3}} - \frac{6\Delta R(x_1 - x_T)}{R_1^{\,4}} - \frac{3(x_1 - x_T) + 4(x_2 - x_1)}{(x_1 - x_T)^2 R_1}$ $- \frac{3(x_2 - x_1)}{R_1^{\,3}} + \frac{R_1[3(x_2 - x_1) + (x_1 - x_T)]}{(x_1 - x_T)^4}$
		$\frac{-2u_1 + u_2 + u_T}{R_1^{\,2}}$ $- \frac{2\Delta R(u_1 - u_T)}{R_1^{\,3}}$, $u \in \{y, z\}$	$\frac{2(-2u_1 + u_2 + u_T)}{R_1^{\,3}} - \frac{6\Delta r(u_1 - u_T)}{R_1^{\,4}}$ $- \frac{3(x_2 - x_1)(u_1 - u_T)}{(x_1 - x_T) R_1^{\,3}} - \frac{(x_2 - x_1)(u_1 - u_T)}{(x_1 - x_T)^3 R_1}$, $u \in \{y, z\}$
	$- \frac{z_2 - z_1}{R_1} + \frac{\Delta R(z_1 - z_T)}{R_1^{\,2}}$	$\frac{2\Delta R(z_1 - z_T)}{R_1^{\,3}} - \frac{z_2 - z_1}{R_1^{\,2}}$	$- \frac{2(z_2 - z_1)}{R_1^{\,3}} + \frac{6\Delta R(z_1 - z_T)}{R_1^{\,4}}$ $+ \frac{3(z_1 - z_T)(x_2 - x_1)}{(x_1 - x_T) R_1^{\,3}} + \frac{(z_1 - z_T)(x_2 - x_1)}{(x_1 - x_T)^3 R_1}$

*) $R_1 = \sqrt{(x_1 - x_T)^2 + (y_1 - y_T)^2 + (z_1 - z_T)^2}$

Table A7.2: RADARSAT-1 parameter values used for the calculation of the co-registration coefficients b_i, $i \in \{0, 1, 2\}$, and their errors Δb_i, $i \in \{0, 1, 2\}$

σ_r/m	40
σ_y/m	200
θ/1°	30
ξ/1°	-159.0
B/m	167
z_1/km	798
f_s/MHz	12.92
pixel spacing/(m/pixel)	11.6
$\vec{S}_1$/m	$\begin{pmatrix} 0 \\ 0 \\ 798 \cdot 10^3 \end{pmatrix}$
$\vec{S}_2$/m	$\begin{pmatrix} 156.1 \\ 0 \\ 798 \cdot 10^3 \end{pmatrix}$
$\vec{B}$/m	$\begin{pmatrix} -156.1 \\ 0 \\ -59.8 \end{pmatrix}$
$\vec{T}$/m	$\begin{pmatrix} 1.38218 \cdot 10^6 \\ 0 \\ 0 \end{pmatrix}$
$\vec{R}_1$/m	$\begin{pmatrix} -1.38218 \cdot 10^6 \\ 0 \\ 798 \cdot 10^3 \end{pmatrix}$

Table A7.3: Collection of the parameter errors for the parameters in table 7.2 a) and 7.2b).

i	0	1	2
b	26.12 m	$9.66 \cdot 10^{-6}$	$-2.47 \cdot 10^{-10}$ m^{-1}
$\sigma_{b_i,x_1} = \left\| \frac{\partial b_i}{\partial x_1} \right\| \sigma_{x_1}$	24.47 m	0.53	0.16 m^{-1}
$\sigma_{b_i,y_1} = \left\| \frac{\partial b_i}{\partial y_1} \right\| \sigma_{y_1}$	0	0	0
$\sigma_{b_i,z_1} = \left\| \frac{\partial b_i}{\partial z_1} \right\| \sigma_{z_1}$	1.22 m	0.92	$4.49 \cdot 10^{-2}$ m^{-1}
$\sigma_{b_i,z_T} = \left\| \frac{\partial b_i}{\partial z_T} \right\| \sigma_{z_T}$	$1.25 \cdot 10^{-5}$ m	$4.29 \cdot 10^{-5}$	$7.62 \cdot 10^{-6}$ m^{-1}
$\frac{\sigma_{b_i}}{b} = \frac{\sqrt{\sum_u \sigma_{b_i,u}^2}}{b}$ $u \in \{x_1, y_1, z_1, z_T\}$	1.08	0.22	0.21

Appendix 8

Relationship of Interferogram Phase Stability and Coherence

This appendix outlines the derivation of a relationship of the phase stability measure (section 4.2.7):

$$\hat{\gamma}' = \frac{\left| \sum_{N} i_n \right|}{\sqrt{\sum_{N} |i_n|^2}} \qquad (A8.1)$$

with respect to the coherence. For statements on the relationship the following measure is examined instead:

$$\gamma' = \frac{|\mathrm{E}\{ i \}|}{\sqrt{\mathrm{E}\{ |i|^2 \}}} \qquad (A8.2)$$

and (A8.1) is considered an estimate of this ratio.

Using the formulae:

$$\mathrm{E}\{ i \} = \gamma \, \mathrm{E}\{ |u_1|^2 \} \, \mathrm{E}\{ |u_2|^2 \}, \qquad (A8.3)$$

$$\mathrm{E}\{ |u|^2 \} = \mathrm{R}_{uu}(0) = \int df \, \mathrm{S}_{uu}(f), \qquad (A8.4)$$

$$\mathrm{E}\{ |i|^2 \} = \mathrm{R}_{ii}(0) = \int df \, \mathrm{S}_{ii}(f), \qquad (A8.5)$$

and

$$\int df \, \overline{\mathrm{S}}_{ii}(f) = 1 + |\gamma|^2 \qquad (A8.6)$$

the following relationship between coherence and the interferogram phase stability is found:

$$|\gamma'|^2 = \frac{|\gamma|^2}{1 + |\gamma|^2} \qquad (A8.7)$$

This means, when γ' is known the coherence magnitude can be calculated:

$$|\gamma|^2 = \frac{|\gamma'|^2}{|\gamma'|^2 - 1}. \qquad (A8.8)$$

Note that in the calculation of the interferogram phase stability measure, it is favourable to reduce the terrain phase $\phi_{terrain}$ before summing up the complex pointers, otherwise the value is underestimated:

$$\hat{\gamma}' = \frac{\left| \sum_N i_n \exp(-j\,\phi_{terrain}(n)) \right|}{\sqrt{\sum_N |i_n|^2}} \qquad (A8.9)$$

References

Armour, B., P. Farris-Manning and P. W. Vachon (1997). The Suitability of RADARSAT's Orbit for Repeat-Pass SAR Interferometry, in: *Proc. Geomatics in the era of RADARSAT*, Ottawa, Canada, 25-30 May 1997, available on CD-ROM.

Askne, J. I. H., P. B. G. Dammert, L. M. H. Ulander and G. Smith (1997). C-band repeat-pass interferometric SAR observations of the forest, *IEEE Transactions on Geoscience and Remote Sensing*, Vol. 35, No. 1, pp. 25-35.

Bamler, R. (1991). Doppler frequency estimation and the Cramér-Rao bound, *IEEE Transactions on Geoscience and Remote Sensing*, Vol. 29, No. 3, pp. 385-390.

Bamler, R. (1992). A comparison of range-Doppler and wavenumber domain SAR focusing algorithms, *IEEE Transactions on Geoscience and Remote Sensing*, Vol. 30, No. 4, pp. 706-713.

Bamler, R. (1995). Optimum look weighting for burst-mode and ScanSAR processing, *IEEE Transactions on Geoscience and Remote Sensing*, Vol. 33, No. 3, pp. 722-725.

Bamler, R. (2000). Interferometric Stereo Radargrammetry: Absolute Height Determination from ERS-ENVISAT Interferograms, in: *Proc. IGARSS'00*, Honolulu, Hawai, 2000, available on CD-ROM.

Bamler, R. and M. Eineder (1996). ScanSAR processing using standard high precision SAR algorithms, *IEEE Transactions on Geoscience and Remote Sensing*, Vol. 34, No. 1, pp. 212-218.

Bamler, R., D. Geudtner, B. Schättler, U. Steinbrecher, J. Holzner, J. Mittermayer, H. Breit and A. Moreira (1998). RADARSAT SAR Interferometry Using Standard, Fine, and ScanSAR Modes, in: *Proc. Radarsat ADRO Final Symposium*, Montreal, 13-15 October 1998, available on CD-ROM.

Bamler, R. and P. Hartl (1998). Synthetic Aperture Radar Interferometry, *Inverse Problems*, No. 14, pp. R1-R54, 1998.

Bamler, R. and J. Holzner (2000). Processing Techniques for Repeat-Pass ScanSAR Interferometry, in: *Proc. EUSAR 2000*, Munich, Germany, 23-25 May 2000, pp. 719-722.

Bamler, R. and J. Holzner (2002). ScanSAR Interferometry for RADARSAT-2 and -3, *Canadian Journal of Remote Sensing*, in print.

Bamler, R. and D. Just (1993). Phase statistics and decorrelation in SAR interferograms, in: *Proc. IGARSS'93*, Tokyo, Japan, IEEE, pp. 980-984.

Bamler, R. and B. Schättler (1993). SAR data acquisition and image formation, SAR geocoding: data and systems, G. Schreier, Karlsruhe, Wichmann, Vol., pp. 53-102.

Bao, M., C. Brüning and W. Alpers (1997). Simulation of ocean waves imaging by an along-track interferometric synthetic aperture radar, *IEEE Transactions on Geoscience and Remote Sensing*, Vol. 35, No. 3, pp. 618-631.

Bara, M., R. Scheiber, A. Broquetas and A. Moreira (2000). Interferometric SAR Signal Analysis in the Presence of Squint, *IEEE Transactions on Geoscience and Remote Sensing*, Vol. 38, No. 5, pp. 2164-2178, September 2000.

Borgeaud, M. and U. Wegmüller (1996). On the use of ERS SAR interferometry for the retrieval of geo- and bio-physical information, in: *Proc. FRINGE 96 ESA Workshop on Applications of ERS SAR Interferometry*, Zürich, Sep 30 - Oct 2, 1996, ESA, http://www.geo.unizh.ch/rsl/fringe96/.

Breit, H., B. Schättler and U. Steinbrecher (1997). A High-Precision Workstation-Based Chirp Scaling SAR Processor, in: *Proc. IGARSS '97*, Singapore, 1997, available on CD-ROM.

Brown, M. A. (1993). ASAR ScanSAR Operation, in: *Proc. SAR Calibration Workshop*, ESTEC, Noordwijk, The Netherlands, 20-24 September 1993, pp. 325-340.

Brûlé, L. and H. Baeggli (2002). RADARSAT-2 Mission Status, in: *Proc. Open Symposium on Propagation and Remote Sensing*, Garmisch Patenkirchen, Germany, 12-15 Feb. 2002.

Brûlé, L. and H. Baeggli (2002). RADARSAT-2 Program Update, in: *Proc. IGARSS'02*, Toronto, Canada, 24-28 June 2002, IEEE international, available on CD-ROM.

Chang, C. Y., M. Y. Jin, Y.-L. Lou and B. Holt (1996). First SIR-C ScanSAR Results, *IEEE Transactions on Geoscience and Remote Sensing*, Vol. 34, No. 5, pp. 1278-1281, September 1996.

Costantini, M. (1997). A novel phase unwrapping method based on network programming, *IEEE Transactions on Geoscience and Remote Sensing*, Vol. 36, No. 3, pp. 813-821, May 1998.

Cumming, I. G. (2001). Model-Based Doppler Estimation for Frame-Based SAR Processing, in: *Proc. IGARSS '01*, Sydney, Australia, 9-13 July 2001, http://www.ece.ubc.ca/sar/papers/group_bibliography.html.

Cumming, I. G., Y. Guo and F. Wong (1997). Analysis and Precision Processing of RADARSAT ScanSAR data, in: *Proc. Geomatics in the Era of RADARSAT*, Ottawa, Canada, 25-30 May 1997, available on CD-ROM.

Cumming, I. G., Y. Guo and F. Wong (1997). A comparison of phase-preserving algorithms for burst-mode SAR data processing, in: *Proc. IGARSS'97*, Singapore, IEEE, pp. 731-733, available on CD-ROM.

Cumming, I. G., P. F. Kavanagh and M. R. Ito (1986). Resolving the Doppler ambiguity for spaceborne synthetic aperture radar, in: *Proc. IGARSS'86*, Zürich, Switzerland, ESA, pp. 1639-1643.

Cumming, I. G., Wong, F. (1998). The Effect of ScanSAR Parameters on Interferogram Quality, in: *Proc. IGARSS '98*, Seattle, USA, July 1998, pp. 2674-2676, available on CD-ROM.

Currie, A. and M. A. Brown (1992). Wide-swath SAR, *IEE Proceedings-F*, Vol. 139, No. 2, pp. 122-135, 12. April 1992.

Datcu, M., L. Dragos and K. Seidel (1996). Wavelet-based Digital Elevation Model Analysis, in: *Proc. EARSeL'96*, Malta.

Davidson, G. W. and R. Bamler (1998). Multiresolution phase unwrapping for SAR interferometry, *IEEE Transactions on Geoscience and Remote Sensing*, Vol. 37, No. 1 Part: 1, pp. 163-174, January 1999.

Eineder, M. and N. Adam (1997). A flexible system for the generation of interferometric SAR products, in: *Proc. IGARSS'97*, Singapore, available on CD-ROM.

Elachi, C. (1988). Spaceborne radar remote sensing: Applications and techniques. New York, NY, IEEE Press.

Eldhuset, K. (1993). ScanSAR Processing and Simulation, in: *Proc. SAR Calibration Workshop*, ESTEC, Noordwijk, The Netherlands, pp. 309-323.

ESA (1997). ENVISAT Mission Operations - Orbit Maintenance, http://envisat.esa.int/m-s/mission/operations.html#envisat orbit

ESA (1997). ENVISAT Operating Modes, http://envisat.esa.int/instruments/asar/descr/operations.html

ESA (2002). ENVISAT, http://envisat.esa.int/

ESA (2002). ERS-1 and ERS-2 Interferometry Baseline Listing, http://earth1.esrin.esa.it/eeo4.588

Ferretti, A., A. Monti-Guarnieri, C. Prati and F. Rocca (1998). Multi-image DEM reconstruction, in: *Proc. IGARSS'98*, Seattle, USA, 6-10 July 1998, IEEE International, Vol. 3, pp. 1367-1369.

Ferretti, A., C. Prati and F. Rocca (1999). Multibaseline InSAR DEM reconstruction: the wavelet approach, *Transactions on Geoscience and Remote Sensing*, Vol. 37, No. 2, pp. 705-715, March 1999.

Fornaro, G. and A. Monti Guarnieri (2002). Minimum Mean Square Error Space-Varying Filtering of Interferometric SAR Data, *IEEE Transactions on Geoscience and Remote Sensing*, Vol. 40, No. 1, pp. 11-21, January 2002.

Frick, H. G., M. Palsetia, R. Carande and J. C. Curlander (2000). COTS SAR Ground Data Processing for PALSAR application, in: *Proc. EUSAR 2000*, Munich, Germany, 23-25 May 2000, pp. 729-731.

Gabriel, A. K. and R. M. Goldstein (1988). Crossed orbit interferometry: theory and experimental results from SIR-B, *International Journal of Remote Sensing*, Vol. 9, No. 5, pp. 857-872.

Gatelli, F., A. Monti Guarnieri, F. Parizzi, P. Pasquali, C. Prati and F. Rocca (1994). The wavenumber shift in SAR interferometry, *IEEE Transactions on Geoscience and Remote Sensing*, Vol. 32, No. 4, pp. 855-865.

Geudtner, D. (1995). Die interferometrische Verarbeitung von SAR-Daten des ERS-1, DLR-Forschungsbericht, 95-28, Oberpfaffenhofen, DLR.

Geudtner, D., Vachon, P. W., Mattar, K. E., Gray, A. L. (1998). RADARSAT Repeat-Pass SAR Interferometry, in: *Proc. IGARSS '98*, Seattle, USA, 1998, pp. 1635-1637, available on CD-ROM.

Geudtner, D., Vachon, P. W., Mattar, K. E., Schättler, B., Gray, A. L. (2001). Interferometric Analysis of RADARSAT Strip-Map Mode Data, *Canadian Journal of Remote Sensing*, Vol. 27, No. 2, pp. 95-108.

Goldstein, R. (1995). Atmospheric limitations to repeat-track radar interferometry, *Journal of Geophysical Research*, Vol. 22, pp. 2517-2520.

Goldstein, R. M., H. A. Zebker and C. L. Werner (1988). Satellite radar interferometry: two-dimensional phase unwrapping, *Radio Science*, Vol. 23, No. 4, pp. 713-720.

Gray, L., K. Mattar and N. Short (1999). Application and limitations of speckle tracking as an interferometric technique for 2-dimensional ice motion studies in polar regions, in: *Proc. FRINGE '99*, http://www.esa.int/fringe99.

Hagberg, J. O., L. M. H. Ulander and J. I. H. Askne (1995). Repeat-Pass SAR Interferometry Over Forested Terrain, *IEEE Transactions on Geoscience and Remote Sensing*, Vol. 33, No. 2, pp. 331-340, March 1995.

Hanssen, R. (1998). Atmospheric heterogeneities in ERS tandem SAR interferometry, DEOS Report, 98.1, Delft, The Netherlands, DEOS.

Hanssen, R. (1999). High-resolution water vapor mapping from interferometric radar measurements, *Science*, Vol. 238, No. 5406, pp. 1297-1298.

Hanssen, R. and R. Bamler (1999). Evaluation of Interpolation Kernels for SAR Interferometry, *IEEE Transactions on Geoscience and Remote Sensing*, Vol. 37, No. 1, pp. 318-321, Jan. 1999.

Hawkins, R. K., J. Wolfe, K. P. Murnaghan and W. Jefferies (2001). Exploring the Elevation Beam Overlap Region in RADARSAT-1 ScanSAR, in: *Proc. CEOS SAR Workshop 2001*, Tokyo, Japan, 2-5 April 2001.

Hensley, S., P. A. Rosen and E. Gurrola (2000). The SRTM Topographic Mapping Processor, in: *Proc. IGARSS '00*, Honolulu, Hawaii, USA, 24-28 July 2000, IEEE International, available on CD-ROM.

Holzner, J. and R. Bamler (2002). Burst-Mode and ScanSAR Interferometry, *IEEE Transactions on Geoscience and Remote Sensing*, Vol. 40, No. 9, pp. 1917-1934, September 2002.

Holzner, J., S. Suchandt, M. Eineder, H. Breit and N. Adam (2001). Co-registration - Geometrical Analysis and Verification for SAR Interferometry Under SRTM Data Conditions, in: *Proc. IGARSS'01*, Sydney, Australia, 9-13 July 2001.

Horstmann, J., W. Koch, S. Lehner and R. Tonboe (2001). Coastal high resolution wind fields retrieved from RADARSAT-1 ScanSAR, in: *Proc. IGARSS '01*, Sydney, Australia, 9-13 July 2001, IEEE 2001 International, Vol. 4, pp. 1747-1749, available on CD-ROM.

Jin, M. Y. (1992). An analysis of the focusing performance of Magellan SAR image data, in: *Proc. IGARSS'92*, Houston, Texas, IEEE, pp. 610-613.

Jin, M. Y. (1994). PRF ambiguity determination for Radarsat ScanSAR system, in: *Proc. IGARSS '94*, Pasadena, CA, USA, August 1994, IEEE International, pp. 1964-1966.

Jin, M. Y. (1996). Optimal Range and Doppler Centroid Estimation for a ScanSAR System, *IEEE Transactions on Geoscience and Remote Sensing*, Vol. 34, No. 2, pp. 479-488, March 1996.

Jordan, R. L., E. R. Caro, Y. Kim, M. Kobrik, Y. Shen, F. V. Stuhr and M. U. Werner (1996). Shuttle radar topography mapper (SRTM), Microwave sensing and synthetic aperture radar, G. Franceschetti, C. J. Oliver, F. S. Rubertone and S. Tajbakhsh, Bellingham, SPIE, Vol. 2958, pp. 412-422.

Jordan, R. L., B. L. Huneycutt and M. Werner (1995). The SIR-C/X-SAR Synthetic Aperture Radar System, *IEEE Transactions on Geoscience and Remote Sensing*, Vol. 33, No. 4, pp. 829-839.

Just, D. and R. Bamler (1994). Phase statistics of interferograms with applications to synthetic aperture radar, *Applied Optics*, Vol. 33, No. 20, pp. 4361-4368.

Karnevi, S., E. Dean, D. J. Q. Carter and S. S. Hartley (1994). Envisat's advanced synthetic aperture radar: ASAR, *ESA Bulletin*, Vol. 76, pp. 30-35.

Karvonen, J. and M. Simila (1998). Classification of sea ice types from ScanSAR RADARSAT images using pulse-coupled neural networks, in: *Proc. IGARSS '98*, Seattle, USA, 6-10 July 1998, IEEE International, Vol. 5, pp. 2505-2508, available on CD-ROM.

Lanari, R., S. Hensley and P. A. Rosen (1998). Chirp z-transform based SPECAN approach for phase-preserving ScanSAR image generation, *IEEE Proceedings Radar, Sonar and Navigation*, Vol. 145, No. 5, pp. 254-261.

Lanari, R., M. Tesauro, E. Sansosti and G. Fornaro (2001). Spotlight SAR Data Focusing Based on a Two-Step Processing Approach, *IEEE Transactions on Geoscience and Remote Sensing*, Vol. 39, No. 9, pp. 1993-2004, September 2001.

Lancashire, D. C. (1998). ScanSAR Calibration, in: *Proc. CEOS SAR Workshop*, ESTEC, Noordwijk, The Netherlands, 3.-6. Feb. 1998, pp. 241-245.

Lee, P. F. and K. James (2001). The RADARSAT-2/3 Topographic Mission, in: *Proc. IGARSS '01*, Sydney, Australia, available on CD-ROM.

Li, S., X. Zhou, K. Morris and M. Jeffries (2001). The spatial variability of summer sea ice in the Amundsen sea seen from MODIS, RADARSAT SCANSAR and LANDSAT 7

ETM+ images, in: *Proc. IGARSS '01*, Sydney, Australia, IEEE International, Vol. 1, pp. 160-162, available on CD-ROM.

Luscombe, A. P. (1988). Taking a Broader View: RADARSAT Adds ScanSAR to its Operations, in: *Proc. IGARSS '88*, Edinburgh, Scotland, 13-16 Sept. 1988, pp. 1027-1032.

Luscombe, A. P. (1993). Using the overlap regions to improve ScanSAR calibration, in: *Proc. CEOS SAR Calibration Workshop*, ESA/ESTEC, Noordwijk, The Netherlands, ESA, Vol. ESA WPP-048, pp. 341-346.

Madsen, S. N. (1987). Spectral properties of homogeneous and non-homogeneous radar images, *IEEE Transactions on Aerospace and Electronic Systems*, Vol. AES-23, No. 4, pp. 583-588.

Madsen, S. N. (1989). Estimating the Doppler centroid of SAR data, *IEEE Transactions on Aerospace and Electronic Systems*, Vol. AES-25, No. 2, pp. 134-140.

Madsen, S. N. (1995). On absolute phase determination techniques in SAR interferometry, in: *Proc. SPIE Conference on Radar Sensor Technology*, Vol. 2487, pp. 393-401.

Madsen, S. N., H. A. Zebker and J. Martin (1993). Topographic Mapping Using Radar Interferometry: Processing Techniques, *IEEE Transactions on Geoscience and Remote Sensing*, Vol. 31, No. 1, pp. 246-255, January 1993.

Mahmood, A., G. Burger and M. Forbes (2001). RADARSAT-1 Canadian Interferometric Mission, in: *Proc. CEOS SAR Workshop 2001*, Tokyo, Japan, 2-5 April 2001, published on CD-ROM.

Mallat, S. (1997). a wavelet tour of signal processing. London, Academic Press Limited.

Marra, M., K. E. Maurice, D. C. Ghiglia and H. G. Frick (1998). Automated DEM extraction using RADARSAT ScanSAR stereo data, in: *Proc. IGARSS'98*, Seattle, USA, 6-10 July 1998, IEEE International, Vol. 5, pp. 2351 -2353.

MDA (1999). RADARSAT-2 Web Site, http://radarsat.mda.ca

Meier, E., U. Frei and D. Nüesch (1993). Cartographic Reference Systems, SAR geocoding: data and systems, G. Schreier, Karlsruhe, Wichmann, Vol., pp. 173-185.

Mittermayer, J. (2000). High Resolution Processing of Synthetic Aperture Radar Data, Electrical Engineering and Information Science, Universität-Gesamthochschule Siegen, Siegen.

Mittermayer, J., A. Moreira, G. W. Davidson and R. Bamler (1996). SIR-C ScanSAR Processing, DLR-Research Report, 96-25, Oberpfaffenhofen, DLR.

Monti Guarnieri, A. and A. Ferretti (2000). Visibility of Permanent Scatterers by ScanSAR, in: *Proc. EUSAR 2000*, Munich, Germany, 23-25 May 2000, pp. 725-728.

Monti Guarnieri, A. and P. Guccione (2001). Optimal "focusing" of low resolution ScanSAR, *IEEE Transactions on Geoscience and Remote Sensing*, Vol. 39, No. 3, pp. 672-683, March 2001.

Monti Guarnieri, A. and C. Prati (1996). ScanSAR focusing and interferometry, *IEEE Transactions on Geoscience and Remote Sensing*, Vol. 34, No. 4, pp. 1029-1038.

Monti Guarnieri, A., C. Prati and F. Rocca (1994). Interferometry with ScanSAR, *EARSeL Newsletter*, No. 20, Dec. 1994.

Monti Guarnieri, A., C. Prati and F. Rocca (1995). Interferometry with ScanSAR, in: *Proc. IGARSS '95*, pp. 550-552.

Monti Guarnieri, A. and C. Prati (1997). SAR interferometry: A 'quick and dirty' coherence estimator for data browsing, *IEEE Transactions on Geoscience and Remote Sensing*, Vol. 1997, No. 35, pp. 3.

Monti Guarnieri, A. and F. Rocca (1999). Combination of Low- and High-Resolution SAR Images for Differential Interferometry, *IEEE Transactions on Geoscience and Remote Sensing*, Vol. 37, No. 4, pp. 2035-2049, July 1999.

Monti Guarnieri, A., F. Rocca, P. Guccione and C. Cafforio (1999). Optimal interferometric ScanSAR focussing, in: *Proc. IGARSS '99*, Hamburg, available on CD-ROM.

Moore, R. K., J. P. Claassen and Y. H. Lin (1981). Scanning spaceborne synthetic aperture radar with integrated radiometer, *IEEE Transactions on Aerospace and Electronic Systems*, Vol. 17, No. 3, pp. 410-420.

Moreira, A., J. Mittermayer and R. Scheiber (1996). Extended Chirp Scaling algorithm for air- and spaceborne SAR data processing in stripmap and ScanSAR image modes, *IEEE Transactions on Geoscience and Remote Sensing*, Vol. 34, No. 5, pp. 1123-1136.

NASDA (2002). ALOS PALSAR Characteristics, http://www.eorc.nasda.go.jp/ALOS/about/2palsar.htm

Nazarenko, D. M., G. Mitchell and G. C. Staples (1997). Use of RADARSAT ScanSAR products for regional mapping in Southeast Asia, in: *Proc. IGARSS '97*, Singapore, 3-8 August 1997, IEEE International, Vol. 2, pp. 1060-1062, available on CD-ROM.

Papathanassiou, K. P., S. R. Cloude and A. Reigber (2000). Single and Multi-baseline Polarimetric SAR Interferometry over Forested Terrain, in: *Proc. EUSAR 2000*, Munich, 23-25 May 2000, pp. 123-126.

Polidori, L. (1991). Description of Terrain as a Fractal Surface, and Application to Digital Elevation Model Quality, *Photogrammetric Engineering & Remote Sensing*, Vol. 57, No. 10, pp. 1329-1332, October 1991.

Popper, K. R. (1963). Conjectures and Refutations. London, Routledge.

Prati, C. and F. Rocca (1992). Range resolution enhancement with multiple SAR surveys combination, in: *Proc. IGARSS'92*, Houston, Texas, IEEE, pp. 1576-1578.

Raney, R. K., A. P. Luscombe, E. J. Langham and S. Ahmed (1991). RADARSAT, *Proceedings of the IEEE*, Vol. 79, No. 6, pp. 839-849, June 1991.

Reed, I. S. (1962). On a Moment Theorem for Complex Gaussian Processes, *IRE Transactions on Information Theory*, pp. 194-195, April 1962.

Rocca, F., C. Prati and A. Monti-Guarnieri (1989). New algorithms for processing of SAR data, 7998/88/F/FL(SC), ESA/ESRIN.

Rodriguez, E. and J. M. Martin (1992). Theory and design of interferometric synthetic aperture radars, *IEE Proceedings-F*, Vol. 139, No. 2, pp. 147-159.

Rosen, P. A., S. Hensley, I. R. Joughin, K. L. Fuk, S. N. Madsen, E. Rodriguez and R. M. Goldstein (2000). Synthetic Aperture Radar Interferometry, *Proceedings of the IEEE*, Vol. 88, No. 3, pp. 333-382, March 2000.

Roth, A. (1999). GEMOS-A System for the Geocoding and mosaicking of interferometric digital elevation models, in: *Proc. IGARSS '99*, Hamburg, Germany, available on CD-ROM.

RSI (1995). RADARSAT Data User Guide, 07/95, http://www.rsi.ca/

Rufenacht, H., R. J. Proulx and P. J. Cefola (1997). Improvement of RADARSAT Image Localization, in: *Proc. Geomatics in the era of RADARSAT*, Ottawa, Canada, 23-25 May 1997.

Rufino, G., A. Moccia and S. Esposito (1998). DEM Generation by Means of ERS Tandem Data, *IEEE Transactions on Geoscience and Remote Sensing*, Vol. 36, No. 6, pp. 1905-1912, 6. November 1998.

Runge, H., M. Werner, M. Eineder, H. Breit, S. Suchandt and D. Massonnet (2001). Advanced Synthetic Aperture Radar Observations with Clusters of SAR Satellites, in: *Proc. ISPRS Joint Workshop 'High Resolution Mapping from Space 2001'*, Hannover, Germany, 19 - 21 September 2001.

Sandven, S., M. Lundhaug, O. Dalen, J. Solhaug, K. Kloster, V. Alexandrov, V. V. Melentyev and Bogdanov (1998). Sea ice investigations in the Laptev Sea using RADARSAT ScanSAR data, in: *Proc. IGARSS '98*, Seattle, USA, 6-10 July 1998, Vol. 5, pp. 2499-2501, available on CD-ROM.

Scheiber, R. and A. Moreira (2000). Co-registration of interferometric SAR images using spectral diversity, *IEEE Transactions on Geoscience and Remote Sensing*, Vol. 38, No. 5, pp. 2164-2178, September 2000.

Schreier, G. (1993). Geometrical Properties of SAR images, SAR geocoding: data and systems, G. Schreier, Karlsruhe, Wichmann, Vol., pp. 103-134.

Schwäbisch, M. (1995). Die SAR-Interferometrie zur Erzeugung digitaler Geländemodelle, DLR-Forschungsbericht, 95-25, Oberpfaffenhofen, DLR.

Seymour, M. (1999). Refining Low-Quality Digital Elevation Models Using Synthetic Aperture Radar Interferometry, PhD Thesis, University of British Columbia, Vancouver, Canada.

Seymour, M. and I. G. Cumming (1998). UPDATING DEM's with RADARSAT INTERFEROMETRY DATA, in: *Proc. Radarsat ADRO Final Symposium*, Montreal, 13-15 October 1998, available on CD-ROM.

Shimada, M., T. Tadono and M. Matsuoka (2002). Calibration and Validation of PALSAR, in: *Proc. IGARSS'02*, Toronto, Canada, 24-28 June 2002, IEEE international, available on CD-ROM.

Thompson, A. A., A. P. Luscombe, K. James and P. Fox (2001). New Modes and Techniques of the RADARSAT-2 SAR, in: *Proc. IGARSS '01*, Sydney, Australia, 16.-20. July 2001, available on CD-ROM.

Tomiyasu, K. (1978). Tutorial review of synthetic-aperture radar (SAR) with applications to imaging of the ocean surface, *Proceedings of the IEEE*, Vol. 66, No. 5, pp. 563-583.

Tomiyasu, K. (1981). Conceptual performance of a satellite borne, wide swath synthetic aperture radar, *IEEE Transactions on Geoscience and Remote Sensing*, Vol. GE-19, No. 2, pp. 108-116.

Touzi, R. and A. Lopes (1996). Statistics of the Stokes parameters and the complex coherence parameters in one-look and multilook speckle fields, *IEEE Transactions on Geoscience and Remote Sensing*, Vol. 34, No. 2, pp. 519-531.

Touzi, R., A. Lopes, J. Bruniquel and P. W. Vachon (1999). Coherence estimation for SAR imagery, *IEEE Transactions on Geoscience and Remote Sensing*, Vol. 37, No. 1, pp. 135-149, January 1999.

USGS (1993). Digital Elevation Models, Data Users Guide, U. S. Dept. Interior Geological Survey, http://mapping.usgs.gov/www/products/dgeosp1.html

Vachon, P. W. and D. Geudtner (1996). RADARSAT SAR Interferometry, http://www.ccrs.nrcan.gc.ca/ccrs/tekrd/rd/ana/interfer/interfre.html

Wegmüller, U. and C. L. Werner (1997). Retrieval of vegetation parameters with SAR interferometry, *IEEE Transactions on Geoscience and Remote Sensing*, Vol. 35, No. 1, pp. 18-24, January, 1997.

Werner, M. (2000). Shuttle Radar Topography Mission (SRTM) Mission Overview, in: *Proc. EUSAR 2000*, Munich, Germany, 23-25 May 2000, pp. 209-212.

Williams, D. R. (2001). Magellan Mission to Venus, http://nssdc.gsfc.nasa.gov/planetary/magellan.html

Wong, F., D. Stevens and I. G. Cumming (1997). Phase-preserving processing of ScanSAR data with modified range Doppler algorithm, in: *Proc. IGARSS'97*, Singapore, IEEE, pp. 725-727.

Woodhouse, I. H. (2000). Stop, look and listen: auditory perception analogies for radar remote sensing, *International Journal of Remote Sensing*, Vol. 21, No. 15, pp. 2901-2913.

Wolfram, S. (1999). The Mathematica Book, Wolfram Media/ Cambridge University Press.

Wornell, G. W. (1993). Wavelet-based representations for the 1/f family of fractal processes, *Proceedings of the IEEE*, Vol. 81, No. 10, pp. 1428-1450.

Zebker, H. A. and R. M. Goldstein (1986). Topographic mapping from interferometric synthetic aperture radar observations, *Journal of Geophysical Research*, Vol. 91, No. B 5, pp. 4993-4999.

Zebker, H. A. and P. Rosen (1994). On the derivation of coseismic displacement fields using differential radar interferometry: the Launders earthquake, in: *Proc. IGARSS'94*, Pasadena, CA, USA, IEEE, pp. 286-288.

Zebker, H. A. and J. Villasenor (1992). Decorrelation in interferometric radar echoes, *IEEE Transactions on Geoscience and Remote Sensing*, Vol. 30, No. 5, pp. 950-959.

Zebker, H. A., C. L. Werner, P. A. Rosen and S. Hensley (1994). Accuracy of topographic maps derived from ERS-1 interferometric radar, *IEEE Transactions on Geoscience and Remote Sensing*, Vol. 32, No. 4, pp. 823-836.